## 2.7 HYPOTHETICAL ACCIDENT CONDITIONS

It was shown in the preceding section that the load combinations for normal conditions of transport do not induce stresses or stress intensities in excess of allowables. Therefore, it is concluded that the effectiveness of the HI-STAR 100 System is not reduced under normal conditions of transport.

The hypothetical accident conditions, as defined in 10CFR71.73 and Regulatory Guide 7.9, are applied to the HI-STAR 100 System in the required sequence. The system is first subjected to a 9 meter (30 foot) drop in the most damaging orientation, then subject to a 1 meter (40 inch) drop onto a 6 inch diameter mild steel pin (of length sufficient to cause damage to the steel structure), followed by a 1475°F temperature fire environment for 30 minutes, and finally to a water immersion test.

The overpack containment boundary is also subjected to deep immersion in accordance with 10CFR71.61.

It is shown in the following subsections that the HI-STAR 100 System meets the standards set forth in 10CFR71, when it is subjected to the hypothetical accident conditions specified in 10CFR71.73. In particular, sufficient analytical and experimental evidence is presented herein to support the conclusion that HI-STAR 100 packaging, when subjected to hypothetical accident conditions, has adequate structural integrity to satisfy the subcriticality, containment, shielding, and temperature requirements of 10CFR71.

### 2.7.1 Free Drop

In this section the performance and structural integrity of the HI-STAR 100 System is evaluated for the most severe drop events. The drop events that are potentially most damaging are the end drops (top or bottom), the side drop, the orientation for which the center of gravity is directly over the point of impact, an oblique drop where the angle of impact is somewhere between center of gravity over corner and a near side drop, and an orientation where package rotation after an impact at one end induces a larger impact deceleration when the other end impacts the target (e.g., slapdown).

The structural assessment of the package is performed in two parts. In the first part, a numerical model to simulate the drop events is prepared and benchmarked against 1/8 scale static tests of the HI-STAR 100 impact limiters, and ¼-scale dynamic drop tests of the HI-STAR 100 Package. This numerical/experimental effort is carried out to confirm that the maximum rigid body decelerations experienced by the package are less than the design basis values set forth in Table 2.1.10. In the second part, the structural integrity of components under the inertia loads due to design basis deceleration levels is evaluated. The deceleration sustained by the internals, such as the fuel basket, are further amplified in recognition of the elasticity of the internal structures. The dynamic amplifier is considered as an added multiplier on the rigid body deceleration in the structural assessments. *Dynamic amplifiers applicable to components of the package have been developed from evaluating the behavior of simplified models.* ~~Appendix 2.K provides the appropriate dynamic amplifiers for each component.~~

Part One: Maximum Rigid Body Deceleration Under 10CFR71.73 Free Drop Event

The determination of the AL-STAR impact limiter performance under postulated 10CFR71.73 free drop events was carried out in six phases as summarized below and further elaborated in Appendix 2.~~A~~H.

i. Characterize honeycomb material crush behavior: Coupons of both unidirectional and cross-core honeycomb materials at different nominal crush strength values were prepared and tested. A typical pressure vs. deflection curve is shown in Figure 2.~~A~~H.2.1 in Appendix 2.~~A~~H. The pressure in the flat portion of the curve denotes the crush pressure.

Mathematical correlation of the data from the population of coupons tested showed that the pressure/crush curve for a honeycomb stock can be represented by one equation wherein the crush pressure, $p_c$, is the sole variable. This commonality in the deformation characteristic of the AL-STAR honeycomb materials of different crush strength is extremely helpful in simplifying the dynamic model for the impact limiter.

ii. AL-STAR Force-Crush Relationship: The AL-STAR impact limiter is a radially symmetric structure whose external and internal diameters are fixed: the I.D. is set by the overpack diameter at its extremities and the O.D. is limited by rail transport considerations to 128". Within this annular space, the arrangement of the aluminum honeycomb material is specified so that the impact limiter can absorb the kinetic energy from a 30' drop event in *any* orientation. The axial dimension of the impact limiter is also limited by considerations of the overall weight of the packaging. To design the impact limiter within the above-mentioned constraints called for a method to predict the force required to crush the impact limiter by a given amount in any given orientation. The mathematical model to define the force-crush (F-d) curve is described in Appendix 2.~~A~~H. The F-d model was used to establish the nominal crush strengths of the honeycomb sectors used in the various locations of the AL-STAR honeycomb volume to obtain the desired energy absorption characteristics in the equipment.

iii. Static Scale Model Tests: The static 1/8 scale model tests consisted of preparing 1/8 scale models of the AL-STAR impact limiter and subjecting them to static crush tests in various orientations under normal and abnormal temperature conditions. One object of these tests was to confirm the validity of the theoretical F-d model. Confirming the structural adequacy of the AL-STAR backing structure (which is a thick carbon steel weldment) and the external skin were also objectives of the scale model test. The 1/8 scale static tests, as described in Appendix 2.~~A~~H, met all project goals: a weakness in the AL-STAR backing structure was identified and corrected in a redesign of the backing structure. The test data also showed that Holtec's F-d model provided a reasonably accurate analytical tool to predict the static crushing behavior of AL-STAR in the various potential crushing orientations. The adequacy of the F-d model to predict static crush behavior was an essential prerequisite for the dynamic test correlation effort that followed.

iv. Dynamic Scale Model Tests: A 1/4 scale model of the HI-STAR 100 Package, including AL-STAR impact limiters, was used for drop testing. The drawings for the 1/4 scale impact limiters are provided in Section 1.4. Appendix 2.~~A~~H herein provides a complete synopsis of the AL-STAR impact limiter design development program, including the 1/4 scale model drop tests which demonstrated the performance of the package. The objectives of the drop tests may be stated as follows:

i. Select a sufficient number of drop orientations to ensure that under the worst-case orientations, the structural adequacy of the package is demonstrated by testing.

ii. Prove that the peak rigid body decelerations experienced by the package in any of the tests is below the Table 2.1.10 design basis value.

iii. Demonstrate that the impact limiters prevent the cask from direct contact with the unyielding surface and remain attached through the end of the drop event.

Four drop configurations, namely, vertical (top end), horizontal (side), center-of-gravity-over-corner (CGOC), and slap-down (fully described in Appendix ~~2.H~~2.*A*) were identified as a complete set capable of realizing the aforementioned objectives. The tests were performed in two distinct series as described below.

The first test series, conducted in August 1997, indicated the need to modify the honeycomb material crush strength utilized. The first dynamic test series also helped quantify the dynamic multiplier applicable to the statically determined honeycomb crush strength under impact conditions.

The second test series showed that the peak deceleration in all four drop orientations tested met the Table 2.1.10 limits. Despite meeting deceleration limits, the attachment bolts between the bottom impact limiter and the overpack failed in the side drop test. This required an additional design improvement to the bottom impact limiter-to-overpack attachment design, and re-performance of the side drop test. For the final four tests used for evaluation in Appendix ~~2.H~~2.*A*, no attachment bolts sustained a failure.

v. AL-STAR Dynamic Response Model: The 1/4 scale tests provided valuable information on the package response which was used to confirm the veracity of Holtec's dynamic simulation model developed for predicting the package response under the other drop conditions. Like all orthotropic materials, the crushing of the honeycomb requires greater force under an impact load than the load necessary to achieve the same extent of crush under static conditions. The conversion of the static "force (F) - crush (d)" model to dynamic conditions simply means applying a dynamic factor to the formula. In other words, under dynamic conditions, the relation between crush force "F" and crush "d" is given as:

$$F = Z\, f(d)$$

where f(d) is the crush force corresponding to the compression "d" under static conditions and Z is the dynamic multiplier function. The value of Z was quantified by the first series of 1/4 scale dynamic scale model test, such that a dynamic response simulation model could be developed that satisfied all equilibrium expectations.

In addition to comparing the predicted peak decelerations with the measured value, the duration of crushing and crush depth predicted by the dynamic model were also compared with the measured test data. The comparisons, presented in Appendix ~~2.H~~2.*A*, confirm the ability of the dynamic model to simulate the behavior of the package under a drop event.

vi. Sensitivity Studies: A significant result from the 1/4 scale model dynamic tests was a complete validation of the dynamic model. For every test performed, the AL-STAR dynamic model was able to simulate the peak accelerations, total crush, *and* crush duration with reasonable agreement. The experimentally benchmarked mathematical model could now be used to simulate drop events for a variety of HI-STAR 100 package weights and honeycomb crush strengths. Results of the simulations to determine the effects of variations in aluminum honeycomb crush strengths and package weights are presented in Appendix ~~2.H~~2.*A*.

The results summarized in Table ~~2.H~~2.*A*.5 of Appendix ~~2.H~~2.*A*.~~5~~ demonstrates that the maximum rigid body deceleration experienced by the HI-STAR 100 package equipped with the AL-STAR impact limiter (whose design is fully articulated in *the applicable drawing*~~Holtec Drawing 1765,~~ in Section 1.4 herein) will be less than 60g's regardless of the orientation of impact. Therefore, in the balance of analyses performed to evaluate the consequences of "free drop" under the provisions of 10CFR71.73, the package will be assumed to be subject to a rigid body deceleration equal to 60 g's. It is clear from inspection of the geometry of the package that the most vulnerable direction of inertia loading for the HI-STAR fuel basket is the transverse direction wherein the flat panels of the basket are subjected to lateral inertia loading from the contained SNF. As mentioned earlier, the flexibility of basket panel acts to further amplify the package deceleration, which must be considered in the evaluation of results from the stress analysis model. In summary, the net result of the work effort described in the foregoing and further elaborated in Appendix ~~2.H~~2.*A* was to confirm the validity of 60g as the *design basis* rigid body deceleration for the 10CFR71.73 drop event.

In Appendix ~~2.H~~2.*A*, additional supporting technical information requested in Paragraph 2.7 of Reg. Guide 7.9 is provided. Information provided includes free-body diagrams, sketches, governing equations, test method for model testing, scaling factors, discussion of the law of similitude, measurements of crush, impact duration, deceleration histograms, effect of tolerances on package response, and demonstration that the model test will give conservative results for peak g-force and maximum deformation.

Additionally, Reg. Guide 7.9 calls for evaluation of the response of the package in terms of stress and strain to components and structural members, including investigation of structural stability as well as the consequences of the combined effects of temperature gradients, pressure, and other loads. Part Two of the work effort, described in the following, fulfills the above Reg. Guide 7.9 stipulations.

Part Two: Stress Analysis

The second part of the analysis is performed using the ANSYS finite element software [2.6.4]. The MPC and overpack models used here are identical to those presented in Section 2.6. The loads are applied to the models in accordance with the load combinations defined in Table 2.1.6 (Load Cases F3), Table 2.1.7 (Load Cases E3), and Table 2.1.9 (Load Cases 1-16) for hypothetical accident conditions of transport. The detailed application of each load case is described in the subsections that follow. The presentation and content follows the formatting requirements of Regulatory Guide 7.9. The results from conditions of "Heat" ether in the following presentation.

The analysis of the different hypothetical accident conditions of transport are carried out using general finite element models of the MPC and the overpack as well as calculations based on simplified models amenable to strength of materials solutions. The analyses using strength of materials solutions focus on specific loading conditions applied to component parts of the MPC and/or the overpack ~~and are reported in detail in a series of appendices. The finite element solutions are presented as a series of tables in Appendices 2.AC (for the MPC) and 2.AE (for the overpack)~~. The finite element analysis of the overpack involves a complex 3-D model of the overpack to which a series of loads are applied. The results from the solutions are then combined in a post-processing phase to make up the different accident load combination. Given the complexity of the overpack finite element analysis model, some discussion of the *stress report* ~~output format and the stress report locations~~ is presented to facilitate an understanding of the conclusions. For each of the load combinations ~~reported in Appendix 2.AE~~, the following components are identified for reporting purposes:

1. Seal
2. Bolts
3. Lid
4. Inner Shell (including the top flange)
5. Intermediate Shells
6. Baseplate
7. Enclosure

The postprocessor collects the nodal stresses *from the finite element solution,* for each of the components in turn, and reports the principal stresses and the stress intensity at selected locations where physical reasoning suggests that high stresses may occur under the different postulated load combinations. In order to identify the minimum safety factor for each of the above components after the load cases are combined, the collection of nodes is sorted by stress intensity magnitude in descending order. Therefore,

since the hypothetical accident condition load combinations involve a comparison of primary stress intensities, a minimum safety factor for each of the defined components in the model may be identified as occurring at the node point with the largest calculated stress intensity. Safety factors are computed using the allowable stress intensities for the material at the reference temperature identified for the component *and reported under one of the seven groups identified above.* ~~Each table in Appendix 2.AE sorts the relevant nodes within the seven component groups identified above. Appendix 2.P contains a table relating the model node numbers to so called "stress report" locations. These stress report locations are then identified by location on the model in two figures in Appendix 2.P. In this manner, a safety factor can be identified with a physical location with little difficulty.~~ *The post-processor collects, sorts, and reports the necessary information to enable documentation of the satisfaction of the applicable requirements.* The following items are collected *and evaluated* ~~in each of the tables in Appendix 2.AE~~*for* ~~concerned with~~ *each* ~~a particular~~ load combination:

Seals: The normal force in each of the springs representing the seal is reported and shown to remain in compression under the load. Maintaining a compressive load in the seal springs assures that there is no separation at the component interfaces.

Bolts: The bolts are initially preloaded by applying an initial strain sufficient to result in the desired pre-stress. Subsequent to the application of the different loads to form a specified load combination, the bolts are shown not to unload.

Lid: For each load combination, the lid primary membrane plus primary bending stress intensities are compared to the allowable values at the designated reference temperature.

Inner Shell: Primary membrane and primary membrane plus bending stress intensity distributions are examined and compared to allowable stress intensity values

Intermediate Shells: The five intermediate shells are examined at stress location points and compared to allowable stress intensities at the appropriate reference temperature. Since accident conditions of transport represent a Level D condition (where the comparison of calculated value vs. allowable value is always based on stress intensity), there is no differentiation between intermediate shells considered as Class 1 or Class 3 components.

Baseplate: Primary membrane plus bending stress intensities are compared to allowable values at the component reference temperature.

Enclosure: The plate and shell elements making up the enclosure for the Holtite-A material are compared to primary membrane stress intensity allowable values.

In the finite element analysis of all load combinations associated with hypothetical accident events, the initial preload case of the bolts and the internal pressure case are included in the final combination. Since no

secondary stresses need be evaluated per the ASME Code requirements for an accident level event, the thermal stress load case for the "Heat" condition is not included as a specific load case. However, the allowable stress intensities used for the safety factor evaluation are obtained at the appropriate "Hea condition reference temperature. In the reporting of safety factors, the variation in allowable stress intensity with temperature is ignored; this introduces an additional measure of conservatism in the reported safety factors since the reference temperatures (Table 2.1.21) are higher than the actual calculated temperatures. For the "Cold" condition, there are no temperature gradients developed. The interaction stresses developed to maintain compatibility under the uniform ambient temperature change are included in the analysis and are treated as primary stresses in the evaluation of the safety factor.

2.7.1.1 End Drop

- Overpack Stress (Load Cases 1,2,9, and 10 in Table 2.1.9)

The overpack is evaluated under both a top end drop and a bottom end drop. In both cases, the impact limiter reaction is assumed to act over the entire area that is backed by structural metal. Given that the total dropped weight is W and that the maximum acceleration is A, the impact

$$|R| = \frac{WA}{g}$$

limiter total reaction load follows from force equilibrium.
This reaction load R is imposed on the appropriate region of the overpack (either lid outer surface or bottom plate outer surface as a uniform pressure load to maximize the bending of the lid or bottom plate.

Since the same finite element model described and used in Section 2.6 for evaluation of loading associated with normal conditions of transport is used here with different applied loads, no further discussion of the model or the analysis methodology is required. Figures 2.1.7 and 2.1.8 show the loading on the overpack in the bottom down and the top down configurations, respectively. The results of the analyses for the top end and bottom end drops are *collected*~~presented in Appendix 2.AE~~ and safety factors from the limiting locations in the model are *reported* in Tables 2.7.5 and 2.7.6 for both heat and cold environments. Table 2.7.5 presents the minimum safety factors for each of the components identified above for the "Heat" condition and Table 2.7.6 presents the safety factors for the "Cold" condition. Within each table, the component is identified, *and* the minimum safety factor reported~~, and the table in Appendix 2.AE identified.~~

- Overpack Stability

Structural stability of the overpack containment inner shell under the end drop is assessed~~ in Appendix 2.J. Appendix 2.J contains a complete stability analysis of the HI-STAR 100 System.~~ The case of the accident end drop ~~(Case 1 in Appendix 2.J)~~ is evaluated for elastic and plastic stability in accordance with the *methodology of* ASME Code Case N-284 [2.1.8]. All required interaction equation requirements set by

[2.1.8] are met. *For this event,*~~It is shown in Appendix 2.J that~~ yield strength limits rather than instability limits govern the minimum safety factor. The minimum safety factor for this case is summarized below:

| Code Case N-284 Minimum Safety Factors - (Load Case 1 and 2 in Table 2.1.9) | | | |
|---|---|---|---|
| Item | Calculated Interaction Value | Allowable Interaction Value† | Safety Factor against Yield† |
| Load Case 1 and 2 in Table 2.1.9 | 0.607 | 1.34 | 2.21 |

†~~We~~ *N*~~n~~ote that in computing the safety factor against yield for this table,~~ we have included~~ the safety factor implicit in the Code Case N-284 allowable interaction equation *is included.*~~We~~ *N*~~n~~ote also that the safety factors given above from the Code Case analysis are all safety factors against the circumferential or longitudinal stresses reaching the material yield stress. The actual safety factors against instability are larger than the factors reported in the table.~~ as can be seen by a perusal of Appendix 2.J~~ In other words, yield strength rather than stability is the limiting condition. Finally, ~~we~~ note that fabrication stresses have been included in the stability calculations even though these stresses are self-limiting. Therefore, all results corresponding to the calculated stability interaction equations ~~in Appendix 2.J~~ are very conservative.

The result for the heat environment bound the similar result for the cold environment since yield strengths and elastic modulus are higher. Therefore, no analysis is performed for stability under cold conditions.

- Closure Bolt Analysis

Stresses are developed in the closure bolts due to pre-load, pressure loads, temperature loads, and accident loads. Closure bolts are explored in detail in Reference [2.6.3], which deals with the analysis of shipping casks. The analysis of the overpack closure bolts under normal conditions of transport has been reported in Section 2.6. *T*~~In~~ this subsection ~~, we~~ present*s* the results for the analysis for the hypothetical accident end drop. The analysis ~~is reported in detail in Appendix 2.U and~~ follows the procedures defined in Reference [2.6.3]. The allowable stresses used for the closure bolts follows that reference. Note that the analyses ~~in Appendix 2.U~~ provide alternative confirmation of the results from the finite element analysis; namely, under any of the identified load combinations, the bolts do not unload.

The following combined load case *is* ~~is analyzed in Appendix 2.U~~ for the hypothetical top end drop accident condition of transport. This drop conservatively assumes a nearly vertical orientation with the impact limiter reaction load applied at the outermost location of the lid. This results in the closure bolts resisting the inertial load from the MPC plus contents in addition to the inertia load from the closure lid itself. In reality, the load from the MPC would not load the bolts.

Top End Drop: Pressure, temperature, and pre-load loads are included.

Reference [2.6.3] reports safety factors defined as the calculated stress divided by the allowable stress for the load combination. This definition of safety factor is the inverse of the definition consistently used in this SAR. In summarizing the closure bolt analyses ~~performed in Appendix 2.U, we report~~ results *are reported* using the safety factor definition of allowable stress divided by calculated stress. The following result for closure lid bolting for the top end drop hypothetical accident condition of transport is obtained. ~~from Appendix 2.U.~~

| Overpack Closure Bolt - Safety Factor (Load Case 2 in Table 2.1.9) | |
|---|---|
| Combined Load Case | Safety Factor on Bolt Tension |
| Average Tensile Stress | 1.30 |

It is seen from the above table that the safety factor is greater than 1.0 as required. Note that the average tensile stress reflects the preload stress required for successful performance of the bolts as well as the applied load from the hypothetical accident drop event.

- MPC Fuel Basket Stability and Stress (Load Case F3.a in Table 2.1.6)

Under top or bottom end drop in a hypothetical accident condition of transport, the MPC is subject to its own amplified self-weight, causing compressive longitudinal stress in the fuel basket cell walls. The following analysis demonstrates that stability or yield is not a credible safety concern in the fuel basket walls under a hypothetical end drop accident condition of transport.

MPC Fuel Basket Stability

Stability of the basket panels, under longitudinal deceleration loading (Load Cases F3.a in Table 2.1.6), is demonstrated in the following manner. ~~From~~ Table 2.2.1 *provides* ~~we have~~ the weight of each fuel basket (including sheathing and Boral). The *corresponding* metal areas of the basket bearing on the MPC baseplate *or top lid* can be computed *for each MPC basket by direct calculation from the appropriate drawings* ~~from the drawings in Section 1.4~~. Dividing weight by *bearing* area and multiplying by the design basis deceleration for the hypothetical accident from Table 2.1.10 gives the *axial stress in the load bearing walls. The results for each basket are compared and the* ~~following~~ *bounding* result *(maximum weight/area) reported below* ~~s~~:~~.~~

| Fuel Basket Compressive Stress For End Drop (Load Case F3.a) | | | |
|---|---|---|---|
| Item | Weight (lb.) | *Bearing* Area (sq. inch) | Stress (psi) |
| *Bounding Basket (at 60g's deceleration)*~~MPC-68~~ | *23,535*~~15,263~~ | *346.61*~~244.9~~ | *4,074*~~3,739~~ |
| ~~MPC-24~~ | ~~17,045~~ | ~~295.7~~ | ~~3,458~~ |

To demonstrate that elastic instability in the basket panels is not credible, ~~we~~ compute the flat panel buckling stress, $\sigma_{cr}$, (critical stress level at which elastic buckling may occur) using the formula in reference [2.6.1].

For elastic stability, Reference [2.6.1] provides the formula for critical axial stress as

$$\sigma_{cr} = \frac{4\pi^2 E}{12(1-\nu^2)}\left(\frac{T}{W}\right)^2$$

where T is the panel thickness and W is the width of the panel, E is the Young's Modulus at the metal temperature and $\nu$ is the metal Poisson's Ratio. The following table summarizes the calculation for the critical buckling stress using the formula given above:

| Elastic Stability Result for a Flat Panel | |
|---|---|
| Reference Temperature | 725 degrees F |
| T(*Bounding basket)*~~MPC-24)~~ | 5/16 inch |
| W *(bounding width)* | 1*1.0*~~0.777~~ inch |
| E | 24,600,000 psi |
| Critical Axial Stress | 7*1,843*~~4,781~~ psi |

It is noted *that* the critical axial stress is an order of magnitude greater than the computed basket axial stress reported in the foregoing. Therefore, it is demonstrated that elastic stability under hypothetical accident condition of transport longitudinal deceleration inertia load is not a concern.

- MPC Fuel Basket Stress

The safety factor against yielding of the basket under longitudinal compressive stress from a design basis inertial loading is given by

SF = 17,100/*4,074*~~3739~~ = 4.*19*~~857~~

where the yield stress of Alloy X has been taken from Table 2.3.1 at 725 degrees F.

Therefore, plastic deformation of the fuel basket under design basis deceleration is not credible.

*Analyses of the Damaged Fuel canisters to be transported in the HI-STAR 100 Package are performed to demonstrate structural integrity under an end drop condition. A summary of the methodology and the results for all canisters is provided in Appendix 2.B.*

- MPC Enclosure Shell Stability

Structural stability of the MPC enclosure shell under the end drop is ~~assessed in Appendix 2.J. The case of the accident end drop (Case 3 in Appendix 2.J) is~~ evaluated for elastic and plastic/-stability in accordance with the ASME Code Case N-284 [2.1.8]. All required interaction equation requirements set by [2.1.8] are met. It is shown ~~in Appendix 2.J~~ that yield strength limits rather than instability limits govern the minimum safety factor. The minimum safety factor for this case is summarized below:

| MPC Shell Elastic/Plastic Stability (Load Case E3.a Table 2.1.7) | | | |
|---|---|---|---|
| Item | Value | Allowable* | Safety Factor |
| Yield | 0.698 | 1.34 | 1.92 |

* For Load Case E3.a, the yield strength criteria in the Code Case N-284 method govern. In this event, ~~we include~~ the safety factor 1.34, built into the Code Case, *is included* in the tabular result in order to obtain the actual safety factor with respect to the yield strength of the material.

- MPC Closure Lid Stress (Load Case E3.a)

The closure lid, the closure lid peripheral weld, and the closure ring are examined for maximum stresses developed during the hypothetical end drop accident event.

~~Appendix 2.L contains stress analysis of the MPC top closure lid for Load Case E3.a .~~ The closure lid is modeled as a *single* simply supported plate and is subject to deceleration from an end drop plus appropriate design pressures. *Results are presented for both the single and dual lid configurations (in parentheses) for top end and bottom end drops* ~~Figure 2.L.1 shows the configuration considered~~. *For the dual lid configuration, the two plates each support their own amplified weight as simply supported plates under a bottom end drop. The inner lid transfers the total load to the outer plate through the peripheral weld between the two lids. Under a top end drop scenario, the inner lid is partially supported by the outer lid and the amplified load is transmitted by a combination of peripheral support and interface contact pressure.* The results for minimum safety factor are reported in the table below:

| MPC Top Closure Lid ~~B~~ Minimum Safety Factors ~~B~~ Load Case E3.a in Table 2.1.7 | | | |
|---|---|---|---|
| Item | Stress(ksi) or Load(lb.) | Allowable Stress (ksi) or Load Capacity (lb.) | Safety Factor |
| Lid Bending Stress ~~B~~ Load Case E3.a *(bottom end drop)* | 4.67*/(7.87)* | 61.05 | 13.1*/(7.76)* |
| *Lid Bending Stress* – Load Case E3.a (top end drop)* | *21.8/(43.6)* | *61.05* | *2.8/(1.4)* |
| Lid-*to-Shell* Peripheral Weld Load ~~B~~ Load Case E3.a | 624,000 | 1,477,000** | 2.37 |
| *Lid-to-Lid Peripheral Weld Load – Load Case E3.a (bottom end drop)* | *304,029* | *481,852**** | *1.58* |

* *Stress computation is conservatively based on peripheral support at the outer diameter of the MPC lid. For a top end drop, the actual support diameter is .77 of the outer diameter. Therefore, an analysis based on an overhung plate would provide stresses reduced by a multiplier of 0.59. Consequently, the safety factors would be amplified by the factor 1.69.*

** *Based on a 0.625" single groove weld and conservatively includes a quality factor of 0.45.*

*** *This is a non-Code weld; limit is based on a 0.1875 groove weld and includes a quality factor of 0.45 for additional conservatism*

Safety factors are greater than 1.0 as required. The limiting condition *for the lid bending evaluation* is a *top*~~bottom~~ end hypothetical accident end drop *because the lid supports the amplified fuel weight as well as the lid amplified self-weight*.

- MPC Baseplate and Canister Stress (Load Case E3.a)

Load Case E3.a provides the limiting accident loading on the baseplate wherein the combined effect of a 60g deceleration plus accident pressure is considered. The top end hypothetical accident condition is limiting in transport and *it is* ~~we~~ assume*d* that accident external pressure acts simultaneously. The results ~~from Appendix 2.N~~ are summarized below:

| MPC Baseplate Minimum Safety Factors – Load Cases E3, Table 2.1.7 | | | |
|---|---|---|---|
| Item | Value (ksi) | Allowable (ksi) | Safety Factor |
| Center of Baseplate - Primary Bending (Load Case E3) | 22.12 | 67.32 | 3.04 |
| Shell Bending Stress at Connection to Baseplate | 31.47 | 67.32 | 2.14 |

*Note*~~We note from the above~~ that all safety factors are greater than 1.0. Also, ~~we~~ note that the calculated stress conservatively includes both primary and secondary self—limiting stress components. For the hypothetical transport drop accident, the safety factor computed for the shell bending stress intensity need only consider the effect of primary membrane plus bending stresses *that*~~which~~ are to be compared against the ultimate stress at temperature for this ASME Code Service Level D event. Since secondary stresses have been included in the evaluation, the reported result for safety factor is conservatively low.

- *Trojan MPC Spacer*

*The Trojan MPC-24E/EF enclosure vessel is 9 inches shorter in length than the generic MPC-24E/EF enclosure vessel. Thus, when the Trojan MPC-24E/EF is transported inside the HI-STAR 100, the axial clearance between the MPC lid and the HI-STAR 100 closure plate is greater than 10 inches. In order to prevent the Trojan MPC from thrusting forward and impacting the closure plate during a top–end drop or a tip-over event (i.e., slapdown), a spacer device is positioned on top of the MPC lid. The Trojan MPC spacer*~~, which, is~~ *depicted in Figure 1.1.5, is fabricated from SA240-304 stainless steel in the shape of a circular I-beam. The web of the spacer measures 1-inch thick and has a mean diameter of 60 inches. The total height of the MPC spacer is 9 inches.*

*During a top end drop, the MPC spacer must support the amplified weight of a fully loaded Trojan MPC-24E/EF. Based on a bounding MPC weight of 90,000 lb (Table 2.2.4) and a bounding deceleration of 60g (Table 2.1.10), the maximum compressive stress in the web is computed as follows.*

*Cross-sectional area of web (A)* $= \pi \times D \times t = \pi (60)\ (1) = 188.5\ in^2$

*Amplified weight of MPC (P)* $= G \times W = (60)\ (90{,}000) = 5.4 \times 10^6\ lb$

*Compressive stress in web* $= P/A = (5.4 \times 10^6) / 188.5 = 28{,}647\ psi$

*From Table 2.1.18, the primary membrane stress intensity limit for Alloy X (of which SA240-304 is a member) under Level D conditions is 44.9 ksi at 400°F. Therefore, the safety factor against compressive failure of the Trojan MPC spacer, per ASME Code Subsection NB stress limits, is*

*SF = 44,900 / 28,647 = 1.56*

2.7.1.2 Side Drop (Load Cases F3 (Table 2.1.6), E3 (Table 2.1.7), and 3 and 11 (Table 2.1.9

- MPC Fuel Basket and Canister Finite Element Analysis (Load Cases E3.b, E3.c in Table 2.1.7 and Load Cases F3.b, F3.c in Table 2.1.6)

The MPC configurations are assessed for a hypothetical accident condition of transport side drop. All fuel cells are loaded with design basis spent nuclear fuel (SNF). Evaluations are performed for the 0 degree and the 45 degree circumferential orientations of the fuel basket as defined in Figures 2.1.3 and 2.1.4 and are obtained using the finite element model described in Section 2.6.

The results for each MPC configuration for the two different drop orientations are *evaluated* ~~presented in Appendix 2.AC in the form of tables~~ for each appropriate load case listed in Tables 2.1.6 and 2.1.7. Analyses are performed only for the hot ambient temperature condition since this is the bounding case for the MPC; as noted in Section 2.6, allowable stresses are lower for the "heat" environmental condition.

- Elastic/Plastic Stability of the MPC Fuel Basket

Following the provisions of Appendix F of the ASME Code [2.1.12] for stability analysis of Subsection NG structures, (F1331.5(a)(1)), a comprehensive buckling analysis is performed using ANSYS. For this analysis, ANSYS's large deformation capabilities are used. This feature allows ANSYS to account for large nodal rotations in the fuel basket, which are characteristic of column buckling. The large deflection option is "turned on" so that equilibrium equations for each load increment are computed based on the current deformed shape. The interaction between compressive and lateral loading, caused by the deformation, is included in a rigorous manner. Subsequent to the large deformation analysis, the basket panel that is most susceptible to buckling failure is identified by a review of the results. The lateral displacement of a node located at the mid-span of the panel is measured for the range of impact decelerations. The buckling or collapse load is defined as the impact deceleration for which a slight increase in its magnitude results in a disproportionate increase in the lateral displacement.

The stability requirement for the MPC fuel basket under lateral loading is satisfied if two-thirds of the collapse deceleration load is greater than the design basis horizontal acceleration (Table 2.1.10). Figures 2.7.1, *through* ~~2.7.2,2.7.5, and~~ 2.7.6 are plots of lateral displacement versus impact deceleration *for representative fuel baskets.* It should be noted that the displacements in Figures 2.7.1, 2.7.2, *2.73, 2.74,* and 2.7.5 are expressed in $1x10^{-1}$ inch and Figure 2.7.6 is expressed in $1x10^{-2}$ inch. The plots clearly show that the large deflection collapse load of the MPC fuel basket is greater than 1.5 times the inertia load corresponding to the design basis deceleration for all baskets in all orientations. Thus, the requirements of Appendix F are met for lateral deceleration loading under Subsection NG stress limits for faulted conditions. Therefore, *it is*~~we~~ concluded that stability of the spent fuel basket cell walls is assured under the hypothetical accident side drop (from 30') condition of transport.

An alternative solution for the stability of the fuel basket panel is obtained using the methodology espoused in NUREG/CR-6322 [2.7.3]. In particular, ~~we consider~~ the fuel basket panels *are considered* as wide plates in accordance with Section 5 of NUREG/CR-6322. ~~We use~~ *E*~~e~~q.(19) in that section *is utilized* with the "K" factor set to the value appropriate to a clamped panel. Material properties are selected corresponding to a metal temperature of 500 degrees F which bounds computed metal temperatures at the periphery of the basket. The critical buckling stress is:

$$\sigma_{cr} = \left(\frac{\pi}{K}\right)^2 \frac{E}{12(1-\nu^2)}\left(h/a\right)^2$$

where h is the panel thickness, a is the unsupported panel length, E is the Young's Modulus of Alloy X at 500 degrees F *(Table 2.3.1)*, ν is Poisson's Ratio, and K=0.65 (per Figure 6 of NUREG/CR-6322).

*P*~~We use p~~arameters appropriate to *a*~~the~~ MPC-24*E basket are used*;~~the results of the finite element stress analyses under design basis deceleration load show that this basket is subject to a large compressive load in the panel.~~ *t*~~T~~he following table shows the results from the finite element stress analysis and from the stability calculation.

| Panel Buckling Results From NUREG/CR-6322 | | | |
|---|---|---|---|
| Item | Finite Element Stress (ksi) | Critical Buckling Stress (ksi) | Factor of Safety |
| Stress | 13.*339*~~717~~ | 49.*826*~~22~~ | 3.*74*~~588~~ |

For a stainless steel member under an accident condition load, the recommended safety factor is 2.12. *It is*~~We~~ *see*n that the calculated safety factor exceeds this value; therefore, *an*~~we have~~ independent~~ly~~ confirm*ation of*~~ed~~ the stability predictions of the large deflection analysis *is obtained* based on classical plate stability *analysis*~~analysis by employing a simplified method~~.

- Overpack Stress Analysis (Load Cases 3 and 11 in Table 2.1.9)

The overpack is assumed to be subject to a 60g side drop in the manner of the load combinations of Table 2.1.9 for both heat and cold environmental conditions as prescribed by Regulatory Guide 7.9. Reaction loads provided by the impact limiters are imposed as vertical pressures at each end of the overpack on areas of the structure that serve as backing. The applied mechanical loading is internal pressure, inertia load from the MPC and inertia load from the overpack self-weight. Figure 2.1.9 shows the assumed loading for this simulation. Figures 2.7.7, and Figures 2.7.11-2.7.13 are useful to aid in understanding the methodology used to apply the MPC loads and the balancing impact limiter reactions. Figure 2.7.7 shows a view of the overpack looking along the longitudinal axis for the general case of an oblique drop. While the intent of the figure is to describe the reaction loads from the impact limiter under a general oblique drop orientation, only the features necessary to elaborate on the side drop reaction load are discussed here. A region defined by the angle θ supports the applied loading in a side drop.

This angle is 18 degrees for the side drop and is chosen based on two considerations. First, the predictions from the theoretical model at the time of maximum "g" loading are examined and a projected loaded area on the top forging and bottom plate estimated. Second, the post-drop evaluation of the tested impact limiters from the one-eighth scale static test and the one-quarter scale dynamic test were visually examined and provided insight into the extent of the loaded region of the overpack at the impact limiter-hard surface interface. From these two evaluations, a conservatively low angle estimate is made for the finite element analysis. Figure 2.7.12 shows the extent around the periphery of the loading imposed by the MPC. From Section 2.6, the angle over which the MPC load is applied to the inner shell of the overpack is 72 degrees from the vertical on each half of the overpack. This angle is determined from the detailed analysis of the MPC enclosure shell and the fuel basket under 60g loading. The inertia load from overpack self-weight is applied by imposing an amplified value for the gravitational constant. Details of the finite element model have been discussed in Section 2.6. The results of the finite element analyses for load cases 3 and 11 in Table 2.1.9, for the overpack, *are post-processed as previously discussed;* ~~are presented in Appendix 2.AE.~~ Tables 2.7.5 and 2.7.6 summarize the results for each overpack component and identify the minimum safety factors. ~~and the referenced table in Appendix 2.AE.~~

2.7.1.3 Corner Drop

Figures 2.1.10 and 2.1.11 show the assumed loading for the bottom center of gravity over corner (CGOC) drop and the top CGOC drop, respectively. The impact limiter reaction bad is applied as a pressure loading acting on two surfaces. From the geometry of the cask, with impact limiters in place, the angle of impact is 67.5 degrees from the horizontal plane. Although the theoretical and tested deceleration levels are below 60g's, the design basis 60g-deceleration load is used as the input loading and applied vertically. Therefore, a 55g load is applied along the longitudinal axis of the cask, and a 23g load is applied perpendicular to the cask longitudinal axis.

The lateral inertia load from the MPC, amplified by the appropriate multiplier corresponding to 23g's, is applied in the manner shown in Figures 2.7.11 and 2.7.12. The longitudinal component of the load from the MPC, amplified by 55g, is applied as a pressure over the inside surface of the lid as shown in Figure 2.7.8. In reality, the load would be applied over a narrow annulus near the outside radius of the lid because of the raised "landing region". To maximize lid and bolt stress, however, the load is applied as a uniform pressure in the finite element model. The corresponding lateral and longitudinal loads from the overpack self-weight are applied by imposing amplified gravitational accelerations in the appropriate directions.

The loading from the impact limiter at the other end of the overpack, not involved in the impact, is applied as a uniform pressure over the surface of the backed area at the other impact limiter. Figure 2.7.10 shows the loading on the outside surface of the bottom plate that arises from the bottom end impact limiter during simulation of a top end drop. The total bottom impact limiter weight is amplified by 55g's and applied as a pressure load. At the top end, where the impact limiter provides the distributed crush force to balance the inertia forces, the balancing reaction loads from the impact limiter are applied as a distributed side pressure

loading and a distributed end surface pressure. The extent of the loaded region for this drop orientation is defined by the angle θ in Figure 2.7.7. For this case, the angle is approximately 68 degrees since a large "backed" area of the impact limiter is involved in resisting the crush. The angle- is consistent with the predictions from the intersection geometry analysis used to develop the force-deformation data used in Appendix ~~2.H~~2.A. That force-crush model has been successfully used to predict maximum decelerations and extent of crush. Static finite element models require setting a fixed origin to insure satisfaction of all equilibrium equations. The center of gravity-over-corner orientation, in theory, provides automatic satisfaction of moment equilibrium so that all forces and moments at such a fixed origin location should be zero.

In this analysis and in the general oblique drop analysis, the fixed point is assumed at a location at the end of the overpack not impacted. The results from the finite element simulation confirm that the computed reactions are negligibly small compared to the applied loads. The loads from internal pressure are self - balancing and do not alter the calculation of equilibrium reactions. *Tables 2.7.5 and 2.7.6 summarize the results from these analyses.*

~~Appendix 2.AE presents the stress intensity results for both drop scenarios for the hot and cold conditions. The safety factors identified in the appropriate tables within Appendix 2.AE are summarized in Tables 2.7.5 and 2.7.6.~~

Results for the MPC and its internals have been discussed in Subsections 2.7.1.1 and 2.7.1.2 for the end and side drops, respectively, under the action of 60-g deceleration and appropriate pressure loading. Under an oblique drop at an angle θ with respect to the target plane (θ = 0 degrees equals the side drop), the MPC and its internals experience deceleration loads parallel and perpendicular to the MPC longitudinal axis. Each of these deceleration components, however, is less than the 60-g design basis deceleration used in the end and side drop analyses. For the pure end drop, all stresses in the fuel basket and in the MPC canister (enclosure vessel) are axial. For the pure side drop, the conservative analysis of a 2-D section of the fuel basket and enclosure vessel gives rise to stresses in a plane perpendicular to the longitudinal axis of the MPC/fuel basket.

The results for any oblique drop can be obtained by a linear combination of the results for pure end drop and pure side drop. That is, the combined stress intensity is formed from the results of the two individual cases, after adjustment for the actual lateral and longitudinal "g" levels experienced by the components.

The MPC lid and baseplate are thick plate components; as such, the stress intensities experienced in the end drop orientation (which loads the lid and/or the baseplate in flexure) bound all other cases. Therefore, in what follows; only the enclosure vessel and the fuel basket need be considered. For each of these structures, the result "$R_\theta$", at a general oblique drop angle θ, is expressed in terms of the result for an end drop "$R_{90}$" and the result obtained for a pure side drop "$R_0$" as:

$$R_\Theta = R_{90}\left(\frac{g_E}{60}\right) + R_0\left(\frac{g_S}{60}\right)$$

where $g_E$ and $g_S$ are the axial and lateral decelerations imposed on the MPC canister and fuel basket during the oblique drop at angle $\theta$.

Since $g_E = 60 \sin \theta$, and $g_S = 60 \cos \theta$,

for a design basis oblique drop where the vertical deceleration is 60 g's, the result for the oblique drop is always expressed in the form,

$R_\theta = R_{90} \sin \theta + R_0 \cos \theta$

The following results are obtained for the end drop and side drop analyses:

End Drop:

Fuel Basket – maximum longitudinal membrane stress = *4,0743,739* psi

Enclosure Vessel – maximum longitudinal compressive stress = 11,260 psi

The enclosure vessel result is obtained from the Code Case N-284 evaluation ~~in Appendix 2.J~~ for a bottom end drop and conservatively bounds the result for a top end drop. The longitudinal compressive stress in the enclosure vessel includes the effect of external pressure.

Side Drop:

Stress intensity results for the fuel basket and enclosure vessel are ~~given in Appendix 2.AC and~~ summarized in Table 2.7.4. From Table 2.7.4, ~~, it is seen that the minimum safety factors for the side drop case are obtained using the stress results from Table 2.AC.15 (fuel basket) and Table 2.AC.17 (enclosure vessel). f~~For the pure side drop, the minimum safety factor for the fuel basket is 1.17 (primary membrane plus primary bending). The corresponding minimum safety factor for the enclosure vessel is 2.64 (again, for primary membrane plus primary bending). The preceding results are obtained by surveying the summary of minimum safety factors in Table 2.7.4 for all MPC's and both fuel basket orientations within the MPC. ~~For the location of minimum safety factors, the stress intensities are obtained from Tables 2.AC.15 and 2.AC.17.~~

For the pure side drop orientation, the stress intensities (SI) associated with the minimum safety factors are:

Fuel Basket SI = 47,060 psi
Enclosure Vessel SI = 24,650 psi

The stress intensities at the most limiting location for the general oblique drop orientation are then computed as:

Fuel Basket SI = *4,0743,739* sin θ + 47,060 cos θ

Enclosure Vessel SI = 11,260 sin θ + 24,650 cos θ

For the corner drop, θ = 67.5° leading to the following final results:

| C.G. OVER CORNER DROP MPC SAFETY FACTORS | | | |
|---|---|---|---|
| Item | Calculated S.I. | Allowable S.I. | Safety Factor |
| Fuel Basket | 21,*773463* psi | 55,450 psi† | 2.558 |
| Enclosure Vessel | 19,836 psi | 65,200 psi †† | 3.29 |

† at 725°F
†† at 450°F

As expected, the safety factors obtained for the corner drop are larger than the corresponding values obtained for the side drop.

~~In the next subsection, R~~results for general oblique drop angles are *now* considered for the overpack. In particular, a 30–degree oblique drop is deemed to be most representative of a scenario where only a primary impact is involved. The general formula utilized in the preceding for the specific case of center-of-gravity-over-corner can also be used for a 30–degree drop angle. The following results are reported for the fuel basket and enclosure vessel.

| 30 DEGREE OBLIQUE DROP MPC SAFETY FACTORS | | | |
|---|---|---|---|
| Item | Calculated S.I. (psi) | Allowable S.I. (psi) | Safety Factor |
| Fuel Basket | 42,*792625* | 55,450† | 1.30 |
| Enclosure Vessel | 26,978 | 65,200†† | 2.42 |

† at 725°F
†† at 450°F

2.7.1.3.1 MPC Lid-to-Shell Weld

The MPC*s* ~~-68F is~~ designed to contain *damaged* spent nuclear fuel (SNF) *or*~~designated as~~ fuel debris, *have*~~from Dresden Unit 1 and Humboldt Bay. In order to provide~~ additional impact strength in the lid-to-shell junction ~~in MPC-68F~~ (to achieve an increased level of protection against secondary containment breach in the lid-shell region under hypothetical accident conditions)~~,~~ the upper portion of the shell is thickened to one inch. The one inch thick shell segment is attached to the lower one-half inch thick shell

through a full penetration, fully radiographed circumferential butt weld (Figure 2.7.22). The thicker shell is given a 1:4 taper in the longitudinal direction, consistent with the guidelines in the ASME Code, to mitigate local discontinuity (secondary) stresses.In addition to thickening the shell, the lid-to-shell (LTS) weld is also enlarged to a 1 ¼ inch deep J-groove (the standard LTS weld in the sister MPC designs is a ¾inch deep J-groove). This difference, unique to the MPCs *with the "F" designation* ~~68F~~, does not affect other calculations for the MPC lid in a non-conservative manner. Since the lid diameter is slightly decreased, stresses in the lid are less.

To preserve the permissible flaw size criterion, the MPC-*XX*~~68~~F J-groove weld *is*~~will~~ also be required to be examined by the liquid penetrant (PT) method at a maximum of 3/8 inch weld depth intervals in addition to root and final pass PTs (if the user chooses not to volumetrically examine the weld).

The LTS region reinforced in the manner illustrated in Figure 2.7.22 is demonstrated to maintain the weld and shell stresses to well below their respective level D stress limits under the most adverse oriented hypothetical drop event. For the LTS region, the most inimical drop orientation is generally recognized as the "top-down corner drop". It is desired to demonstrate that the closure weld, under the most limiting assumptions of load distribution, does not experience shear stresses that could induce local weld failure. It is apparent from the lid weld configuration (Figure 2.7.22) that the closure ring serves to protect the lid-to-shell groove weld from direct shear action under a top-down corner drop event. However, for purposes of analysis, it is assumed that the closure ring is absent. Therefore, an extreme condition of contact between the MPC and the overpack under a corner drop exists. The following assumptions are used for this analysis:

1. The total fuel weight + *damaged fuel container* is *limited to 1680*~~550~~ lb‡ x *24*~~68~~ assemblies.
2. Contact occurs at a single point because of manufacturing and assembly tolerances.
3. The MPC is constrained within the transport overpack and does not experience an angular acceleration.
4. Linear elastic behavior is assumed for all equilibrium analyses.
5. The maximum deceleration is 39 g's (per Appendix ~~2.H~~*2.A*).

Figure 2.7.19 shows a free body diagram of the loaded MPC at the instant of contact. At the point of contact with the overpack, the net load P balances the inertia load from the MPC.

From Table 2.2.*4*~~1~~,

W = ~~*4100039,641 lb. (bounds empty MPC for damaged fuel)* (empty MPC 68) + *40,320550 x 68 = 81,32077,041 lb.*~~*90,000 lb (bounding MPC weight)*

~~‡ Fuel assembly weight (400 lbs) plus Damaged Fuel Container weight (150 lbs)~~

Figure 2.7.20 shows a free body diagram of the MPC lid assuming that the initial contact location is on the shell. $P_1$ is the weight of the fuel, fuel basket, and lid multiplied by the longitudinal component of the deceleration. It is clear that for this case, the closure weld shear stress $\tau_w(y)$ is uniformly distributed around the periphery.

Figure 2.7.21 shows a free body diagram of the MPC lid assuming that the initial contact location is on the periphery of the top closure itself. Only longitudinal load components are shown in the figure. It is clear that for this assumption on contact point, the closure weld stress distribution has a varying distribution around the periphery in order to insure moment equilibrium. For this case, the weld shear stress is given by:

$$\tau_w = \frac{P\cos\phi - P_1}{2\pi R t_w}$$

The linear component of the weld stress is computed to equilibrate the moment PR cos ϕ about the center of the MPC lid. The maximum value of this weld shear stress component is:

$$\tau_{MAX} = \frac{PR\cos\phi}{\pi R^2 t_w}$$

The following geometry is assumed:

$t_w$ = 1.25"
R = (68.375/2)" – 1.0" – 1.25/3" = 32.771"
= radius to centroid of closure weld

ϕ = 19.792°

$P_1$ = 39 cos ϕ (10,400 lb + *16,400~~21,300~~*13,000 lb + *47,600~~40,320~~37,400* lb)

Where: the top closure lid weight = 10~~0~~,400 lb, [Table 2.2.*44*]
the fuel basket weight = *16,400~~21,300~~*13,000 lb, [*~~Bounds~~*-Table 2.2.*~~41~~4*]
and the fuel + *damaged fuel canister* weight = *700~~168055~~0* lb. x *68~~24~~68* = *47,600~~40,320~~37,400* lb.

Substituting the appropriate values gives:

$\tau_w$ = *2,224~~1,326~~2,207* psi

$\tau_{MAX}$ = *25,660~~23,190~~1,970* psi

There is an additional component of weld shear stress due to the design basis pressure differential of (100–40) psi. This produces an average shear stress:

$\tau_p = 787$ psi

Adding all components together yields a maximum weld shear stress:

$\tau_{TOTAL} = 28,670$~~25,300~~4,964 psi

The primary membrane stress in the enclosure shell has a distribution to balance the force and moment produced by the closure weld stress. The cross section area and metal moment of inertia of the enclosure shell are:

$A = 211.7$ in$^2$

$I = 120,130$ in$^4$

The net force produced by the closure weld is:

$$F = P\cos\phi - P_i$$

The net moment is

$M = PR\cos\phi$~~$\phi$~~

Computing the mean stress in the shell,

$$\sigma = \frac{F}{A} + \frac{MR_M}{I} = 33,070\,psi$$

$$where \quad R_M = \frac{68.375"}{2} - 0.5" = 33.7"$$

The shear stress due to the net pressure adds to the shear stress from the impact. The resulting maximum membrane stress in the shell is:

$\sigma = 37,110$~~33,090~~29,451 psi

The preceding calculations show that:

1. The closure weld stress (maximum value) = $28,670$~~25,300~~4,964 psi
2. The maximum MPC shell axial stress to balance the weld stress = $37,110$~~33,090~~29,452 psi (compressive)

The above stresses are the maximum values that will be obtained in the lid weld and shell under the limiting impact scenario postulated in the foregoing. These stresses are then compared to the appropriate acceptance criteria. *The allowable stresses are based on a metal temperature of 200°F As maximum decay heats are limited for damaged fuel, this temperature is considered to be bounding.* ~~In Table 3.4.24, the temperature for the MPC lid inside surface at the periphery is reported to be less than 200° F for the standard MPC-68 with design basis fuel. The MPC-68F is limited to decay heat loads well below the standard MPC-68, but the temperature of 200° F is conservatively applied to the MPC-68F in this analysis to determine the acceptable stress limits.~~

The acceptable shear stress in the MPC lid-to-shell weld is equal to 0.42 times the ultimate strength of the Alloy X material at 200° F, or 0.42 *x*~~X~~ 71 ksi (Table 2.3.1) = 29,820 psi. Therefore, the safety factor for the weld shear stress is:

SF (weld shear stress) = 29,82*09/28,670~~25,300~~4,964* = 1.*041~~819~~*

The acceptable stress for the MPC shell is taken as $P_L$ from Table 2.1.18, or 72 ksi. Adding the internal pressure circumferential stress from a net pressure of 60 psig (stress = $p$~~P~~$_L R_M/t$) to the maximum MPC shell axial stress ~~of 29,451 psi~~ *gives the*~~,~~ a stress intensity ~~of 31,473 is computed~~. Therefore, the safety factor for the MPC shell is:

SF (MPC shell) = 72,000/*(37,110~~33,090+4,044)~~1,473* = *1.94~~2.28~~*

Based on the safety factors reported above and the conservative assessment of the ~~MPC-68F~~ closure region, it is demonstrated that the MPC*s, designed to carry damaged fuel or fuel debris, have an* ~~68F~~ inner containment boundary ~~does~~*which does* not breach under the worst case hypothetical drop accident condition.

2.7.1.4 Oblique Drops

Appendix ~~2.H~~*2.A* contains results of analytical simulations for various orientations of the cask at impact. In Appendix ~~2.H~~*2.A*, *it is shown*~~we show~~ that lateral decelerations are large for the near side drop (slapdown) and decrease as the angle of orientation, with respect to the horizontal plane, increases. Therefore, it is likely that results presented in Subsections 2.7.1.1 through 2.7.1.3 are bounding for all orientations other than the near side drop (slapdown) in that at any other angle, the resulting g-loads in each direction (longitudinal and lateral) are smaller than the bounding deceleration loads applied in the end, side, and corner drops. Nevertheless, based on the results obtained in Appendix ~~2.H~~*2.A*, the case of an oblique drop with primary impact at 30 degrees from the horizontal is analyzed in detail. This case covers all orientations where the maximum deceleration load occurs and is reacted by the primary impact limiter. For this case, moment equilibrium includes inertia loads from overpack rotation as well as linear deceleration. For the 30-degree drop orientation at the primary impact location, the design basis deceleration load is applied with 52g lateral component and 30g longitudinal component. The loads are applied in the same

manner as discussed in Subsection 2.7.1.3 with one additional complication. In contrast to the center of gravity over corner orientation where moment equilibrium is automatically satisfied when the loads are correctly applied, the applied loads and the reaction loads from the impact limiter are not initially in moment equilibrium. No inertial loading due to overpack rotational motion at the instant being considered is included. Without an additional inertial moment loading component, a large reaction force would develop at the far-removed arbitrary fixed reference point because the impact limiter reaction loads are offset from the overpack and MPC inertia loads from the linear decelerations. Figure 2.7.14 shows the overpack in a general oblique orientation. Appropriate arrows show the impact limiter reaction forces and the components of the applied linear decelerations ~~are also provided~~. The loads from the MPC are not shown on the figure but they are applied as previously described for the corner drop. It is clear that moment equilibrium is not satisfied unless reaction loads develop at the arbitrarily chosen fixed support location far removed from the impact point. In the real drop scenario, since there is only a primary impact reaction, the cask must have angular accelerations imposed to insure moment equilibrium since the fixed point is an artifact to meet the requirements of the finite element analysis. To zero this reaction load at the point far-removed from the impact location, an additional load case with a unit angular velocity imposed at the mass center of the system and no other loads is developed. An angular acceleration is internally generated by ANSYS for this load case. The solution to this load case provides a reaction at the hypothetical fixed point assumed at the end of the overpack far removed from the impact location to balance the imposed inertial moment. The addition of this load case, with proper magnitude and sign ascribed to the input angular velocity, serves to eliminate all reactions at the far-removed fixed point. By adding this inertia moment load case, both force and moment equilibrium equations are satisfied for the oblique drop case where there is only a single impact limiter providing external forces to react the cask motion. With reference to Figure 2.7.7, the extent of the impact limiter loaded region on the overpack for this case is $\theta = 63$ degrees. This angle is estimated from the projected geometry from the theoretical analysis in Appendix ~~2.H~~2.*A*. Figure 2.7.9 shows a side view of the top forging with the end loading from the impact limiter applied as a pressure over the loaded region.

*The finite element solution provides* ~~Appendix 2.AE presents the~~ stress intensity results ~~for both drop scenarios~~ for the hot and cold conditions. The safety factors ~~identified in the appropriate tables within Appendix 2.AE~~ are summarized in Tables 2.7.5 and 2.7.6 (identified as Load Cases 20 and 21 corresponding to the "heat" and "cold" environmental conditions*)*. ~~Node locations are also identified for use with Appendix 2.P to correlate with actual physical locations in the model.~~

The near side drop with impact at the secondary impact limiter (slapdown) is a special case that also merits detailed analysis. For this case, the angle of the cask with the target is near zero degrees, similar to that used for the side drop analysis. The nature of the equilibrium equations is quite different, however. For the side drop, Figure 2.7.17 shows that equilibrium is satisfied by impact limiter reaction pressures at both impact locations. The reaction lateral pressure distribution at each impact limiter is distributed in the manner described by Figure 2.7.7. For the side drop evaluation, no introduction of a rotational component to the overpack is required to insure moment equilibrium. For the analysis of the near side drop secondary impact case, all of the reaction force required to insure that force equilibrium is maintained under the inertia induced loads, is imposed at the location of the secondary impact limiter. Figure 2.7.18 shows a side view of the

overpack with the reaction load applied over a specified arc in the same manner as described by Figure 2.7.7. At the time of peak secondary impact deceleration, the theoretical analysis predicted minimal axial deceleration. Therefore, to perform the stress analysis using the finite element model, no axial deceleration is imposed. Referring to Figure 2.7.7, the angle θ for this evaluation is chosen on the basis of observed experimental results and theoretical prediction. The angle is related to the angle associated with the observed crush depth of the impact limiter itself. For a near side drop, *the* ~~if we know the~~ outer diameter of the impact limiter *is known,* and *if the crush depth is observed, calculated, or measured,* ~~observe, calculate, or measure the crush depth,~~ the angular extent of impact limiter crushed material is easily determined. The outer radius, "Ri" of the impact limiter, and the observed and calculated crush depth (see results in Appendix ~~2.H~~*2.A* for a full scale impact limiter), "d", are:

Ri = 64" ; d = 15"

Therefore, the angle "φ" -(on either side of a vertical diameter through the impact limiter) that is associated with the extent of loaded crushed surface of the impact limiter is obtained from simple geometry as:

$\cos(\varphi) = 1 - d/Ri$

The angle over which the load is applied at the crushed surface of the impact limiter is calculated to be:

φ = 40 degrees (measured from the vertical, on both sides of the vertical centerline).

The angle of significant reaction loads on the interface surface of the top forging, is greater than this angle. However, it is conservative to perform the finite element analysis of the "slapdown" secondary impact event, using the load angle

θ = φ = 40 degrees.

Note that this angle used for the "slapdown" evaluation is larger than the conservative value used to evaluate the side drop. This reflects the increased crush imparted to the impact limiter since the entire amplified load is reacted at the top end. The load from the MPC is imposed on the appropriate inside surface of the inner shell as a uniform load in the same manner as for the side drop analysis. Moment equilibrium is provided by imposing the additional pure rotation on the overpack sufficient to generate opposite reaction forces that zero out the combined reactions at the "balance point" from the applied inertia decelerations plus the pure rotation case. Because the MPC is constrained within the overpack, no departure from a uniform load transfer to the overpack is anticipated. Therefore, the enforcement of moment equilibrium for this condition is ensured solely by the determination of a proper balancing moment by determining an appropriate angular acceleration for the overpack. This assumption has little effect on the computation of the primary stress intensity distribution that results from the impact.

The results of the analysis are *tabulated and combined with other load conditions,* ~~tabulated in Appendix 2.AE~~ and the combined load case is designated *as "Load Case 22".* ~~as "Load Case 22". Detailed results are found in Table 2.AE.27 in Appendix 2.AE.~~ Bolt preload, internal pressure, and the inertia loads are combined to form this "slapdown" simulation. The top-end secondary impact analysis reported herein bounds a similar analysis of the bottom end secondary impact case. Summary results for minimum safety factors are reported in Table 2.7.5 only for the "Heat" environmental condition as previous results have demonstrated that this case produces the minimum safety factors. Only primary stress intensities are surveyed and reported in accordance with -ASME requirements. Also evaluated is the bolt stress, the net friction force, and the state of the seals and lands. From the *post-processed results* ~~tabular results in Appendix 2.AE (Table 2.AE.27)~~, it is concluded that no bolts are overstressed, no portion of the seals suffer unloading, and that there is sufficient frictional force to insure that the lid is maintained in position.

The preceding discussion focussed on the transport overpack analyses. The minimum safety factors for the MPC fuel basket and enclosure vessel, for arbitrary drop orientation, are obtained from the general formulation in the preceding subsection 2.7.1.3. The angle that provides the maximum combined stress intensity (S.I.) can be determined by classical means, and the minimum safety factor established. The results are summarized in the table below:

| GENERAL OBLIQUE DROP ORIENTATION<br>MPC – SAFETY FACTORS | | | | |
|---|---|---|---|---|
| Item | Drop Orientation Angle (Degrees) | Calculated S.I. (psi) | Allowable S.I. (psi) | Safety Factor |
| Fuel Basket | 4.54 | 47,208 | 55,450 | 1.17 |
| Enclosure Vessel | 24.55 | 27,100 | 65,200 | 2.41 |

2.7.1.5 Comparison with Allowable Stresses

Tables 2.7.4 through 2.7.8 summarize the limiting safety factor obtained for each hypothetical free drop accident condition of transport defined by the requirements of Regulatory Guide 7.9. In particular, Table 2.7.4 is a summary of safety factors from the analyses of the MPC fuel basket and enclosure vessel, and Tables 2.7.5 and 2.7.6 report safety factors from the overpack analyses. Finally, Tables 2.7.7 and 2.7.8 contain safety factor summary results from miscellaneous evaluations reported within the text. From these results, ~~we can construct~~ tables *are constructed that* ~~which~~ summarize limiting safety factors for all of the hypothetical accident conditions of transport that are associated with drop events. Tables 2.7.1 through Tables 2.7.3 present the overall summary of the most limiting safety factor for each of the components of interest for all hypothetical accident conditions of transport. *It is* ~~We~~ *concluded* from these tables that large factors of safety exist in the fuel basket, in the MPC shell, and in the various components of the overpack under all hypothetical accident conditions of transport associated with free drop events.

It is noted that the overpack finite element results are developed using a 3-D model of the overpack. Even though symmetry conditions reduce the size of the model, there are over 8000 elements and 11000 nodes. ~~Tables 2.7.5 and 2.7.6 report the evaluation of the safety factors at specific nodal locations in the finite element model. As noted in the preceding, Appendix 2.P contains tables and figures necessary to locate the physical region of the overpack where these nodes are placed. In Appendix 2.P, stress report locations are identified at points along the length of the overpack and at forty five degree intervals around the half-periphery. To locate a physical area of the package where a particular safety factor is calculated, first, the ANSYS node number is identified in the table. With the node number known, Table 2.P.2 in Appendix 2.P identifies the "stress report location". Figures 2.P.1 and 2.P.2 are then used to locate the physical area of the particular component where the safety factor is evaluated.~~

~~It is obvious that T~~*t*he postulated accident conditions all tend to load localized regions of the overpack. As an illustration, consider Load Case 20, the 30-degree oblique top-end impact with the target. The limiting results for safety factors are reported in Table 2.7.5. Figures 2.7.15 and 2.7.16 show stress intensity distributions for the inner shell and *for* the assemblage of intermediate shells, respectively. *As expected, t*~~T~~he regions of highest stress intensity are naturally concentrated near~~est~~ the impacted region~~. The limiting node points listed in Table 2.7.5 for these components (for Load Case 20) can be located by reference to Appendix 2.P and its tables and figures.~~

2.7.2 Puncture

- Overpack Structural Components

10CFR71 mandates that a puncture event be considered as a hypothetical accident condition. For this event, it is postulated that the package falls freely through a distance of 1 meter and impacts a 6 inch diameter mild steel bar. The effects of the puncture drop are most severe when the steel bar is perpendicular to the impact surface. Therefore, all puncture analyses assume that the bar is perpendicular to the impact surface. It is assumed that the steel bar has a flow stress equal to 48,000 psi, which is representative of mild steel. The maximum resisting force can then be calculated as

$$F_R = \frac{\pi D^2}{4} \times 48{,}000\ psi = 1.357 \times 10^6\ lb$$

where D equals the diameter of the steel bar.

Since the maximum force applied to the cask is limited to the above value~~, we can compute~~ the average deceleration of the cask *can be computed*~~if it were to be~~ assum*ing*~~ed~~ *it* to be rigid. The average deceleration of the cask (plus contents) (weight = W) is determined as:

$$|A_p| = \frac{F_R\, g}{W}$$

For a bounding (low) weight of 2340,000 lb. (Table 2.2.1), for example, the rigid body average deceleration over the time duration of impact, is 5.965g.

Candidate locations for impact that have the potential to cause the most severe damage are near the center of the closure plate (top-end puncture), the center of the bottom plate (bottom puncture), and the center height of the overpack shells (side puncture). In accordance with Regulatory Guide 7.9, ~~we must assess~~ local damage near the point of impact and the overall effect on the package *must be assessed.*

An estimate of local puncture resistance is obtained by using Nelms' equation [2.7.1] that is generally applicable only for lead backed shells. Nevertheless, it is useful to obtain an indication as to whether a potential problem exists in the HI-STAR 100 System. The equation is applied using an ultimate strength of 70,000 psi that is appropriate for the selected impact regions. Nelms' equation predicts a minimum thickness of material necessary to preclude significant puncture damage. For the HI-STAR 100 System

$$t_m = \left( W / S_u \right)^{0.71} = 2.65 \quad inch$$

Inasmuch as the HI-STAR 100 overpack has substantially more material thickness in the baseplate, the closure plate, the top flange and the inner plus the initial intermediate shell, the overpack meets local puncture requirements as required by Nelms' equation.

The global effects of puncture are calculated using the overpack model described in Section 2.6, which is the same model that is used for the drop assessments. Figures 2.1.12 through 2.1.14 show free body diagrams of the overpack for the side, top, and bottom puncture events, respectively. In each case, the nodes on the surface of the overpack that directly impact the steel bar are fixed in all degrees of freedom. By then applying ~~an~~ acceleration, $A_p$, a reaction force develops at those nodes equal in magnitude with $F_R$. ~~The results for all puncture events are presented in Appendix 2.AE.~~ Tables 2.7.5 and 2.7.6 summarize the safety factors for the overpack components obtained f*or the puncture acceleration computed above*~~rom the relevant tables in Appendix 2.AE~~ for both heat and cold environmental conditions. Note that for the stress intensities in the lid and baseplate, the highest stresses are exactly under the impact point. The re*sults* ~~ported results in Appendix 2.AE~~ include the effect of the interface contact stress between the puncture pin and the plate surface. This local effect is not required to be included in the stress intensity comparison with allowable values for the hypothetical accident. Therefore, in the reporting of safety factors, ~~we do not include~~ the effect of local surface pressure *is not included*; rather, ~~we use~~ the radial and tangential stresse*s* at the load point *are used* to form the stress intensity and set the lateral surface stress to zero. Tables 2.7.5 and 2.7.6 specifically identify this item by a note. Figure 2.7.17 shows the stress intensity distribution in the lid resulting from a top-end puncture analysis. The localized nature of the stress intensity distribution is clearly evident. The reported safety factors in the summary tables are adjusted to eliminate the effect of non-primary stress components.

- Closure Bolts

The methodology to analyze closure bolts is provided in reference [2.6.3] prepared for analysis of shipping casks. The analysis of the overpack closure bolts under normal conditions of transport, in accordance with the provisions of [2.6.3], has been reported in Section 2.6. In this subsection, the *similar* analysis for the hypothetical puncture accident is summarized. The analysis ~~is reported in detail in Appendix 2.U and~~ follows the procedures defined in Reference [2.6.3] *and uses the*~~. The~~ allowable stresses ~~used~~ for the closure bolts *in*~~follows~~ that reference.

The following combined load case is analyzed ~~in Appendix 2.U~~ for the hypothetical pin puncture accident condition of transport.

Puncture: Pressure, temperature, and pre-load loads are included.

Reference [2.6.3] reports safety factors defined as the calculated stress combination divided by the allowable stress for the load combination. This definition of safety factor is the inverse of the definition consistently used in this SAR. In summarizing the closure *bolt analysis,* ~~bolt analyses performed in Appendix 2.U,~~ results are reported using the *SAR* safety factor definition of allowable stress divided by calculated stress. The following result for closure lid bolting for the top end drop hypothetical accident condition of transport is obtained ~~from Appendix 2.U~~.

| Overpack Closure Bolt - Safety Factor (Load Case 7 in Table 2.1.9) | |
|---|---|
| Item | Safety Factor on Bolt Tension |
| Average Tensile Stress in Bolt | *1.86*~~1.39~~ |

2.7.3 Thermal

In this subsection, the structural consequences of the thirty-minute fire event are evaluated using the metal temperature data from Section 3.5 where a detailed analysis of the fire and post-fire condition is presented. Specifically, it desired to establish that:

1. The metal temperature, averaged across any section of the containment boundary, remains below the maximum permissible temperature for the Level A condition in the ASME Code for NB components. Strictly speaking, the fire event is a Level D condition for which Subsection NB of the ASME Code, Section III does not prescribe a specific metal temperature limit. The Level A limit is imposed herein for convenience because it obviates the need for creep considerations to ascertain post-fire containment integrity.

2. The external skin of the overpack, directly exposed to the fire will not slump (i.e., suffer rapid primary creep). This condition is readily ruled out for steel components if the metal temperature remains below 50% of the metal melting point.

3. Internal interferences among the constituents of the HI-STAR 100 System do not develop due to their differential thermal expansion during and after the fire transient.

4. Overpack closure bolts will not unload during a transport fire.

5. The helium retention boundary and the containment boundary both continue to perform their function as ASME "NB" pressure vessels.

2.7.3.1 Summary of Pressures and Temperatures

The following peak temperatures (per Tables 3.5.4 and 3.4.11) and pressures are used in Subsections 2.7.3.2, 2.7.3.3, and 2.7.3.4.

| | |
|---|---|
| Overpack closure plate/bolts | 514 degrees F (post-fire) |
| Overpack bottom plate | 662 degrees F (post-fire) |
| Overpack outer closure | 226~~17~~ degrees F (initial pre-fire cold temperature); 1348 degrees F (maximum) |
| Overpack containment shell | ~~(~~*395 degrees F* ~~419 degrees F) (24 degrees F)~~*(MPC –Shell* post-fire *temp.* - increment of 24 degrees *F (*-from data in Table 3.4.11*))* |
| MPC-Shell | 419 degrees F (post-fire) |
| Basket (center) | 751 degrees F (post-fire) |
| Basket (periphery) | ~~(~~*478 degrees F* ~~419 degrees F) + (59 degrees F)~~ *(MPC-Shell post fire + 59 degrees F* ~~normal condition basket periphery to shell temperature difference~~ *(*from data in Table 3.4.11*))* |

It should be noted that the overpack containment shell, closure plate, and bottom plate temperatures are not specifically reported in Table 3.5.4. The temperatures listed above are based on the closest temperature report location. The overpack containment shell temperature is the lowest temperature which occurs prior to the fire accident and is used for the differential thermal expansion analysis. The overpack containment shell temperature falls (post-fire) below the outside basket temperature and subsequently lags the basket temperature by 24 degrees F. The 24 degree F lag is the same lag that occurs in the normal heat condition listed in Table 3.4.11 (i.e., 306 degrees F for the MPC outer shell surface - 282 degrees F for the overpack inner surface). This will maximize the potential for interference between the overpack and the

MPC. Similarly, the temperature difference between the MPC shell and the fuel basket periphery will be essentially the same exists in the normal heat conditions of transport. Therefore, from Table 3.4.11, the basket peripheral temperature for the fire event analyses is set as the MPC shell temperature plus the maximum difference (365-306) degrees F from the table.

Subsection 3.5.3 contains a discussion of the peak bulk temperatures occurring during and after the fire transient. It is concluded in that section that:

1. The containment boundary protected by the intermediate shells remains below 500 degrees F (SA-203-E material).
2. The containment boundary that is within the confines of the impact limiters remains below 700 degrees F (SA-350 LF3 material).
3. The portion of the containment boundary directly exposed to the fire may have local outer surface temperatures in excess of 700 degrees F, but the bulk metal temperature of the material volume remains under 700 degrees F (SA-350 LF3 material).

The conclusions in Subsection 3.5.3 enable the statement that the containment boundary metal bulk temperatures remain at or below the upper limits permitted by the ASME Code. Therefore, stress evaluations that make comparisons to allowable stresses to demonstrate that the containment boundary continues to perform as a viable pressure vessel use allowable stresses that are given in the ASME Code (i.e., there is no extrapolation of allowable stresses beyond the recognized code limits). For the helium retention boundary stress calculations, however, allowable stresses for a conservatively high temperature (see Table 2.1.2 and 2.1.21) are used when pressure vessel code compliance is demonstrated.

From Table 3.5.4 in Subsection 3.5.4 of Chapter 3, it is concluded that:

> The maximum temperature of the ferritic steel material in the body of the HI-STAR 100 overpack (the outer enclosure and the intermediate shells outside of the containment boundary is well below 50% of the material melting point. (The melting point of carbon and low alloy steels is approximately 2750 *degrees* °F, per Mark's Standard Handbook, Ninth Edition, pp 6-11.)
>
> The shielding experiences temperatures above its stated limit for effectiveness. This means that a limited loss of shielding effectiveness may occur. The shielding analysis in Chapter 5 (Subsection 5.1.2) recognizes this and conservatively assumes that all shielding is lost in post-fire shielding analyses.

Pressures during the fire transient are bounded by the internal and the external design pressures for accident conditions for the MPC shell as stated in Section 2.1. For internal pressure, Table 3.5.3 supports this conclusion. The following calculation is presented to support the conclusion for MPC external pressure.

The overpack annulus initial fill pressure is 14 psig (max.) per the specification in Chapter 7. The overpack annulus lower bound fill temperature is 70 degrees F. The fire condition MPC shell peak temperature is 419 degrees F per Table 3.5.4 and the use of this as the average gas temperature in the annulus is conservative.

Using the above data, the fire condition peak pressure in the annulus between the overpack and the MPC shell is calculated by using the ideal gas law with constant volume assumed in the gap as:

$p_{fire}$= (14+14.7) x (419 + 460)/(70 + 460) = 47.6 psia = 32.9 psig.

2.7.3.2 Differential Thermal Expansion

The methodology for establishing that there will be no restraint of free thermal expansion has been presented in Subsection 2.6.1.2 for normal conditions of transport. The same methodology is applied in this subsection to evaluate the potential for component interference during and after the postulated hypothetical fire. ~~Differential thermal expansion due to the fire accident is considered in Appendix 2.G.~~ For conservatism, ~~we~~ use the temperatures in the overpack and the MPC temperatures that will maximize the potential for interference between the overpack and the MPC regardless of at what point in time the temperatures occurred. It is shown that there is no structural restraint of free-end expansion in the axial or radial directions under the most limiting temperature difference between the hot basket and the colder overpack/enclosure vessel. Thus, the ability to remove fuel by normal means is not inhibited by structural constraint of free-end expansion. The table below summarizes the results obtained ~~in Appendix 2.G~~ for the limiting MPC temperature distributions assumed.

| THERMOELASTIC DISPLACEMENTS IN THE MPC AND OVERPACK UNDER FIRE CONDITION | | | | |
|---|---|---|---|---|
| **CANISTER - FUEL BASKET** | | | | |
| | Radial Direction(in.) | | Axial Direction (in.) | |
| Worst Case Unit | Initial Clearance | Final Gap | Initial Clearance | Final Gap |
| Bound*ing*~~s~~ MPC-~~24,68~~ | 0.1875 | 0.117 | 2.0 | 1.672 |
| **CANISTER – OVERPACK** | | | | |
| | Radial Direction (in.) | | Axial Direction (in.) | |
| Worst Case Unit | Initial Clearance | Final Gap | Initial Clearance | Final Gap |
| Bound*ing* ~~s~~-MPC-~~24,68~~ | 0.09375 | 0.004 | 0.625 | 0.291 |

Using the most conservative assumptions (i.e., do not consider a real "snapshot" in time during and after the fire, but rather assume the most detrimental temperature distribution occurs at the same instant in time) that maximize the potential for interference, it is demonstrated that no restraint of free thermal expansion in either the radial or axial directions occurs.

2.7.3.3 Stress Calculations

Under the fire accident, pressures in the MPC and overpack increase simultaneously, while the allowable strengths of the material may decrease from their values under normal conditions of transport. The MPC and overpack stresses are shown below (allowables are taken from Tables 2.1.21). It is required that both the helium retention boundary and the containment boundary meet Level D Service Limits of the ASME Code and continue to function as pressure vessels.

2.7.3.3.1 MPC

- Top Closure

The MPC Top Closure analysis for the fire condition is ~~considered in Appendix 2.L (~~Load Case E5 in Table 2.1.7~~)~~. The top closure is *conservatively modeled as a simply supported plate* considered to *be loaded by*~~support~~ the accident internal pressure plus self-weight *acting in the same direction.* For determination of the safety factor, the value of allowable stress from Table 2.1.20 appropriate to the fire temperature is used. The table below summarizes the result *(where a multiplier of 2.0 has been incorporated to reflect the bounding dual lid design)*:~~.~~

| MPC Top Closure Safety Factor for Load Case E5 in Table 2.1.7 | | | |
|---|---|---|---|
| Item | Value (ksi) | Allowable (ksi) | Safety Factor |
| Bending Stress | *3.158 x 21.99* | 54.23 | *8.5927.3* |

- Baseplate

Under the fire accident condition, the baseplate is subject to accident internal pressure *(200 psi)*. If the HI-STAR 100 is assumed to be in the vertical position, then the baseplate also may support the weight of the fuel basket and the fuel loading. If the HI-STAR 100 is assumed to be oriented in the horizontal position, then the baseplate supports only internal pressure. For a conservative analysis, it is assumed that the internal pressure stress and the stress from basket weight and from fuel weight add. This Load Case E5 *is summarized below:* ~~from Table 2.1.7 is reported in Appendix 2.N. The first row in the table below summarizes the calculation in Appendix 2.N.~~ The second row is the result that is obtained if the basket and fuel weight is neglected~~. This result is not reported in Appendix 2.N~~ but is easily calculated from the data available there.

| MPC Baseplate Safety Factor under Hypothetical Fire Accident | | | |
|---|---|---|---|
| Item | Value (ksi) | Allowable (ksi) | Safety Factor |
| Baseplate Bending Stress (Including Basket and Fuel Weight) | *46.328630.46* | 54.23 | 1.*1778* |
| Baseplate Bending Stress (Neglecting Basket, ~~and~~ Fuel, *and Self-~~weight~~* Weight) | *42.2826.43* | 54.23 | *1.282.05* |

- Shell

The MPC shell is examined for elastic/plastic stability under the fire accident external pressure ~~in Appendix 2.J. The~~*using the* ASME Code Case N-284 analysis method ~~is used~~. The result from the stability analysis for Load Case E5 in Table 2.1.7 is summarized below:

| MPC Canister Safety Factor - Stability under External Accident Pressure | | | |
|---|---|---|---|
| Item | Calculated Interaction Factor | Allowable Interaction Factor | Safety Factor |
| Elastic Stability | 0.845 | 1.00 | 1.18 |

The shell is also analyzed for stress under the accident internal pressure by using the Lame' solution previously used in Section 2.6. The stress due to the internal accident pressure of 125 psi is (P = pressure, r = MPC radius, t = shell thickness):

$$\sigma_1 = \frac{Pr}{t} = \frac{(125\,\text{psi})\ (68.375\,\text{in}/\ 2)}{0.5\,\text{in}} = 8{,}547\,\text{psi}$$

$$\sigma_2 = \frac{Pr}{2\,t} = 4{,}273\,\text{psi}$$

$$\sigma_3 = -P = -125\,\text{psi}$$

The maximum stress intensity is $\sigma_1 - \sigma_3 = 8{,}672$ psi

The safety factor is,

$$SF = \frac{36.15\,\text{ksi}}{8.672\,\text{ksi}} = 4.16$$

2.7.3.3.2 Overpack

The overpack stresses for normal heat conditions of transport *are reported in Section 2.6* ~~are reported in Appendix 2.AE~~. Since these stress solutions are based on linear elasticity, the stresses reported ~~in Appendix 2.AE~~ can be scaled up to account for the accident internal pressure and the safety factor computed based on the allowable stress for the fire temperature.

Generally, in the fire accident case, only primary stresses are of interest to demonstrate continued containment. Secondary stresses may be included in the evaluation, but they merely demonstrate additional levels of conservatism Table 2.6.~~45~~ gives the safety factor for the primary stress case of $T_h + P_i + F + W_s$.

The highest stress occurs in the inner shell, and has the value 2,832 psi.

The ratio of the accident pressure to normal pressure is (Table 2.1.1) $\frac{125}{100} = 1.25$.

Using this factor, the safety factor is computed as follows:

For the inner shell at 500 degree F fire temperature per Table 2.1.21, the allowable membrane stress intensity under the fire condition is compared to the amplified mean stress and the safety factor computed as

$$SF = \frac{45.4\,\text{ksi}}{3.54 + 0.125\,\text{ksi}} = 12.39$$

2.7.3.3.3 Closure Bolts

Under the fire transient, it is required to demonstrate that the closure bolts do not unload to the extent that the pressure boundary is breached. To that end, ~~Appendix 2.V contains~~ an analysis of the fire condition *is carried out* with the purpose of determining the bolt tensile stress under the applied loading. That is, it is shown that the bolts do not unload under the fire condition. *The methodology employed for this analysis is that presented in the report, "Stress Analysis for Closure Bolts for Shipping Casks" [2.6.3]. The*

*loadings applied are fire temperature, bolt preload, and internal pressure. Results from the analysis lead to the following conclusion:* ~~The following conclusion is reached in Appendix 2.V.~~

The average bolt tensile stress under the conditions of pressure, preload, and thermal effects appropriate to the hypothetical fire accident condition of transport is ~~94.4~~*95.1*% of the average bolt tensile stress computed under the normal heat condition of transport. Therefore, it is concluded that there will be only minor unloading of the closure bolts and no breach of containment.

2.7.3.3.4 Bounding Thermal Stresses During the Fire Transient

Regulatory Guide 7.6, Section C.7 states that the extreme total stress intensity range between the initial state and accident conditions should be less than twice the adjusted value of the alternating stress intensity at 10 cycles given by the appropriate fatigue curves. It is demonstrated here that under very conservative assumptions on the calculation of thermal stresses, this regulatory requirement is met by the HI-STAR 100 System.

Under the fire transient, thermal gradients can lead to secondary or peak stresses due to local constraint by adjacent material that is at a lower temperature. The ASME Code does not require that secondary stresses be held to any limit for Level D Service Conditions. Nevertheless, bounding calculations are performed here to estimate the magnitude of the thermal stress. The most limiting secondary stress intensity -state arises by conservatively assuming complete restraint of material by surrounding cooler material and has the solution:

$$|\sigma| = E\,\alpha\Delta T$$

where

| | |
|---|---|
| E = | Young's Modulus at temperature |
| $\alpha$ = | coefficient of linear thermal expansion |
| $\Delta$T = | temperature change from 70 degrees F, the assumed assembly temperature |

For the fuel basket, $\Delta$T = 775 - 70 = 705 degrees F. The use of 775 degrees F is justified as follows:

The peak temperature of the fuel basket is 950 degrees F during the fire per Table 2.1.2. For a conservative estimate of the temperature between *two adjacent points* on the fuel basket, use the bounding hypothetical accident temperature limit for the enclosure vessel lid or baseplate from Table 2.1.2 as representative of the change between *two adjacent points* on the fuel basket. Therefore, no extrapolation of data is required for the calculations to follow.

From the material property table for Alloy X,

$E = \quad 24.282 \times 10^6$ psi

$\alpha = \quad 9.853 \times 10^{-6}$ inch/inch- degree F

Therefore,

$\sigma = \quad 24.282 \times 9.853 \times 705 = 168{,}672$ psi

The conservative assumption is made that the maximum peak stress intensity due to mechanical loading plus thermal constraint occur at the same point at the same instant in time and reaches the value of $S_u$ at room temperature. Thus, the total stress intensity range from assembly to this hypothetical conservative state is

$S_R = \quad 168{,}672 + 75{,}000 = 243{,}672$ psi

The alternating stress intensity range, after accounting for temperature effects of Young's Modulus, is

$$S_a = \frac{S_R}{2} x \frac{\text{Young's Modulus } (70° \text{ F})}{\text{Young's Modulus } (775° \text{ F})}$$

$$= 121{,}836 \text{ psi } x \frac{28.14}{24.282} = 141{,}194 \text{ psi}$$

For the overpack, the most severely constrained material is at the bottom plate. Material properties for this calculation are the values available at 700 degrees F and the peak temperature is conservatively set at 700 degrees F.

Young's Modulus = E = $24.9 \times 10^6$ psi (at 700 degrees F)

Coefficient of linear thermal expansion = $\alpha = 7.52 \times 10^{-6}$ inch/inch-degrees F (Estimated)

Therefore, the secondary stress intensity due to fully constrained thermal growth is

$\sigma = 24.9 \times 7.52 \times (700\text{-}70) = 117{,}966$ psi

Conservatively, assuming that the membrane plus primary bending stress intensity achieves the ultimate strength at room temperature, at the same location in space and at the same instant in time, gives the total

stress intensity range at this hypothetical location as

$$S_R = 117,966 + 75,000 = 192,966 \text{ psi}$$

The alternating stress intensity range, after accounting for temperature effects of Young's Modulus, is

$$S_a = \frac{192,966}{2} x \frac{28.14}{24.9} = 109,037 \text{ psi}$$

These computed values for bounding alternating stress intensities are used in the next subsection for comparisons with allowable values.

2.7.3.4 Comparison of Fire Accident Results with Allowable Stresses

Stress

The safety factors for the MPC and overpack during a fire are addressed in Section 2.7.3.3. The lowest safety factors are 1.18 and 1.24 for the MPC and overpack, respectively.

Bounding Fire Transient

In accordance with Regulatory Position C.7 of the Regulatory Guide 7.6, Figure I-9.2.1 of ASME, Section III, Appendix I, gives the 10–cycle alternating stress intensity range as

$S_{ALT}$ (Alloy X) = 700,000 psi

Using the calculated stress intensity range from Subsection 2.7.3.3, the safety factor for the MPC basket is

$$SF = \frac{700,000}{141,194} = 4.96$$

Figure I-9.1 of ASME Section III, Appendix I is used for the overpack even though the temperature is limited to below 700 degrees F. It is conservative to use this curve for this short time event since increased

temperatures will improve the material ductility. From that table, the 10--cycle alternating stress intensity range is given as 400,000 psi. Therefore using the aforementioned calculated results for stress intensity

$$SF = \frac{400{,}000}{109{,}037} = 3.67$$

range from Subsection 2.7.3.3, the safety factor is computed as:

*An analysis of the threaded holes in the top closure has been performed to assess the length of engagement and stress requirements imposed on the connection by the transport loads. The methodology used to evaluate the connection is that set forth in Machinery's Handbook and uses the specific characteristics of the threaded joint. As part of the calculation* ~~It is shown in Appendix 2.A,~~ *it is demonstrated that* ~~that~~ the bolt force required to maintain the seal (seal seating load plus pressure force) is only ~~17~~*27*% of the total bolt preload force *that must be applied to ensure bolt performance under the various drop scenarios.* That is, there is ~~83~~*73*% excess capacity. Therefore, under the preload condition the reduction in bolt force due to the fire transient plus accident pressure is not sufficient to unload the seal.

The above calculations demonstrate that the requirements of Paragraph C.7 of Regulatory Guide 7.6 are satisfied.

2.7.4 Immersion - Fissile Material

In order for the spent nuclear fuel in the HI-STAR 100 System to become flooded with water, a leak must develop in both the overpack containment structure and the MPC enclosure vessel. The analysis provided demonstrates that both the overpack containment boundary and the MPC enclosure vessel meet the applicable stress and stress intensity allowables for normal conditions of transport and hypothetical accident conditions. Therefore, no leak will develop.

10CFR71.73(c)(5) specifies that fissile material packages, in those cases where water inleakage has not been assumed for criticality analysis, must be evaluated for immersion under a head of water of at least 0.9 m (3 ft.) in the attitude for which maximum leakage is expected. The criticality analyses presented in Chapter 6 conservatively assumes flooding with water at optimum moderation. Therefore, this paragraph is not applicable. However, analysis is presented to demonstrate that there is no water inleakage and verify that the flooded assumption made in the criticality analysis is conservative.

A head of water at a depth of 0.9 m (3 ft.) is equal to 1.3 psi. This pressure is bounded by the MPC enclosure vessel normal condition of transport and hypothetical accident condition external pressures listed in Table 2.1.1. The head of water (1.3 psi) is also bounded by the hypothetical accident condition external pressure for the overpack. Analysis provided in this chapter demonstrates that both the overpack containment boundary and the MPC enclosure vessel meet the applicable stress and stress intensity allowables for normal conditions of transport and hypothetical accident conditions. Therefore, there is no in-leakage of water into the overpack or MPC under a head of water at a depth of 0.9 m (3 ft.).

## 2.7.5 Immersion - All Packages

Deep submergence of the HI-STAR 100 System in 200 meters (656 ft.) of water creates an external pressure load equal to 284 psi which is less than the external design pressure of 300 psi. This condition is established as Load Case 18 in Table 2.1.9. Since the containment boundary is not punctured, stability of the package can be evaluated considering an undamaged package. The results for an external pressure of 300 psi bound the results for 21.7 psi gauge pressure that is established in 10CFR71.73(c)(6) as the applicable external pressure for this evaluation. *The* ~~Appendix 2.J examines the~~ elastic/plastic stability of the overpack *has been examined* using the methodology of ASME Code Case N-284. In the analysis, all structural resistance to the external pressure is *conservatively* concentrated in the inner containment shell. No credit is given to any structural support by the intermediate shells. The external pressure is assumed to act directly on the outer surface of the inner containment shell and the secondary fabrication stress is assumed to add to the stress due to the deep submergence pressure. The results ~~from Appendix 2.J~~ for this case are summarized below:~~.~~

Overpack Stability using ASME Code Case N-284 - Load Case 18 in Table 2.1.9

| Item | Value from Interaction Curve | Allowable Interaction Curve Value | Safety Factor |
|---|---|---|---|
| Yield Stress Limit | 0.577 | 1.34 | 2.32 |
| Elastic Stability | 0.253 | 1.0 | 3.95 |

It is noted that Code Case N-284 imposes limits on both stress and stability and includes a built-in safety factor of 1.34 for the Level D Service Limit. Therefore, the first row in the table above reports the true safety factor existing against exceeding the yield stress in the inner containment shell; the second row in the table provides the safety factor against elastic instability of the inner shell. The large values for the safety factors that are obtained, even with the conservative assumptions, attests to the ruggedness of the inner containment shell.

The analysis performed above for a 300 psi external pressure also confirms that the package meets the requirements of 10CFR71.61 that a 290 psi external pressure can be supported without any instability.

## 2.7.6 Summary of Damage

The results presented in Subsections 2.7.1 through 2.7.5 show that the HI-STAR 100 System meets the requirements of 10CFR71.61 and 10CFR71.73. All safety factors are greater than 1.0 for the hypothetical accident conditions of transport. Therefore, the HI-STAR 100 package, under the hypothetical accident conditions of transport, has adequate structural integrity to satisfy the subcriticality, containment, shielding, and temperature requirements of 10CFR71.

Table 2.7.1

MINIMUM SAFETY FACTORS FOR THE MPC FUEL BASKET UNDER HYPOTHETICAL ACCIDENT CONDITIONS OF TRANSPORT

| **Load Case Number** | **Load Combination*** | **Safety Factor** | **Location in SAR where Calculations or Results are Presented** |
|---|---|---|---|
| F3 | | | |
| F3.a | D + H', end drop | *4.194.27* | *Subsection* 2.7.1.1; Table 2.7.7 |
| F3.b | D + H', 0° side drop | *1.161.17* | ~~2.AC;~~ Table 2.7.4 |
| F3.c | D + H', 45° side drop | 1.28 | ~~2.AC;~~ Table 2.7.4 |

* The symbols used for loads are defined in Subsection 2.1.2.1.1.

Table 2.7.2

MINIMUM SAFETY FACTORS FOR THE MPC ENCLOSURE VESSEL FOR HYPOTHETICAL CONDITIONS OF TRANSPORT

| Load Case Number | Load Combination† | Safety Factor | Location in SAR where Calculations or Results are Presented | |
|---|---|---|---|---|
| E3 | | | | |
| E3.a | D + H' + $P_o$, end drop | *1.4~~2.37~~*<br>3.04<br>1.92 | Lid<br>Base*plate*<br>Shell | ~~2.L;~~ Table 2.7.7<br>~~2.N;~~ Table 2.7.7<br>~~2.J;~~ Table 2.7.7 |
| E3.b | D + H' + $P_i$, 0 *deg.*~~°~~ side drop | 2.14<br>1.16<br>~~1.43~~ | Shell<br>Supports<br>~~Supports~~ | *Table 2.7.4~~2.AC~~*<br>*Table 2.7.4~~2.AC~~*<br>~~2.AD~~ |
| E3.c | D + H' + $P_i$, 45 *deg.*~~°~~ side drop | 2.74<br>1.51 | Shell<br>Supports | *Table 2.7.4~~2.AC~~*<br>*Table 2.7.4~~2.AC~~* |
| E5 | $P_i^*$ or $P_o^*$ | *8.59~~27.3~~*<br>*1.17~~1.78~~*<br>1.18 *(buckling)*<br>4.16 *(mean stress)* | Lid<br>Base*plate*<br>Shell | ~~2.L;~~ Table 2.7.7<br>~~2.N;~~ Table 2.7.7<br>~~2.J ;~~ Table 2.7.7<br>*Subsection* 2.7.3.3.*1* |

† The symbols used for loads are defined in Subsection 2.1.2.1.1.

Table 2.7.3

MINIMUM SAFETY FACTORS FOR THE OVERPACK FOR HYPOTHETICAL ACCIDENT CONDITIONS OF TRANSPORT

| Load Case Number | Load Combination† | Safety Factor | Location in SAR where Calculations or Results are Presented |
|---|---|---|---|
| 1 | $T_h + D_{ba} + P_i + F + W_s$ | 2.21 | ~~2.AE;~~ Table 2.7.8 |
| 2 | $T_h + D_{ta} + P_i + F + W_s$ | 1.75 | ~~2.AE;~~ Table 2.7.5 |
| 3 | $T_h + D_{sa} + P_i + F + W_s$ | 2.19 | ~~2.AE;~~ Table 2.7.5 |
| 4 | $T_h + D_{ea} + P_i + F + W_s$ | 1.49 | ~~2.AE;~~ Table 2.7.5 |
| 5 | $T_h + D_{ga} + P_i + F + W_s$ | 2.60 | ~~2.AE;~~ Table 2.7.5 |
| 6 | $T_h + P_s + P_i + F + W_s$ | 2.80 | ~~2.AE;~~ Table 2.7.5 |
| 7 | $T_h + P_t + P_i + F + W_s$ | 2.03 (see note 1) | ~~2.AE;~~ Table 2.7.5 |
| 8 | $T_h + P_b + P_i + F + W_s$ | 1.46 | ~~2.AE;~~ Table 2.7.5 |
| 9 | $T_c + D_{ba} + P_o + F + W_s$ | 4.17 | ~~2.AE;~~ Table 2.7.6 |
| 10 | $T_c + D_{ta} + P_o + F + W_s$ | 1.87 | ~~2.AE;~~ Table 2.7.6 |
| 11 | $T_c + D_{sa} + P_o + F + W_s$ | 2.19 | ~~2.AE;~~ Table 2.7.6 |
| 12 | $T_c + D_{ea} + P_o + F + W_s$ | 1.73 | ~~2.AE;~~ Table 2.7.6 |
| 13 | $T_c + D_{ga} + P_o + F + W_s$ | 2.65 | ~~2.AE;~~ Table 2.7.6 |
| 14 | $T_c + P_s + P_o + F + W_s$ | 3.05 | ~~2.AE;~~ Table 2.7.6 |
| 15 | $T_c + P_t + P_o + F + W_s$ | 2.09 (see note 1) | ~~2.AE;~~ Table 2.7.6 |
| 16 | $T_c + P_b + P_o + F + W_s$ | 1.46 | ~~2.AE;~~ Table 2.76 |
| 17 | $T_f + P_i + F + W_s$ | pre-load maintained ~~(see Section 2.7.3.4)~~ | *Subsection 2.7.3.~~42.V~~* |
| 18 | $P_o$* | 2.32 | ~~2.J~~; Table 2.7.8 |
| 19 | $P_i^* + T_f + F + W_s$ | 12.4 | *Subsection* 2.7.3.3.2 |
| 20 | $T_h + D_{ga} + P_i + F + W_s$ | 1.77 | ~~2.AE~~; Table 2.7.5 |
| 21 | $T_c + D_{ga} + P_i + F + W_s$ | 1.84 | ~~2.AE~~; Table 2.7.6 |
| 22 | $T_c + D_{ga} + P_i + F + W_s$ | 2.14 | ~~2.AE~~; Table 2.7.5 |

Note: 1. This reported stress is directly under the point of impact. Therefore, the calculated value does not represent a primary stress; however, primary stress levels are met by this peak stress intensity.

† The symbols used here are defined in Subsection 2.1.2.1.1

Table 2.7.4 - FINITE ELEMENT ANALYSIS RESULTS
MINIMUM SAFETY FACTORS FOR MPC COMPONENTS UNDER ACCIDENT CONDITIONS

| Component - Stress Result | MPC-24 | | *MPC-32* | | MPC-68 | |
|---|---|---|---|---|---|---|
| | 30 Ft. Side Drop, 0° Orientation Load Case F3.b or E3.b | 30 Ft. Side Drop, 45° Orientation Load Case F3.c or E3.c | *30 Ft. Side Drop, 0° Orientation Load Case F3.b or E3.b* | *30 Ft. Side Drop, 45° Orientation Load Case F3.c or E3.c* | 30 Ft. Side Drop, 0° Orientation Load Case F3.b or E3.b | 30 Ft. Side Drop, 45° Orientation Load Case F3.c or E3.c |
| Fuel Basket – Primary Membrane ($P_m$) | *2.80~~2.69~~* ~~(852)~~ ~~[2.AC.14]~~ | *3.85~~3.78~~* ~~(852)~~ ~~[2.AC.20]~~ | *2.78* | *3.90* | 3.07 ~~(1603)~~ ~~[2.AC.64]~~ | 4.30 ~~(1603)~~ ~~[2.AC.70]~~ |
| Fuel Basket - Local Membrane Plus Primary Bending ($P_L + P_b$) | *1.19~~1.17~~* ~~(1012)~~ ~~[2.AC.15]~~ | *1.29~~1.28~~* ~~(632)~~ ~~[2.AC.21]~~ | *1.19* | *1.28* | 2.64 ~~(1033)~~ ~~[2.AC.65]~~ | 1.56 ~~(774)~~ ~~[2.AC.71]~~ |
| Enclosure Vessel - Primary Membrane ($P_m$) | *6.43~~6.84~~* ~~(1210)~~ ~~[2.AC.16]~~ | *6.88~~6.91~~* ~~(1232)~~ ~~[2.AC.22]~~ | *5.77* | *6.95* | 5.65 ~~(1770)~~ ~~[2.AC.66]~~ | 7.13 ~~(1864)~~ ~~[2.AC.72]~~ |
| Enclosure Vessel - Local Membrane Plus Primary Bending ($P_L + P_b$) | *4.24~~2.64~~* ~~(1138)~~ ~~[2.AC.17]~~ | *4.28~~3.20~~* ~~(1225)~~ ~~[2.AC.23]~~ | *2.14* | *3.56* | 3.07 ~~(1770)~~ ~~[2.AC.67]~~ | 2.74 ~~(1866)~~ ~~[2.AC.73]~~ |
| Basket Supports - Primary Membrane ($P_m$) | *N/A* ~~4.81~~ ~~(1096)~~ ~~[2.AC.18]~~ | *N/A* ~~6.93~~ ~~(1102)~~ ~~[2.AC.24]~~ | *2.72* | *3.83* | 6.68 ~~(1699)~~ ~~[2.AC.68]~~ | 8.68 ~~(1644)~~ ~~[2.AC.74]~~ |
| Basket Supports - Local Membrane Plus Primary Bending ($P_L + P_b$) | *N/A* ~~6.48~~ ~~(1096)~~ ~~[2.AC.19]~~ | *N/A* ~~5.04~~ ~~(1088)~~ ~~[2.AC.25]~~ | *3.89* | *4.75* | 1.16 ~~(1704)~~ ~~[2.AC.69]~~ | 1.51 ~~(1649)~~ ~~[2.AC.75]~~ |

~~Notes: 1. Corresponding ANSYS element number shown in parentheses (Appendices 2.W through 2.AB provide element locations).~~
~~2. Corresponding appendix table number shown in brackets.~~

*Table 2.7.4 (Continued) - FINITE ELEMENT ANALYSIS RESULTS*
*MINIMUM SAFETY FACTORS FOR MPC COMPONENTS UNDER ACCIDENT CONDITIONS*

| *Component - Stress Result* | *MPC-24E/EF* | |
|---|---|---|
| | *30 Ft. Side Drop, 0 deg° Orientation Load Case F3.b or E3.b* | *30 Ft. Side Drop, 45 deg° Orientation Load Case F3.c or E3.c* |
| *Fuel Basket – Primary Membrane ($P_m$)* | *2.75* | *3.80* |
| *Fuel Basket - Local Membrane Plus Primary Bending ($P_L + P_b$)* | *1.16* | *1.28* |
| *Enclosure Vessel - Primary Membrane ($P_m$)* | *6.41* | *6.88* |
| *Enclosure Vessel - Local Membrane Plus Primary Bending ($P_L + P_b$)* | *3.15* | *4.14* |

Table 2.7.5 - FINITE ELEMENT ANALYSIS RESULTS
MINIMUM SAFETY FACTORS FOR OVERPACK COMPONENTS UNDER ACCIDENT CONDITIONS (Hot Environment)

| Component – Stress Result | 30 Ft. Bottom End Drop Load Case 1 | 30 Ft. Top End Drop Load Case 2 | 30 Ft. Side Drop Load Case 3 | 30 Ft. C.G. Over-the-Bottom-Corner Drop Load Case 4 |
|---|---|---|---|---|
| Lid – Local Membrane Plus Primary Bending ($P_L + P_b$) | 34.04<br>~~(501)~~<br>~~[2.AE.9]~~ | 1.75<br>~~(501)~~<br>~~[2.AE.10]~~ | 2.60<br>~~(501)~~<br>~~[2.AE.11]~~ | 7.76<br>~~(501)~~<br>~~[2.AE.12]~~ |
| Inner Shell – Local Membrane Plus Primary Bending ($P_L + P_b$) | 4.35<br>~~(10790)~~<br>~~[2.AE.9]~~ | 10.02<br>~~(11025)~~<br>~~[2.AE.10]~~ | 2.19<br>~~(280)~~<br>~~[2.AE.11]~~ | 2.93<br>~~(5420)~~<br>~~[2.AE.12]~~ |
| Inner Shell – Primary Membrane ($P_m$) | 4.48<br>~~(48)~~<br>~~[2.AE.9]~~ | 7.39<br>~~(281)~~<br>~~[2.AE.10]~~ | 2.45<br>~~(281)~~<br>~~[2.AE.11]~~ | 2.33<br>~~(5421)~~<br>~~[2.AE.12]~~ |
| Intermediate Shells - Local Membrane Plus Primary Bending ($P_L + P_b$) | 6.63<br>~~(10792)~~<br>~~[2.AE.9]~~ | 7.95<br>~~(286)~~<br>~~[2.AE.10]~~ | 2.33<br>~~(53)~~<br>~~[2.AE.11]~~ | 1.49<br>~~(5426)~~<br>~~[2.AE.12]~~ |
| Baseplate - Local Membrane Plus Primary Bending ($P_L + P_b$) | 7.05<br>~~(27)~~<br>~~[2.AE.9]~~ | 21.6<br>~~(1)~~<br>~~[2.AE.10]~~ | 4.71<br>~~(1)~~<br>~~[2.AE.11]~~ | 2.78<br>~~(1)~~<br>~~[2.AE.12]~~ |
| Enclosure Shell - Primary Membrane ($P_m$) | 16.44<br>~~(55)~~<br>~~[2.AE.9]~~ | 12.23<br>~~(288)~~<br>~~[2.AE.10]~~ | 2.19<br>~~(55)~~<br>~~[2.AE.11]~~ | 5.48<br>~~(55)~~<br>~~[2.AE.12]~~ |

Notes: 1. *Load cases are defined in Table 2.1.9.*~~Corresponding ANSYS node number shown in parentheses.~~

~~2. Corresponding appendix table shown in brackets.~~

~~5.Load cases are defined in Table 2.1.9~~

Table 2.7.5 (continued) - FINITE ELEMENT ANALYSIS RESULTS
MINIMUM SAFETY FACTORS FOR OVERPACK COMPONENTS UNDER ACCIDENT CONDITIONS (Hot Environment)

| Component - Stress Result | 30 Ft. C.G. Over-the-Top-Corner Drop-Load Case 5 | Side Puncture Load Case 6 | Top End Puncture Load Case 7 | Bottom End Puncture Load Case 8 | 30 Ft.. – 30 degree Drop Load Case 20 | 30 Ft.. – Slapdown Load Case 22 |
|---|---|---|---|---|---|---|
| Lid – Local Membrane Plus Primary Bending ($P_L + P_b$) | 3.69 ~~(479)~~ ~~[2.AE.13]~~ | 5.70 ~~(501)~~ ~~[2.AE.14]~~ | 2.03 (See Note ~~2~~3) ~~(479)~~ ~~[2.AE.15]~~ | 6.29 ~~(501)~~ ~~[2.AE.16]~~ | 1.77 ~~(479)~~ ~~[2.AE.25]~~ | 2.22 ~~(501)~~ ~~[2.AE.27]~~ |
| Inner Shell – Local Membrane Plus Primary Bending ($P_L + P_b$) | 3.16 ~~(2968)~~ ~~[2.AE.13]~~ | 2.80 ~~(156)~~ ~~[2.AE.14]~~ | 29.29 ~~(11023)~~ ~~[2.AE.15]~~ | 9.52 ~~(10790)~~ ~~[2.AE.16]~~ | 2.78 ~~(280)~~ ~~[2.AE.25]~~ | 2.73 ~~(2968)~~ ~~[2.AE.27]~~ |
| Inner Shell – Primary Membrane ($P_m$) | 2.60 ~~(2969)~~ ~~[2.AE.13]~~ | 5.95 ~~(155)~~ ~~[2.AE.14]~~ | 26.5 ~~(281)~~ ~~[2.AE.15]~~ | 10.61 ~~(48)~~ ~~[2.AE.16]~~ | 2.45 ~~(2969)~~ ~~[2.AE.25]~~ | 2.14 ~~(2969)~~ ~~[2.AE.27]~~ |
| Intermediate Shells - Local Membrane Plus Primary Bending ($P_L + P_b$) | 3.52 ~~(2970)~~ ~~[2.AE.13]~~ | 6.19 ~~(166)~~ ~~[2.AE.14]~~ | 32.52 ~~(11025)~~ ~~[2.AE.15]~~ | 15.12 ~~(10792)~~ ~~[2.AE.16]~~ | 3.28 ~~(2970)~~ ~~[2.AE.25]~~ | 2.88 ~~(2970)~~ ~~[2.AE.27]~~ |
| Baseplate - Local Membrane Plus Primary Bending ($P_L + P_b$) | 6.95 ~~(27)~~ ~~[2.AE.13]~~ | 21.62 ~~(1)~~ ~~[2.AE.14]~~ | 28.62 ~~(1)~~ ~~[2.AE.15]~~ | 1.46 ~~(1)~~ ~~[2.AE.16]~~ | 27.32 ~~(27)~~ ~~[2.AE.25]~~ | 17.9 ~~(1)~~ ~~[2.AE.27]~~ |
| Enclosure Shell - Primary Membrane ($P_m$) | 3.56 ~~(5661)~~ ~~[2.AE.13]~~ | 4.53 ~~(167)~~ ~~[2.AE.14]~~ | 51.32 ~~(2976)~~ ~~[2.AE.15]~~ | 29.9 ~~(55)~~ ~~[2.AE.16]~~ | 8.02 ~~(5661)~~ ~~[2.AE.25]~~ | 2.40 ~~(288)~~ ~~[2.AE.27]~~ |

Notes:
1. *Load cases are defined in Table 2.1.9.*~~Corresponding ANSYS node number shown in parentheses.~~
2. *Stress Intensity computed just outboard of the loaded area since surface stress is not a primary stress component.*~~Corresponding appendix table shown in brackets.~~
3. ~~Stress Intensity computed just outboard of the loaded area since surface stress is not a primary stress component~~
4. ~~Load cases are defined in Table 2.1.9.~~

Table 2.7.6 - FINITE ELEMENT ANALYSIS RESULTS
MINIMUM SAFETY FACTORS FOR OVERPACK COMPONENTS UNDER ACCIDENT CONDITIONS (Cold Environment)

| Component – Stress Result | 30 Ft. Bottom End Drop Load Case 9 | 30 Ft. Top End Drop Load Case 10 | 30 Ft. Side Drop Load Case 11 | 30 Ft. C.G. Over-the-Bottom-Corner Drop Load Case 12 |
|---|---|---|---|---|
| Lid – Local Membrane Plus Primary Bending ($P_L + P_b$) | 30.29 ~~(501)~~ ~~[2.AE.17]~~ | 1.87 ~~(501)~~ ~~[2.AE.18]~~ | 2.73 ~~(501)~~ ~~[2.AE.19]~~ | 8.00 ~~(501)~~ ~~[2.AE.20]~~ |
| Inner Shell – Local Membrane Plus Primary Bending ($P_L + P_b$) | 4.17 ~~(47)~~ ~~[2.AE.17]~~ | 9.69 ~~(280)~~ ~~[2.AE.18]~~ | 2.19 ~~(280)~~ ~~[2.AE.19]~~ | 2.94 ~~(5420)~~ ~~[2.AE.20]~~ |
| Inner Shell – Primary Membrane ($P_m$) | 4.37 ~~(10791)~~ ~~[2.AE.17]~~ | 7.33 ~~(11024)~~ ~~[2.AE.18]~~ | 2.47 ~~(281)~~ ~~[2.AE.19]~~ | 2.36 ~~(5421)~~ ~~[2.AE.20]~~ |
| Intermediate Shells - Local Membrane Plus Primary Bending ($P_L + P_b$) | 4.95 ~~(49)~~ ~~[2.AE.17]~~ | 8.66 ~~(11029)~~ ~~[2.AE.18]~~ | 2.61 ~~(53)~~ ~~[2.AE.19]~~ | 1.73 ~~(5426)~~ ~~[2.AE.20]~~ |
| Baseplate - Local Membrane Plus Primary Bending ($P_L + P_b$) | 7.73 ~~(27)~~ ~~[2.AE.17]~~ | 17.07 ~~(1)~~ ~~[2.AE.18]~~ | 4.80 ~~(1)~~ ~~[2.AE.19]~~ | 2.73 ~~(1)~~ ~~[2.AE.20]~~ |
| Enclosure Shell - Primary Membrane ($P_m$) | 20.08 ~~(10882)~~ ~~[2.AE.17]~~ | 18.4 ~~(11031)~~ ~~[2.AE.18]~~ | 2.45 ~~(55)~~ ~~[2.AE.19]~~ | 5.71 ~~(55)~~ ~~[2.AE.20]~~ |

Notes:
1. *Load cases are defined in Table 2.1.9.*~~Corresponding ANSYS node number shown in parentheses.~~
2. ~~Corresponding appendix table shown in brackets.~~
3. ~~Load cases are defined in Table 2.1.9.~~

Table 2.7.6 (continued) - FINITE ELEMENT ANALYSIS RESULTS
MINIMUM SAFETY FACTORS FOR OVERPACK COMPONENTS UNDER ACCIDENT CONDITIONS (Cold Environment)

| Component – Stress Result | 30 Ft. C.G. Over-the-Top-Corner Drop Load Case 13 | Side Puncture Load Case 14 | Top End Puncture Load Case 15 | Bottom End Puncture Load Case 16 | 30 Ft.. – 30 degree Drop Load Case 21 |
|---|---|---|---|---|---|
| Lid – Local Membrane Plus Primary Bending ($P_L + P_b$) | 3.91 ~~(479)~~ ~~[2.AE.21]~~ | 5.91 ~~(501)~~ ~~[2.AE.22]~~ | 2.09 (See Note ~~2~~3) ~~(479)~~ ~~[2.AE.23]~~ | 6.64 ~~(501)~~ ~~[2.AE.24]~~ | 1.84 ~~(479)~~ ~~[2.AE.26]~~ |
| Inner Shell – Local Membrane Plus Primary Bending ($P_L + P_b$) | 3.21 ~~(2968)~~ ~~[2.AE.21]~~ | 3.05 ~~(156)~~ ~~[2.AE.22]~~ | 24.97 ~~(280)~~ ~~[2.AE.23]~~ | 8.54 ~~(47)~~ ~~[2.AE.24]~~ | 2.78 ~~(280)~~ ~~[2.AE.26]~~ |
| Inner Shell – Primary Membrane ($P_m$) | 2.65 ~~(2969)~~ ~~[2.AE.21]~~ | 7.60 ~~(155)~~ ~~[2.AE.22]~~ | 17.03 ~~(281)~~ ~~[2.AE.23]~~ | 9.59 ~~(10791)~~ ~~[2.AE.24]~~ | 2.48 ~~(2969)~~ ~~[2.AE.26]~~ |
| Intermediate Shells - Local Membrane Plus Primary Bending ($P_L + P_b$) | 4.10 ~~(2970)~~ ~~[2.AE.21]~~ | 7.06 ~~(166)~~ ~~[2.AE.22]~~ | 27.55 ~~(11025)~~ ~~[2.AE.23]~~ | 14.9 ~~(49)~~ ~~[2.AE.24]~~ | 3.81 ~~(2970)~~ ~~[2.AE.26]~~ |
| Baseplate - Local Membrane Plus Primary Bending ($P_L + P_b$) | 7.08 ~~(27)~~ ~~[2.AE.21]~~ | 29.69 ~~(27)~~ ~~[2.AE.22]~~ | 47.25 ~~(1)~~ ~~[2.AE.23]~~ | 1.46 ~~(1)~~ ~~[2.AE.24]~~ | 21.91 ~~(27)~~ ~~[2.AE.26]~~ |
| Enclosure Shell - Primary Membrane ($P_m$) | 4.13 ~~(5561)~~ ~~[2.AE.21]~~ | 5.17 ~~(167)~~ ~~[2.AE.22]~~ | 57.21 ~~(55)~~ ~~[2.AE.23]~~ | 76.5 ~~(288)~~ ~~[2.AE.24]~~ | 9.64 ~~(5661)~~ ~~[2.AE.26]~~ |

Notes:
1. *Load cases are defined in Table 2.1.9.*~~Corresponding ANSYS node number shown in parentheses.~~
2. *Surface pressure not included in safety factor evaluation since it is not a primary stress.*~~Corresponding appendix table shown in brackets.~~
3. ~~Surface pressure not included in safety factor evaluation since it is not a primary stress.~~
4. ~~Load cases are defined in Table 2.1.9.~~

Table 2.7.7

MINIMUM SAFETY FACTORS FOR MISCELLANEOUS ITEMS - MPC FUEL BASKET/CANISTER - HYPOTHETICAL ACCIDENT CONDITIONS OF TRANSFER

| Item | Loading | Safety Factor | Location in SAR Where *Calculations or Results are Presented*~~Detailed Analysis Performed~~ |
|---|---|---|---|
| Fuel Basket Axial Stress | End Drop | *4.19*~~4.27~~ | Subsection 2.7.1.1 |
| Fuel Basket Axial Stress | Fire Transient (Regulatory Position C.7 of Regulatory Guide 7.6) | 4.96 | Subsection 2.7.3.4 |
| MPC Canister Stability | 30' End Drop (Load Case E3.a, Table 2.1.7) | 1.92 | ~~2.J;~~ Subsection 2.7.1.1 |
| MPC Top Closure Lid Bending Stress | 30' End Drop (Load Case E3.a in Table 2.1.7) | *2.8 (single lid)*~~13.1~~ *1.4 (dual lid)* | ~~2.L;~~ Subsection 2.7.1.1 |
| MPC Top Closure Lid – Loading in Peripheral Weld | 30' End Drop (Load Case E3.a in Table 2.1.7) | 2.37 | ~~2.L;~~ Subsection 2.7.1.1 |
| MPC Baseplate Bending Stress | 30' End Drop (Load Case E3.a in Table 2.1.7) | 3.04 | ~~2.N;~~ Subsection 2.7.1.1 |
| MPC Canister at Connection to Baseplate | 30' End Drop (Load Case E3.a in Table 2.1.7) | 2.14 | ~~2.N;~~ Subsection 2.7.1.1 |
| MPC Top Closure Lid Bending Stress | Fire accident (Load Case E5 in Table 2.1.7) | *8.59*~~27.3~~ | ~~2.L;~~ Subsection 2.7.3.3.*1* |
| MPC Baseplate Bending Stress | Fire accident (Load Case E5 in Table 2.1.7) | *1.17*~~1.78~~ | ~~2.N;~~ Subsection 2.7.3.3.*1* |
| MPC Canister Stability | Fire accident (Load Case E5 in Table 2.1.7) | 1.18 | ~~2.J;~~ Subsection 2.7.3.3.*1* |
| MPC Shell Mean Stress | Fire accident (Load Case E5 in Table 2.1.7) | 4.16 | Subsection 2.7.3.3.1 |

Table 2.7.8

MINIMUM SAFETY FACTORS FOR MISCELLANEOUS ITEMS - OVERPACK - HYPOTHETICAL ACCIDENT CONDITIONS OF TRANSPORT

| Item | Loading | Safety Factor | Location in SAR Where *Calculations or Results are Presented*~~Detailed Analysis Performed~~ |
|---|---|---|---|
| Overpack Stability | 30' End Drop (Load Cases 1 and 2 in Table 2.1.9) | 2.21 | ~~2.J;~~ Subsection 2.7.1.1 |
| Closure Bolts | 30' End Drop (Load Case 2 in Table 2.1.9) | 1.30 | ~~2.U;~~ Subsection 2.7.1.1 |
| Closure Bolts | Top End Puncture | ~~1.39~~*1.86* | ~~2.U;~~ Subsection 2.7.2 |
| Overpack Inner Shell Mean Stress | Fire Transient | 12.39 | Subsection 2.7.3.3.*2* |
| Overpack Stress | Fire Transient (Regulatory Position C.7 of Regulatory Guide 7.6) | 3.67 | Subsection 2.7.3.4 |
| Overpack Stability (Yield Stress Criteria) | Immersion (Load Case 18 in Table 2.1.9) | 2.32 | ~~2.J;~~ Subsection 2.7.5 |
| Overpack Stability (Stability Criteria) | Immersion (Load Case 18 in Table 2.1.9) | 3.95 | ~~2.J;~~ Subsection 2.7.5 |

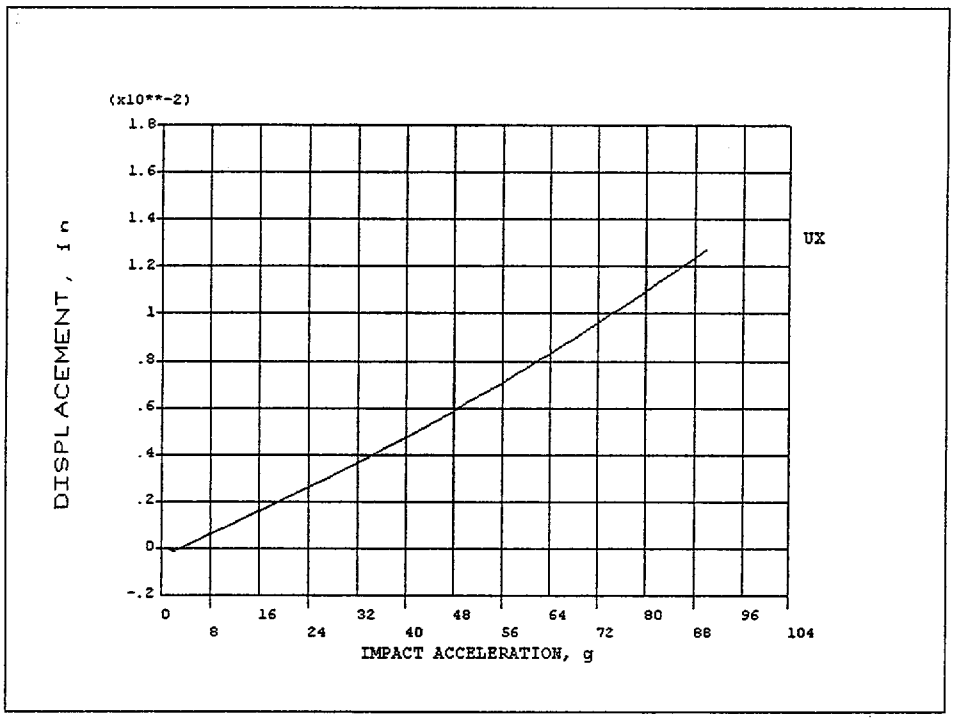


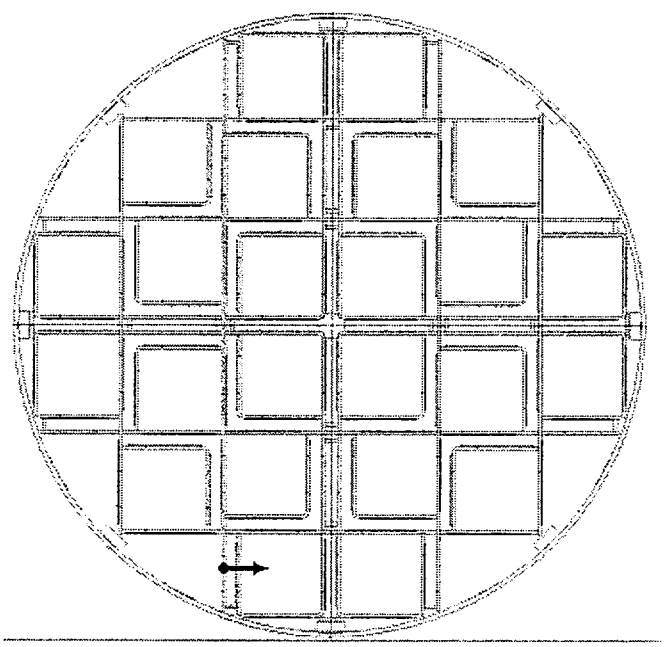

FIGURE 2.7.1; NON-LINEAR BUCKLING ANALYSIS FOR MPC-24
DISPLACEMENT vs. IMPACT ACCELERATION (0° DROP)

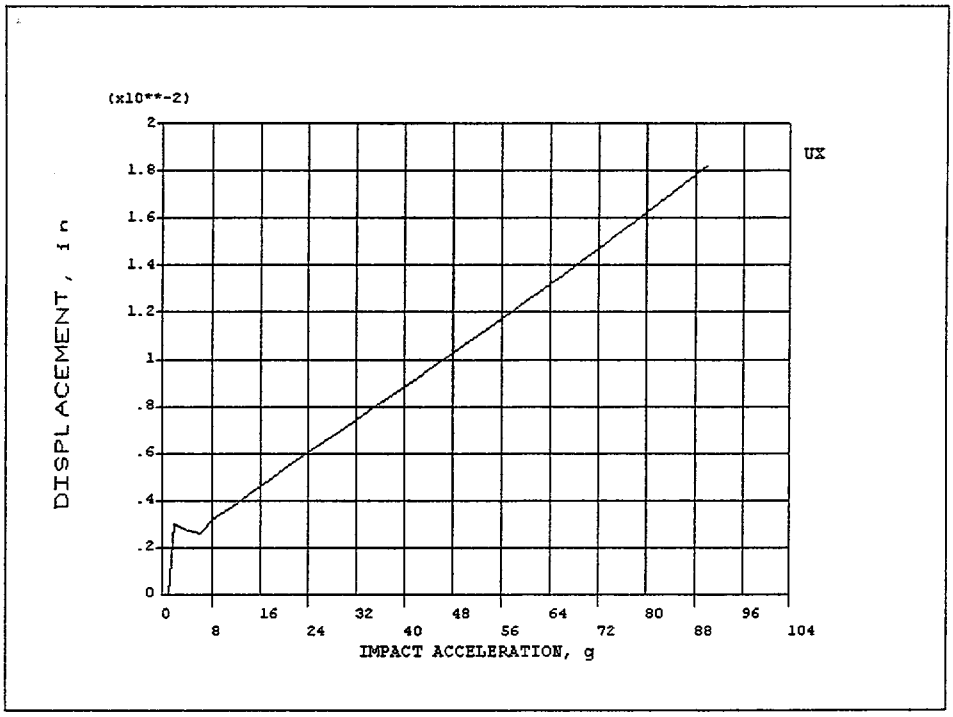


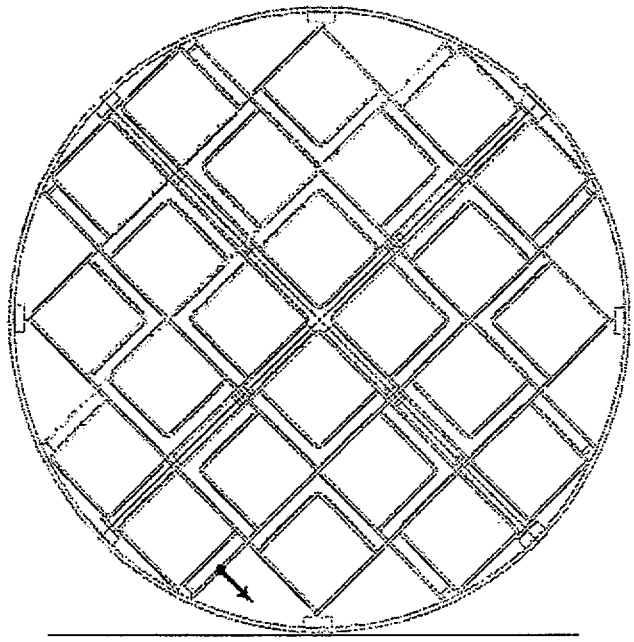

FIGURE 2.7.2; NON-LINEAR BUCKLING ANALYSIS FOR MPC-24
DISPLACEMENT vs. IMPACT ACCELERATION (45° DROP)

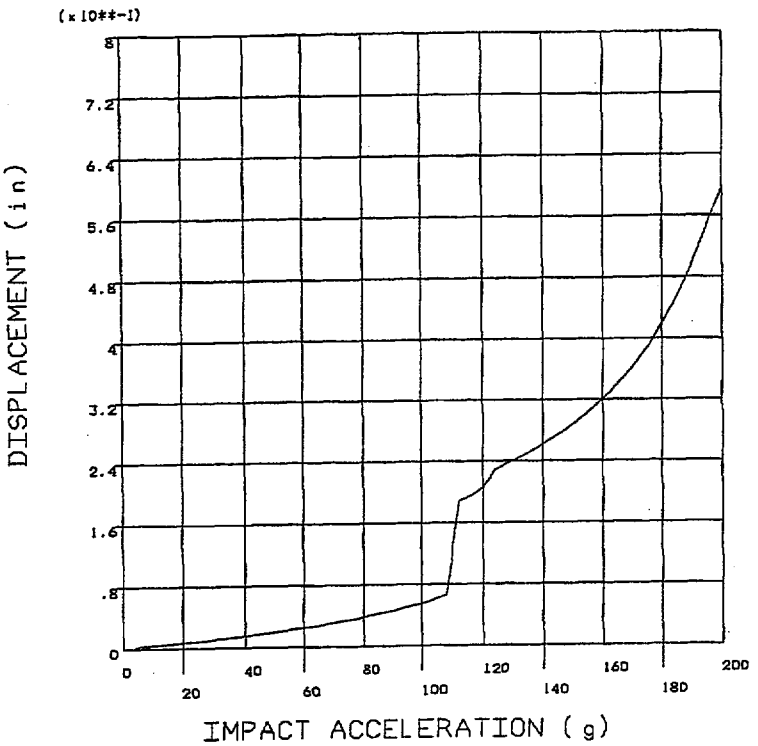


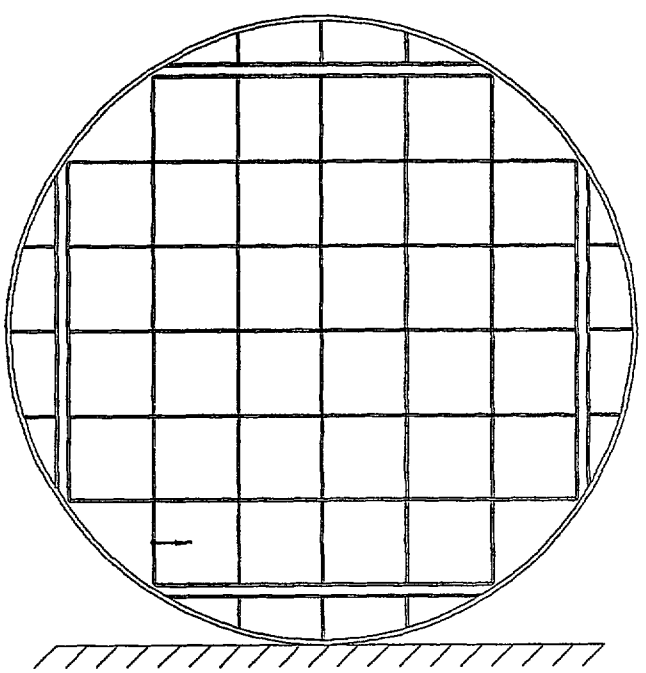

FIGURE 2.7.3 ; NON-LINEAR BUCKLING ANALYSIS FOR MPC-32
DISPLACEMENT Vs. IMPACT ACCELERATION ( 0° DROP )

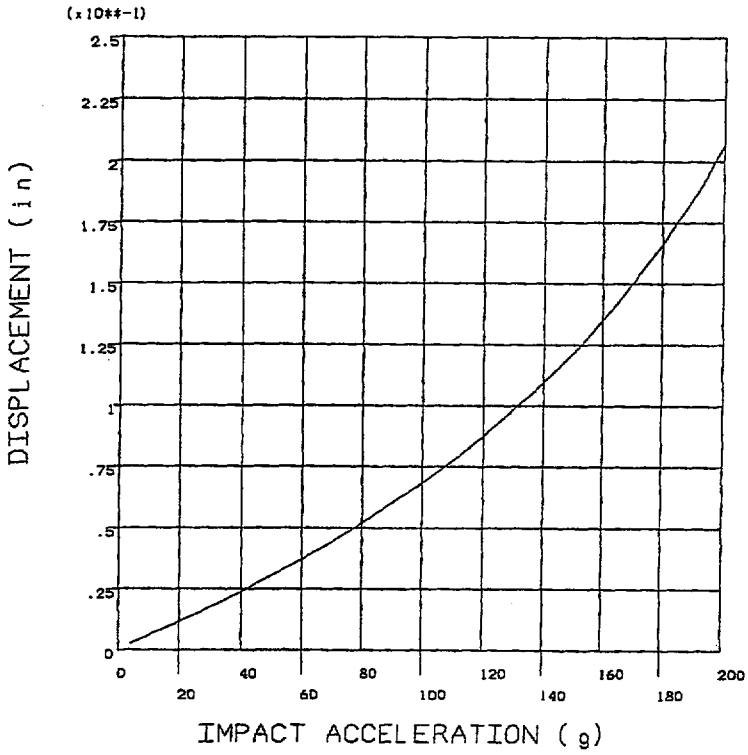


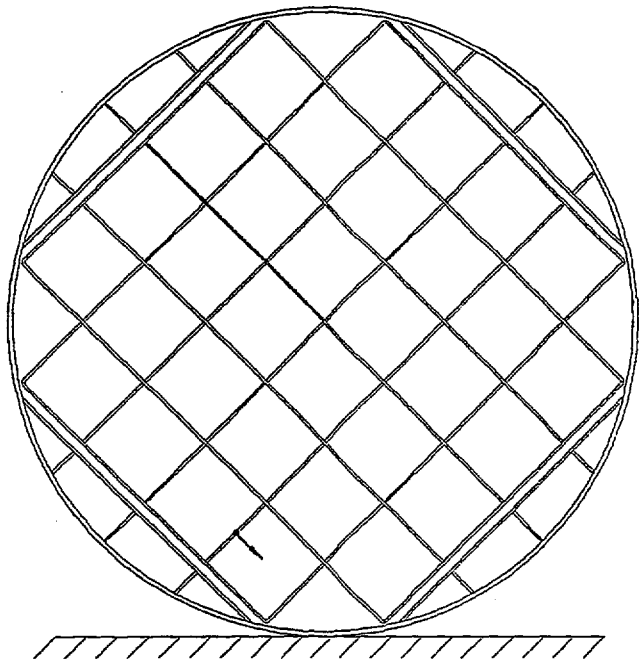

FIGURE 2.7.4 ; NON-LINEAR BUCKLING ANALYSIS FOR MPC-32
DISPLACEMENT Vs. IMPACT ACCELERATION ( 45° DROP )

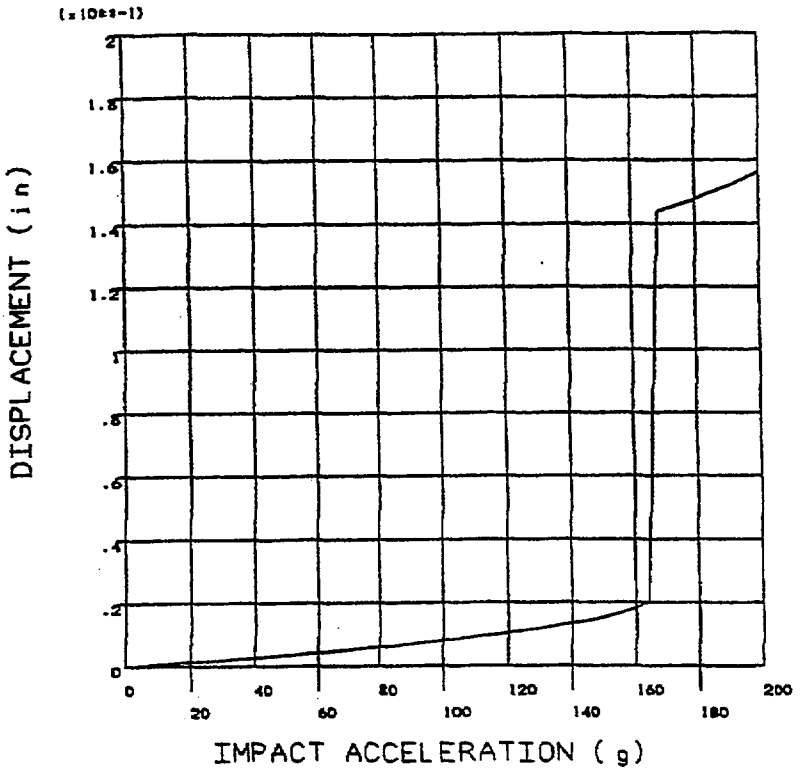


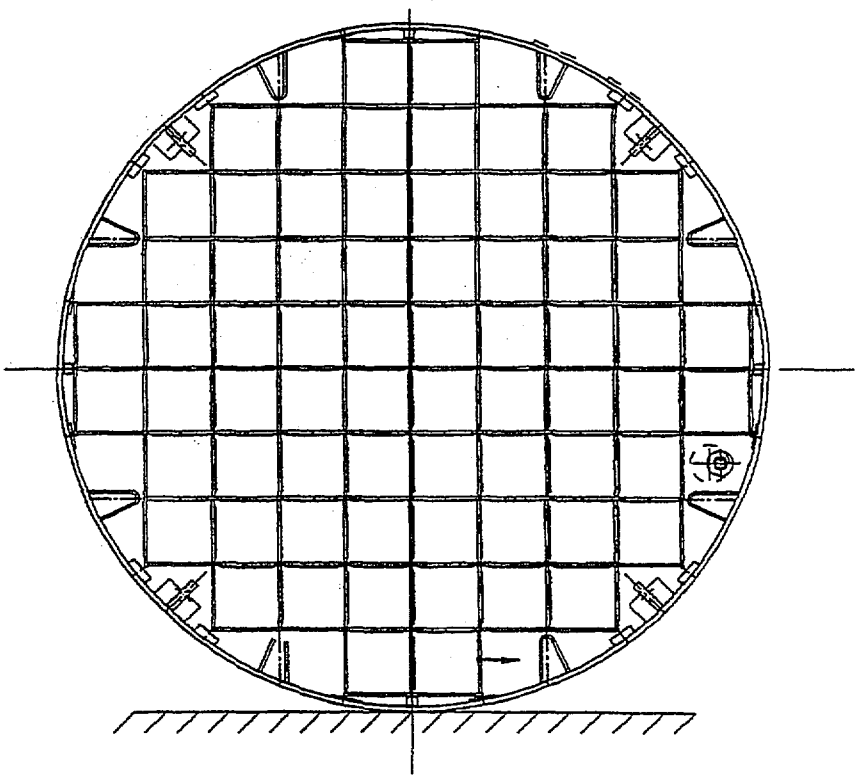

FIGURE 2.7.5; NON-LINEAR BUCKLING ANALYSIS FOR MPC-68
DISPLACEMENT Vs. IMPACT ACCELERATION (0° DROP)

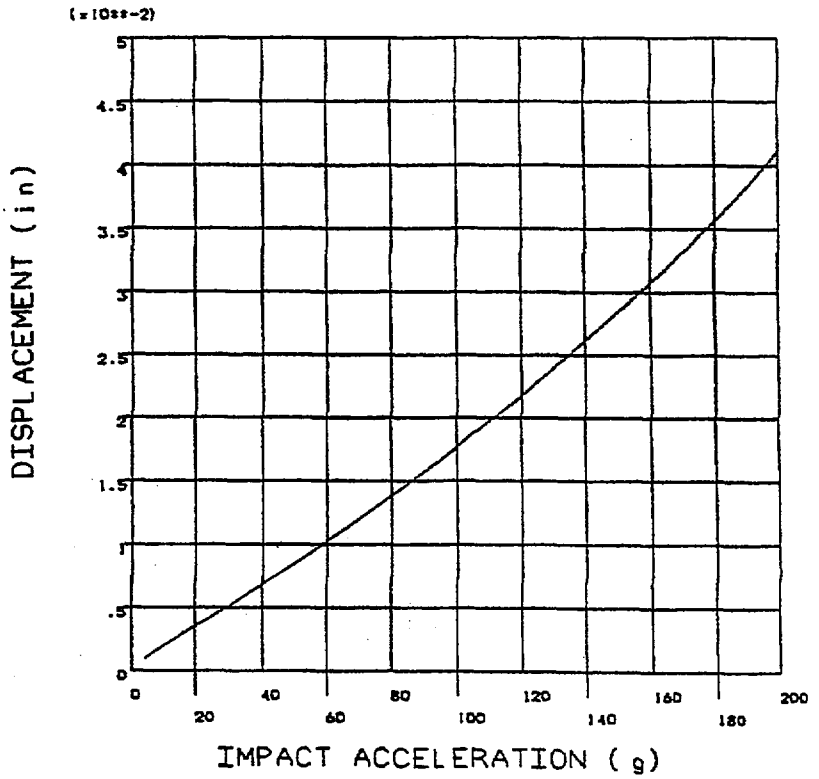


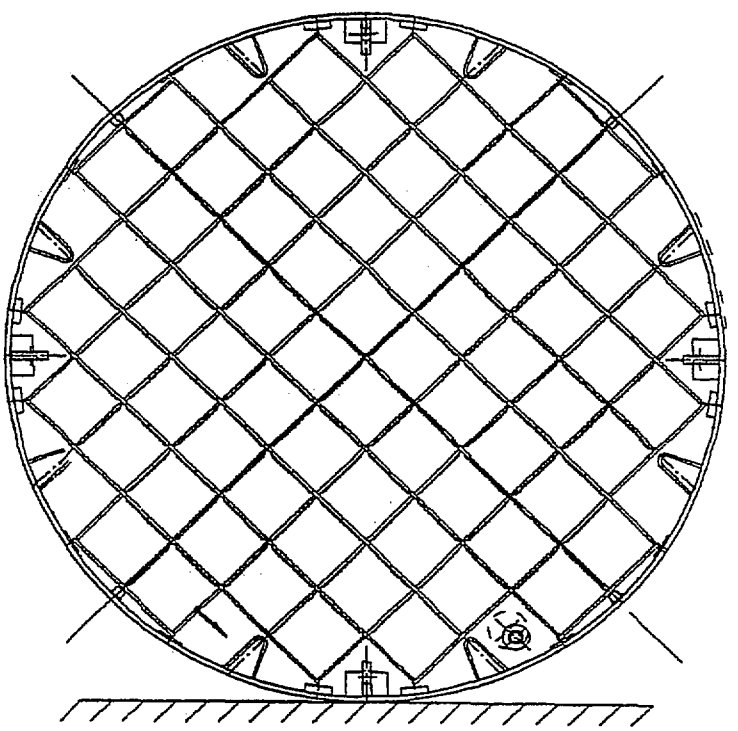

FIGURE 2.7.6; NON-LINEAR BUCKLING ANALYSIS FOR MPC-68
DISPLACEMENT Vs. IMPACT ACCELERATION ( 45° DROP )

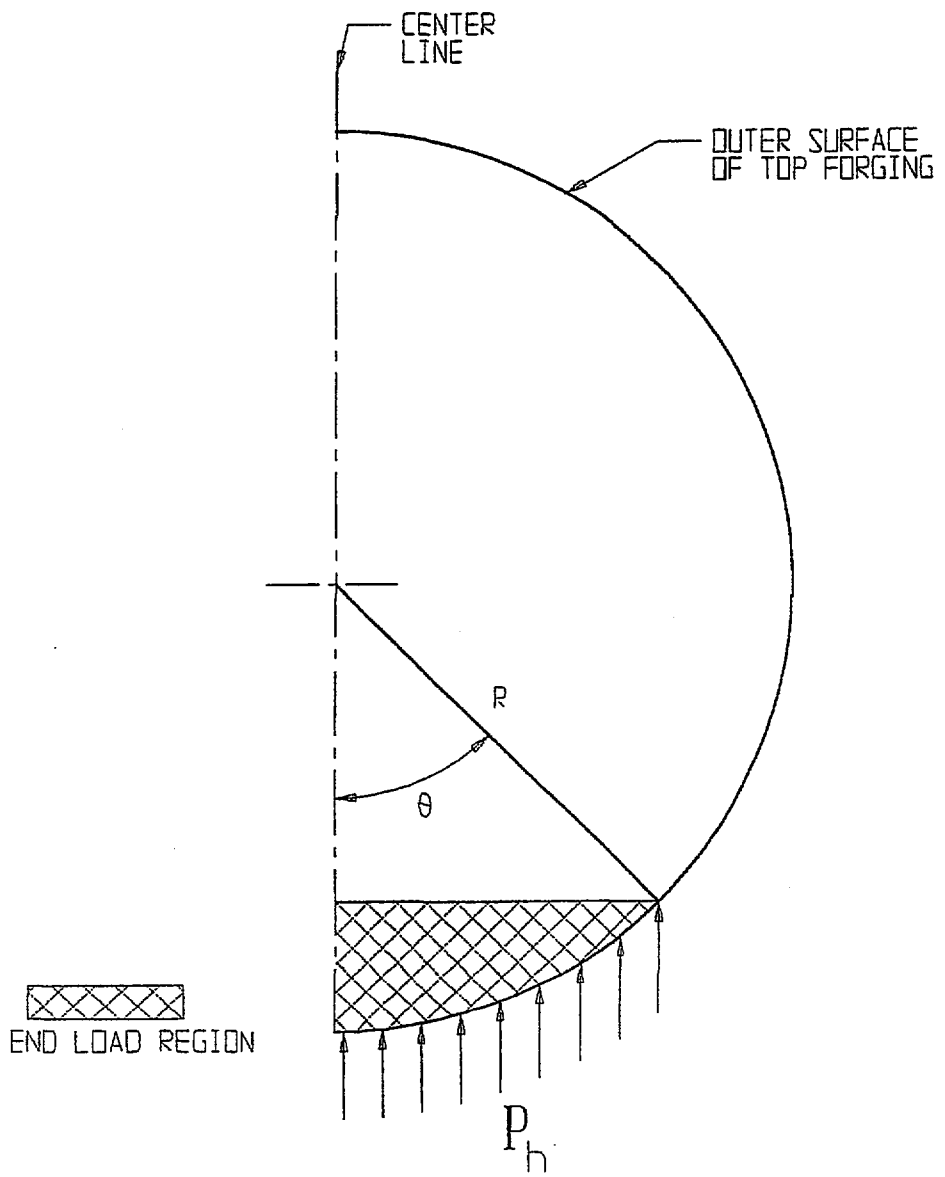


FIGURE 2.7.7; IMPACT LIMITER LOADED AREAS ON THE OVERPACK

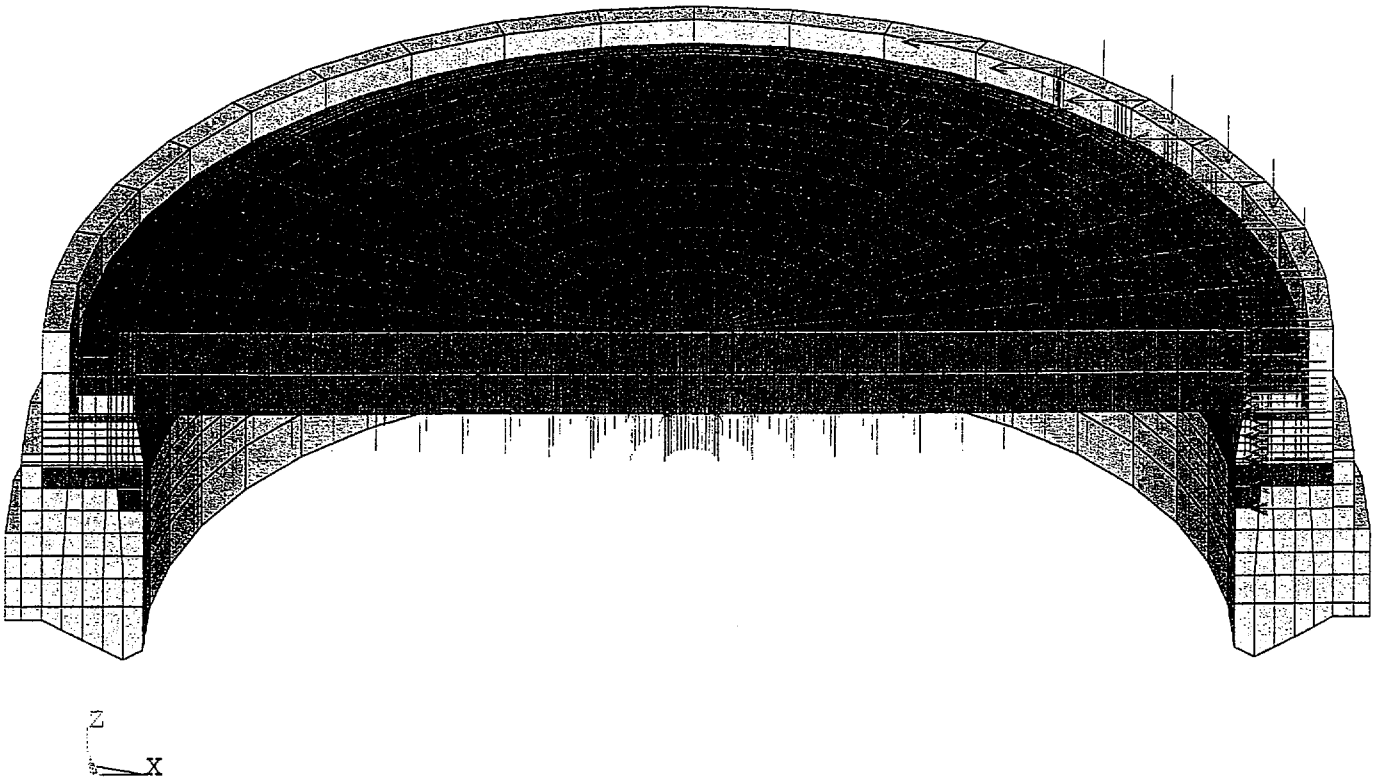


FIGURE 2.7.8 TOP LID LOADING – DROP ANALYSIS

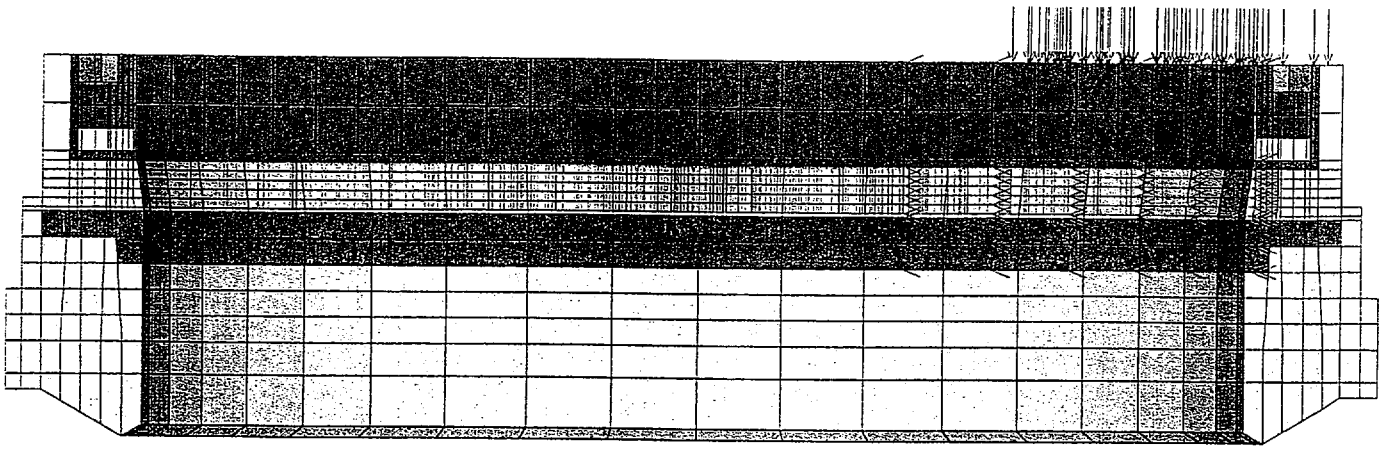


FIGURE 2.7.9 SIDE VIEW OF TOP FORGING SHOWING END LOADS

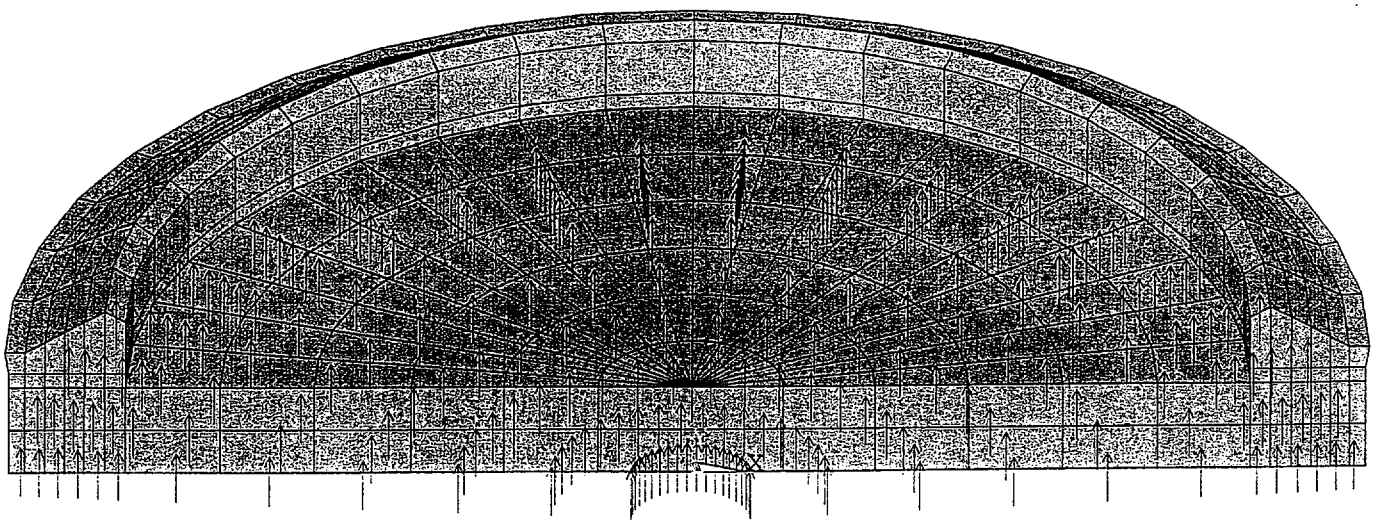

FIGURE 2.7.10 BASEPLATE LOADING FROM IMPACT LIMITER – TOP END DROP

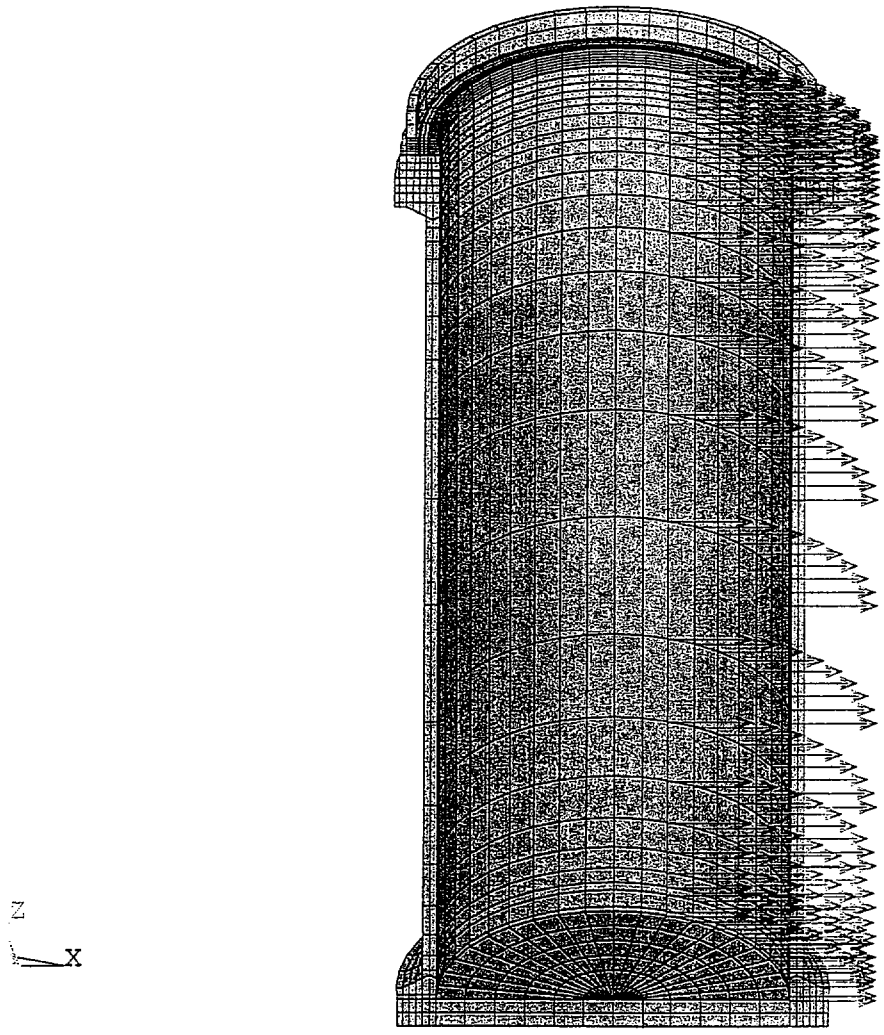


FIGURE 2.7.11 LOADING FROM MPC ON INNER SHELL

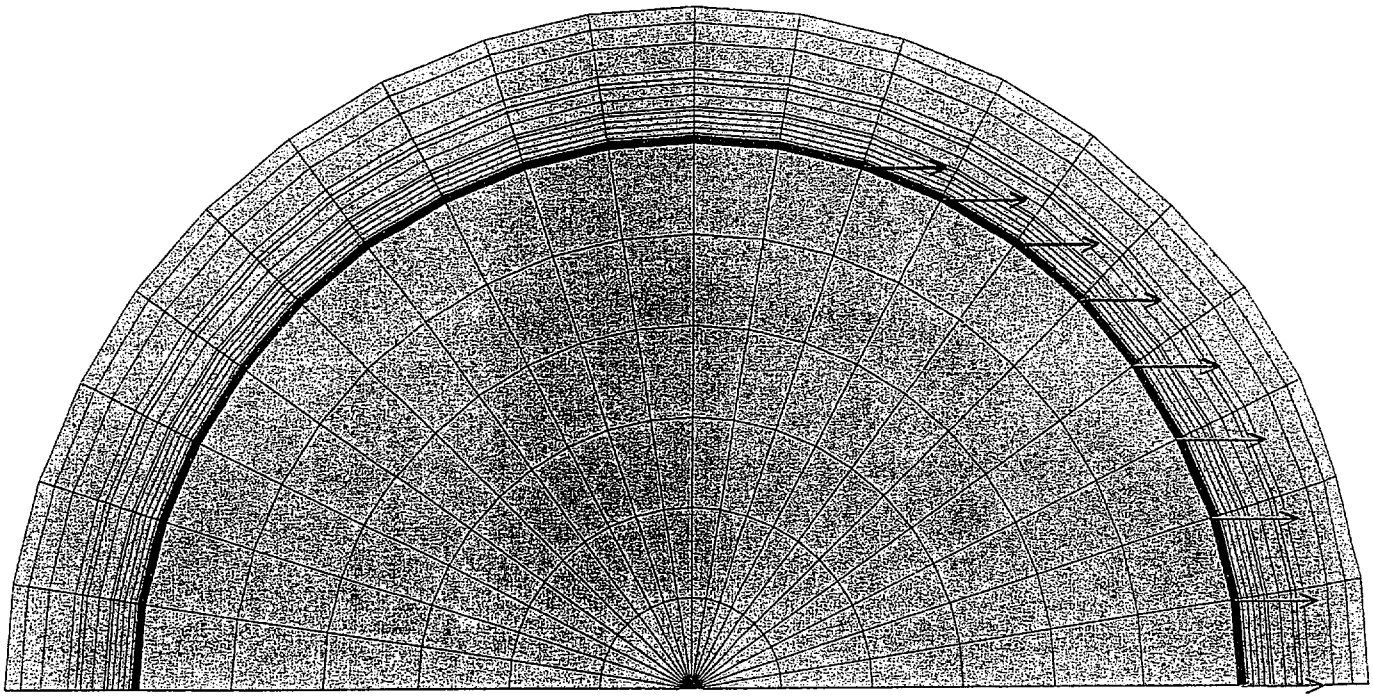


FIGURE 2.7.12 END VIEW SHOWING MPC LOADING ON INNER SHELL

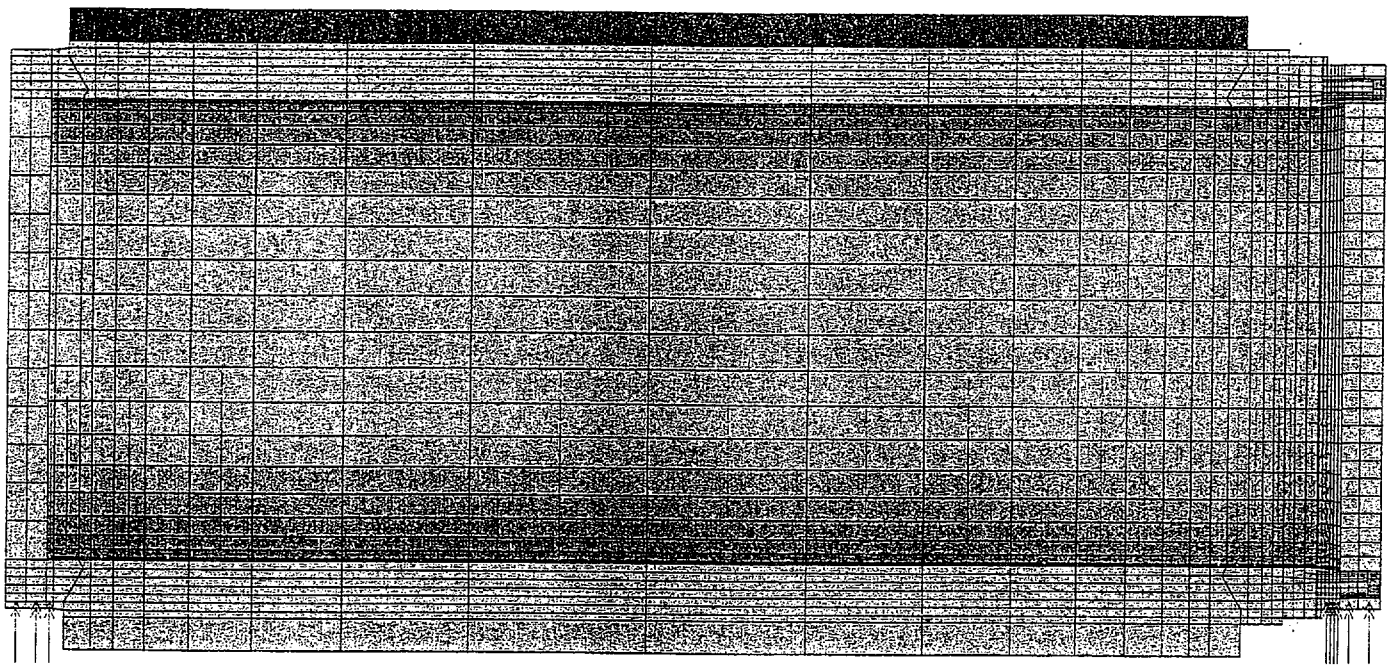

'GURE 2.7.13 LOAD FROM IMPACT LIMITER AT SUPPORT LOCATIONS – SIDE DROP

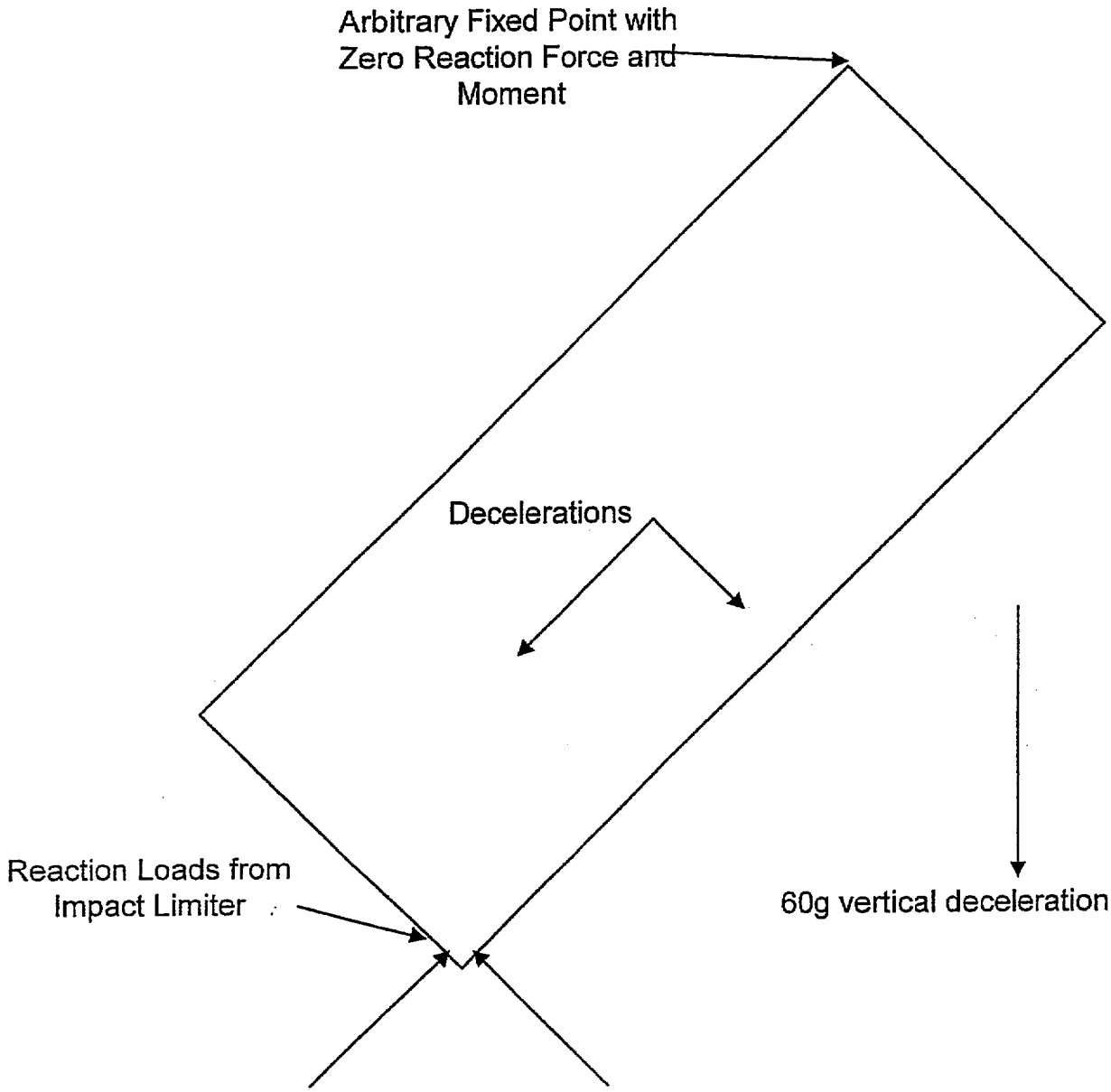


**FIGURE 2.7.14 OBLIQUE DROP SHOWING OFFSET OF IMPACT LIMITER REACTION LOAD FROM APPLIED INERTIA LOADS**

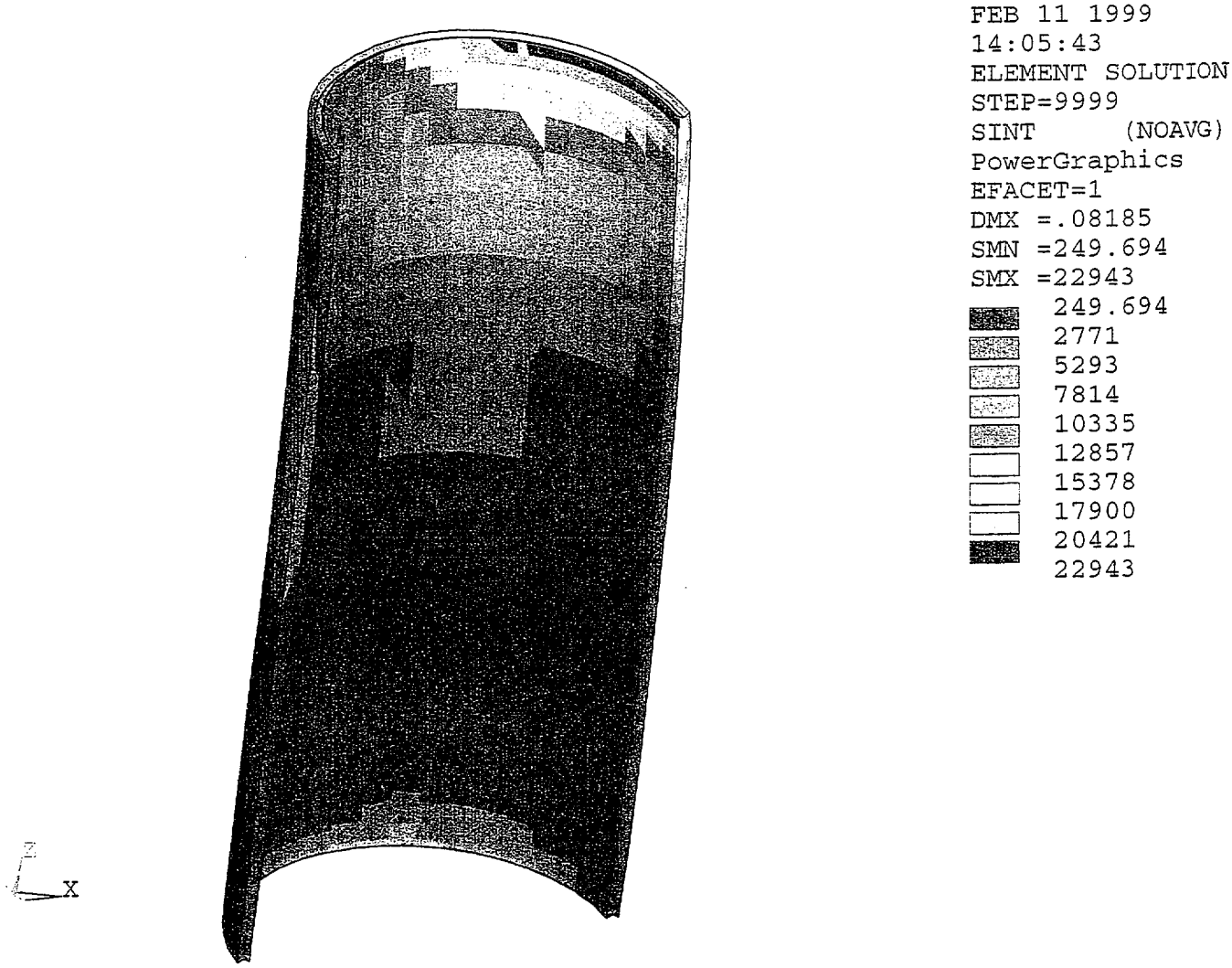


FIGURE 2.7.15 – INNER SHELL STRESS INTENSITY DISTRIBUTION – "HEAT" CONDITION – 30 DEGREE – TOP END IMPACT

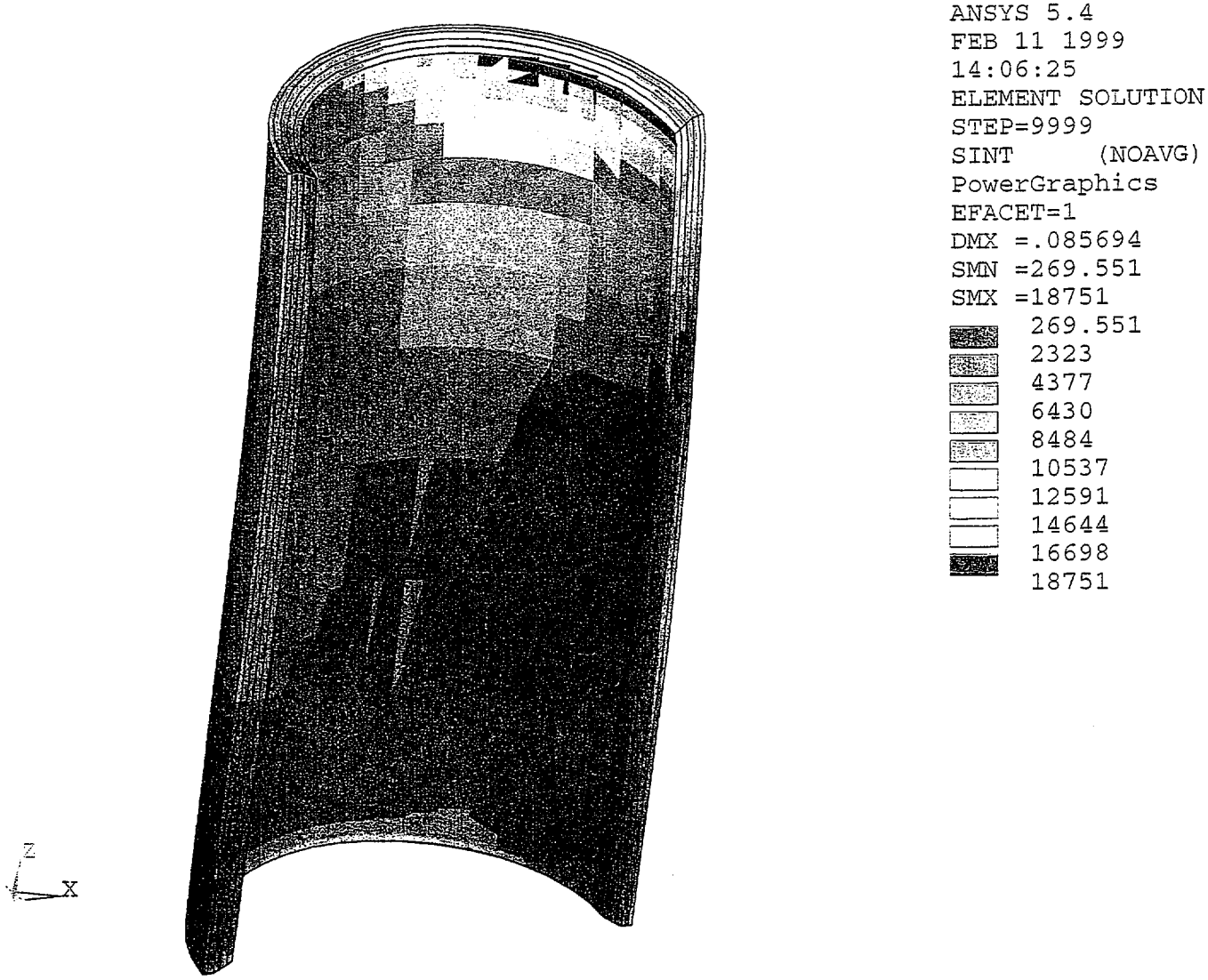


FIGURE 2.7.16 – INTERMEDIATE SHELL-STRESS INTENSITY DISTRIBUTION – "HEAT" CONDITION – 30 DEGREE – TOP – END IMPACT

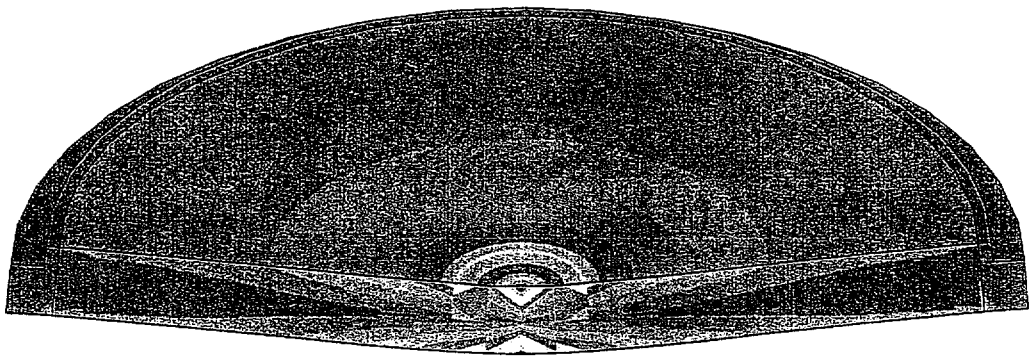


FIGURE 2.7.17 – LOCALIZED STRESS INTENSITY DISTRIBUTION IN LID – TOP END PUNCTURE (DEFORMED SHAPE EXPANDED FOR CLARITY)

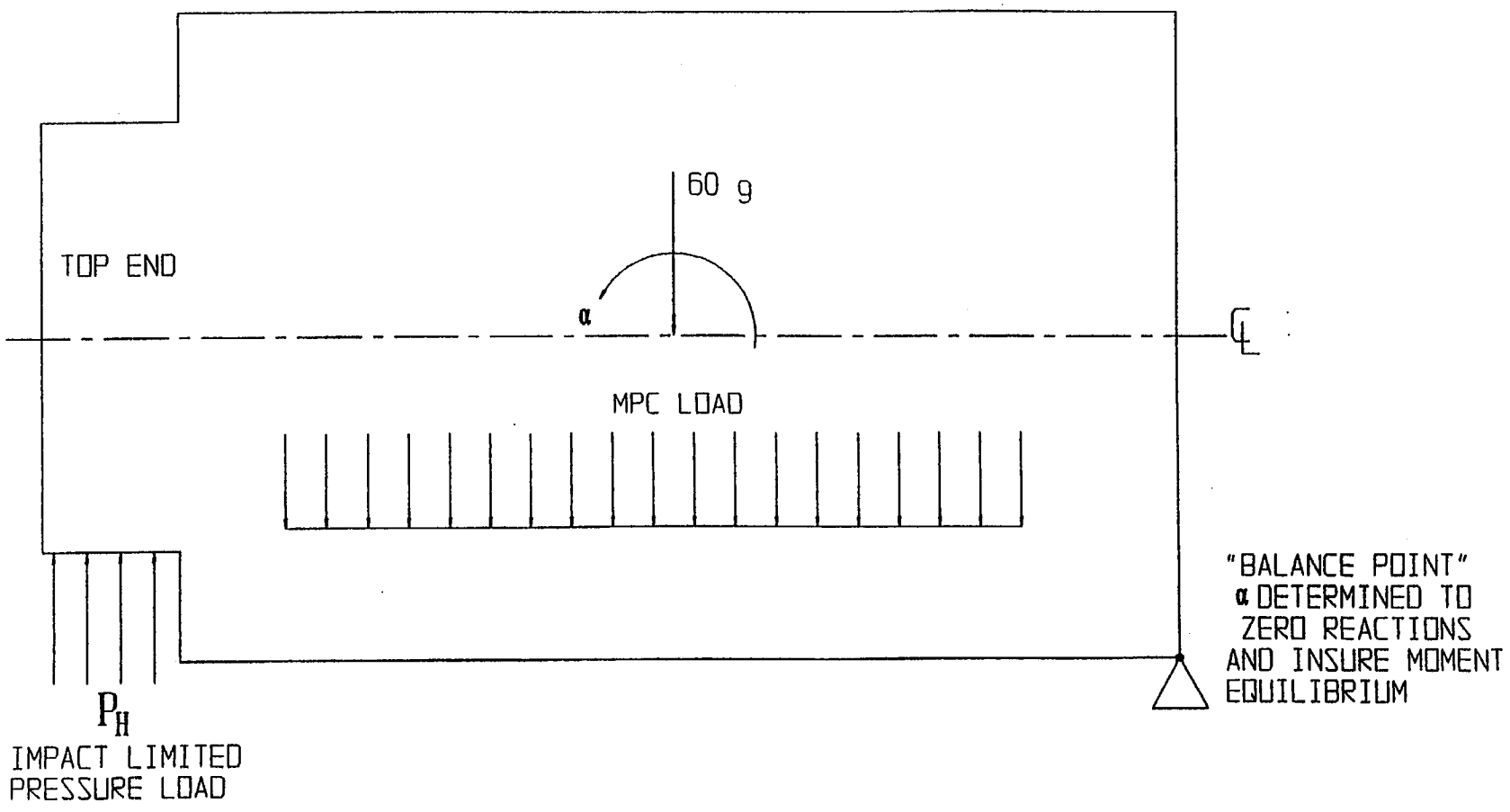


FIGURE 2.7.18; IMPACT LOADS FOR SLAPDOWN FINITE ELEMENT ANALYSIS

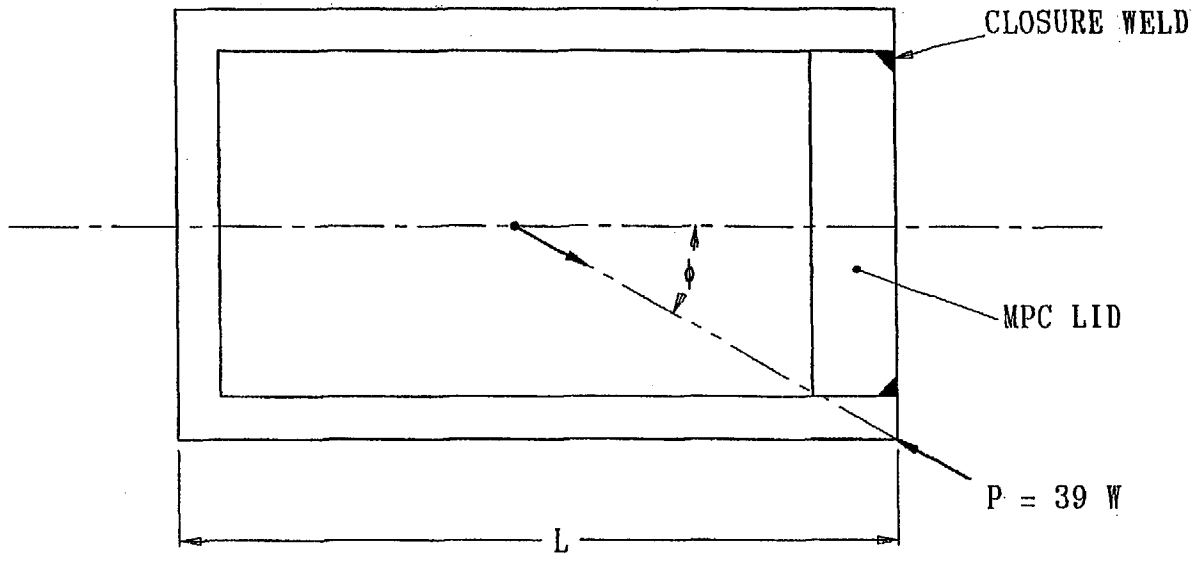


FIGURE 2.7.19; FREE BODY OF MPC FOR CORNER DROP

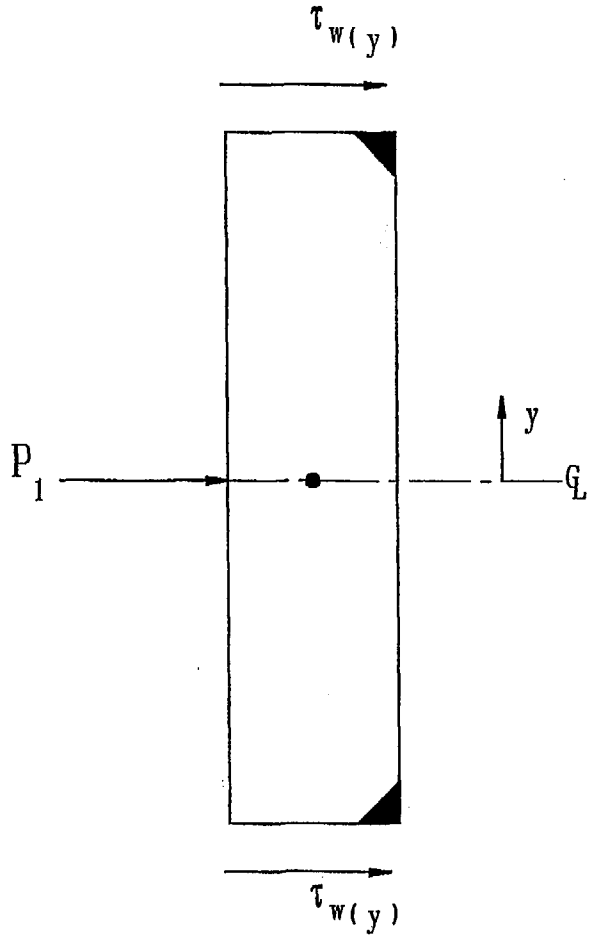


FIGURE 2.7.20; FREE BODY OF MPC LID - IMPACT ON SHELL

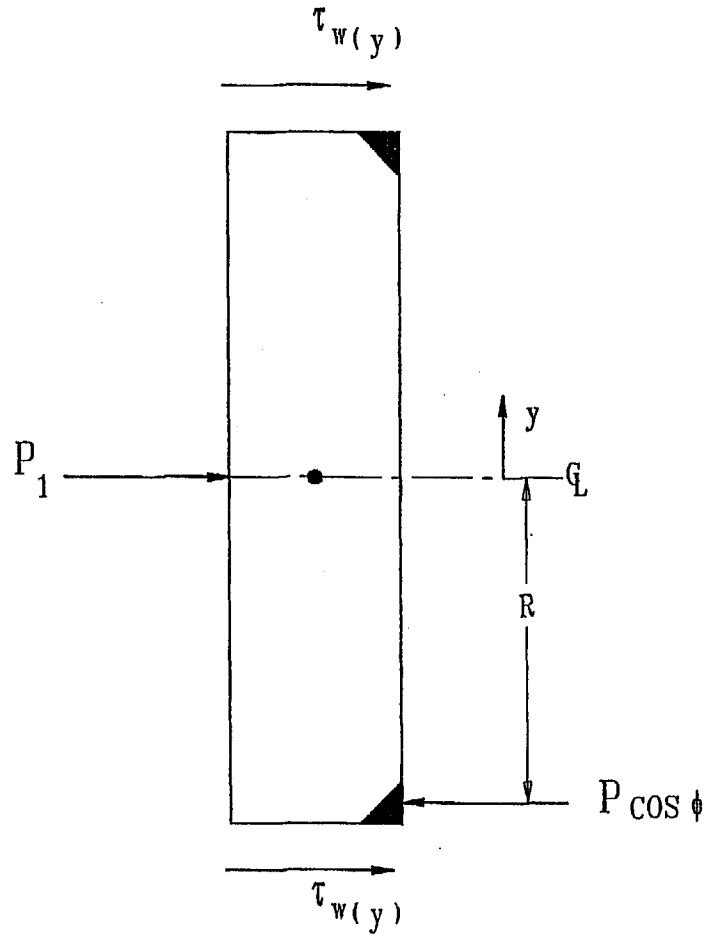


FIGURE 2.7.21; FREE BODY OF MPC LID - IMPACT ON TOP CLOSURE

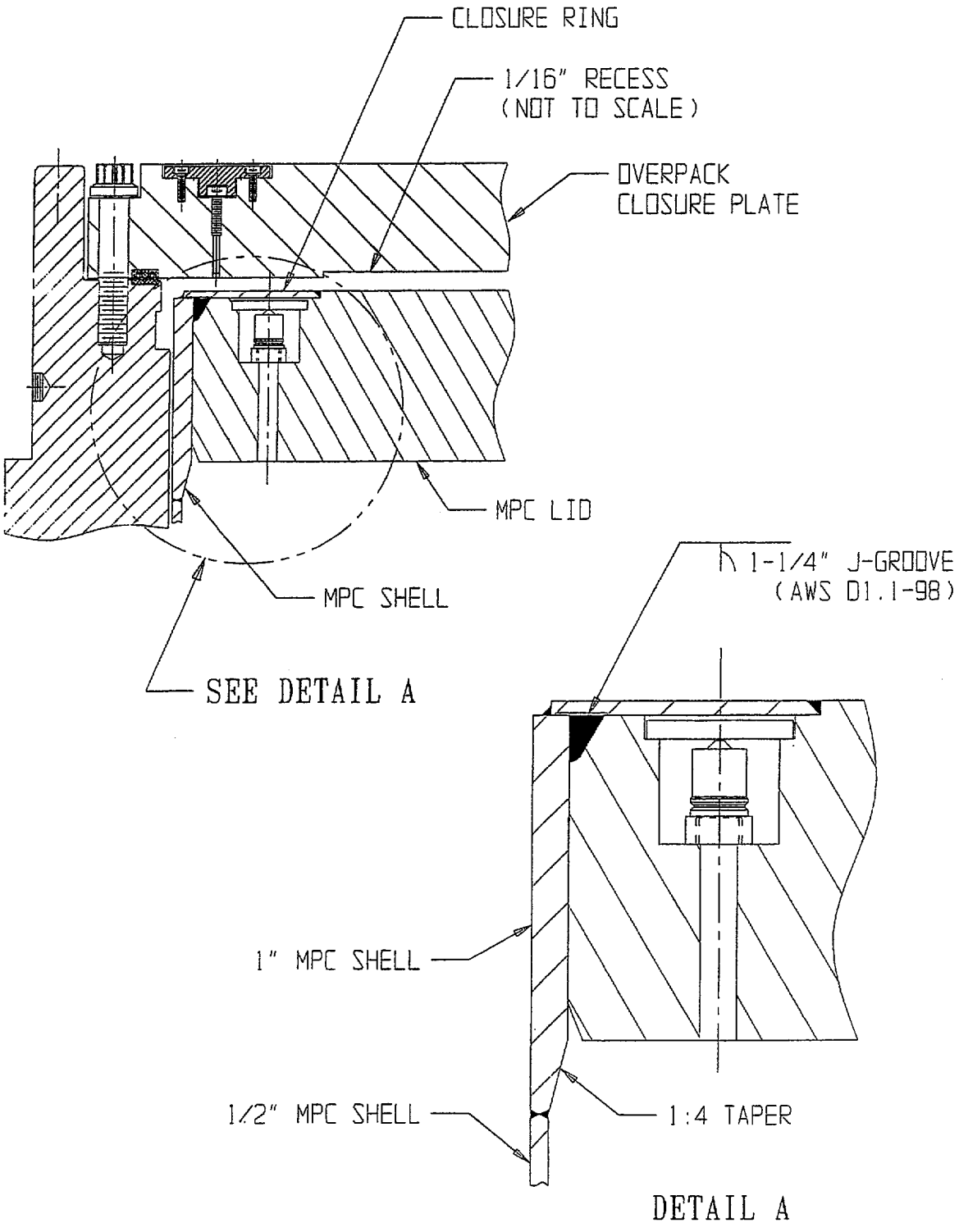


FIGURE 2.7.22; MPC-68F CLOSURE REGION

## 2.8 SPECIAL FORM

This section is not applicable to the HI-STAR 100 System. This application does not seek approval for transport of special form radioactive material as defined in 10CFR71.4.

## 2.9 FUEL RODS

The cladding of the fuel rods is the initial confinement boundary in the HI-STAR 100 System. Analyses have been performed in Chapter 3 to ensure that the maximum temperature of the fuel cladding is below the Pacific Northwest Laboratory's threshold values for various cooling times. These temperature limits ensure that the fuel cladding will not degrade in an inert helium environment. Additional details on the fuel rod cladding temperature analyses for the spent fuel to be loaded into the HI-STAR 100 System are provided in Chapter 3.

The dimensions of the storage cell openings in the MPC are equal to or greater than those used in spent fuel racks supplied by Holtec International. Thousands of fuel assemblies have been shuffled in and out of these cells over the years without a single instance of cladding failure. The vast body of physical evidence from prior spent fuel handling operations provides confirmation that the fuel handling and loading operations with the HI-STAR 100 MPC will not endanger or compromise the integrity of the cladding or the structural integrity of the assembly.

The HI-STAR 100 System is designed and evaluated for a maximum deceleration of 60g's. Studies of the capability of spent fuel rods to resist impact loads [2.9.1] indicate that the most vulnerable fuel can withstand greater than 60 g's in the side impact orientation. Therefore, limiting the HI-STAR 100 System to a maximum deceleration of 60 g's (perpendicular to the longitudinal axis of the overpack during all normal and hypothetical accident conditions) ensures that fuel rod cladding integrity is maintained. In [2.9.1], it is assumed that the fuel rod cladding provides the only structural resistance to bending and buckling of the rod. For accidents where the predominate deceleration is directed along the longitudinal axis of the overpack, [2.9.1] also demonstrates that no elastic instability or yielding of the cladding will occur until the deceleration level is well above the HI-STAR 100 limit of 60g's. The solutions presented in [2.9.1], however, assume that the fuel pellets are not intimately attached to the cladding when subjected to an axial deceleration load that may cause an elastic instability of the fuel rod cladding.

The limit based on classical Euler buckling analyses performed by Lawrence Livermore National Laboratory in [2.9.1] is 82 g's. In the LLNL report, the limiting axial load to ensure fuel rod stability is obtained by modeling the fuel rod as a simply supported beam with unsupported length equal to the grid strap spacing. The limit*ing* load under this condition is:

$$F = \pi^2 EI/L^2$$

In the preceding formula, E = Young's Modulus of the cladding, I = area moment of inertia of the cladding, and L = spacing of the grid straps.

Assuming that F = WxA/g with W being the weight of a fuel rod, and A = the deceleration, the Euler buckling formula can be expressed as

$$A/g = \pi^2 ( ER^3tn/W_{fr}L^2) = \pi^2\beta$$

In the preceding formula, g = gravity, n = number of fuel rods in the fuel assembly, $W_{fa}$ = the total weight of the fuel assembly, t = cladding wall thickness, and R = cladding mean radius.

Using the preceding formula, a survey of a large variety of fuel assembly types in [2.9.1] concluded that a 17 x 17 PWR assembly resulted in the minimum value for deceleration and results in the lower bound limit of:

A/g = 82

The fuel pellet weight was omitted from the analysis in [2.9.1] by virtue of the assumption that under axial load, the cladding did not support the fuel pellet mass. Since the results may not be conservative because of the assumption concerning the behavior of the fuel pellet mass, a new analysis of the structural response of the fuel cladding is presented here... It is demonstrated that the maximum axially oriented deceleration that can be applied to the fuel cladding is in excess of the design basis deceleration specified in this SAR. Therefore, the initial confinement boundary remains intact during a hypothetical accident of transport where large axially directed decelerations are experienced by the HI-STAR 100 package.

The analysis reported here considers the most limiting fuel rod in the fuel assembly. Most limiting is defined as the fuel rod that may undergo the largest bending (lateral) deformations in the event of a loss of elastic stability. The fuel rod is modeled as a thin-walled elastic tube capable of undergoing large lateral displacements in the event that high axial loads cause a loss of stability (i.e., the non-linear interaction of axial and bending behavior of the elastic tube is included in the problem formulation). The fuel rod and the fuel pellet mass is included in the analysis with the fuel pellet mass assumed to contribute only its mass to the analysis. In the HI-STAR 100 spent fuel basket, continuous support to limit lateral movement is provided to the fuel assembly along its entire length. The extent of lateral movement of any fuel rod in a fuel assembly is limited to: (1) the clearance gap between the grid straps and the fuel basket cell wall at the grid strap locations; and, (2) the maximum available gap between the fuel basket cell wall and the fuel rod in the region between the grid straps. Note that the grid straps act as fuel rod spacers at the strap locations; away from the grid straps, however, there is no restraint against fuel rod –to-rod contact under a loading giving rise to large lateral motion of the individual rods. Under the incremental application of axial deceleration to the fuel rod, the fuel rod compresses and displaces from the axially oriented inertial loads experienced. The non-linear numerical analysis proceeds to track the behavior of the fuel rod up to and beyond contact with the rigid confining walls of the HI-STAR 100 fuel basket.

The analysis is carried out for the "most limiting" spent fuel assembly. The "most
herein is based on the simple elastic stability formula assuming buckling occurs only between grid straps. This is identical to the methodology employed in [2.9.1] to identify the fuel assembly that limits design basis axial deceleration loading. Table 2.9.1 presents tabular data for a wide variety of fuel assemblies. Considerable data was obtained using the tables in [2.9.2]. The configuration with the lowest value of "Beta" is the most limiting for simple elastic Euler buckling between grid straps; the Westinghouse 14x14 Vantage,"W14V", PWR configuration is used to obtain results.

The material properties used in the non-linear analysis are those for irradiated Zircalloy and are obtained from [2.9.1]. The Young's Modulus and the cladding dynamic yield stress are set as:

$E = 10{,}400{,}000$ psi

$\sigma_y = 80{,}500$ psi

The fuel cladding material is assumed to have no tensile or compressive stress capacity beyond the material yield strength.

Calculations are performed for two limiting assumptions on the magnitude of resisting moment at the grid straps. Figures 2.9.1 through 2.9.9 aid in understanding the calculation. It is shown in the detailed calculations that the maximum stress in the fuel rod cladding occurs subsequent to the cladding deflecting and contacting the fuel basket cell wall. Two limiting analyses are carried out. The initial analysis assumes that the large deflection of the cladding between two grid straps occurs without any resisting moment at the grid strap supports. This maximizes the stress in the free span of the cladding, but eliminates all cladding stress at the grid strap supports. It is shown that this analysis provides a conservative lower bound on the limiting deceleration. The second analysis assumes a reasonable level of moment resistance to develop at the grid straps; the level developed is based on an assumed deflection shape for the cladding spans adjacent to the span subject to detailed analysis. For this second analysis, the limiting decelerations are much largerwith the limit stress level occurring in the free span and at the grid strap support locations.

It is concluded that the most conservative set of assumptions on structural response still lead to the conclusion that the fuel rod cladding remains intact under the design basis deceleration levels set for the HI-STAR 100.

## Table 2.9.1 FUEL ASSEMBLY DIMENSIONAL DATA

| Array ID | Array Name | Rod O.D. (in.) | Clad Thk. (in.) | $R_{mean}$ (in.) | # of Rods | Assy Wt. (lb.) | Rod Length (in.) | # of Spans | Average Span (in.) | Material Modulus | BETA |
|---|---|---|---|---|---|---|---|---|---|---|---|
| | | | | | PWR | | | | | | |
| 14x14A01 | W14OFA | 0.4000 | 0.0243 | 0.20608 | 179 | 1177 | 151.85 | 6 | 25.30833 | 10400000 | 0.525127806 |
| 14x14A02 | W14OFA | 0.4000 | 0.0243 | 0.20608 | 179 | 1177 | 151.85 | 6 | 25.30833 | 10400000 | 0.525127806 |
| 14x14A03 | W14V | 0.4000 | 0.0243 | 0.20608 | 179 | 1177 | 151.85 | 6 | 25.30833 | 10400000 | 0.525127806 |
| 14x14B01 | W14STD | 0.4220 | 0.0243 | 0.21708 | 179 | 1302 | 152.4 | 6 | 25.4 | 10400000 | 0.550863067 |
| 14x14B02 | XX14TR | 0.4170 | 0.0295 | 0.21588 | 179 | 1215 | 152 | 6 | 25.33333 | 10400000 | 0.708523868 |
| 14x14B03 | XX14STD | 0.4240 | 0.0300 | 0.21950 | 179 | 1271.2 | 149.1 | 8 | 18.6375 | 10400000 | 1.337586884 |
| 14x14C01 | CE14 | 0.4400 | 0.0280 | 0.22700 | 176 | 1270 | 147 | 8 | 18.375 | 10400000 | 1.398051576 |
| 14x14C02 | CE14 | 0.4400 | 0.0280 | 0.22700 | 176 | 1220 | 137 | 8 | 17.125 | 10400000 | 1.67556245 |
| 14x14D01 | W14SS | 0.4220 | 0.0165 | 0.21513 | 180 | 1247 | 126.68 | 6 | 21.11333 | 24700000 | 1.31385062 |
| 15x15A01 | CE15P | 0.4180 | 0.0260 | 0.21550 | 204 | 1360 | 140 | 9 | 15.55556 | 10400000 | 1.677523904 |
| 15x15B01 | W15OFA | 0.4220 | 0.0245 | 0.21713 | 204 | 1459 | 151.85 | 6 | 25.30833 | 10400000 | 0.569346561 |
| 15x15B02 | W15V5H | 0.4220 | 0.0245 | 0.21713 | 204 | 1459 | 151.85 | 6 | 25.30833 | 10400000 | 0.569346561 |
| 15x15B03 | W15 | 0.4220 | 0.0243 | 0.21708 | 204 | 1440 | 151.83 | 6 | 25.305 | 10400000 | 0.571905185 |
| 15x15B04 | W15 | 0.4220 | 0.0243 | 0.21708 | 204 | 1443 | 151.83 | 6 | 25.305 | 10400000 | 0.570716193 |
| 15x15B05 | 15(2a-319) | 0.4220 | 0.0242 | 0.21705 | 204 | 1472 | 151.88 | 6 | 25.31333 | 10400000 | 0.556610964 |
| 15x15C01 | SPC15 | 0.4240 | 0.0300 | 0.21950 | 204 | 1425 | 152 | 6 | 25.33333 | 10400000 | 0.73601861 |
| 15x15C02 | SPC15 | 0.4240 | 0.0300 | 0.21950 | 204 | 1425 | 152 | 6 | 25.33333 | 10400000 | 0.73601861 |
| 15x15C03 | XX15 | 0.4240 | 0.0300 | 0.21950 | 204 | 1432.8 | 152.065 | 6 | 25.34417 | 10400000 | 0.731386148 |
| 15x15C04 | XX15 | 0.4170 | 0.0300 | 0.21600 | 204 | 1338.6 | 139.423 | 9 | 15.49144 | 10400000 | 1.996693327 |
| 15x15D01 | BW15 | 0.4300 | 0.0265 | 0.22163 | 208 | 1515 | 153.68 | 7 | 21.95429 | 10400000 | 0.854569793 |
| 15x15D02 | BW15 | 0.4300 | 0.0265 | 0.22163 | 208 | 1515 | 153.68 | 7 | 21.95429 | 10400000 | 0.854569793 |
| 15x15D03 | BW15 | 0.4300 | 0.0265 | 0.22163 | 208 | 1515 | 153.68 | 7 | 21.95429 | 10400000 | 0.854569793 |
| 15x15G01 | HN15SS | 0.4220 | 0.0165 | 0.21513 | 204 | 1421 | 126.72 | 6 | 21.12 | 24700000 | 1.305875606 |
| 16x16A01 | CE16 | 0.3820 | 0.0250 | 0.19725 | 236 | 1430 | 161 | 10 | 16.1 | 10400000 | 1.270423729 |

## Table 2.9.1 FUEL ASSEMBLY DIMENSIONAL DATA (continued)

| Array ID | Array Name | Rod O.D. (in.) | Clad Thk. (in.) | $R_{mean}$ (in.) | # of Rods | Assy Wt. (lb) | Rod Length (in.) | # of Spans | Average Span (in.) | Material Modulus | BETA |
|---|---|---|---|---|---|---|---|---|---|---|---|
| 16x16A02 | CE16 | 0.3820 | 0.0250 | 0.19725 | 236 | 1300 | 146.499 | 9 | 16.27767 | 10400000 | 1.367126598 |
| 17x17A01 | W17OFA | 0.3600 | 0.0225 | 0.18563 | 264 | 1373 | 151.635 | 7 | 21.66214 | 10400000 | 0.613275783 |
| 17x17A02 | W17OFA | 0.3600 | 0.0225 | 0.18563 | 264 | 1365 | 152.3 | 7 | 21.75714 | 10400000 | 0.611494853 |
| 17x17B01 | W17STD | 0.3740 | 0.0225 | 0.19263 | 264 | 1482 | 151.635 | 7 | 21.66214 | 10400000 | 0.634902014 |
| 17x17B02 | W17P+ | 0.3740 | 0.0225 | 0.19263 | 264 | 1482 | 151.635 | 7 | 21.66214 | 10400000 | 0.634902014 |
| 17x17C01 | BW17 | 0.3790 | 0.0240 | 0.19550 | 264 | 1505 | 152.688 | 7 | 21.81257 | 10400000 | 0.687604262 |
| | | | | | | BWR | | | | | |
| 6x6A02 | XX/ANF6 | 0.5645 | 0.0360 | 0.29125 | 36 | 328.4 | 116.65 | 4 | 29.1625 | 10400000 | 1.192294364 |
| 6x6C01 | HB6 | 0.5630 | 0.0320 | 0.28950 | 36 | 270 | 83 | 3 | 20.75 | 10400000 | 2.500527046 |
| 7x7A01 | HB7 | 0.4860 | 0.0330 | 0.25125 | 49 | 276 | 83.2 | 3 | 20.8 | 10400000 | 2.233705011 |
| 7x7B01 | GE-7 | 0.5630 | 0.0320 | 0.28950 | 49 | 682.5 | 159 | 7 | 19.875 | 10400000 | 1.467601583 |
| 7x7B02 | GE-7 | 0.5630 | 0.0370 | 0.29075 | 49 | 681 | 164 | 7 | 20.5 | 10400000 | 1.619330439 |
| 7x7B03 | GE-7 | 0.5630 | 0.0370 | 0.29075 | 49 | 674.4 | 164 | 7 | 20.5 | 10400000 | 1.635177979 |
| 7x7B04 | GE-7 | 0.5700 | 0.0355 | 0.29388 | 49 | 600 | 161.1 | 7 | 20.1375 | 10400000 | 1.887049713 |
| 7x7B05 | GE-7 | 0.5630 | 0.0340 | 0.29000 | 49 | 600 | 161.1 | 7 | 20.1375 | 10400000 | 1.736760659 |
| 8x8B03 | GE-8 | 0.4930 | 0.0340 | 0.25500 | 63 | 681 | 164 | 7 | 20.5 | 10400000 | 1.2906798 |
| 8x8C02 | GE-8R | 0.4830 | 0.0320 | 0.24950 | 62 | 600 | 159 | 7 | 19.875 | 10400000 | 1.352138354 |
| 8x8C03 | GE-8R | 0.4830 | 0.0320 | 0.24950 | 62 | 600 | 163.71 | 7 | 20.46375 | 10400000 | 1.27545448 |
| 9x9D01 | XX/ANF9 | 0.4240 | 0.0300 | 0.21950 | 79 | 575.3 | 163.84 | 8 | 18.20444 | 10400000 | 1.367212516 |
| 10x10E01 | XX10SS | 0.3940 | 0.0220 | 0.20250 | 96 | 376.6 | 89.98 | 4 | 17.996 | 24700000 | 3.551678654 |

Array ID, Rod OD, Clad Thk and # of Rods from Tables 6.2.1 and 6.2.2.

Rmean, Average Span and THETA are Calculated.

Zircaloy Modulus from LLNL Report [2.9.1].

Stainless Steel (348H) Modulus from ASME Code, Section III, Part D.

## Table 2.9.1 FUEL ASSEMBLY DIMENSIONAL DATA (continued)

PWR Assy. Wt., Rod Len. and # of Spans (exc. as noted below) from DOE/RW-0184, Vol. 3, UC-70, -71 and -85, Dec. 1987.
Assy. Wt., Rod Len. and # of Spans for 15x15B03, 15x15B04, 15x15C01 and 15x15C02 from ORNL/TM-9591/V1-R1.
BWR Assy. Wt., Rod Len. and # of Spans (exc. as noted below) from ORNL/TM-10902.
Assy. Wt., Rod Len. and # of Spans for 6x6A02, 9x9D01 and 10x10E01 from DOE/RW-0184, Vol. 3, UC-70, -71 and -85, Dec. 1987.
Assy. Wt., Rod Len. and # of Spans for 7x7B04 and 7x7B05 from ORNL/TM-9591/V1-R1.
Assy. Wt. for 8x8C02 and 8x8C03 from ORNL/TM-9591/V1-R1.

In the following, a physical description of the structural instability problem is provided with the aid of Figures 2.9.1 to 2.9.9. A stored fuel assembly consists of a square grid of fuel rods. Each fuel rod consists of a thin-walled cylinder surrounding and containing the fuel pellets. The majority of the total weight of a fuel rod is in the fuel pellets; however, the entire structural resistance of the fuel rod to lateral and longitudinal loads is provided by the cladding. Hereinafter, the use of the words "fuel rod", "fuel rod cladding", or just "cladding" means the structural thin cylinder. The weight of the fuel pellets is conservatively assumed to be attached to the cladding for all discussions and evaluations.

Figure 2.9.1 shows a typical fuel rod in a fuel assembly. Also shown in Figure 2.9.1 are the grid straps and the surrounding walls of the spent fuel basket cell walls. The grid straps serve to maintain the fuel rods in a square array at a certain number of locations along the length of the fuel assembly. When the fuel rod is subject to a loading causing a lateral deformation, the grid strap locations are the first locations along the length of the rod where contact with the fuel basket cell walls occurs. The fuel basket cell walls are assumed to be rigid surfaces. The fuel rod is assumed *to be* subject*ed* to some axial load and ~~most likely~~ has some slight*ly* initially deformed shape. For the purposes of the analysis, it is assumed that displacement under load occurs in a 2-D plane and that the ends of the fuel rod cladding have a specified boundary condition to restrain lateral deflection. The ends of the fuel rod cladding are assumed to be simply supported and the grid straps along the length of the fuel assembly are assumed to have gap "$g_1$" relative to the cell walls of the fuel basket. The figure shows a typical fuel rod in the assembly that is located by gaps "$g_2$" and "$g_3$" with respect to the fuel basket walls. Because the individual fuel rod is long and slender and is not perfectly straight, it will deform under a small axial load into the position shown in Figure 2.9.2. The actual axial load is due to the distributed weight subject to a deceleration from a hypothetical accident of transport. For the purposes of this discussion, it is assumed that some equivalent axial load is applied to one end of the fuel rod cladding. Because of the distributed weight and the fact that a deceleration load is not likely to be exactly axially oriented, the predominately axial load will induce a lateral displacement of the fuel rod cladding between the two end supports. The displacement will not be symmetric but will be larger toward the end of the cladding where support against the axial deceleration is provided. Depending on the number of grid straps, either one or two grid straps will initially make contact with the fuel basket cell wall and the contact will not be exactly centered along the length of the cell. Figure 2.9.3 illustrates the position of the fuel rod after the axial load has increased beyond the value when initial contact occurred and additional grid straps are now in contact with the cell wall. The maximum stress in the fuel rod will occur at the location of maximum curvature and will be a function of the bending moment ($F_2$ x($g_2$-$g_1$)).

At some load $F_3 > F_2$, either the limit*ing* stress in the fuel rod cladding is achieved or the rod begins to experience large lateral movements between grid plates because of the coupling between axial and lateral load and deformation. Figure 2.9.4 shows the deformation mode experienced by the fuel rod cladding caused by the onset of an instability between two grid straps that are in contact with the fuel basket cell wall.

Once the lateral displacement initiates, the rod displaces until contact with the cell wall occurs at the mid point "A" ( see Figure 2.9.5) or the cladding stress exceeds the cladding material yield strength. Depending on the particular location of the fuel rod in the fuel assembly, the highest stressed portion of the fuel rod will

occur in the segment with the larger of the two gaps "$g_2$" and "$g_3$". For the discussion to follow, assume that- $g_2 > g_3$. The boundary condition at the grid strap is conservatively assumed as simply-supported so that the analysis need not consider what happens in adjacent spans between grid straps. At this point in the loading process, the maximum bending moment occurs at the contact point and has the value-$F_4 \times (g_2-g_1)$. Figure 2.9.5 shows the displaced configuration at the load level where initial contact occurs with the fuel cell wall. If the maximum fuel rod stress (from the bending moment and from the axial load) equals the yield stress of the fuel rod cladding, it is assumed that $F_3 = F_4$ is the maximum axial load that can be supported. The maximum stress in the fuel rod cladding occurs at point "A" in Figure 2.9.5 since that location has the maximum bending moment. If the cladding stress is still below yield, additional load can be supported. As the load is further increased, the bending moment is decreased and replaced by reaction loads, "V", at the grid strap and the contact point. These reaction loads V are shown in Figure 2.9.7 and are normal to the cell wall surface. Figure 2.9.6 shows the configuration after the load has been further increased from the value at initial contact. There are two distinct regions that need to be considered subsequent to initial contact with the fuel basket cell wall. During the additional loading phase, the point "A" becomes two "traveling" points, A, and A'. Since the bending moment at A' and A is zero, the moment $F_5 \times (g_2-g_1)$ is balanced by forces V at the grid strap and at point A or A'. This is shown in Figure 2.9.7 where the unsupported length current "a" is shown with the balancing load. At this point in the process, two "failure" modes are possible for the fuel rod cladding.

The axial load that develops in the unsupported region between the grid strap and point A' causes increased deformation and stress in that segment, or,

The straight region of the rod, between A and A', begins to experience a lateral deformation away from the cell wall.

Note that in this latter scenario, the slope at A or A' remains zero so this should never govern unless the flat region becomes large. The final limit*ing* load occurs when the maximum stress in either portion of the rod exceeds the yield stress of the tube. In what follows, the most limiting fuel assembly from the array of fuel types considered is subject to detailed analysis and the limit*ing* load established. This limit axial load is considered as the product of the fuel rod weight times the deceleration. Therefore, establishing the limit*ing* load to reach cladding material yield establishes the limiting axial deceleration that can be imposed.

The preceding discussion has assumed end conditions of simple support for conservatism. The location of the fuel rod determines the actual free gap between grid straps. For example, a fuel rod furthest from the cell wall that resists lateral movement of the assembly moves to close up all of the clearances that exist between it and the resisting cell wall. The clearance between rods is the rod pitch minus the rod diameter. In a 14 x 14 assembly, there are 13 clearance gaps plus an additional clearance $g_3$ between the nearest rod and the cell wall. Therefore, the gap $g_2$ is given as

$g_2 = 13(\text{pitch-diameter}) + g_3$

Figure 2.9.9 provides an illustration of the fuel rod deformation- for a case of 5 fuel rods in a column. Clearly for this case, the available lateral movement can be considerable for the "furthest" fuel rod. On the other hand, for this fuel rod, there will be considerable moment resistance at the grid strap from the adjacent section of the fuel rod. The situation is different when the rod being analyzed is assumed to be the closest to the cell wall. In this case, the clearance gap is much smaller, but the moment resistance provided by adjacent sections of the rod is reduced. For calculation purposes, we assume that a moment resistance is provided as M = f x K— for the fuel rod under analysis where

K = 3EI/L , L= span between grid straps, and "f" is an assumed fraction of K

The preceding result for the rotational spring constant assumes a simple support at each end of the span with an end moment "M" applied. Classical strength of materials gives the result for the spring constant. The arbitrary assumption of a constant reduction in the spring constant is to account for undetermined interactions between axial force in the rod and the calculated spring constant. As the compressive force in the adjacent members increases, the spring constant will be reduced. On the other hand, as the adjacent span contacts its near cell wall, the spring constant increases. On balance, it should be conservative to assume a considerable reduction in the spring constant available to the span being analyzed in detail. As a further conservatism, ~~we also use~~ the angle defined by the geometry *is used without* ~~and not~~ includ*ing*~~e~~ any additional elastic displacement shape. This will further reduce the value of the resisting moment at any stage of the solution. In the detailed calculations, two limiting cases are examined. To limit the analysis to a single rod, it is assumed that after "stack-up" of the rods (see Figure 2.9.9), the lateral support provided by the cell wall supports all of the rods. That is, the rods are considered to have non-deforming cross-section.

Numerical Analysis - Based on the tabular results in Table 2.9.1, the fuel assembly with the smallest value for the deceleration based on the classical Euler buckling formula is analyzed in detail. The following input data is specified for the limiting 14 x 14 assembly [2.9.2]:

Inside dimension of a HI-STAR 100 fuel basket cell
$s := 8.75 \cdot in$

Outside envelope dimension of grid plate
$gp := 7.763 \cdot in$

Outer diameter of fuel rod cladding
$D := .4 \cdot in$

Wall thickness of cladding
$t := .0243 \cdot in$

Weight of fuel assembly (including end fittings)
$W := 1177 \cdot lbf$

Number of fuel rods + guide/instrument
tubes in a column or row
$n := 14$

Overall length of fuel rod between assumed end support
$L_t := 151 \cdot in$

Length of fuel rod between grid straps
$L_s := 25.3 \cdot in$

Average clearance to cell wall at a grid strap location
assuming a straight and centered fuel assembly
$g_1 := .5 \cdot (s - gp)$

$g_1 = 0.494\,in$

Rod pitch
$pitch := 0.556 \cdot in$

$Clearance := (n - 1) \cdot (pitch - D)$

$Clearance = 2.028\,in$

Minimum available clearance for lateral movement of a fuel
rod between grid straps
$g_3 := g_1 + .5 \cdot [gp - (n \cdot D + Clearance)]$

$g_3 = 0.561\,in$

Maximum available clearances for lateral movement of a
fuel rod between grid straps
$g_2 := g_3 + Clearance$

$g_2 = 2.589\,in$

Young's Modulus of Zircalloy [2.9.1]
$E := 10400000 \cdot psi$

Dynamic Yield Strength of Zircalloy [2.9.1]

$\sigma_y := 80500 \cdot psi$

Geometry Calculations:

Compute the metal cross section area A, the metal area moment of inertia I, and the total weight of a single fuel rod (conservatively assume that end fittings are only supported by fuel rods in the loading scenario of interest).

$$A := \frac{\pi}{4} \cdot \left[ D^2 - (D - 2 \cdot t)^2 \right]$$

$$I := \frac{\pi}{64} \cdot \left[ D^4 - (D - 2 \cdot t)^4 \right]$$

$A = 0.029\,in^2$

$I = 5.082 \times 10^{-4}\,in^4$

$$W_r := \frac{W}{n^2}$$

$W_r = 6.005\,lbf$

As an initial lower bound calculation, assume no rotational support from adjacent spans and define a multiplying factor

$f := 0.0$

Compute the rotational spring constant available from adjacent sections of the rod.

$$K := 3 \cdot E \cdot \frac{I}{L_s} \cdot f$$

$K = 0\,lbf \cdot in$

Now compute the limit*ing* load, if applied at one end of the fuel rod cladding, which causes an overall elastic instability and contact with the cell wall. Assume buckling in a symmetric mode for a conservatively low result. The purpose of this calculation is solely to demonstrate the flexibility of the single fuel rod. No resisting moment capacity is assumed to be present at the fittings.

$$P_0 := \pi^2 \cdot E \cdot \frac{I}{L_t^2}$$

$P_0 = 2.288\,lbf$

Note that this is less than the weight of the rod itself. This demonstrates that in the absence of any additional axial support, the fuel rod will bow and be supported by the cell walls under a very small axial load. In reality, however, there is additional axial support that would increase this initial buckling load.

The stress induced in the rod by this overall deflected shape is small.

$$Stress_1 := \frac{P_0 \cdot g_1 \cdot D}{2 \cdot I}$$

$$Stress_1 = 444.32\,psi$$

$$Stress_d := \frac{P_0}{A}$$

$$Stress_d = 79.76\,psi$$

The conclusion of this initial calculation is that grid straps come in contact; ~~and we need only~~ consider*ation of* what happens between a grid strap *is the only region that requires further investigation.* ~~We~~ *F*~~f~~irst calculate the classical Euler buckling load based on a pin-ended rod and assume~~ing~~ conservatively that the entire weight of the rod is providing the axial driving force. This gives a conservatively low estimate of the limiting deceleration that can be resisted before a perfectly straight rod buckles.

$$a_{lim1} := \pi^2 \cdot E \cdot \frac{I}{L_s^2 \cdot W_r}$$

$$a_{lim1} = 13.57$$

The rigid body angle of rotation at the grid strap under this load that causes contact is:

$$\theta_1 := \operatorname{atan}\left[2 \cdot \frac{(g_2 - g_1)}{L_s}\right]$$

$$\theta_1 = 9.406\,deg$$

Conservatively assume resisting moment at the grid is proportional to this "rigid body" angle:

$$M_r := K \cdot \theta_1$$

$$M_r = 0\,in \cdot lbf$$

(in this first analysis, no resisting moment is assumed)

The total stress at the grid strap due to the axial force and the resisting moment is

$$\sigma_{gs} := \frac{W_r \cdot a_{lim1}}{A} + \frac{M_r \cdot D}{2 \cdot I}$$

$$\sigma_{gs} = 2841.172\,psi$$

The total stress at the contact location is

$$Stress_2 := \frac{\left[W_r \cdot a_{lim1} \cdot (g_2 - g_1) - M_r\right] \cdot D}{2 \cdot I}$$

$$Stress_2 = 6.721 \times 10^4 \text{ psi}$$

$$Stress_{2d} := \frac{W_r \cdot a_{lim1}}{A}$$

$$Stress_{2d} = 2841.172 \text{ psi}$$

$$Stress_{2t} := Stress_2 + Stress_{2d}$$

$$Stress_{2t} = 7.005 \times 10^4 \text{ psi}$$

This is the maximum value of the stress at this location since, for further increase in axial load, the moment will decrease with consequent large decrease in the total stress.

The safety factor is

$$\frac{\sigma_y}{Stress_{2t}} = 1.149$$

The axial load in the unsupported portion of the beam at this instant is

$$P_{ax} := \frac{(W_r \cdot a_{lim1})}{\cos(\theta_1)}$$

$$P_{ax} = 82.599 \text{ lbf}$$

At this point in the load process, a certain axial load exists in the unsupported span on either side of the contact point. However, since the unsupported span is approximately 50% of the original span, the allowable deceleration limit is larger. As the axial load is incrementally increased, the moment at the contact point is reduced to zero with consequent increases in the lateral force V at the grid strap and at the contact points A and A'. Figure 2.9.8 provides the necessary information to determine the elastic deformation that occurs in the unsupported span as the axial load increases and the contact points separate (and, therefore, decreasing the free span).

From geometry, coupled with the assumption that the deflected shape is a half "sin" function with peak value $\delta$, the following relations are developed:

Assume "a" is a fraction of 50% of the span (the following calculations show only the final iterated assumption for the fraction

$\varepsilon := .9$

$$a := \varepsilon \cdot \left(\frac{L_s}{2}\right)$$

$a = 11.385\,\text{in}$

Calculate "b" in Figure 2.9.8

$$b := \left[(a)^2 + (g_2 - g_1)^2\right]^{.5}$$

$b = 11.576\,\text{in}$

An equation for $\delta$ can be developed from the geometric relation

$$\frac{(g_2 - g_1)}{a} := \frac{b}{2(R - \delta)}$$

*(please note that the above equation is imported from the electronic spreadsheet program MathCad. The solid rectangle appearing after the equation is a MathCad symbol designating that no computations are performed on that line)*

The inverse of the radius of curvature, R, at the point of peak elastic deflection of the free span, is computed as the second derivative of the assumed sin wave deflection shape. Based on the geometry in Figure 2.9.8, the peak deflection is:

$$\delta := .5 \cdot \left[\left[a \cdot \frac{b}{2 \cdot (g_2 - g_1)}\right]^2 + 4 \cdot \left(\frac{b}{\pi}\right)^2\right]^{.5} - a \cdot \frac{b}{4 \cdot (g_2 - g_1)}$$

$\delta = 0.426\,\text{in}$

For the assumed "a", the limiting axial load capacity in the unsupported region is conservatively estimated as:

$$a_{lim2} := \pi^2 \cdot E \cdot \frac{I}{(b)^2 \cdot W_r}$$

$a_{lim2} = 64.816$

The corresponding rigid body angle is:

$$\theta_2 := \text{atan}\left[1 \cdot \frac{(g_2 - g_1)}{a}\right]$$

$\theta_2 = 10.429\,\text{deg}$

The axial load in the unsupported portion of the beam at this instant is

$$P_{ax} := \frac{(W_r \cdot a_{lim2})}{\cos(\theta_2)}$$

$P_{ax} = 395.763\,\text{lbf}$

The resisting moment is

$M_r := K \cdot \theta_2$

$M_r = 0\,\text{in}\cdot\text{lbf}$

The total stress in the middle of the unsupported section of free span "b" is

$$\text{stress}_3 := \frac{(P_{ax} \cdot \delta - M_r) \cdot D}{2 \cdot I}$$

$\text{stress}_3 = 6.635 \times 10^4\,\text{psi}$

$$\text{stress}_{3d} := \frac{P_{ax}}{A}$$

$\text{stress}_{3d} = 1.38 \times 10^4\,\text{psi}$

$\text{stress}_{3t} := \text{stress}_3 + \text{stress}_{3d}$

$\text{stress}_{3t} = 8.015 \times 10^4\,\text{psi}$

The safety factor is

$$\frac{\sigma_y}{\text{stress}_{3t}} = 1.004$$

The total stress at the grid strap due to the axial force and ~~any~~ the resisting moment is

$$\sigma_{gs} := \frac{W_r \cdot a_{lim2}}{A} + \frac{M_r \cdot D}{2 \cdot I}$$

$\sigma_{gs} = 1.357 \times 10^4\,\text{psi}$

The safety factor is

$$\frac{\sigma_y}{\sigma_{gs}} = 5.932$$

For this set of assumptions, the stress capacity of the rod cladding has been achieved, so that the limit*ing* deceleration is:

$A_{limit} := a_{lim2}$

$A_{limit} = 64.816$

This exceeds the design basis for the HI-STAR 100 package.

If there is any restraining moment from the adjacent span, there is a possibility of exceeding the rod structural limits at that location due to the induced stress. Therefore, the above calculations are repeated for an assumed moment capacity at the grid strap.

$f := 1.$

$K := 3 \cdot E \cdot \frac{I}{L_s} \cdot f$

The rigid body angle of rotation at the grid strap under this load that causes contact is:

$\theta_1 := \operatorname{atan}\left[ 2 \cdot \frac{(g_2 - g_1)}{L_s} \right]$

$\theta_1 = 9.406\,\text{deg}$

Conservatively assume resisting moment at the ~~grid a~~*grid a* function of this angle, is

$M_r := K \cdot \theta_1$

$M_r = 102.875\,\text{in}\cdot\text{lbf}$

The total stress at the grid strap due to the axial force and the resisting moment is

$\sigma_{gs} := \frac{W_r \cdot a_{lim1}}{A} + \frac{M_r \cdot D}{2 \cdot I}$

$\sigma_{gs} = 4.333 \times 10^4\,\text{psi}$

The total stress at the contact location is

$\text{Stress}_2 := \frac{\left[W_r \cdot a_{lim1} \cdot (g_2 - g_1) - M_r\right] \cdot D}{2 \cdot I}$

$\text{Stress}_2 = 2.672 \times 10^4\,\text{psi}$

$$Stress_{2d} := \frac{W_r \cdot a_{lim1}}{A}$$

$Stress_{2d} = 2841.172\,psi$

$Stress_{2t} := Stress_2 + Stress_{2d}$

$Stress_{2t} = 2.956 \times 10^4\,psi$

This is the maximum value of the stress at this location since, for further increase in axial load, the moment will decrease with consequent large decrease in the total stress.

The axial load in the unsupported portion of the beam at this instant is

$$P_{ax} := \frac{\left(W_r \cdot a_{lim1}\right)}{\cos\left(\theta_1\right)}$$

$P_{ax} = 82.599\,lbf$

At this point in the load process, a certain axial load exists in the unsupported span on either side of the contact point. However, since the unsupported span is approximately 50% of the original span, the allowable deceleration limit is larger. As the axial load is incrementally increased, the moment at the contact point is reduced to zero with consequent increases in the lateral force V at the grid strap and at the contact points A and A'. Figure 2.9.8 provides the necessary information to determine the elastic deformation that occurs in the unsupported span as the axial load increases and the contact points separate (and, therefore, decreasing the free span).

From geometry, coupled with the assumption that the deflected shape is a half "sine" function with peak value "δ", the following relations are developed:

Assume "a" is a fraction of 50% of the span (the following calculations show only the final iterated assumption for the fraction

$\varepsilon := .7$

$$a := \varepsilon \cdot \left(\frac{L_s}{2}\right)$$

$a = 8.855\,in$

Calculate "b" in Figure 2.9.8

$$b := \left[(a)^2 + \left(g_2 - g_1\right)^2\right]^{.5}$$

$b = 9.1\,in$

The inverse of the radius of curvature, R, at the point of peak elastic deflection of the free span, is computed as the second derivative of the assumed sin wave deflection shape. Based on the geometry in Figure 2.9.8, the peak deflection is:

$$\delta := .5\cdot\left[\left[a\cdot\frac{b}{2\cdot(g_2 - g_1)}\right]^2 + 4\cdot\left(\frac{b}{\pi}\right)^2\right]^{.5} - a\cdot\frac{b}{4\cdot(g_2 - g_1)}$$

$\delta = 0.427\,\text{in}$

For the assumed "a", the limiting axial load capacity in the unsupported region is conservatively estimated as:

$$a_{lim2} := \pi^2\cdot E\cdot\frac{I}{(b)^2\cdot W_r}$$

$a_{lim2} = 104.9$

The corresponding rigid body angle is:

$$\theta_2 := \text{atan}\left[1\cdot\frac{(g_2 - g_1)}{a}\right]$$

$\theta_2 = 13.314\,\text{deg}$

The axial load in the unsupported portion of the beam at this instant is

$$P_{ax} := \frac{(W_r\cdot a_{lim2})}{\cos(\theta_2)}$$

$P_{ax} = 647.331\,\text{lbf}$

The resisting moment is

$M_r := K\cdot\theta_2$

$M_r = 145.619\,\text{in}\cdot\text{lbf}$

The total stress in the middle of the unsupported section of free span "b" is

$$\text{stress}_3 := \frac{(P_{ax}\cdot\delta - M_r)\cdot D}{2\cdot I}$$

$\text{stress}_3 = 5.145\times 10^4\,\text{psi}$

$$\text{stress}_{3d} := \frac{P_{ax}}{A}$$

$stress_{3d} = 2.257 \times 10^4 psi$

$stress_{3t} := stress_3 + stress_{3d}$

$stress_{3t} = 7.402 \times 10^4 psi$

The safety factor is

$$\frac{\sigma_y}{stress_{3t}} = 1.088$$

The total stress at the grid strap due to the axial force and ~~any the~~*any the* resisting moment is

$$\sigma_{gs} := \frac{W_r \cdot a_{lim2}}{A} + \frac{M_r \cdot D}{2 \cdot I}$$

$\sigma_{gs} = 7.928 \times 10^4 psi$

The safety factor is

$$\frac{\sigma_y}{\sigma_{gs}} = 1.015$$

For this set of assumptions, the stress capacity of the rod cladding has been achieved, so that the limit deceleration is:

$A_{limit} := a_{lim2}$

$A_{limit} = 104.9$

Conclusions

An analysis has demonstrated that for the most limiting PWR fuel assembly stored in the HI-STAR 100 fuel basket, a conservative lower bound limit on acceptable axial decelerations exceeds the 60g design basis of the cask. For a reasonable assumption of moment resisting capacity at the grid straps, the axial deceleration limit exceeds the design basis by a large margin.

It is concluded that fuel rod integrity is maintained in the event of a hypothetical accident condition leading to a 60g design basis deceleration in the direction normal to the target.

FUEL ROD DEFORMATION PHASES

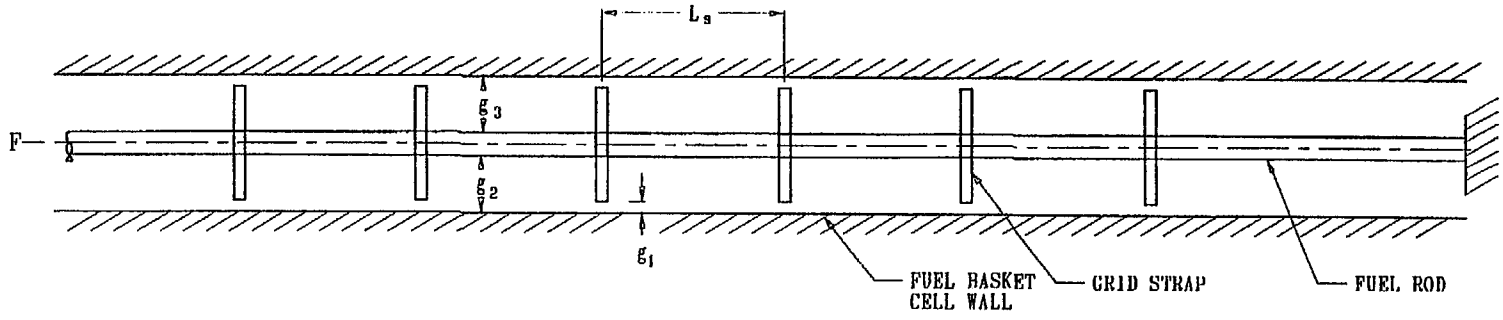


FIGURE 2.9.1; $g_1 > 0$

FUEL ROD DEFORMATION PHASES

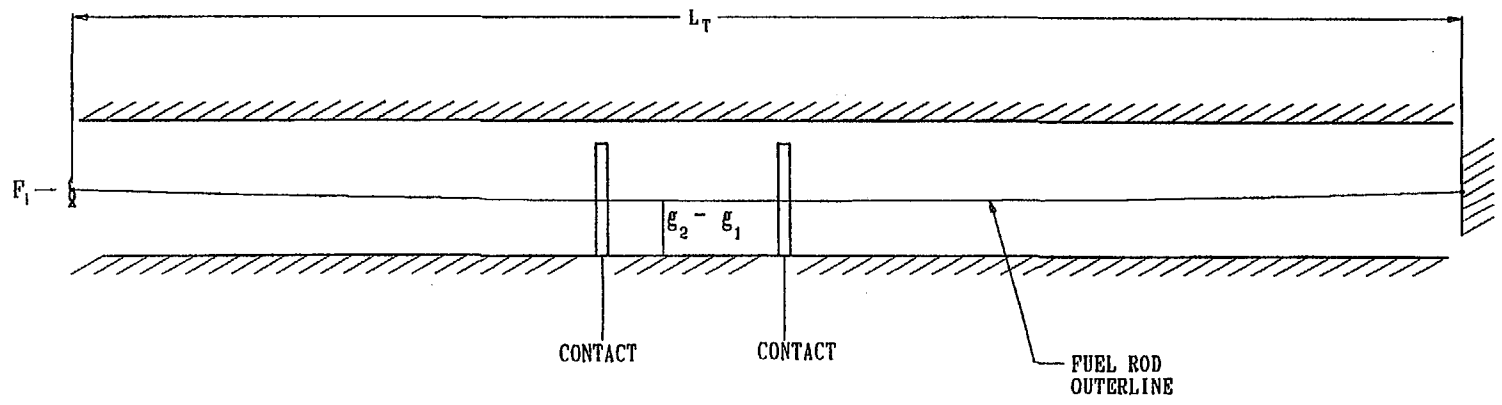


FIGURE 2.9.2; $g_1 = 0$

FUEL ROD DEFORMATION PHASES

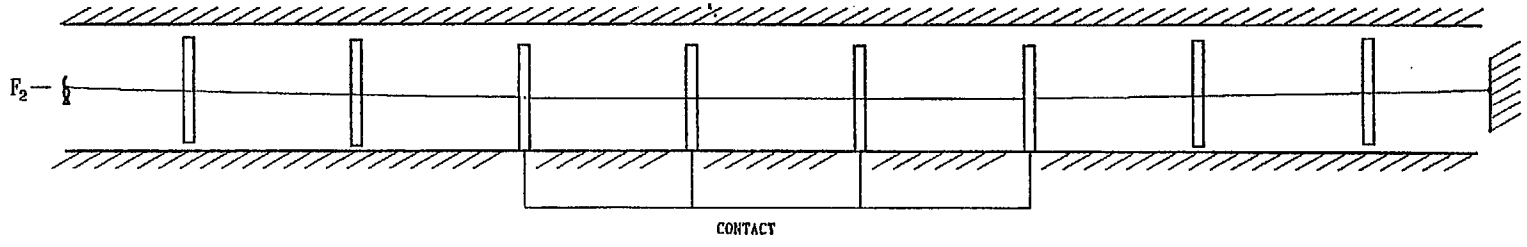


FIGURE 2.9.3; $g_1 = 0$, $F_2 > F_1$

FUEL ROD DEFORMATION PHASES

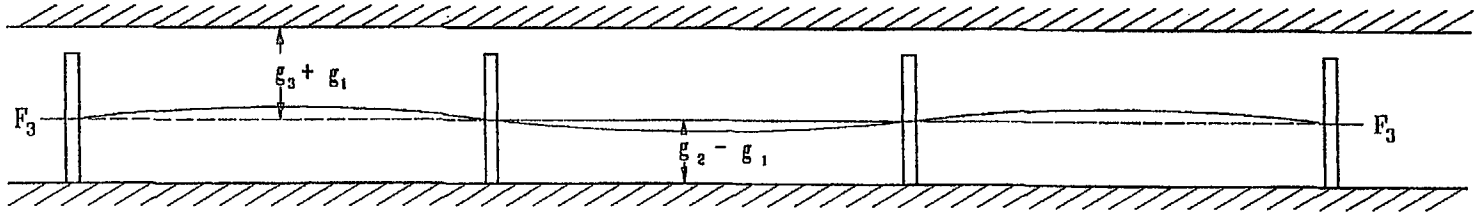


FIGURE 2.9.4; INTER-GRID STRAP DEFORMATION $F_3 > F_2$

FUEL ROD DEFORMATION PHASES

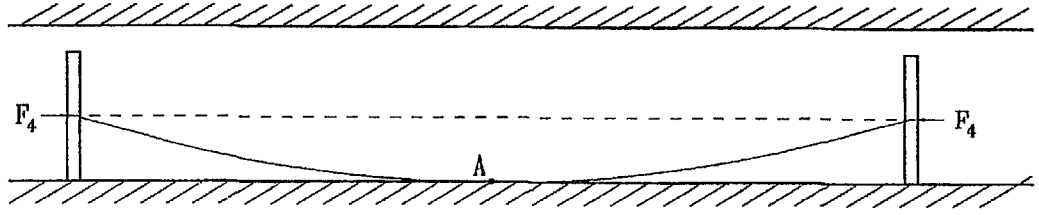


FIGURE 2.9.5; POINT CONTACT AT LOAD $F_4$
MAXIMUM BENDING MOMENT AT A

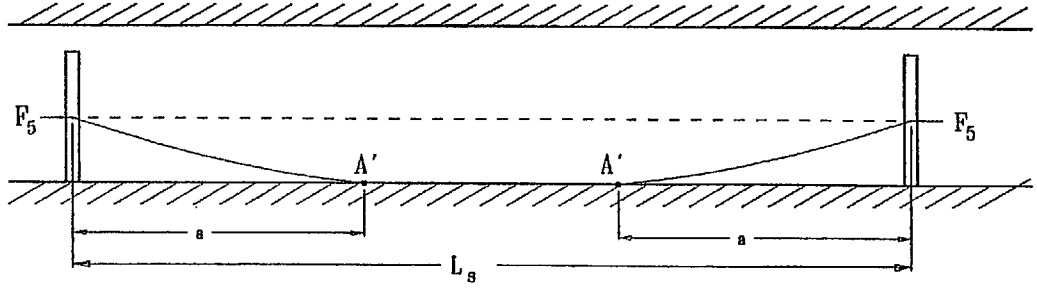


FIGURE 2.9.6; EXTENDED REGION OF CONTACT
$F_5 > F_4$ , ZERO BENDING MOMENT AT A'

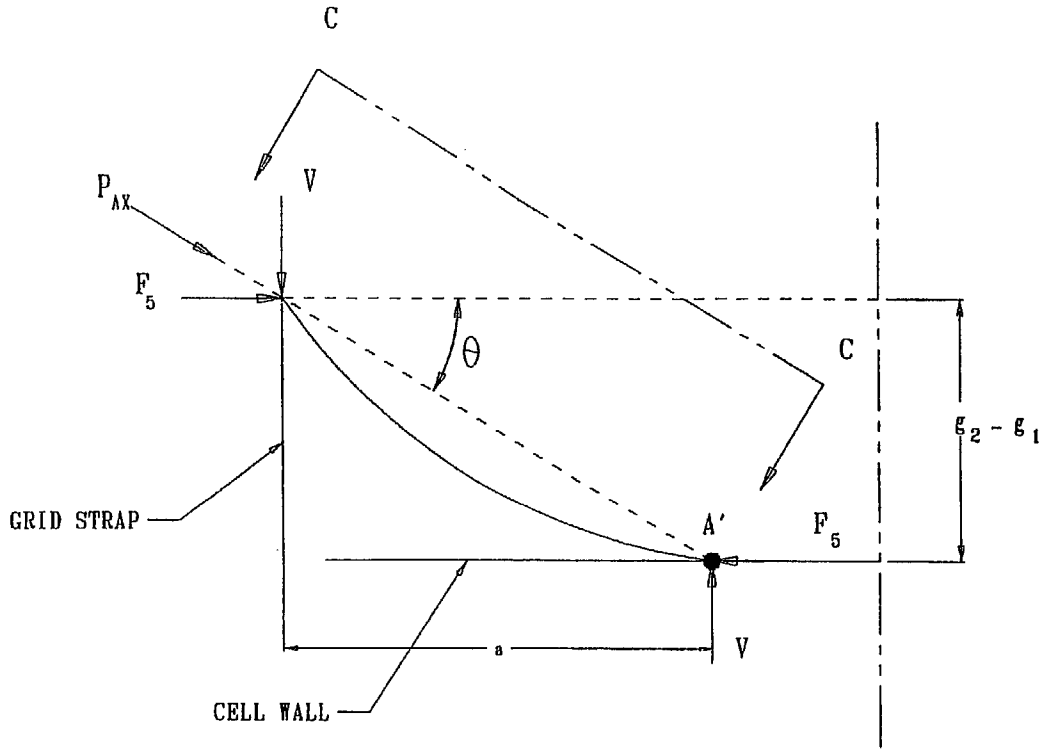


FIGURE 2.9.7; FREE BODY DIAGRAM WHEN MOMENT AT A' = 0
$P_{AX} = F_5/COS(\theta)$. RESISTING MOMENT $M_R$
AT GRID STRAP NOT SHOWN

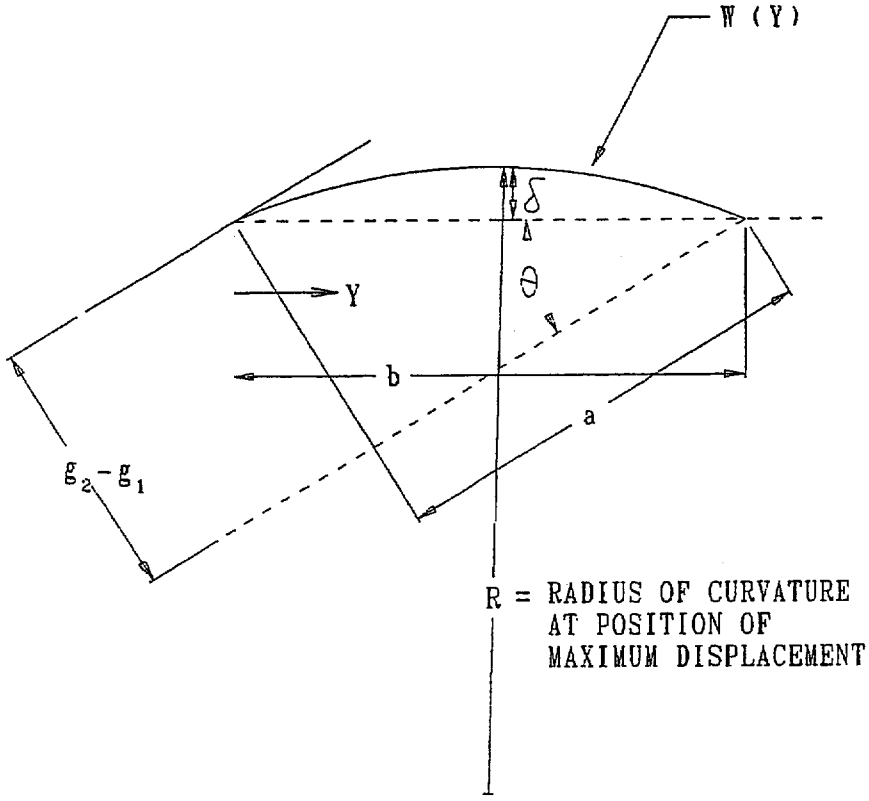


$$Z = R - \delta$$

$$W(Y) = \delta \, SIN( \pi Y / b )$$

FIGURE 2.9.8; VIEW C - C

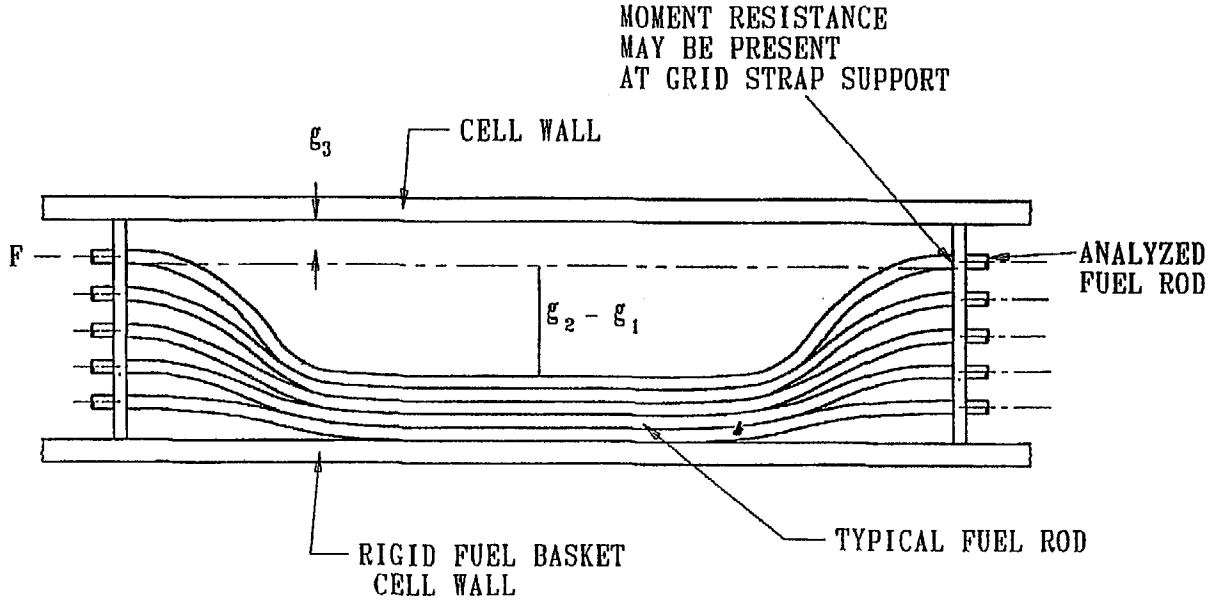


FIGURE 2.9.9; EXAGGERATED DETAIL SHOWING MULTIPLE FUEL RODS SUBJECT TO LATERAL DEFLECTION WITH FINAL STACKING OF ROD COLUMN

## 2.10 MISCELLANEOUS ITEMS

### 2.10.1 Appendices

*The following appendices are included as supplementary material for Chapter 2 of the SAR.* ~~This section contains a summary listing of appendices to Chapter 2 of the SAR.~~

APPENDIX 2.A: IMPACT LIMITER CHARACTERISTICS, DYNAMIC SIMULATION OF HYPOTHETICAL ACCIDENT EVENT, AND SCALE MODEL TESTS

*(This appendix was 2.H in previous SAR revisions; it has been renumbered reflecting the removal of other appendices from the SAR)*

*APPENDIX 2.B: SUMMARY OF RESULTS FOR STRUCTURAL INTEGRITY OF DAMAGED FUEL CANISTERS*

*ALL OTHER APPENDICES (2.C through 2.AO) - DELETED*

### 2.10.2 Summary of NUREG -1617/10CFR71 Compliance

This subsection provides a "road map" of technical information to demonstrate that the SAR in compliance with the provisions of NUREG-1617 and associated referenced sections of 10CFR71 necessary to certify the HI-STAR 100 package for transport.

**Description of Structural Design**

The package structural design description and the contents of the application meet the requirements of 10CFR 71.31 and Regulatory Guide 7.9. Applicable sections where this is demonstrated are 1.2.1; 1.3; 1.4; and 2.1.

The codes and standards used in the package design are listed in 1.3. The use of the ASME Boiler and Pressure Vessel Code is in compliance with NUREG/CR-6407, "Classification of Transportation Packaging and Dry Spent Fuel Storage Components".

**Material Properties**

There are no significant chemical, galvanic or other reactions among the packaging components, among package contents, or between the packaging components and the contents in dry or wet environment conditions. The applicable subsection where this is demonstrated is 2.4.4.

The effects of radiation on materials are considered and package containment is constructed from materials that meet the requirements of Reg. Guides 7.11 and 7.12. Applicable subsections where this is demonstrated are: 1.2.1; 2.1.2; and, 2.4.4.

**Lifting and Tie-Down Standards for All Packages**

Lifting and Tie-Down systems meet 10CFR 71.45 standards. The applicable section where this is demonstrated is 2.5.

**General Considerations for Structural Evaluation of Packaging**

The packaging structural evaluation meets the requirements of 10CFR 71.35. Applicable chapters and/or sections where this is demonstrated are: 2.5; 2.6; 2.7

**Normal Conditions of Transport**

The packaging structural performance under normal conditions of transport demonstrate that there will be no substantial reduction in the effectiveness of the packaging. The applicable section where this is demonstrated is 2.6.

**Hypothetical Accident Conditions**

The packaging structural performance under the hypothetical accident conditions demonstrates that the packaging has adequate structural integrity to satisfy the subcriticality, containment, shielding, and temperature requirements of 10CFR Part 71. The applicable section where this is demonstrated is 2.7.

**Special Requirement for Irradiated Nuclear Fuel Shipments**

The containment structure meets the 10CFR 71.61 requirements for irradiated nuclear fuel shipments. The applicable section where this is demonstrated is 2.7.

**Internal Pressure Test**

The containment structure meets the 10CFR 71.85(b) requirements for pressure test without yielding. The applicable subsection where this is demonstrated is 2.6.1.4.3.

## 2.11 REFERENCES


[2.1.1] 10CFR Part 71, "Packaging and Transportation of Radioactive Materials", Title 10 of the Code of Federal Regulations, Office of the Federal Register, Washington, D.C.

[2.1.2] Regulatory Guide 7.8, "Load Combinations for the Structural Analysis of Shipping Casks for Radioactive Material", Revision 1, March, 1989, U.S. Nuclear Regulatory Commission.

[2.1.3] 10CFR Part 72, "Licensing Requirements for the Storage of Spent Fuel in an Independent Spent Fuel Storage Installation", Title 10 of the Code of Federal Regulations, Office of the Federal Register, Washington, D.C.

[2.1.4] Regulatory Guide 7.6, "Design Criteria for the Structural Analysis of Shipping Cask Containment Vessels", Revision 1, March, 1978, U.S. Nuclear Regulatory Commission.

[2.1.5] ASME Boiler & Pressure Vessel Code, Section III, Subsection NB, American Society of Mechanical Engineers, 1995.

[2.1.6] ASME Boiler & Pressure Vessel Code, Section III, Subsection NG, American Society of Mechanical Engineers, 1995.

[2.1.7] ASME Boiler & Pressure Vessel Code, Section III, Subsection NF, American Society of Mechanical Engineers, 1995.

[2.1.8] Code Case N-284, "Metal Containment Shell Buckling Design Methods", Section III, Division 1, Class MC, Approval Date 8/25/80.

[2.1.9] NUREG-0612, "Control of Heavy Loads at Nuclear Power Plants," United States Nuclear Regulatory Commission, July, 1980.

[2.1.10] ANSI N14.6-1993, "American National Standard for Special Lifting Devices for Shipping Containers Weighing 10,000 Pounds (4,500 kg) or More for Nuclear Materials," American National Standards Institute, Inc.

[2.1.11] ASME Boiler & Pressure Vessel Code, Section II, Part D, American Society of Mechanical Engineers, 1995.

[2.1.12] ASME Boiler & Pressure Vessel Code, Section III, Appendices, American Society of Mechanical Engineers, 1995.

[2.1.13] Regulatory Guide 7.11, "Fracture Toughness Criteria of Base Material for Ferritic Steel Shipping Cask Containment Vessels with a Maximum Wall Thickness of 4 Inches", United States Nuclear Regulatory Commission, June, 1991.

[2.1.14] Regulatory Guide 7.12, "Fracture Toughness Criteria of Base Material for Ferritic Steel Shipping Cask Containment Vessels with a Wall Thickness Greater Than 4 Inches But Not Exceeding 12 Inches", United States Regulatory Commission, June, 1991.

[2.1.15] NUREG/CR-1815, "Recommendations for Protecting Against Failure by Brittle Fracture in Ferritic Steel Shipping Containers Up to Four Inches Thick."

[2.1.16] Aerospace Structural Metals Handbook, Manson.

[2.1.17] ARMCO Product Data Bulletin S-22

[2.1.18] NUREG-1617 Standard Review Plan for Transportation Packages for Spent Nuclear Fuel (Draft Report, March 1998).

[2.3.1] Hexcel Corporation Publication TSB 120, "Mechanical Properties of Hexcel Honeycomb Materials".

[2.3.2] Test Report For Aluminum Honeycomb Static Compression Testing Under Different Temperatures, Holtec Proprietary Report HI-981979, June 1998.

[2.4.1] NRC Bulletin 96-04: Chemical, Galvanic or Other Reactions in Spent Fuel Storage and Transportation Casks, July 5, 1996.

[2.4.2] L.W. Ricketts, Fundamentals of Nuclear Hardening of Electronic Equipment, Robert E. Krieger Publishing Company, Malabar, FL, 1986.

[2.4.3] D.R. Olander, "Fundamental Aspects of Nuclear Reactor Fuel El TID-26711-P1, 1976.

[2.6.1] Theory of Elastic Stability, S.P. Timoshenko and J. Gere, McGraw Hill.~~, 2nd Edition.~~

[2.6.2] Mark's Standard Handbook for Mechanical Engineering, 9th ed.

[2.6.3] Mok, Fischer, and Hsu, "Stress Analysis of Closure Bolts for Shipping Casks" (NUREG/CR-6007-UCRL-ID-110637), Lawrence Livermore National Laboratory/Kaiser Engineering, 1993.

[2.6.4] ANSYS Finite Element Code, Version 5.2, ANSYS Inc., 1995.

[2.7.1] Shappert, L.B., "Cask Designer's Guide: A Guide for Design, Fabrication, and Operation of Shipping Casks for Nuclear Applications," ORNL-RSIC-68, Oak Ridge National Laboratories, Feb. 1970.

[2.7.2] American Society of Civil Engineers, Structural Analysis and Design of Nuclear Power Plants, ASCE No. 58.

[2.7.3] NUREG/CR-6322, "Buckling Analysis of Spent Fuel Basket", Lawrence Livermore National Laboratory, May, 1995.

[2.9.1] Chun, Witte, Schwartz, "Dynamic Impact Effects on Spent Fuel Assemblies", UCID-21246, Lawrence Livermore National Laboratory, October 20, 1987.

[2.9.2] Physical and Decay Characteristics of Commercial LWR Spent Fuel, Oak Ridge National Laboratory Report, J. Roddy, H. Claiborne, R. Ashline, P. Johnson, and B. Rhyne, ORNL/TM-9591/V1-R1, 1/86.

# APPENDIX ~~2.H~~2.A: DESIGN, TESTING, AND COMPUTER SIMULATION OF THE AL-STAR™ IMPACT LIMITER

## ~~2.H~~2.A.1 INTRODUCTION

As stated in Subsection 2.7, the central purpose of the AL-STAR™ impact limiter is to limit the package maximum deceleration, $\alpha_{max}$, under a postulated drop event to a specified design value. For the regulatory 9-meter hypothetical free drop event, the AL-STAR design is engineered to limit the maximum rigid body deceleration to 60 times the acceleration due to gravity (Table 2.1.10). The HI-STAR packaging, consisting of the loaded overpack and top and bottom impact limiters (illustrated in Figure ~~2.H~~2.A.1.1) is essentially a cylindrical body with a rigid interior (namely, the overpack) surrounded by a pair of relatively soft crushable structures. The crushable structure (impact limiter) must deform and absorb the kinetic energy of impact without detaching itself from the overpack, disintegrating, or otherwise malfunctioning. A falling cylindrical body may theoretically impact the target surface in an infinite number of orientations; the impact limiter must limit decelerations to below 60g's and preserve the limiter-to-overpack connection regardless of the impact orientation. Figure ~~2.H~~2.A.1.2 presents the side drop event. In general, a drop event orientation is defined by the angle of the HI-STAR 100 longitudinal axis, $\theta$, with the impact surface. In this notation, $\theta = 0$ means a side drop and $\theta = 90°$ implies a vertical or end drop scenario. Inasmuch as the top and bottom impact limiter are made of identical crush material, the top or bottom vertical drop events are mathematically and physically equivalent as far as the impact limiter design is concerned. In any orientation, the drop height is measured from the lowest point on the package.

An intermediate value of $\theta$, $\theta = 67.5°$, warrants special mention. At $\theta = 67.5$ degrees, the point of impact is directly below the center of gravity (C.G.) of the HI-STAR 100 package. This drop orientation is traditionally called the C.G.-over-corner (CGOC) configuration. The CGOC orientation is the demarcation line between single and dual impact events. At $90° > \theta > 67.5°$, the leading end of the packaging (denoted as the "primary" impact limiter) is the sole participant in absorbing the incident kinetic energy. At $\theta < 67.5°$ drop orientations, the initial impact and crush of the leading (primary) impact limiter is followed by the downward rotation of the system with the initial impact surface acting as the pivot, culminating in the impact of the opposite (secondary) impact limiter on the target surface. In the dual impact scenarios, the first and second impact limiter crush events are referred to as the "primary" and "secondary" impacts, respectively. It is reasonable to speculate that for certain values of $\theta$, the secondary impact may be the more severe of the two. As stated earlier, the design of AL-STAR must ensure that $\alpha_{max} \leq 60$, regardless of the value of $\theta$.

The AL-STAR attachment design must ensure that both impact limiters remain attached to the cask during and after the impact event. The impact limiters are also required to prevent cask body-to-unyielding target contact.

Finally, the package design must satisfy all criteria in ambient temperature conditions ranging from -20° to 100°F, and with humidity ranging from 0 to 100%. Therefore, the impact limiter design must be functionally insensitive to temperature and environmental conditions.

An aluminum honeycomb-based impact limiter design was selected as the preferred material for development. The detailed design of the AL-STAR impact limiters is presented in Holtec Drawing 1765 located in Section 1.4. A pictorial view of AL-STAR is presented in Figure ~~2.H~~2.*A*.1.3.

Figure ~~2.H~~2.*A*.1.3 indicates that in addition to the crushable honeycomb, the AL-STAR contains two internal cylindrical shells (also denoted as "rings"), which are stiffened with radial gussets. These carbon steel shells are sized to behave as undeformable surfaces during impact events. They are essentially the "backbone" of the impact limiter, lending a predictability to the impact limiter crush behavior and forcing the energy absorption to occur in the honeycomb metal mass. The design of this backbone structure was a subject of in-depth computer and experimental 1/8 scale static testing, as documented in Holtec Report HI-962501 [~~2.H~~2.*A*.4] and summarized in Section ~~2.H~~2.*A*.4 herein.

Another noteworthy aspect of the AL-STAR impact limiter design is the arrangement of uniaxial and cross core (biaxial) honeycombs. Regions of the honeycomb space that experience impact loading in only one direction are equipped with unidirectional honeycomb sectors. The regions where the direction of the impact loads can vary have cross-core (bi-directional) honeycomb material, as detailed in Subsection 2.3.1.5.

To summarize, the design objectives of the AL-STAR impact limiter are set down as five discrete items, namely:

i. Limit peak deceleration ($\alpha_{max}$) to 60g's under all potential drop orientations.

ii. Impact limiter must not detach from the cask under a 9-meter drop event, under any impact orientation.

iii. The impact limiters must bring the cask body to a complete stop, such that the overpack does not come in physical contact with the target surface.

iv. Crush material must be equally effective at -20° and 100°F, with humidity ranging from 0 to 100%.

v. All external surfaces must be corrosion-resistant.

The last two objectives are realized by utilizing aluminum honeycomb (Type 5052) as crush material and stainless steel (Type 304), for the external skin enclosure. As shown in the ASME Code (Section II, Part D, Table Y-1), the essential property of the constituent material for the honeycomb and the

external skin, namely the yield strength remains constant in the –20° F to 100° F range. The surface of the carbon steel impact limiter backbone is painted to limit corrosion.

The remaining design objectives, namely, limiting of the maximum rigid body deceleration, $\alpha_{max}$, to 60 g's under a 9-meter drop event, maintaining positive attachment of the AL-STAR impact limiters to the overpack, and preventing contact of the overpack with the unyielding surface, are demonstrated by a combination of numerical simulations and scale model static and dynamic testing. This was accomplished through a research and development effort that is broadly subdivided into six phases, as follows:

Phase 1: Characterize the honeycomb pressure-deflection relationship.

Phase 2: Propose a force (static) vs. crush (F vs. d) model for AL-STAR.

Phase 3: Perform 1/8 scale model static compression tests to validate the force-crush model and to establish the adequacy of the AL-STAR backbone structure.

Phase 4: Conduct 9-meter quarter-scale model dynamic drop tests in selected limiting drop configurations and obtain test data.

Phase 5: Simulate the experimental drop tests with a suitable "dynamic model" and establish that the dynamic model predictions of deceleration, crush and event time duration reasonably match the experimentally measured values. A reasonable prediction of the peak decelerations of each drop event is the minimum for the dynamic model to be acceptable.

Phase 6: Utilize the experimentally confirmed dynamic model to evaluate the effects of tolerances on crush properties and on package weight, and to confirm the adequacy of the full-scale impact limiter design.

It is of crucial importance that the dynamic model benchmarked in Phase 5 be of high reliability, since it becomes the analytical model for the accident-event response prediction of the packaging when tolerances on material behavior and package mass are considered (Phase 6).

In this appendix, a description of the overall program and results for each of the six phases is presented.

### ~~2.H~~2.A.2 Phase 1: Material Pressure-Crush Relationship

The extent of deflection, $\Delta$, sustained by a honeycomb material when subjected to a uniform pressure, p, is an essential element of information in the impact limiter design. Towards this end, coupon specimens of uniaxial and cross-core honeycomb of various nominal crush strengths and densities were compression-tested by the material manufacturer. The results showed that all honeycomb coupons shared some common load-deflection characteristics, namely:

The initial pressure-deflection curve resembled an elastic material (pressure roughly proportional to deflection).

Upon reaching a limiting pressure, the material crushed at near constant pressure until the crush reached approximately 60-70 percent of the initial thickness. The required crush force had to increase rapidly to achieve small incremental crushing for strains beyond approximately 60-70 percent.

Figure ~~2.H~~2.A.2.1 shows a typical static pressure-deflection curve for a 1"-thick honeycomb specimen. The curve with the initial peak is that of an un-precrushed honeycomb specimen; the curve without the peak (shown as a dashed line only where a difference occurs) corresponds to a pre-crushed specimen. Dynamic testing subsequently showed that removal of the initial peak by pre-crushing the material was a desired feature whenever a large flat area of honeycomb material experienced a crush force (such as in a 90 degree end drop).

Curve fitting of data from all tested coupons indicated that a single mathematical relationship between the applied pressure and compression strain could be developed. The mathematical relationship can provide a reasonable fit for coupons of all crush strengths (crush strength defined as the pressure corresponding to the flat portion of the curve in Figure ~~2.H~~2.A.2.1; i.e., it is the constant pressure at which the honeycomb undergoes near-perfect plastic deformation). In other words, the pressure, p, for a given strain, $\varepsilon$, is represented by a unique function of the crush pressure, $p_c$, i.e.

$$p = f(p_c, \varepsilon)$$

The relationship between p and compression strain was used in the subsequent mathematical efforts to simulate AL-STAR crush behavior. The above mathematical relation was developed to simulate material behavior for a honeycomb material under both non-pre-crushed and pre-crushed conditions.

### ~~2.H~~2.A.3 Phase 2: Static Force-Crush Prediction Model

An essential step towards the development of a reliable dynamic model to simulate the impact of a dropped HI-STAR 100 package is to develop a static force-crush model that can subsequently be validated by scale model tests. The force-crush model should reliably duplicate the resistance provided by an impact limiter for a range of crush orientations for the full range of crush depths.

The required force-crush model for AL-STAR is developed using the concept of interpenetration, which is explained using the case of the side drop ($\theta = 0$) as an example (Figure ~~2.H~~2.A.3.1(a)).

The condition existing in all impact limiter drop scenarios is that the relatively soft honeycomb material lies between two "hard" surfaces that are advancing towards each other during the impact. One of these two rigid surfaces is the essentially unyielding target (Rigid Body 1) and the other is the structural backbone of the impact limiter (Rigid Body 2). While the target surface is flat, the backbone structure is

cylindrical in profile. When squeezed between the two surfaces, the honeycomb material (at each instant in time) will crush at one or both interface locations. To determine which interface surface will undergo crushing at a given point during the impact event, the concept of interpenetration area is utilized as explained below.

In this concept, two separate crush scenarios, one assuming that the crush occurs at the external interface (target-to-impact limiter), and the other assuming that the crushing is at the internal interface (structural backbone/overpack-to-impact limiter), are compared at each instant during a simulated compression of the impact limiter. A metal honeycomb impact limiter, in general, may have multiple honeycomb material sections crushing at each interface. For simplicity in explaining the concept of interpenetration, we assume that each of the interfaces is characterized by a uniform distribution of honeycomb having crush pressures $p_1$ and $p_2$, respectively. To determine the resistive force developed to crush the impact limiter by a small amount, d, against the external target, the impact limiter is assumed to penetrate the target by the amount "d" without deformation. The resulting area $A_1$ for the case of side drop, illustrated in Figure ~~2.H~~2.A.3.1(b), can be computed as an algebraic expression in the amount of approach, d. (For oblique drop events, ANSYS [~~2.H~~2.A.1] or CADKEY [~~2.H~~2.A.2] are used to compute interpenetration area as a function of incremental interpenetration.) The pressure-compression relationship for the honeycomb stock at the external interface provides the crush pressure $p_1$ that develops due to deformation "d". The total force required for crush "d", at the external interface, is therefore equal to $p_1A_1$.

In the second (independent) scenario, the impact limiter external surface is assumed to undergo no movement; rather, the backbone structure (along with the overpack) advances towards the target by an amount d (Figure ~~2.H~~2.A.3.1(c)). Once again, assuming that the cylindrical rigid body moves through an amount "d", the resistance pressure developed in the honeycomb material lying in the path of penetration is available from the appropriate material pressure-compression curve. If the pressure corresponding to the deformation is $p_2$ and the projected area at the internal interface is $A_2$, then the total resistive force encountered in realizing an approach equal to "d" between the overpack-backbone assemblage and the target under this latter scenario is $p_2A_2$. In an actual drop event, at each instant during the event, incremental crush occurs at one of the two interfaces. If $p_1A_1 < p_2A_2$ at a given instant then crushing will occur at the external interface. Likewise, $p_1A_1 > p_2A_2$ will imply that crushing will occur internal to the impact limiter. The smaller of $p_1A_1$ and $p_2 A_2$ is the required crush force and the corresponding location of crush is where the honeycomb material will compress to realize the approach equal to d. This "inequality test" to determine where crushing occurs is performed at every increment of crush during the simulation of the event. The appropriate value of the crush force is used in the equilibrium equations at that instant. The concept of interpenetration at two interfaces has been confirmed during testing of the impact limiters; the total crush is observed to be a sum of compression at each of the two interfaces.

To construct a mathematical force-deformation relationship for AL-STAR in any given orientation, the above process is repeated as the crush "d" is increased in small increments starting with the beginning of compression (d = 0). It is quite clear that the development of the force-deflection model (F-d model)

for AL-STAR in any orientation is a straightforward analysis in 3-D geometry. The F-d curve for AL-STAR for any given value of θ can be developed where, other than the geometry of the impact limiter, the crush strengths p of the honeycomb materials utilized in the impact limiter are the only other required inputs.

The force (F) vs. crush (d) relationship developed using the foregoing method is referred to as the F-d model that is subject to validation by appropriate 1/8 scale model compression tests described in the following section.

### ~~2.H~~2.A.4 Phase 3: One-Eighth Scale Model Static Compression Tests

The 1/8 scale model tests consist of subjecting scaled replicas of the full-size AL-STAR to static compression tests in an engineered fixture such that the force-compression curve for the scaled model can be obtained in various orientations of compression. The scale model is made by making the diameters and length of the model one-eighth of the full-size AL-STAR. The thicknesses of the backbone components (i.e., the inner and outer shells and gussets), and the external skin (see Figure ~~2.H~~2.A.1.3) are also scaled to one-eighth times the corresponding dimensions (to the nearest sheet metal gage, where applicable) in the full-size AL-STAR. In the one-eighth model, the performance of the attachment system is not assessed nor is the cask body modeled. However, the interface between overpack and impact limiter where the compression load is resisted is properly simulated. The crush pressure is a material property of the energy absorbing material; therefore, the material (and its density) is not scaled. The 1/8 scale model, therefore, has approximately $(1/8)^3$, or 1/512 the volume and weight of the full-size unit. Holtec documents [~~2.H~~2.A.3, ~~2.H~~2.A.4] provide complete details on the 1/8 scale model geometry and fabrication. The static compression behavior of such a 1/8-scale model is correlated with that of a full-size unit using the geometric scaling information. For example, under an axial compression test the area under crush in the scale model will be 1/64 of the full-size AL-STAR (recall that the diameter is scaled down by a factor of 8). Therefore, the crush force (which is crush force pressure times the area under crush) will be 1/64 of the full-size unit. On the other hand, the crush stroke (extent of deformation before "lock up") will be 1/8 of the full-size AL-STAR because the axial length of the scale model (which corresponds to the height of the crush column in axial compression) is one-eighth of the full-size hardware. Thus, the total energy absorbed (force times compression) will be $(1/8)^3$ of the full-size unit. The same scaling factor can be shown to apply in all directions of crush.

In summary, the 1/8 scale model scales the geometric dimensions of AL-STAR. The previously discussed F-d model is required to translate the force-crush relationship from the 1/8 scale replica to the full-size unit. In order to use the analytical F-d model as a valid vehicle for predicting the force-crush of the full-size (or quarter-scale) AL-STAR, it is necessary to check its prediction ability against actual test data from 1/8-scale model static compression tests.

The objectives of static scale model tests are twofold:

i. Determine whether the static force-crush relationship predicted by the F-d model appropriately simulates the actual relationship determined by test;

ii. Determine whether the backbone structure of the AL-STAR impact limiter is sufficiently rigid to withstand and transmit the large loads associated with the postulated accident scenarios.

### ~~2.H~~2.A.4.1 Static Compression Tests on Initial Candidate Crush Material

To assess compression performance, a QA validated AL-STAR static test procedure was prepared [~~2.H~~2.A.3] for the one-eighth scale model static compression tests and a series of cold and hot static compression tests performed on an impact limiter configuration with the initial candidate crush material. Holtec calculation package HI-961501 [~~2.H~~2.A.4] contains a comprehensive documentation of the 1/8 scale static test program and results for the impact limiter configuration. A summary of the complete test program and test results is presented below.

Four 1/8-scale models were fabricated with details of the impact limiter carefully scaled, including the stiffening cylinders and the stainless steel skin. No impact limiter attachment bolts were incorporated in the model.

Aluminum honeycomb segments provided for the 1/8-scale models were manufactured utilizing the same procedures and processes as for the full-scale impact limiter. As stated earlier, the crush strengths were not scaled because they are considered as material properties.

An adjustable 1/8 scale static test fixture was designed, analyzed, and fabricated. The test fixture interfaced with the impact limiter and simulated the overpack hard surface. The test fixture could be adjusted to simulate any crush orientation. Figure ~~2.H~~2.A.4.1 shows the test fixture and the 1/8 scale impact limiter being loaded in the heavy-load testing machine.

The following static one-eighth scale test series were carried out:

| Test No. | Orientation, degrees | Temperature |
|---|---|---|
| 1 | 0 (side) | +120°F |
| 2 | 30 (oblique) | Ambient |
| 3 | 60 (oblique) | Ambient |
| 4 | 90 (end) | -30°F |

For all tests except the end compression (where the orientation is immaterial), the circumferential orientation of the impact limiter was selected so that the initial point of contact between the impact

limiter and the test machine was at the interface of two aluminum honeycomb secttions. After each test, the impact limiters were cut open and examined.

Observations Based on 1/8 Scale Model Testing

- Effect of Ambient Temperature:

  The end compression test was performed with the impact limiter cold (-30°F), the side compression test was performed with the impact limiter hot (+120°F), and the two oblique tests performed at ambient temperature. The material behavior showed no influence of test temperature. This confirms the expected result since the aluminum honeycomb and stainless steel skin yield strengths are insensitive to temperature in the range of interest (-20° F to 100° F) as prescribed in Table Y-1 of the ASME Code.

- Side compression orientation - 0 degree:

  The inner stiffening cylinder experienced considerable permanent deformation. The gussets which buttress the inner cylinder buckled. The outer stiffening cylinder performed elastically.

- Oblique compression orientation:

  Two oblique orientation static tests were performed. The 30-degree oblique test again showed the need to thicken the inner stiffening cylinder and to rearrange the stiffening gussets.

  The 60-degree oblique test was a complete success; no plastic deformation of the backbone structure was indicated.

  As would be expected, in those cases where the hard region (backbone structure) of the impact limiter sustained deformations, the scale model exhibited greater flexibility in the physical testing than the analytical prediction (the flexibility of the backbone structure added to the crush of the honeycomb resulting in a greater total measured deflection).

- End compression orientation - 90 degree:

  The end-compression orientation is, structurally speaking, the least complicated of the four test configurations. The loading of the AL-STAR scale model in this test is purely axisymmetric. The initial peak in the pressure/deformation curve seen in the coupon tests (Figure ~~2.H~~2.*A*.2.1) was clearly evident in the axial (end) compression test (Figure ~~2.H~~2.*A*.4.3). The backbone structure performed without sustaining plastic deformation.

- Comparison of experimental and analytical predictions

Out of the four static 1/8-scale model tests, two tests (side compression and 30-degree oblique) were unsatisfactory because the backbone structure of the impact limiter did not remain elastic. These tests served to identify the need to reinforce the AL-STAR backbone structure. The other tests, namely end-compression (90 degree) and 60-degree oblique, wherein the backbone structure performed as designed, showed close agreement with the numerical model. Figures ~~2.H~~2.*A*.4.3 and ~~2.H~~2.*A*.4.4, respectively, show the static test results for 90-degree (end-compression) and 60 degree (oblique) cases, along with the prediction of the F-d model. There is good agreement between the computer model and the test data.

In summary, the 1/8 scale model static test program identified the required design changes to the internal structure of the impact limiters. The 1/8 scale model tests showed that the load-compliance characteristics of AL-STAR are insensitive to the changes in the ambient environment. A comparison of the test results with the mathematical model predictions from the F-d model indicated that the mathematical model was in good agreement with 1/8-scale static crush tests whenever the backbone structure performed as required (i.e. remained elastic). Since the crush geometry of the scale model was *not altered* by the strengthening of the backbone, any subsequent reinforcing of the backbone did not alter the F-d relationship for the impact limiter. The two successful static tests that showed excellent agreement with the computer F-d model, therefore, continued to serve as a valid benchmark of the numerical model after the backbone is stiffened. The reinforced backbone structure is incorporated into the final design drawings for the AL-STAR, and was confirmed as acceptable during the dynamic (1/4-scale) model drop tests. Subsequent to the one-quarter scale dynamic tests and the analytical correlation (Phases 4-6), three additional 1/8$^{th}$ scale confirmatory static tests were performed on impact limiters that included the internal backbone structure and the final crush material orientations used in the quarter-scale drop tests and in the analytical correlation. These additional confirmatory static tests were performed at room temperature. The tests simulated the crush orientation corresponding to the side drop, the "center-of-gravity-over corner" drop, and the end drop, respectively. Force-deflection results from the static test are compared with the predictions from the theory for the 1/8$^{th}$-scale impact limiters. Subsection ~~2.H~~2.*A*.10 discusses the results obtained from these three additional static tests.

### ~~2.H~~2.*A*.5 Phase 4: 9 Meter Quarter-Scale Model Drop Tests

The one-quarter scale model dynamic tests provide physical confirmation of the HI-STAR impact limiter design and the performance of the attachment system. The quarter-scale and full-scale design of the impact limiter is presented in *drawings*~~Holtec Drawing 1765,~~ in Section 1.4.

In the 1/4 scale model drop test program, an instrumented scale model of the HI-STAR 100 dual-purpose cask was assembled with the top and bottom AL-STAR impact limiters, raised to a height of 9 meters (measured from the lowest point on the package), and then released to free fall onto an unyielding concrete and steel armor target (unyielding target). The impact limiter attachment system is reproduced in the model using the appropriate scale for bolt diameters, etc.

A detailed description of the quarter-scale model, instrumentation, data acquisition, and data processing is presented in a proprietary Holtec document [~~2.H~~2.A.7]; a concise self-contained summary is provided in the following.

~~2.H~~2.A.5.1 Test Plan:

The drop test program was performed at the drop testing facilities at the Oak Ridge National Laboratory. The target at the ORNL facility complies with guidance of IAEA Safety Series 37, Article A-618.

The quarter-scale model testing of the package required the design and fabrication of scale models of AL-STAR, the HI-STAR overpack, and the multi-purpose canister. The quarter-scale replicas of AL-STAR were prepared using the scaling procedure described previously in the context of the 1/8 scale model. In the scale model for the MPC and the overpack, the emphasis is in scaling the weight and moment of inertia, because it is these properties (translational as well as rotational) which are key to the response in the drop event. A schematic of the MPC design used in the scale model is shown in Figure ~~2.H~~2.A.5.1. The weight of the MPC replica was set at 1,380 lbs (to simulate an 88,320 lb loaded multi-purpose canister). ~~The design drawing of the MPC scale model is provided in Section 1.4 (Drawing 1547).~~

The overpack scale model likewise is a cylindrical body whose length and outside diameter are 1/4, whose weight is 1/64, and whose mass moment of inertia is 1/1024 of the respective design parameters in the full-size hardware, as summarized below:

| Key Quarter Scale HI-STAR Overpack Model Data | | | |
|---|---|---|---|
| Length (inch) | O.D. (nominal) (inch) | Overpack Plus MPC Weight (lb.) | Mass Moment of Inertia About a Transverse Centroidal Axis (Overpack Plus MPC) (lb.-in$^2$) |
| 50.7813 | 21 | 3,733 | 1.351E+06 |

Figures ~~2.H~~2.A.5.2 through ~~2.H~~2.A.5.4 illustrate the principal geometric data of the quarter-scale overpack model. These figures are adapted from the design drawing 1546 (proprietary) provided in Section 1.4 of this report. It is evident from the above description that the quarter-scale model is, from a geometrical and inertia standpoint, a quarter-scale emulation of a 84" diameter x 203.125" long, 238,900 lb. (approximate) HI-STAR system (overpack and loaded MPC). Finally, the attachment bolts which join the impact limiter to the overpack are also scaled down to 25% of their size in the full-size hardware (in both diameter and thread engagement length), as can be seen from Figures ~~2.H~~2.A.5.3 and ~~2.H~~2.A.5.4 or *the applicable drawing*~~Drawing 1546~~ in Section 1.4.

The one-quarter scale drop tests were performed with four discrete orientations of the cask longitudinal axis with respect to the impact surface, as defined below.

Test A – Vertical Drop (Top End): The cask is dropped such that the deceleration of the cask upon impact is essentially vertical.

Test B: Center of Gravity-Over-Corner (CGOC): For HI-STAR 100, C.G.-over-corner means an orientation wherein the axis of the cask is at 67.5° from the horizontal at the instant of release at the 9-meter height. This test seeks to establish the adequacy of the impact limiter under non-symmetric impact loading.

Test C – Side Drop: The cask is held horizontal with the lowest point on the package 9 meters above the target surface when released for free fall. In this test, both impact limiters participate, and the impact impulse is essentially equally divided between them.

Test D – Slapdown: In this test, the cask axis is held at 15° from the horizontal with the lowest point of the cask assembly at 9 meters from the impact surface. The orientation is such that the top end impact limiter impacts the surface first and the bottom end impact limiter experiences the secondary impact.

Each of the four tests has distinct impact characteristics. For example, in the "side drop" test both impact limiters will strike the target simultaneously; only one impact limiter sustains impact in the "end drop" test. The CGOC test involves a primary impact on one impact limiter at an angle such that the gravity vector is oriented with a line passing through the cask center of gravity and the lowest corner of the limiter. Finally, the slapdown test involves impact at both impact limiters with a very slight time separation. These four tests are deemed to adequately represent the limiting impact scenarios under the hypothetical accident conditions of 10CFR71.73.

The torque values used to secure the attachment bolts in the scale model package warrant special mention. The impact limiter attachment bolts serve two major functions during transportation:

1. During normal transport, the attachment bolts ensure that the impact limiters remain attached to the HI-STAR 100 overpack during a 10g axial deceleration as mandated by 10CFR71.45, and during exposure to normal vibratory loading that may reasonably be expected during the course of a normal transport operation. To ensure against loss of attachment due to vibratory loading during normal transport, an initial bolt pre-stress of 30,000 psi has been set, based on common engineering practice. For the bolt diameters specified for the HI-STAR 100 package, the pre-load torque ~~specified in Appendix 2.AF~~ is 245 ft-lb and 1,500 ft-lb for the top and bottom impact limiter attachment bolts, respectively.

2. During the hypothetical accident, the attachment bolts ensure that the impact limiters remain attached to the HI-STAR 100 overpack during and after the impact with the unyielding surface.

The bottom impact limiter is attached to the overpack by 16 bolts aligned with the longitudinal axis of the overpack and arranged in a circular pattern (Figure ~~2.H~~2.A.5.4 shows the bottom view of the one-quarter scale replica). These bolts perform their function by developing tensile stress to resist loading during the hypothetical accident. Because of close clearances with the overpack shielding, the bottom impact limiter also has a set of eight circumferentially arranged alignment pins that fit into mating holes in the overpack bottom plate. These mating holes are plugged when the impact limiter is not in place.

The top impact limiter is attached to the overpack using twenty radial bolts *that*~~which~~ are designed to resist relative motion and transfer loads by shear (Figure ~~2.H~~2.A.5.3 shows the top view of the one-quarter scale replica).

Although the attachment analyses ~~in Appendix 2.AF~~ do not require pre-load (by application of an initial bolt torque) to demonstrate that the required performance during normal transport conditions is achieved, the presence of pre-load serves only to enhance the performance of bolting which resists loads by developing tensile bolt forces (bottom impact limiter attachment bolts). Pre-stress in the bottom impact limiter attachment bolts serves to develop an interfacial pressure between the two components being joined together. This interfacial pressure acts as a reserve against separation at the interface of the impact limiter and the overpack when the external force or moment act to separate them during the drop event. The actual tensile stress bolt will rise significantly over the initial pre-stress if and only if the external load acting to break apart the interface is large enough to cancel out the interfacial pressure.

The effect of pre-load on the performance of bolting *that*~~which~~ resists loads by shear (top impact limiter attachment bolts) is different. The presence of both tensile stress (due to bolt pre-load) and shear stress in the bolt (due to the impact loads in a drop event) will increase the maximum principal stress in the bolt, which will consequently reduce the shear capacity of the bolts. Applying a pre-load in excess of the required amount in the 1/4 scale HI-STAR 100 drop tests will therefore result in a conservative evaluation of the top impact limiter attachment bolts.

Based on the initial torque values set in the full-scale package, the appropriate bolt pre-load torque for the 1/4-scale impact limiter attachment bolts is (to the nearest foot-pound):

Top impact limiter (radial) bolts: 4 ft-lb. (full scale equivalent = 245 ft.-lb~~. per Appendix 2.AF~~)
Bottom impact limiter (axial) bolts: 23 ft-lb. (full scale equivalent =1500 ft.-lb.~~ per Appendix 2.AF~~)

Since a bolt pre-load will enhance the performance of bolts (located at the bottom impact limiter interface) that resist loading by developing tensile stress, the bolt torque was conservatively set at 20 ft-lb. or below for the bottom impact limiter bolts. Since a bolt pre-load will degrade the performance of

bolts (located at the top impact limiter interface) that resist loading by developing shear stress, the bolt torque was conservatively set at 4 ft-lb. or above for the top impact limiter bolts.

The end drop onto the top impact limiter tests the resistance of the twenty radial attachment bolts against failure from shear. The use of an initial torque value (15 ft-lb.), in excess of 4 ft-lb., is conservative for evaluation of the performance of the bolts to resist shearing strains (i.e., as noted earlier, due to an interaction relation between tension and shear, the presence of any tensile strain will reduce the allowable shear strain prior to failure).

The C.G. over corner drop used an initial torque of 15 ft-lb., a value below the mandated value of 20 ft-lb. on the bottom impact limiter. This is again conservative for the evaluation of the performance of the bottom impact limiter attachment bolts, since the presence of additional prestress would enhance the ability of the bolts to retain the impact limiter in position.

The slapdown test was performed using low initial bolt torque values for both impact limiters that simulated "hand-tight" values. Thus, there is almost no contribution from pre-load on the bolts on either impact limiter. In the slapdown drop, the bottom impact limiter experienced the largest deceleration. This test demonstrated that the use of a lower pre-load on the most highly loaded attachment bolt does not affect the ability of the bolts to perform their required function.

Finally, the final side drop used the bolt pre-loads that correlate with the final bolt pre-loads specified (top impact limiter - 4 ft-lb.; bottom impact limiter - 20 ft-lb.) for the one-quarter scale tests.

A minimum of five calibrated unidirectional accelerometers was installed on the test package for each test. Schematics of the accelerometer locations and numbering system for all four tests are presented in Figures ~~2.H~~2.*A*.5.5 and ~~2.H~~2.*A*.5.6.

The accelerometers are placed at three axial locations along the height of the overpack model and at different circumferential locations at each axial location. The placement of the accelerometers axially reflects locations consistent with the detailed 2-D finite element analyses of the MPC that conservatively neglected the effect of stiffening provided to the MPC shell by the MPC baseplate. Figure 2.5.*A*~~H~~.2 shows the three cutouts of the outer 5/8" thick cylinder that are machined flat to position the accelerometers. The following table provides the locations of the accelerometers.

| ACCELEROMETER LOCATIONS FOR ONE-QUARTER SCALE DROP TESTS | | | | | | | | |
|---|---|---|---|---|---|---|---|---|
| NUMBER | TOP END DROP | | SIDE DROP | | SLAPDOWN | | CG-OVER-CORNER | |
| | Axial (inch) | Peripheral (degrees) | Axial (inch) | Peripheral (degrees) | Axial (inch) | Peripheral (degrees) | Axial (inch) | Peripheral (degrees) |
| 1 | 44.78125 | 0 | 5 | 0 | 44.781 25 | 0 | 5 | 0 |
| 2 | 25 | 0 | 25 | 0 | 25 | 0 | 5 | +120 |
| 3 | 5 | 0 | 44.78125 | 0 | 5 | 0 | 5 | -120 |
| 4 | 44.78125 | +120 | 25 | +90 | 44.781 25 | +120 | 44.7812 5 | 0 |
| 5 | 44.78125 | -120 | 25 | -90 | 44.781 25 | -120 | 44.7812 5 | +120 |
| 6 | 5 | +120 | -- | -- | 5 | +120 | 44.7812 5 | -120 |

Notes:

1. All accelerometer axial distances measured from top end surface of overpack model (without impact limiters in place).
2. Peripheral locations measured from plane containing accelerometer #1; clockwise direction, viewed from Section A-A in Figures ~~2.H~~2.*A*.5.5 and ~~2.H~~2.*A*.5.6, is positive.

In addition to recording the deceleration during impact, a high-speed camera and a video camera were used to record the test events. The high-speed camera was used to confirm orientation angles just prior to impact and to aid in the evaluation of extent of crush subsequent to the test. The tests were conducted by attaching the ¼ scale package to a 15-ton mobile crane through appropriate rigging and lifting the package to the required height. An electronically activated guillotine-type cable cutter device was used for releasing the package for free fall. An array of photographs labelled Figures ~~2.H~~2.*A*.5.7 through ~~2.H~~2.*A*.5.13 provide pre-test and post-test visuals of the package. These photographs show quite clearly that the post-crush impact limiters maintained their own physical integrity and *the* ~~their~~ attachment~~s~~s to the overpack scale model suffered no failures.

The following acceptance criteria for the scale model dynamic drop tests were identified in the Test Plan [~~2.H~~2.*A*.11]:

- Filtered decelerations limited to a maximum of 60g's (after scaling to full-scale geometry) for all drop orientations.
- No impact of the cask body on the target surface.
- No separation of impact limiters from the cask body through the entire drop event.

### ~~2.H~~2.A.5.2 Results of First Series of Drop Tests

The first series of three one-quarter scale drop tests (types A, B, and C denoted above) were performed in August 1997 and produced significant information [~~2.H~~2.A.5]. Table ~~2.H~~2.A.1 shows the maximum filtered decelerations registered in the three one-quarter scale tests after the test results are scaled up to the full-scale AL-STAR (by dividing test results by four).

Table ~~2.H~~2.A.1: Peak Decelerations from August 1997 Tests

| Test I.D. | Orientation | Deceleration (g) |
|---|---|---|
| A. | End Drop | 134 |
| B. | C.G.-Over-Corner | 37.84 |
| C. | Side Drop | 51.3 |

The peak filtered deceleration in the first end-drop test was clearly above the 60g-design limit established for the HI-STAR 100 design. The reasons for this discrepancy were determined to be the use of a low value of the dynamic multiplier assumed in designing the impact limiter, and the lack of pre-crush of the honeycomb material. Numerical analyses also indicated that the honeycomb compression modulus was dependent on the impact limiter velocity during the drops. This confirms laboratory data available in the historical literature [~~2.H~~2.A.9]. The velocity and deceleration information obtained from the first round dynamic drop tests enabled development of a simple dynamic correlation multiplier to be applied to the honeycomb material's static F-d behavior. This multiplier is an additional "experimentally based" input term in the computer prediction model for simulation of dynamic drop events [~~2.H~~2.A.6]. Data from the initial test series shows that this multiplier is independent of test orientation and is a function of the ratio of crush velocity during the crushing process divided by the impact velocity at the initiation of crush. Based on the numerical analysis of the August 1997 tests, the honeycomb material was appropriately revised with new crush strengths and new sets of ¼ scale model impact limiters were manufactured. The correlation of the August 1997 quarter-scale tests with the numerical results from the computer model is presented in section ~~2.H~~2.A.6.

In summary, the chief contribution of the August tests, therefore, lay in providing the database to quantify the crushing characteristic of the honeycomb material under dynamic conditions [~~2.H~~2.A.6]. Since none of these tests is ascribed to confirmation of the final performance of the AL-STAR impact limiters, no accelerometer raw or filtered results are included herein. The full set of acceleration data (both raw and filtered) is provided in [~~2.H~~2.A.5].

### ~~2.H~~2.A.5.3 Results of the Second Series of Drop Tests

The second round of one-quarter scale dynamic drop tests, conducted in December 1997 and February 1998, using the new (lower crush strength) impact limiter materials, occurred in three phases. The first phase consisted of the top end drop, CGOC drop, and side drop tests. While the

decelerations in all cases were within the design limit, the attachment system for the bottom impact limiter did not survive the side drop test. The attachment system was redesigned prior to the remaining (slapdown) test. The slapdown test is considered to be the most definitive test of the cask/impact limiter attachment integrity. The slapdown test was successfully completed, with the bottom impact limiter remaining in place during and after the secondary impact, on December 29, 1997 in Phase 2 of the second test series. In order to confirm the adequacy of the attachment system under side drop conditions, the side drop test was repeated in February 1998 during Phase 3. This test reconfirmed the attachment system integrity.

The results from the second round test series demonstrates that the HI-STAR 100 package meets all test acceptance criteria, namely:

- Appropriately filtered decelerations of less than 60g's (after appropriate scaling to reflect the full-size mass and geometry) for all tested orientations;

- All attachment bolts remained intact, ensuring that the impact limiters do not separate from the cask body through and after the drop event;

- No impact of the cask body on the target surface.

Figures ~~2.H~~2.A.5.14 through ~~2.H~~2.A.5.21, drawn from reference ~~2.H~~2.A.7, provide the raw (unfiltered) and filtered deceleration time-histories for each of the four drop scenarios for the key accelerometers used to assess package performance. The accelerometer station numbers indicated in these accelerograms are located by referring to Figures ~~2.H~~2.A.5.5 or ~~2.H~~2.A.5.6, as applicable. The test report [~~2.H~~2.A.7] provides the necessary background to justify the use of this data to evaluate package performance. The following remarks are pertinent concerning the results presented in Figures ~~2.H~~2.A.5.14 through ~~2.H~~2.A.5.21.

End Drop Decelerations (Figures ~~2.H~~2.A.5.14, ~~2.H~~2.A.5.15, and ~~2.H~~2.A.5.15a-c)

All accelerometers for this test recorded decelerations in the direction of crush. Two accelerometers were subsequently determined to be defective (documented in [~~2.H~~2.A.7]). The figures show the raw, the filtered response at 450Hz cut-off frequency, and a combined plot of the raw and filtered data covering a reduced time period. All of these results are obtained from the records from the working accelerometers. All working accelerometers gave essentially identical response; the final evaluation of performance presented herein is the average of the response from the accelerometers deemed to be recording correctly. Figures ~~2.H~~2.A.5.15b and ~~2.H~~2.A.5.15c demonstrate that the sensitivity to cut-off filter frequency is small even up to 1250Hz.

Center of Gravity Over Corner Decelerations (Figures ~~2.H~~2.A.5.16, ~~2.H~~2.A.5.17, and ~~2.H~~2.A5.17a)

The CGOC test was performed immediately after the end drop using the same set of accelerometers. The evaluation of the data after this test clearly determined that the same two accelerometers deemed suspect in the end drop test was also providing erroneous date here. Subsequent independent plate impact tests that definitively showed that these accelerometers were indeed faulty are documented in [~~2.H~~2.*A*.7]. The acceleration data in the figures represents the vertical acceleration obtained by appropriate combination of the raw time data from the longitudinal and lateral mounted accelerometers on the inclined scale model cask. The raw vertical accelerations were then subject to filtering to remove non-rigid body behavior. Raw, filtered, and combined raw and filtered data over the strong response time period are presented.

Slap Down Decelerations (Figures ~~2.H~~2.*A*.5.18, ~~2.H~~2.*A*.5.19, and ~~2.H~~2.*A*.5.19a)

Although the initial release of the package was at an angle of 15 degrees from the horizontal, the high-speed camera showed that impact occurred with the overpack longitudinal axis at an angle of 7.2 degrees from the horizontal. The numerical simulation of this test reflected the actual angle of impact rather than the initial setting at nine meters. The results for all accelerometers (raw data and filtered) are provided in [~~2.H~~2.*A*.7]. The raw and filtered data presented in the figures here represent the deceleration at the bottom end of the package that experiences the larger magnitude secondary impact. Numerical analysis demonstrated that the peak deceleration from secondary impact is insensitive to impact angles between 5 and 12 degrees from the horizontal and decreases as the angle increases above 12 degrees. Raw, filtered, and combined raw and filtered data over the strong response time period are presented.

Side Drop Decelerations (Figures ~~2.H~~2.*A*.5.20, ~~2.H~~2.*A*.5.21, and ~~2.H~~2.*A*.5.21a)

Both impact limiters are supposed to impact the target simultaneously in this test. An evaluation of the individual accelerometer data and an examination of the high-speed camera film clearly indicated that there was a small angle existing between the overpack longitudinal axis and the target horizontal surface at the moment of impact. This caused the expected result that accelerometer readings at one end of the package were slightly higher than readings at the other end. The results for raw and filtered data represent results obtained by averaging the data from the accelerometers at the ends of the package. Raw, filtered, and combined raw and filtered data over the strong response time period are presented.

The filter frequency used for the End Drop and CGOC Drop is 450 Hz. The filter frequency used for the Slap Down and Side Drops was 350 Hz. These filter frequencies were established by examination of the power spectral density function for each raw data trace that clearly showed that the majority of the energy occurred at frequencies well below the cut-off frequency. Independent confirmation of the appropriateness of the cut-off frequencies was made by determining the lowest frequency of elastic vibration of the package acting as either a bar or a simply supported beam. As described above, the sensitivity to cut-off frequency was examined for the end drop case by re-analyzing the data for three cut-off frequencies.

Table ~~2.H~~2.A.2 provides the peak deceleration data culled from the above-mentioned accelograms for the four drop scenarios after filtering to remove high frequency effects. The table contains the results from the actual 1/4-scale experiments scaled up to the full-size packaging. The test report [~~2.H~~2.A.7] provides the detailed information on this final one-quarter scale dynamic drop test series with raw and filtered outputs from all accelerometers. The test report also includes details on the filtering methodology, on the data reduction, and on the evaluation of the performance of the various accelerometers used in each of the tests.

In all of the four final one-quarter scale dynamic drop tests, the impact limiter attachments successfully performed without a single attachment bolt failure (ensuring that the impact limiters did not separate from the overpack), rigid body decelerations were below 60 g's, and the cask body did not contact the unyielding target surface. Also, additional crush margin remained in the aluminum honeycomb material.

Table ~~2.H~~2.A.2: Peak Decelerations from AL-STAR™ Drop Tests (Second Series)

| Test Case | Orientation | Peak Decelerations (g) |
|---|---|---|
| A | End-Drop | 53.9 |
| B | C.G.-over-Corner | 38.8 |
| C | Side Drop | 45.7 |
| D | Slap-Down | 59 |

## ~~2.H~~2.A.6 Phase 5: Numerical Prediction Model for Dynamic Analysis

The numerical prediction model for dynamic drop events utilizes the previously discussed force-crush (F-d) model and incorporates the information into the dynamic equations of equilibrium. Using the procedure discussed previously, the static F-d curves for the AL-STAR impact limiter under the four drop scenarios are readily constructed. Figures ~~2.H~~2.A.6.1 to ~~2.H~~2.A.6.4, respectively, provide the static force vs. crush plots for the full scale impact limiter with test orientations for drop cases A, B, C, and D (primary impact). An appropriate analytical fit for each curve is developed using the commercial graphing package Deltagraph [~~2.H~~2.A.8]. Figures ~~2.H~~2.A.6.1 through ~~2.H~~2.A.6.4 also provide curves for upper and lower bound material strengths.

We now discuss the application of the F-d model to the prediction of impact limiter performance in a dynamic drop environment. In symbolic form, we can write the static resistive (crush) force, F, as a function of the crush depth, $\Delta$, where a zero value for $\Delta$ represents an uncrushed condition.

$$F = f(\Delta)$$

The above symbolic formula represents the data on Figures ~~2.H~~2.A.6.1 to ~~2.H~~2.A.6.4 in analytical form. We have previously explicitly discussed the mathematical concepts underlying the above formulation by referencing the particular case of a side drop. In general, the static F-d curve can be expressed as a sum of local crush pressures multiplied by interface areas where the interface areas may be a function of the current crush. That is, the mathematical relation for static compression (which is validated by comparison to static testing) is also expressible in the form

$$f(\Delta) = \sum_i p_i A_i$$

where $p_i$ are the crush pressures of the materials participating in the crush and $A_i$ are the interface areas associated with the different crush strengths. The determination of the areas $A_i$ as a function of crush depth, $\Delta$, has previously been discussed within the context of interpenetration.

The dynamic model for simulating a packaging drop event consists of solving the classical Newtonian equations of motion. In the case of a unidirectional impact such as an end drop ($\theta$=90°), side drop ($\theta$=0), or CGOC drop, the equation of motion simply reduces to:

$$M \frac{d^2\Delta}{dt^2} = Force + Mg$$

where: M = mass of system undergoing deceleration

$d^2\Delta/dt^2$ = second derivative of package movement (which is equal to the impact limiter crush because the target is immovable and rigid).

The resistive "Force" opposes the downward movement and is given by the static force-crush functional relationship (appropriate for the drop orientation) multiplied by a dynamic multiplier Z. As noted earlier, there is historical evidence that metal honeycomb crush pressure is a linear function of velocity [~~2.H~~2.A.9]. The Holtec correlation of the August 1997 test data by numerical simulation [~~2.H~~2.A.6] also confirmed that the best correlation is achieved if the dynamic multiplier is represented by a linear function of local crush velocity ($d\Delta/dt$). Introducing the dynamic multiplier, the dynamic equation of force equilibrium for a case involving only primary impacts becomes

$$M \frac{d^2\Delta}{dt^2} = ZF + Mg = Zf(\Delta) + Mg$$

The above equation is a second order non-linear differential equation in the time coordinate t, which can be solved for the post-contact event using any standard equation solver package. The initial condition is: @ t = 0, $\Delta = 0$, $d\Delta/dt = V_o$ (approach velocity at impact). We note that since the acceleration is an explicit function of both deformation and velocity, maximum acceleration will not, in general, occur at the instant when the velocity of the package is zero.

If the impact event involves both primary and secondary impacts, as is the case for the slapdown event (indeed any event wherein $\theta<67.5°$), then both the mass M and rotational moment of inertia I are involved. The modeling of a dual impact event is only slightly more involved than the single variable modeling of the single impact case discussed above. Figure ~~2.H~~2.A.6.5 pictorially illustrates the sequence of events leading to an appropriate mathematical model. Figure ~~2.H~~2.A.6.6 provides the appropriate free-body diagrams associated with each portion of the event.

In the first step, the inertia force of the falling package is resisted by the crush force developed at the primary impact location. While the downward momentum of the package is dissipated by the resistive force, the package also experiences the overturning couple produced by the non-co-linearity of the inertia force (which acts at the centroid) and the resistive force which acts at the primary impact zone (Figure ~~2.H~~2.A.6.5(a)). The dynamic equation of force equilibrium is given above in terms of the downward movement of the package centroid and the resistive force static compression curve, modified by the dynamic factor Z, appropriate to the initial orientation at primary impact. The package decelerates and then begins to overturn, in effect pivoting about the initial point of contact in the primary impact region, gathering angular momentum as the second impact limiter (mounted at the far end) approaches the target surface. Referring to Figure ~~2.H~~2.A.6.5(b), the dynamic equation insuring moment equilibrium during the overturning (before the initiation of the secondary impact) phase can be written as

$$I_p \frac{d^2\phi}{dt^2} = -MgR\cos(\phi)$$

where $I_p$: moment of inertia of the package about the pivot point

$\phi$ : angular acceleration with respect to the horizontal plane

R: radial distance of the package C.G. with respect to the pivot point.

The initial conditions for this phase are: t= 0, $\phi = \theta$, $d\phi/dt = 0$ where t is now redefined at the initiation of rotational motion.

Finally, the secondary impact commences wherein the angular momentum of the package plus any linear momentum not dissipated by the primary impact is dissipated by the crushing of the second impact limiter. During the secondary impact phase, the equation of dynamic moment equilibrium can be written by inspection of Figure ~~2.H~~2.A.6.5(c):

$$I_p \frac{d^2\phi}{dt^2} = -MgR\cos(\phi) + Zf(D\phi)D$$

where f(Dϕ) is the static resistive force at the secondary impact location under compression Dϕ, Z is the current dynamic multiplier appropriate to the secondary impact location, D is the moment arm, and $I_p$ is the moment of inertia of the package about the pivot point. During this phase of the motion, the equation of dynamic force equilibrium is modified to reflect dynamic resistive forces from both impact limiters since the entire package may continue to move toward
the target surface with both impact limiters providing a dynamic resistive force. Therefore, during the final phase of the impact event, the dynamic force equilibrium equation can be written as

$$M\frac{d^2\Delta}{dt^2} = Z_1F_1 + Z_2F_2 + Mg$$

where $Z_i$ and $F_1$ (i=1,2) represent the dynamic multiplier and static compression force appropriate to the primary and secondary impact limiter behavior during the final phase of the event. The dynamic multipliers $Z_i$ (i =1,2) reflect the current value of the local crush velocities at each of the limiters.

The above formulation assumes, for simplicity, that the pivot point does not slide during the overturning or secondary impact phases.

It is evident from the foregoing that the impact limiter is essentially simulated by a non-linear spring whose static force-deformation curve is known a' priori (from the F-d model) as a function of the drop orientation. The solution of this rigid body dynamics problem featuring up to two non-linear springs can be determined using any one of several standard software packages available in the public domain. Holtec International utilizes the commercial package WORKING MODEL [~~2.H~~2.A.10], which has been validated in the company's QA system for this purpose.

The dynamic simulation model, constructed in the manner of the foregoing, was utilized to simulate all seven one-quarter scale drop events (three in the first series, four in the second series). In order to develop a high level of confidence, it was decided that the model should be validated at all three levels, namely, a comparison of acceleration, crush, and duration of impact. In other words, to be acceptable, the numerical prediction model must predict $\alpha_{max}$, maximum crush sustained $d_{max}$, and the duration of impact, with reasonable accuracy. Since the actual crush $d_{max}$ could be measured, and the duration of

impact and $\alpha_{max}$ were available from accelerometer data, comparison between theory and experiment with respect to all three key indicators was possible. Tables ~~2.H~~2.A.3 and ~~2.H~~2.A.4 provide the results in a concise form for all of the one-quarter scale dynamic drop tests for the first and second series, respectively.

Note that in the tables, the comparison is made after scaling up the model results to reflect a full-scale package.

Table ~~2.H~~2.A.3: Comparison Between Test Data and Prediction Model Results (First Test Series)

| | Deceleration (g's) | | Total Crush Depth (inch) | | Impact Duration (milli-seconds) | |
|---|---|---|---|---|---|---|
| Case I.D. | Predicted | Measured | Predicted | Measured | Predicted | Measured |
| A. End-Drop | 134.2 | 134.0 | 2.42 | 2.42 | 3.5 | Not measured |
| B. C.G.O.C. | 37.8 | 37.84 | 16 | 16 | 13.25 | 16.6 |
| C. Side Drop | 50.5 | 51.3 | 9.1 | 9.51 | 8.25 | 10.74 |

Table ~~2.H~~2.A.4: Comparison Between Test Data and Prediction Model Results (Second Test Series)

| | Deceleration (g's) | | Total Crush Depth (inch) | | | Impact Duration (milli-seconds) | |
|---|---|---|---|---|---|---|---|
| Case I.D. | Predicted | Measured | Predicted | Measured | Max. Available | Predicted | Measured |
| A. End Drop | 53.0 | 53.9 | 11.3 | 10.6 | 17.659 | 38.8 | 37.2 |
| B. C.G.-Over-Corner | 38.7 | 38.8 | 12* | 9.82* | 25.06 | 51.0 | 61/45.2 |
| C. Side Drop | 43.5 | 45.7 | 10.9 | 12.5 | 16 | 38.5 | 53.1 (averaged value) |
| D. Slap-Down | | | | | | | |
| Primary | 46.4 | 49.0 | 9.50 | 10.7 | 16 | 48.5 | 44.4 |
| Secondary | 59.9 | 59.0 | 12.8 | 13.5 | 16 | 35.8 | 41.2 |

* For C.G.-Over-Corner, only crush at the external interface is measured.

It is evident from both Tables ~~2.H~~2.A.3 and ~~2.H~~2.A.4 that the numerical prediction model is robust in predicting all seven impact tests. Not only are peak values of $\alpha_{max}$ for each test predicted with good agreement, but also the crush depth and impact duration is also reliably simulated.

A perusal of the numerical results in Table ~~2.H~~2.A.4 yields two additional insights into the behavior of AL-STAR which are most helpful in the "fine tuning" of the full-scale AL-STAR design:

i. The maximum deceleration, $\alpha_{max}$, predicted as well as measured, under the most limiting scenario (slapdown), is close to the permissible limit of 60g's.

ii. The maximum crush, predicted as well as measured, in all drop scenarios, is well below the available limit (i.e., the value at which the crush material will "lock up").

The state-of-the-art manufacturing technology for aluminum honeycombs permits the material to be manufactured within a total tolerance range of 12 to 13% (between the maximum and minimum values). The above observations suggest that the upper and lower bound range of crush pressures for the honeycomb material in the AL-STAR impact limiter should be set at 95% and 82% of the values of honeycomb material used in the second series quarter-scale tests.

Finally, the agreement between the predictions and measured data in the above correlation effort fosters a high level of confidence in the numerical model, which can now be used to conduct sensitivity studies.

### ~~2.H~~2.A.7 Phase 6: Simulation of the Effects of Material Crush Strength Variation, Package Mass Tolerances, and Oblique Drop Orientations

Having ensured the technical reliability of the numerical prediction model, it is now necessary to evaluate the system behavior under all "limiting conditions". As noted earlier, the impact limiter materials are insensitive to environmental temperature changes within the limits of –20° F and 100° F. Therefore, limiting conditions are broadly defined here as arising from two sources:

i. Variation in the impact limiter honeycomb crush strength due to material manufacturing tolerance.

ii. Variation in the package weight (due to different MPC types that may be transported in the HI-STAR 100 overpack, and manufacturing tolerances in fabrication of the overpack and impact limiters).

iii Variation in package angle of impact with the target.

To examine all limiting scenarios, additional simulations using the mathematical model were performed. The crush strength of the honeycomb material was varied within the range permitted in the Holtec Drawing 1765. The packaging weight was set at its upper bound and lower bound value (upper bound weight is 280,000 lb., and lower bound weight is 270,000 lb. based on values listed in Table 2.2.1). Three additional drop orientations (30 degree, 45 degree, and 60 degree orientation angle, measured from the horizontal) that were not the subject of tests were also analyzed numerically using input crush strength data that would maximize the decelerations with an average weight. The purpose of these additional simulations with varied drop angle is to ascertain which, if any, oblique drop orientation merits detailed finite element stress analysis to meet the requirements of the Regulatory Guide. Figures

~~2.H~~2.A.7.1-~~2.H~~2.A.7.3 provide the static crush force vs. crush depth information used in the dynamic simulation of these accident events. Table ~~2.H~~2.A.5 provides key output data, peak decelerations and maximum crush, as obtained from these numerical simulations.

Table ~~2.H~~2.A.5: Sensitivity of Package Response to Package Weight, Crush Material Strength Variations, and Package Orientation at Impact

| Orientation | Case | Deceleration (g's) | Maximum Total Crush (2-interfaces) (inch) | Available Crush Stroke (inch) |
|---|---|---|---|---|
| End Drop | Max. Strength, Min. Weight | 52.85 | 11.4 | 17.659 |
| | Min. Strength, Max. Weight | 46.3 | 12.8 | 17.659 |
| C.G. Over Corner | Max. Strength, Min. Weight | 38.25 | 17.0 | 25.06 |
| | Min. Strength, Max. Weight | 35.6 | 18.5 | 25.06 |
| Side Drop | Max. Strength, Min. Weight | 42.5 | 11.2 | 16 |
| | Min. Strength, Max. Weight | 37.5 | 12.7 | 16 |
| Slap Down (secondary impact bounds) | Max. Strength, Min. Weight | 58.5 | 13.2 | 16 |
| | Min. Strength, Max. Weight | 52.6 | 15.1 | 16 |
| Oblique Drop – 30 degrees | Max. Strength, Min. Weight | 36.44 | 19.57 | 24.1 |
| Oblique Drop – 45 degrees | Max. Strength, Min. Weight | 35.62 | 22.39 | 25.72 |
| Oblique Drop – 60 degrees | Max. Strength, Min. Weight | 38.01 | 19.2 | 25.65 |

The following conclusions are readily derived from Table ~~2.H~~2.A.5 results:

i. The maximum value of $\alpha_{max}$ is less than 60g's in all cases.

ii. The total crush of the impact limiter is below the available "stroke", i.e., the overpack body will not contact the unyielding target surface nor will any "lock-up" of the crush material occur.

iii. The three oblique drop simulations considered all produce approximately the same vertical deceleration from the primary impact. The decelerations resulting from the subsequent secondary impact, after rotation of the HI-STAR 100, are all below the value obtained from the simulation of the "slapdown" at low angles of impact. If the "limiting" oblique drop is considered as the simulation providing maximum deceleration perpendicular to the longitudinal axis of the cask, then the drop most likely to develop the largest bending of the overpack in the oblique orientation is at 30 degree orientation (from the horizontal axis). Therefore, this case is subjected to detailed stress analysis in Section 2.7 with the applied impact loading (along and perpendicular to the cask axis) balanced solely by the cask inertia forces and moments.

In conclusion, the above work provides full confidence that the HI-STAR 100 packaging will perform in the manner set forth in the NRC regulations (10CFR71.73) under all conceivable hypothetical accident conditions of transport.

### ~~2.H~~2.A.8 One-Foot Drop

Paragraph 2.6 of Reg. Guide 7.8 requires evaluation of the package response under a one-foot drop onto a flat unyielding surface in a position that is expected to inflict maximum damage.

Using the prediction model, the maximum deceleration sustained by the package under the one-foot end and side drop scenarios, the latter expected to produce maximum stress in the fuel basket, was computed. Table ~~2.H~~2.A.6 provides summary results for the limiting case of minimum package weight and upper bound material crush strength (so as to maximize the decelerations).

Table ~~2.H~~2.A.6: Peak Decelerations Under One-Foot Drop Event

| Scenario | Max. Deceleration in g's | Crush (inch) | Duration of Impact (milli-seconds) |
|---|---|---|---|
| 90° End Drop | 17.25 | 0.85 | 20.0 |
| 0° Side Drop | 11.45 | 1.33 | 26.0 |

## ~~2.H~~2.A.9 Equivalent Dynamic Factor (EDF)

It is instructive to compute an effective equivalent dynamic factor on the predicted static crush force corresponding to the instant of maximum deceleration during the drop event. Table ~~2.H~~2.A.7 presents the pseudo-deceleration (obtained by dividing the static force by the mass of the package) and the predicted deceleration; the ratio of the two is the "equivalent dynamic factor
equal to the peak dynamic crush force divided by the static resistance force at the coincident instance of crush when the dynamic crush force is maximized. Note that the differences in package weight used in the table below reflect the actual weight of the impact limiters used in each one-quarter scale drop test (after increasing to full-scale equivalent values).

Table ~~2.H~~2.A.7: Equivalent Dynamic Factor (EDF) for Different Drop Scenarios

| | Predicted Force (lbs) x $10^{-7}$ | | | Predicted Max. Deceleration | | |
|---|---|---|---|---|---|---|
| Scenario | Static | Dynamic | Participating Package Weight (lbs) | Pseudo-Accn (static) | Dynamic (from Table ~~2.H~~2.A.4) | EDF |
| | | | | | | |
| End Drop | 1.0785 | 1.454 | 274,336 | 39.313 | 53 | 1.348 |
| CGOC Drop | 0.8 | 1.059 | 273,680 | 29.231 | 38.7 | 1.324 |
| Side Drop | 0.4 | 0.597 | 137,270* | 29.14 | 43.5 | 1.493 |
| Slapdown | 0.345 | 0.6607 | † | † | 59.9 | 1.915 |

* Only half of the total package weight participates at each impact limiter.

† Indeterminate for this drop configuration.

The last column of the above table demonstrates that the EDF, as defined above, is not a constant value independent of drop orientation.

## ~~2.H~~2.A.10 Additional 1/8th Scale Static Tests

Three additional static crush tests on 1/8th scale impact limiters have been performed subsequent to the completion of all quarter-scale dynamic testing and theoretical correlation. The F-d test results for each of three impact limiter orientations are compared with the analytical F-d predictions in Figures ~~2.H~~2.A.10.1-~~2.H~~2.A.10.3. Figure ~~2.H~~2.A.10.1 compares test results with theoretical prediction for the crush orientation corresponding to a side impact, Figure ~~2.H~~2.A.10.2 presents the results for the Center-of-Gravity-Over-Corner impact orientation, and Figure ~~2.H~~2.A.10.3 presents results for the end impact orientation. In all tests, the crush material orientation and location duplicated the final

configurations subjected to quarter-scale tests. The internal backbone structure was also faithfully reproduced. The welds were also scaled to the extent practical given the thin material gages used for the one-eighth-scale model. In the three figures, the solid line without symbols represents the predictions of the theory developed for the F-d curves, while filled circles represent test results. Within the range tested for each orientation, good agreement is observed between theory and test for the side and CGOC crush orientation. For the end drop orientation, however, the tested results suggest that inclusion of some elastic behavior at the cask-impact limiter interface into the theory might improve the static correlation. The dynamic test results presented in Table ~~2.H~~2.A.4, however, demonstrate conclusively that the prediction of peak deceleration, extent of crush, and impact duration would not be affected by these elastic effects that "smooth" the abrupt "staircase" shape of the F-d curve.

### ~~2.H~~2.A.11 Conclusions

The AL-STAR impact limiter design was subjected to a series of static and dynamic tests to validate its functional performance. The 1/8 model static tests conducted under cold and hot, as well as ambient conditions, confirmed that AL-STAR's functional characteristics are independent of the environmental temperature conditions in the range specified in 10CFR71.73. The successful static tests on the 1/8 scale model (namely, end test and 60° oblique test) also correlated well with the theoretical force-crush model developed by Holtec. Subsequent static tests, performed after the final successful one-quarter scale dynamic tests, provided additional confirmation of the validity of the fundamental F-d model.

The static compression tests were followed by quarter-scale drop tests. The first series, in August 1997, consisting of three tests, provided the necessary test data to determine the dynamic multiplier applicable to the honeycomb materials. The numerical model for simulating the dynamic crushing of AL-STAR showed good agreement with the first test series data when the correct dynamic factor was incorporated in the computer model (Table ~~2.H~~2.A.3).

While the prediction model for simulating AL-STAR crushing under 9-meter drop conditions was extremely well correlated, the peak deceleration under the end- drop condition in the August 1997 tests exceeded the acceptance criteria.

The second series of tests wherein the crush strength of the honeycomb was lowered (as selected by the prediction model), performed as expected. The agreement between the test data and the prediction model is high (Table ~~2.H~~2.A.4).

The prediction model for AL-STAR therefore stands correlated with seven (7) quarter-scale drop events. The first three tests used different honeycomb crush strength materials than the last four, proving the ability of the prediction model to predict the AL-STAR crush performance for a wide range of crush material properties. The backbone structure of AL-STAR, enhanced after the 1/8-model static compression tests, performed as designed in all seven quarter-scale drop tests.

Finally, the AL-STAR-to-overpack attachment system remained intact and the cask did not contact the unyielding target during all four final dynamic tests.

## ~~2.H~~2.A.12 References


[~~2.H~~2.A.1] ANSYS 5.3 Ansys Inc., 1996.

[~~2.H~~2.A.2] CADKEY, Version 7, 1996.

[~~2.H~~2.A.3]~~*~~ Project Procedure No. HPP-5014-5, HI-STAR Aluminum Honeycomb 1/8 Scale Impact Limiter Static Test Procedure.

[~~2.H~~2.A.4]~~*~~ HI-STAR 1/8 Scale Impact Limiter Test Report, HI-961501, Holtec International, June 1996.

[~~2.H~~2.A.5]~~*~~ Holtec Report HI-971774, Impact Limiter Test Results – 30' Drop Tests – August 1997

[~~2.H~~2.A.6]~~*~~ Holtec Report HI-971783, Improved Correlation of ORNL 30' Drop Tests August 1997

[~~2.H~~2.A.7]~~*~~ Holtec Report HI-981891, "Impact Limiter Test Report - Second Series", (Rev. 1), 1998.

[~~2.H~~2.A.8] Deltagraph Pro 3.5, Deltapoint Software, 1995.

[~~2.H~~2.A.9] J.M. Lewallen and E.A. Ripperger, Energy Dissipating Characteristics of Trussgrid Aluminum Honeycomb, SMRL RM-5, University of Texas Structural Mechanics Research Laboratory, 1962.

[~~2.H~~2.A.10] Working Model 3.0, Knowledge Revolution, 1995.

[~~2.H~~2.A.11] HI-STAR 100 Impact Limiter Test Program, Holtec Report No. HI-951278.


~~* These proprietary documents have been previously docketed on Docket No. 71-9261.~~

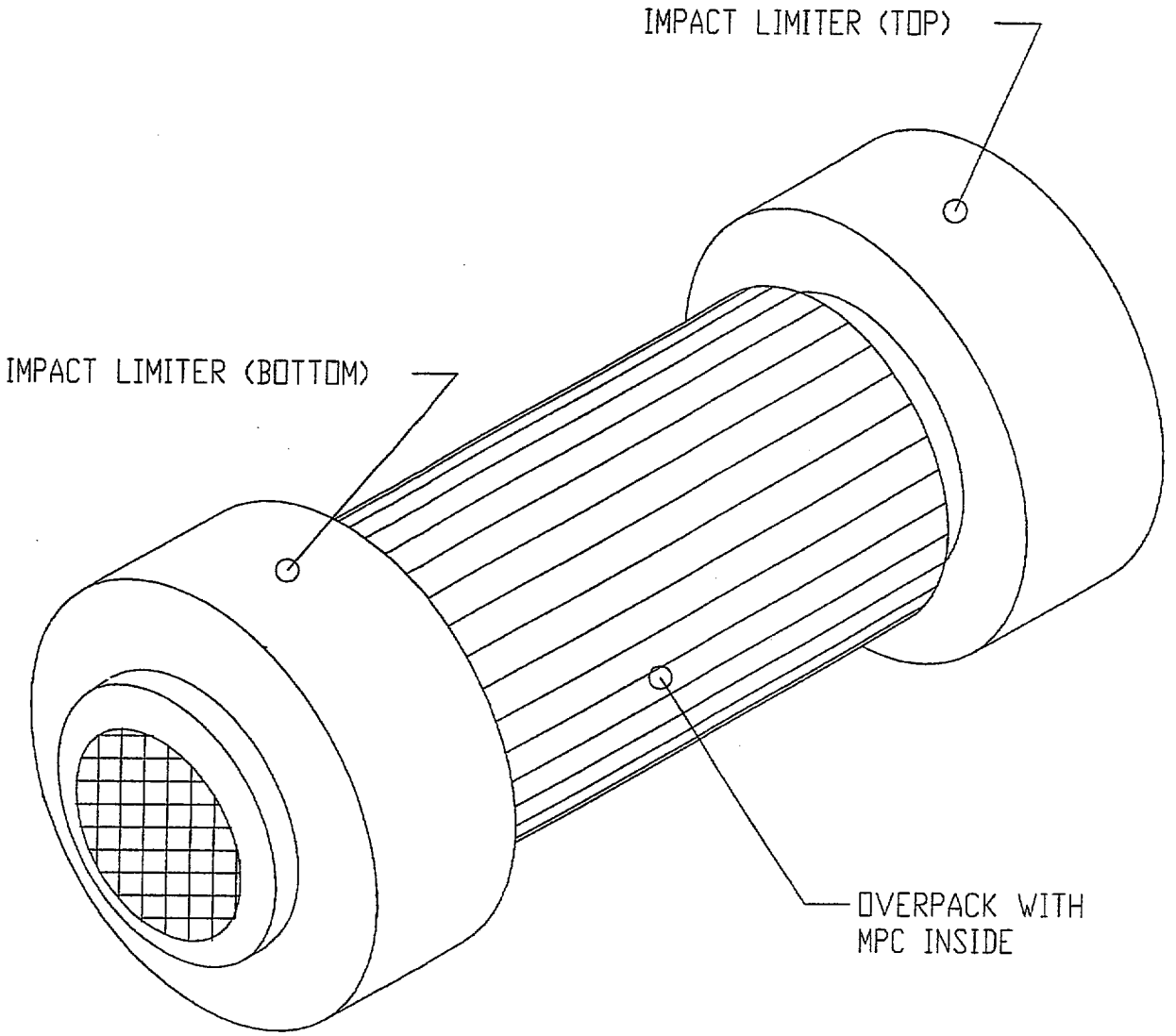


FIGURE 2.A.1.1; HI-STAR 100 PACKAGE WITH TOP AND BOTTOM IMPACT LIMITERS

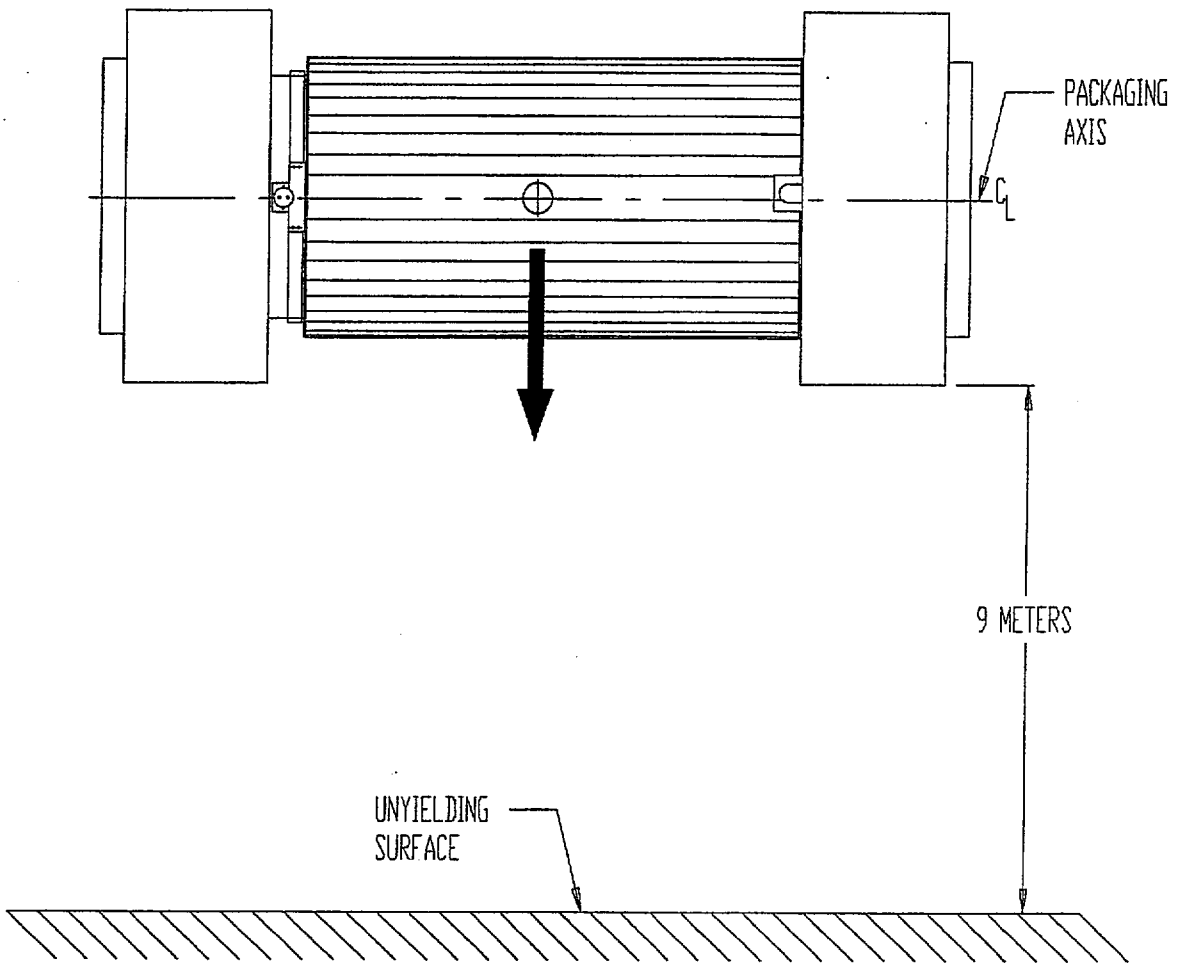


FIGURE 2.A.1.2; DROP FROM 9 METERS ON TO AN ESSENTIALLY UNYIELDING SURFACE (HYPOTHETICAL ACCIDENT CONDITION)

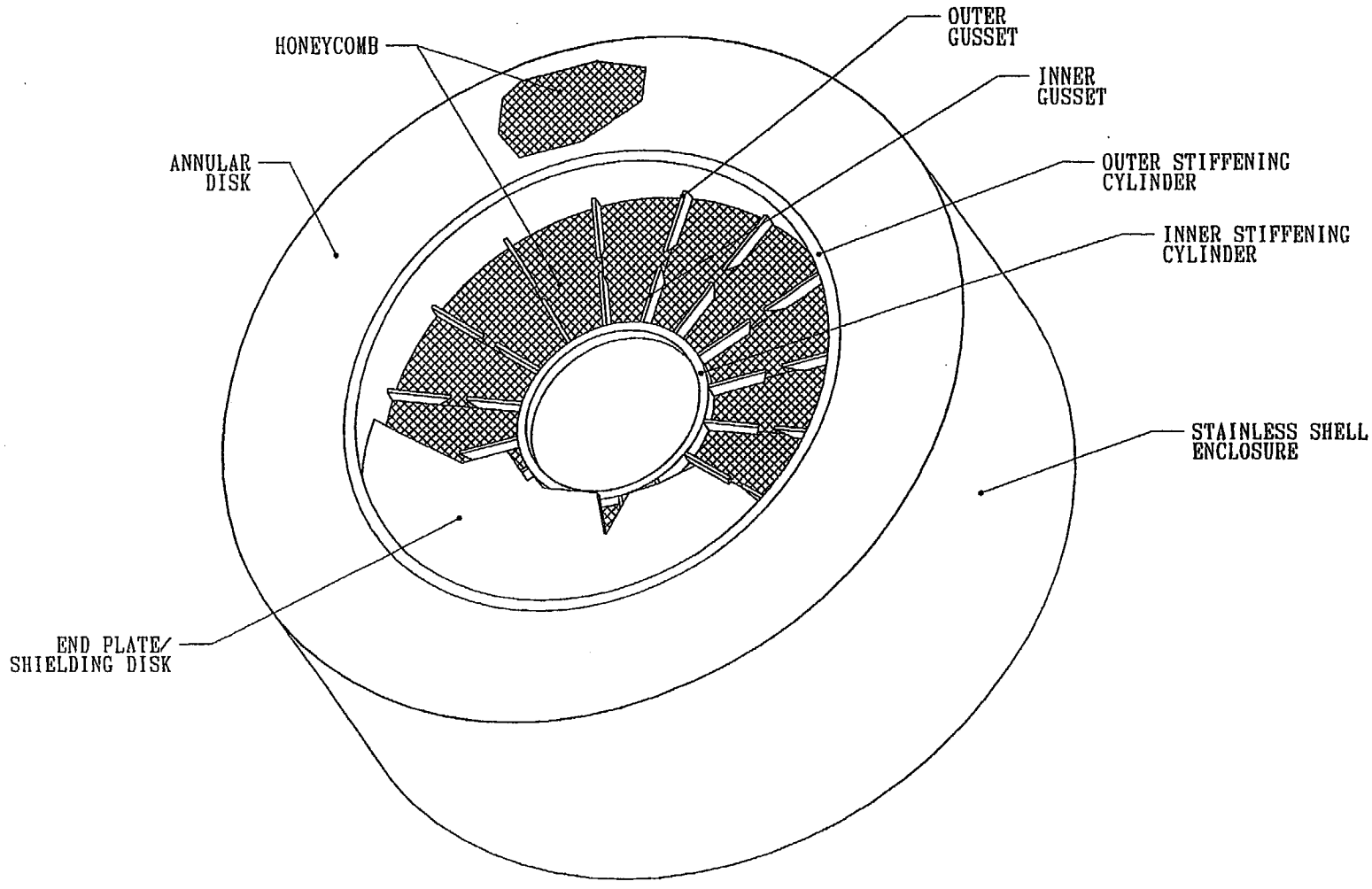


FIGURE 2.A.1.3; PICTORIAL VIEW OF AL-STAR (WITH A PORTION REMOVED)

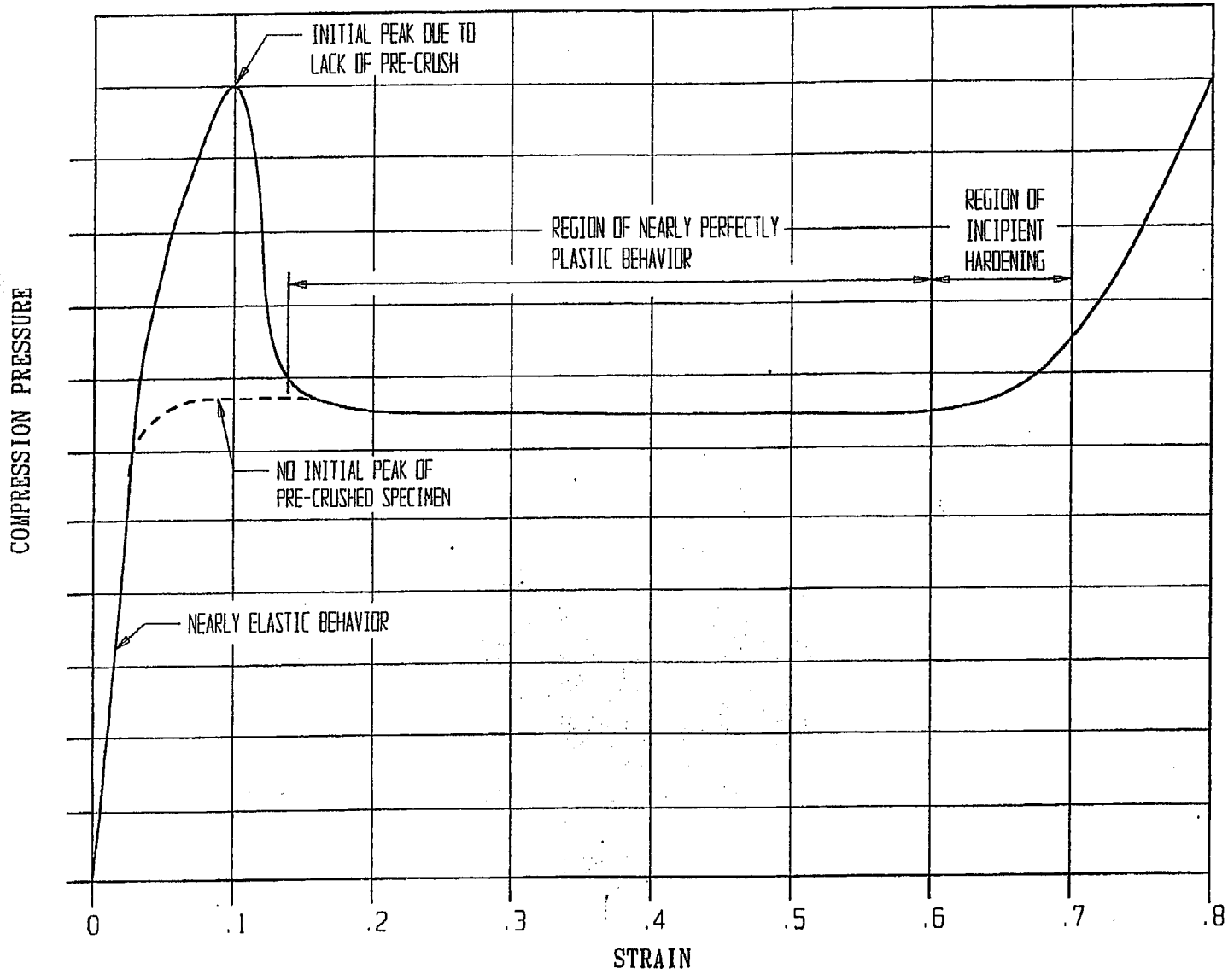


FIGURE 2.A.2.1; PRESSURE-CRUSH STRAIN CURVE (STATIC TESTING)

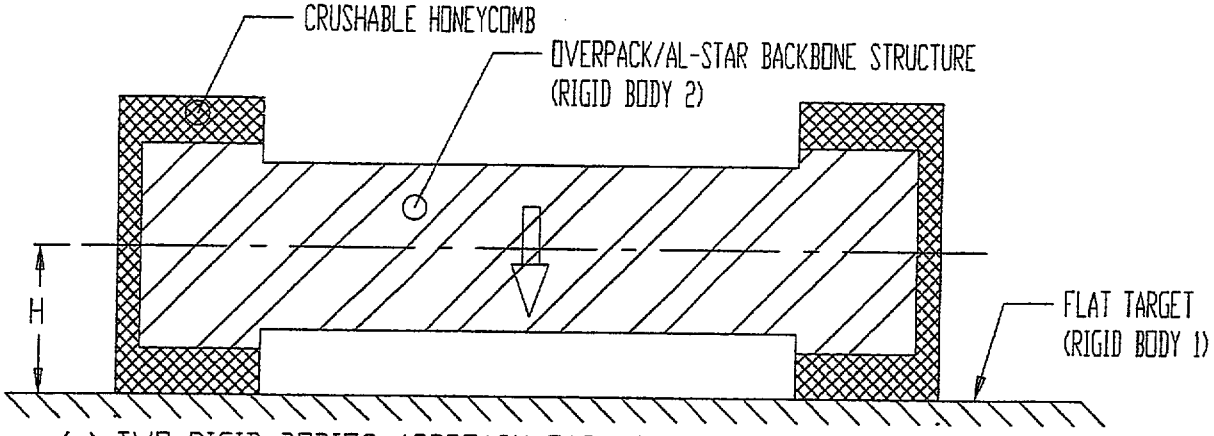


(a) TWO RIGID BODIES APPROACH EACH OTHER WITH A SOFT CRUSHABLE METAL MASS BETWEEN THEM (INITIATION OF CRUSHING)

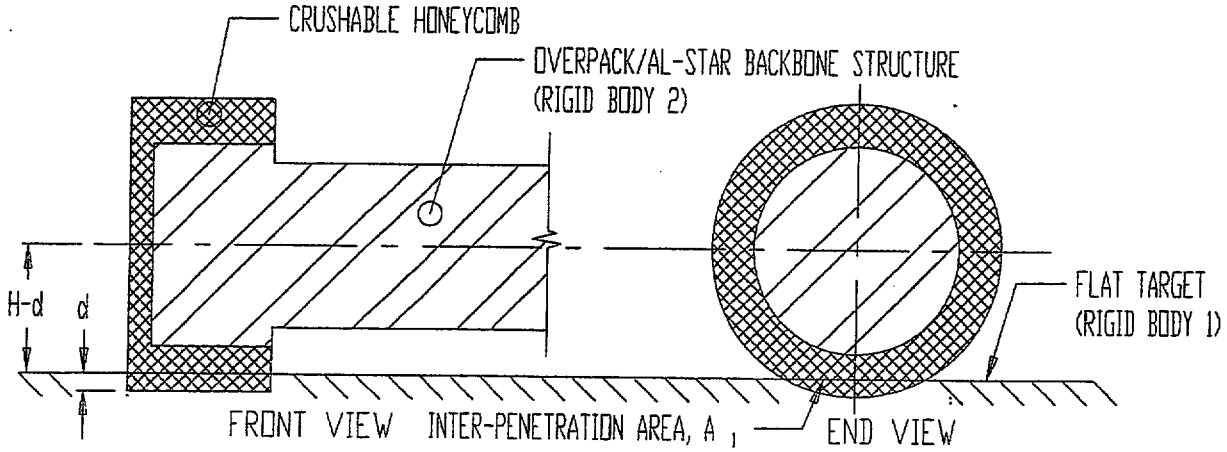


(b) SCENARIO ONE: CRUSHING OCCURS AT THE AL-STAR/TARGET INTERFACE; DEFORMATION = d; NO CRUSH AT AL-STAR BACKBONE/HONEYCOMB INTERFACE

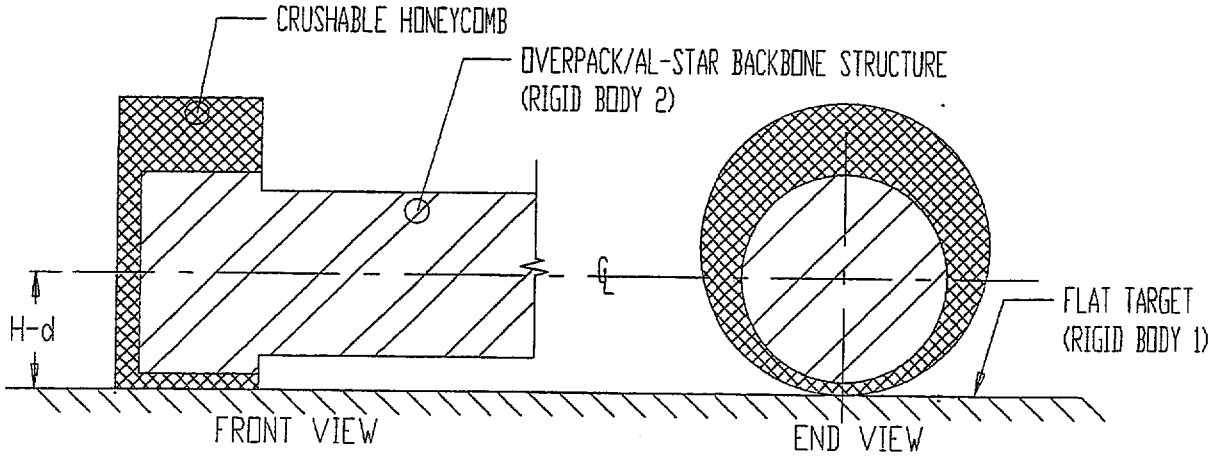


(c) SCENARIO TWO: CRUSHING OCCURS AT THE AL-STAR BACKBONE/HONEYCOMB INTERFACE.; NO CRUSH AT THE AL-STAR/TARGET INTERFACE

FIGURE 2.A.3.1; ILLUSTRATION OF THE FORCE-CRUSH MODEL CONSTRUCTION USING THE EXAMPLE OF THE SIDE DROP EVENT.

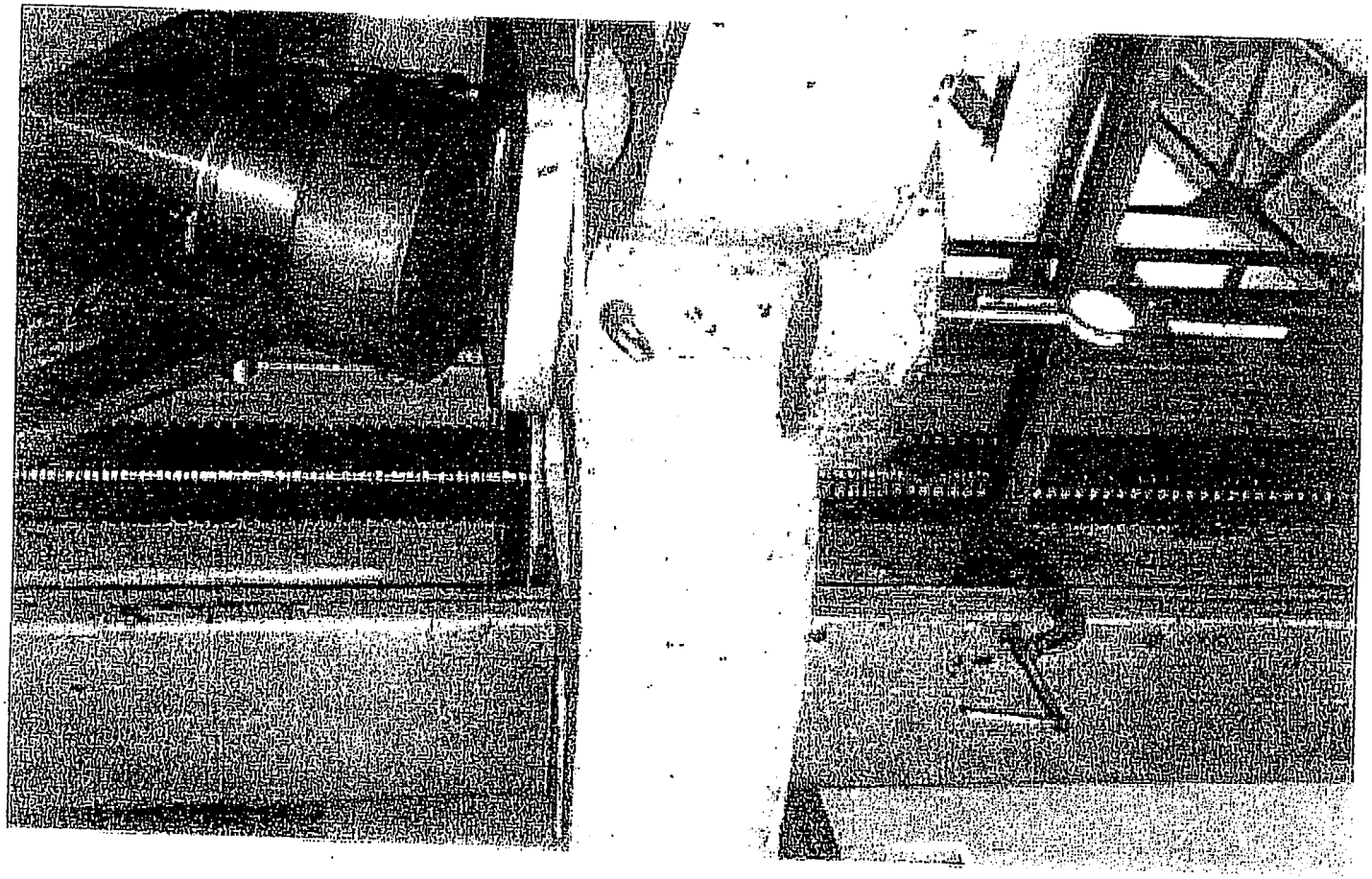

FIGURE 2.A.4.1 ; **TEST FIXTURE**

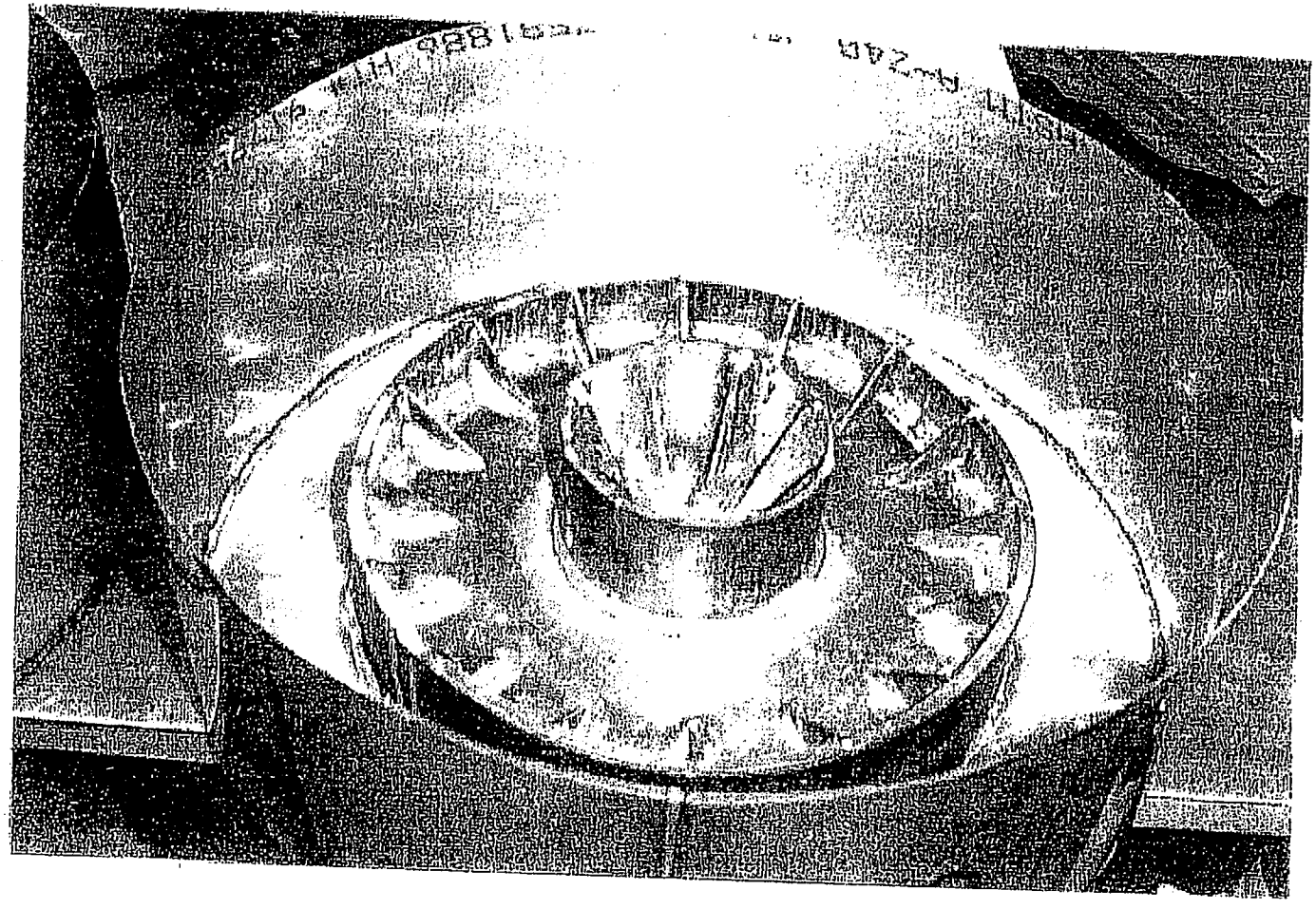

FIGURE 2.A.4.2 ; INTERNAL STIFFENING STRUCTURE IN 1/8 SCALE MODEL

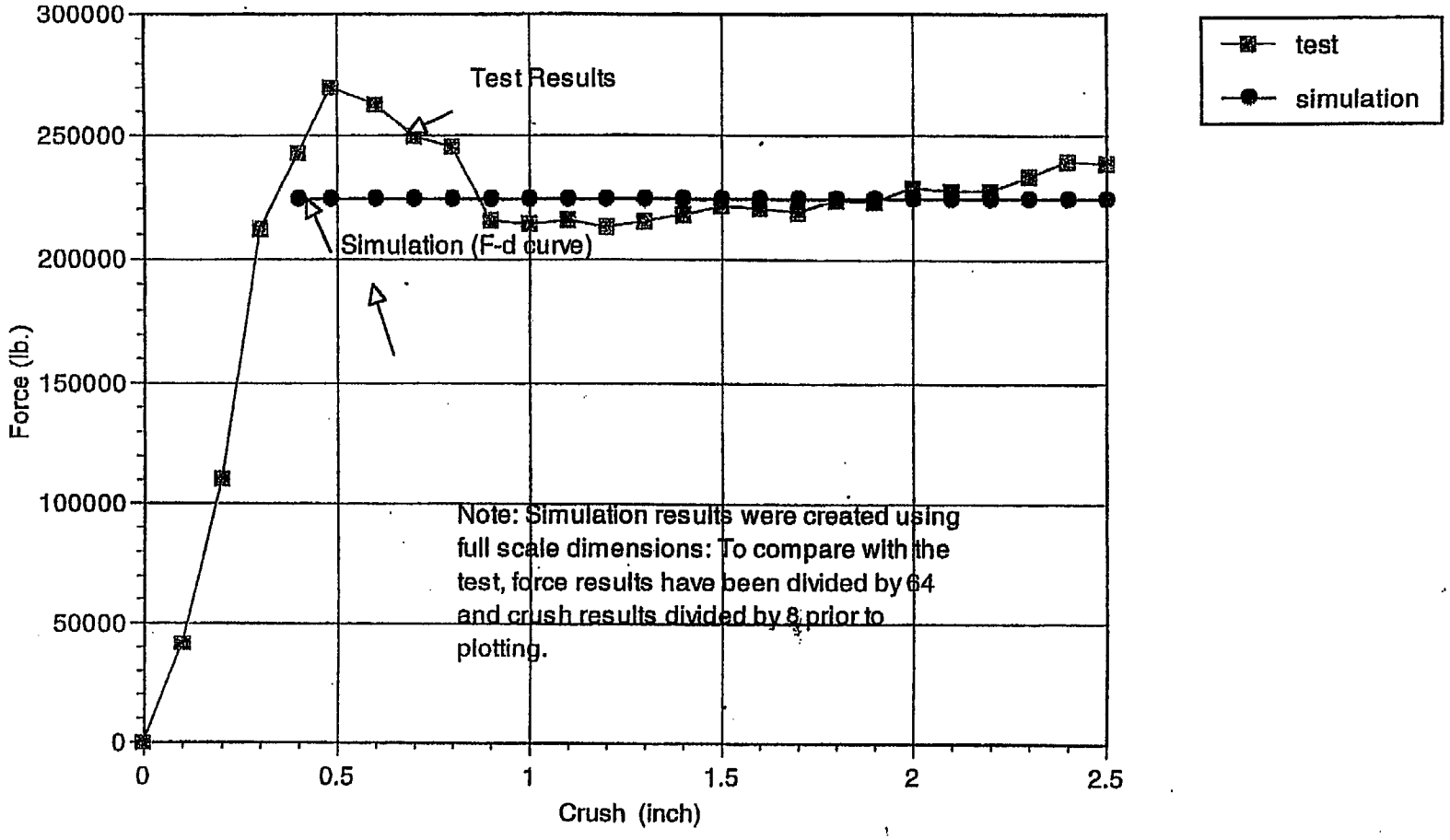


FIGURE 2.A.4.3 - 1/8th Scale Initial Impact Limiter Configuration - Comparison of Static Force-Crush Data from Test and Simulation - END DROP

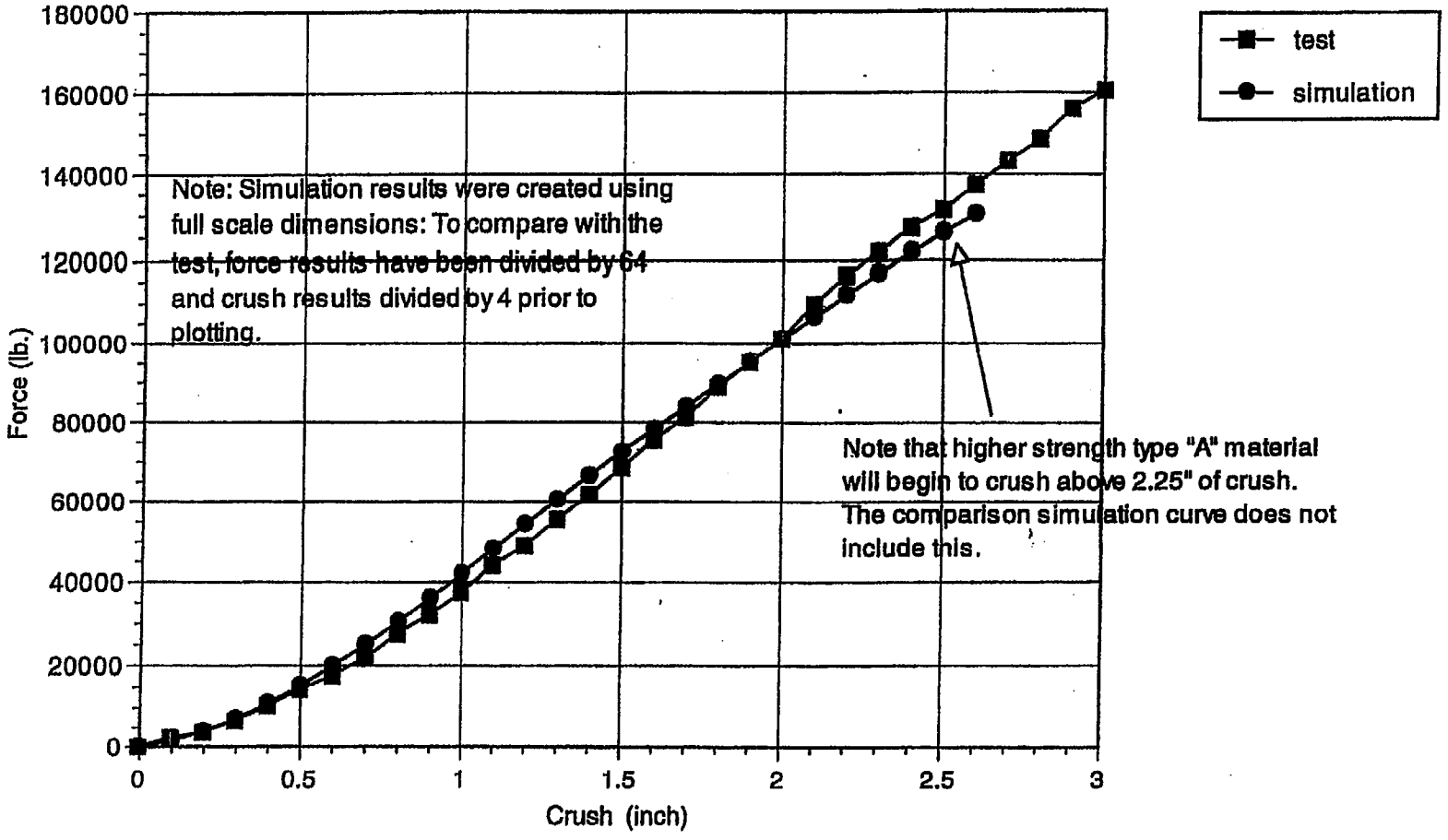


FIGURE 2.A.4.4 : 1/8th Scale Initial Impact Limiter Configuration - Comparison of Static Force-Crush Data from Test and Simulation - 60 DEGREE CRUSH

FIGURE WITHHELD AS SENSITIVE
UNCLASSIFIED INFORMATION

FIGURE 2.A.5.1: QUARTER SCALE MODEL OF LOADED MPC FOR
QUARTER SCALE DROP TEST EXPERIMENT

# FIGURE WITHHELD AS SENSITIVE UNCLASSIFIED INFORMATION

FIGURE **2,A,5,** OVERPACK QUARTER SCALE MODEL (CROSS SECTION VIEW)

# FIGURE WITHHELD AS SENSITIVE UNCLASSIFIED INFORMATION

FIGURE 2.A.5.3; OVERPACK QUARTER SCALE MODEL (TOP VIEW)

# FIGURE WITHHELD AS SENSITIVE UNCLASSIFIED INFORMATION

FIGURE **2,A-5,4j** OVERPACK QUARTER SCALE MODEL (BOTTOM VIEW)

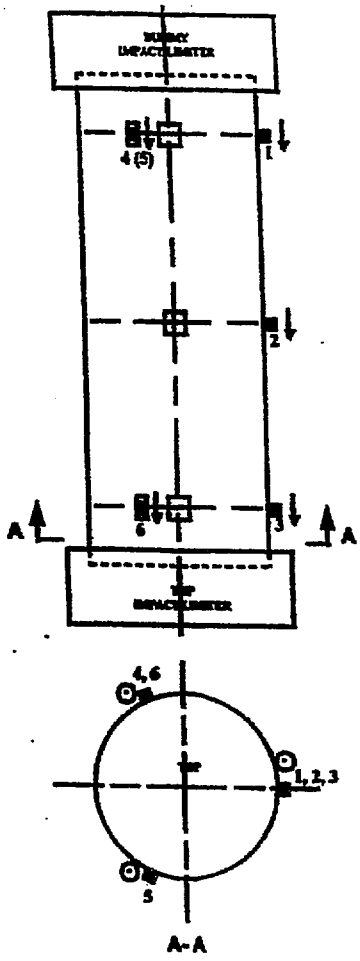


**(a) Accelerometer Location - Top End Drop**

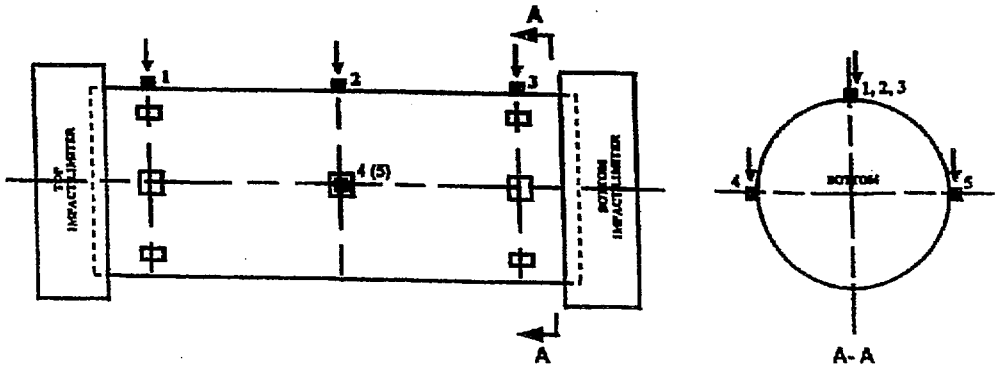


FIGURE 2.A.5.5 ; ACCELEROMETER LOCATIONS FOR END AND SIDE DROPS

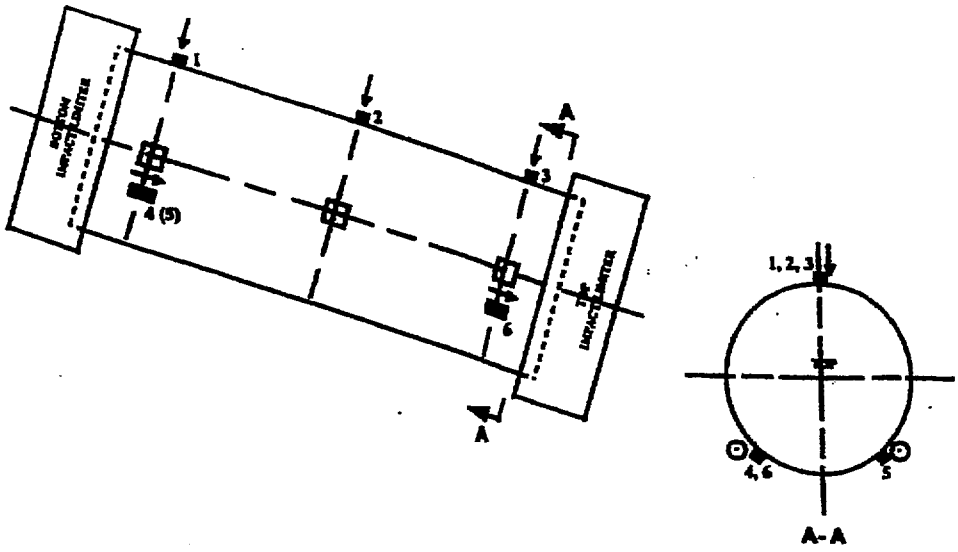


(c) Accelerometer Location - Slap Down Drop

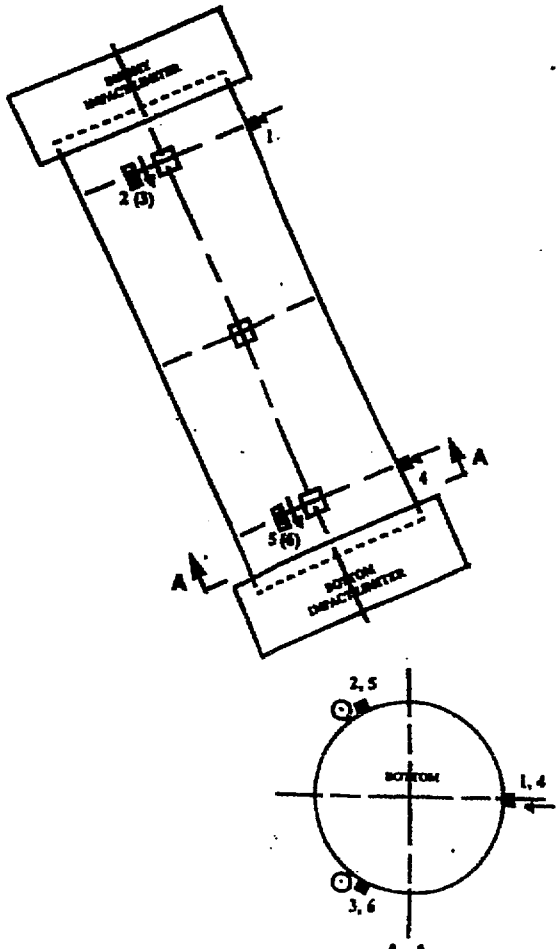




FIGURE 2A.5.6 ; ACCELEROMETER LOCATIONS FOR SLAP DOWN AND CG0C DROP!

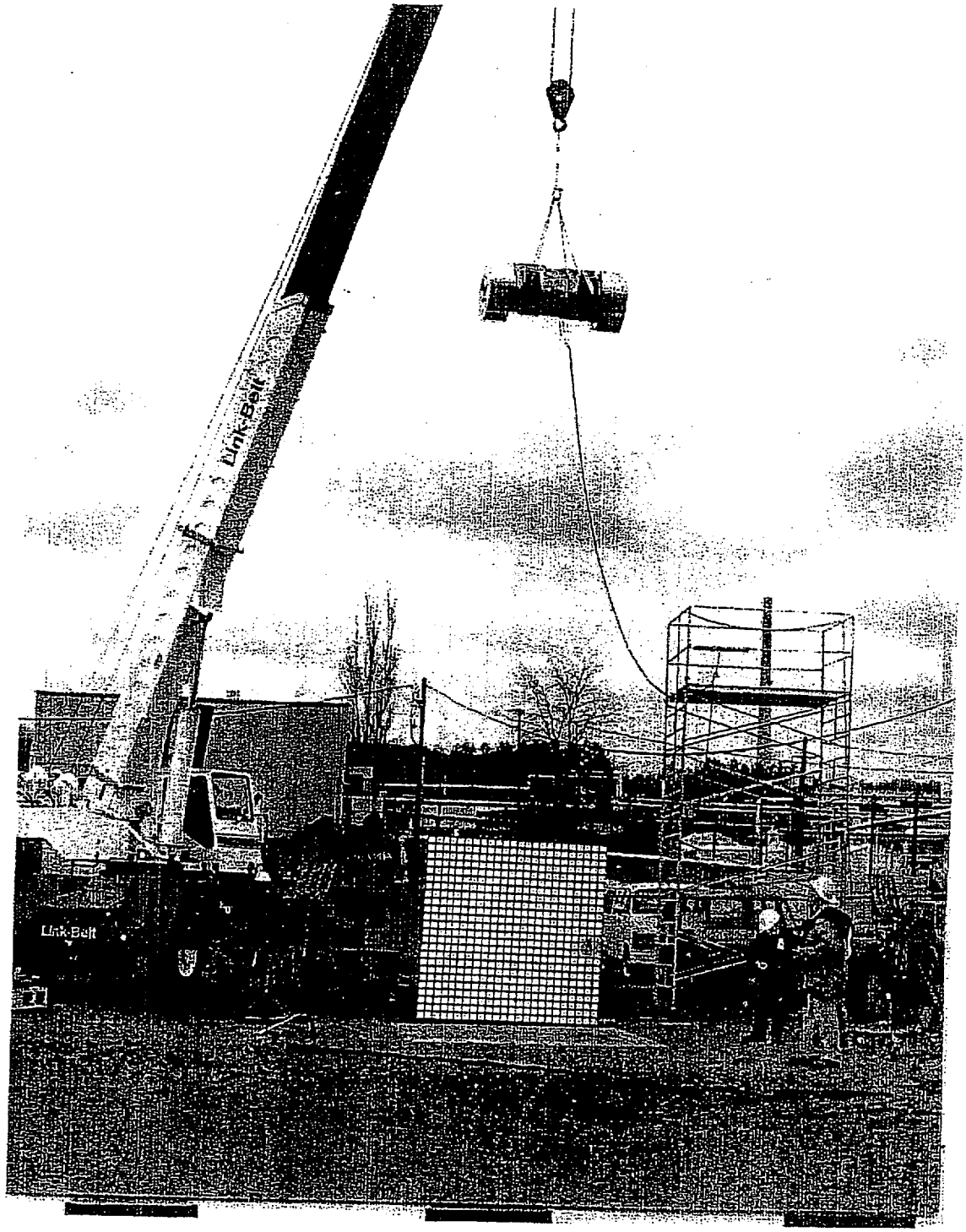


FIGURE 2.A.5.7 : ¼ SCALE HI-STAR 100 PACKAGING
AT 30 FT (9 M) PRIOR TO SIDE DROP

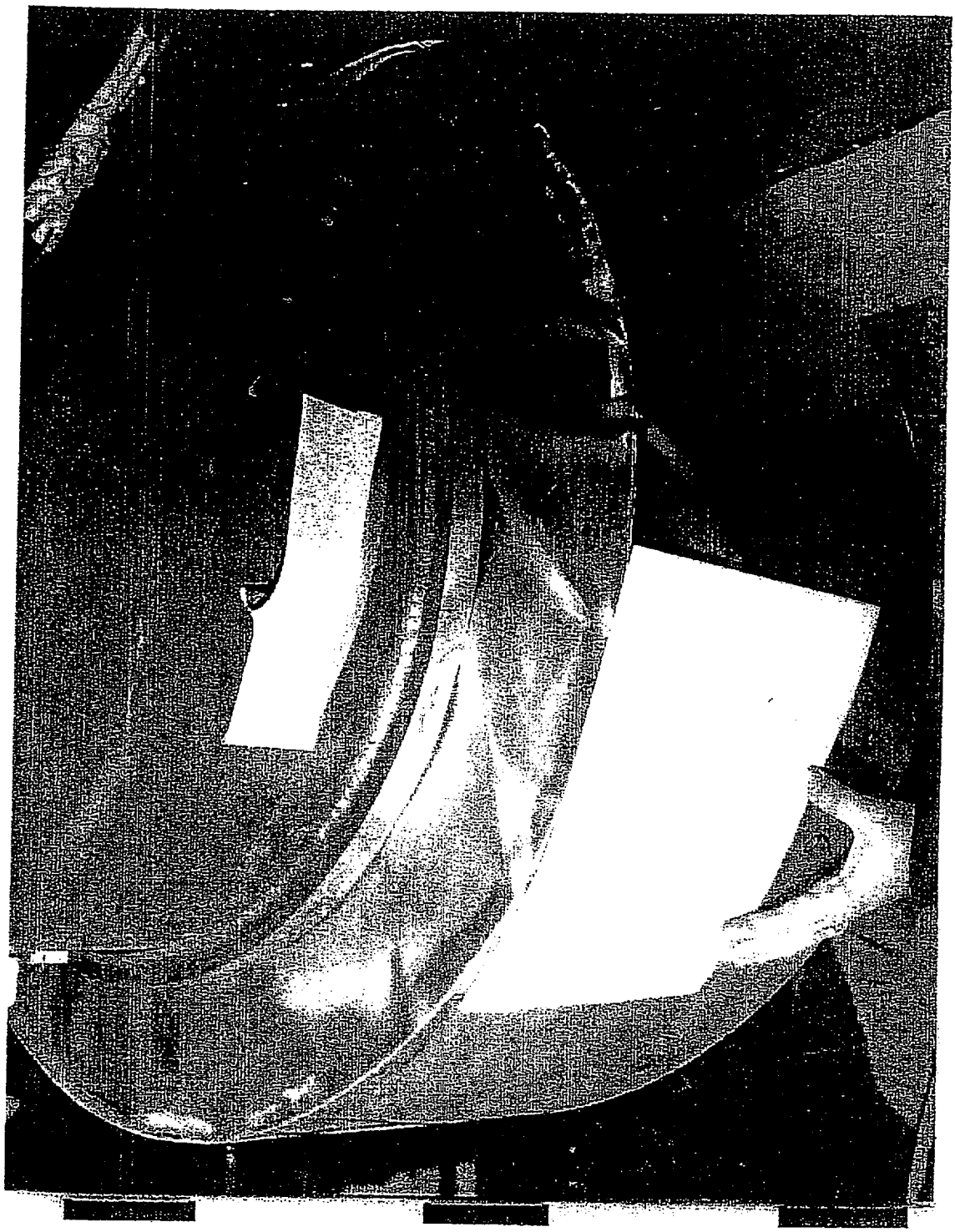

FIGURE 2.A.5.8 ; ¼ SCALE BOTTOM IMPACT LIMITER AFTER SIDE DROP

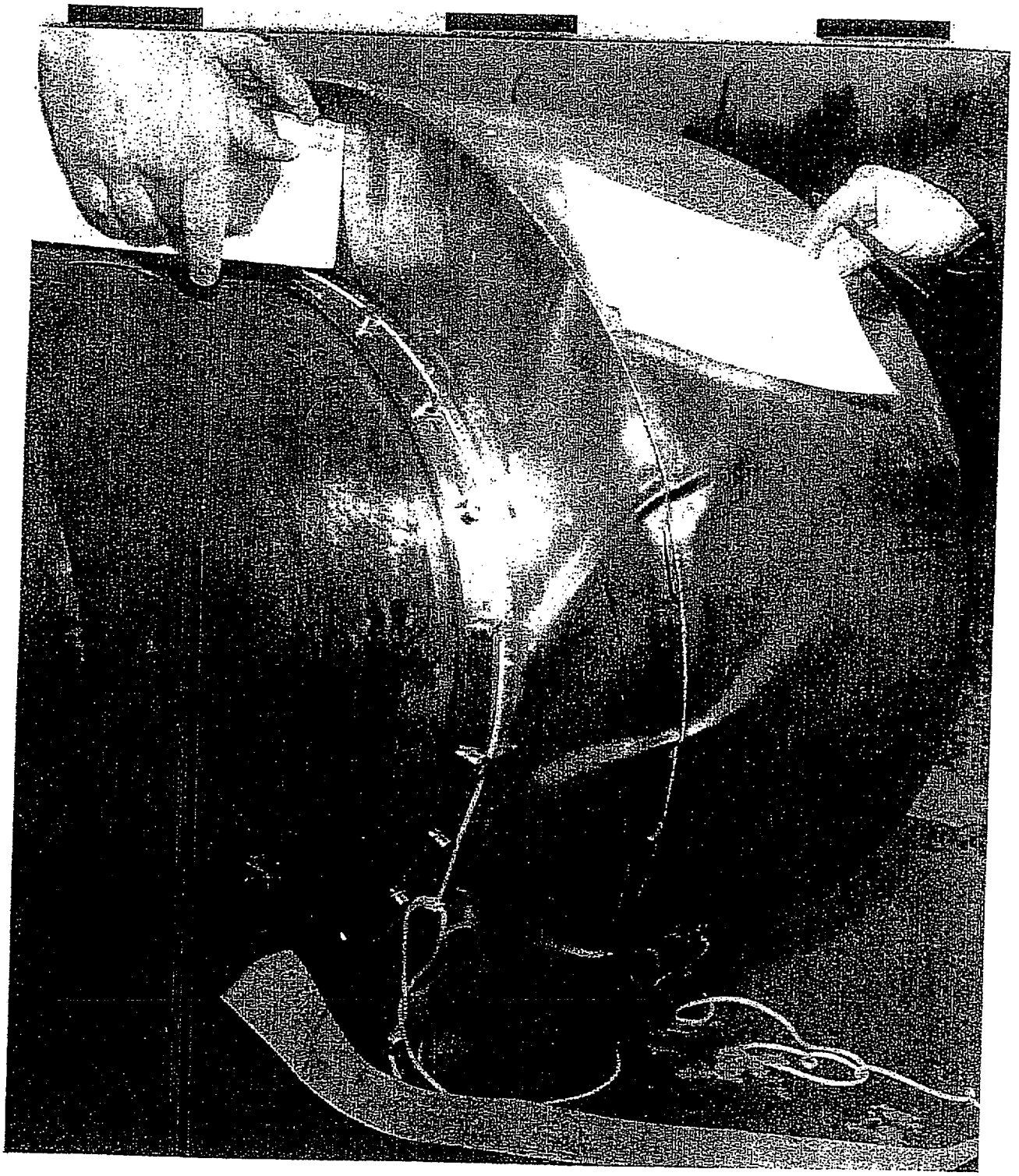

**FIGURE 2.A.5.9 :** 1/4 SCALE TOP IMPACT LIMITER AFTER SIDE DROP

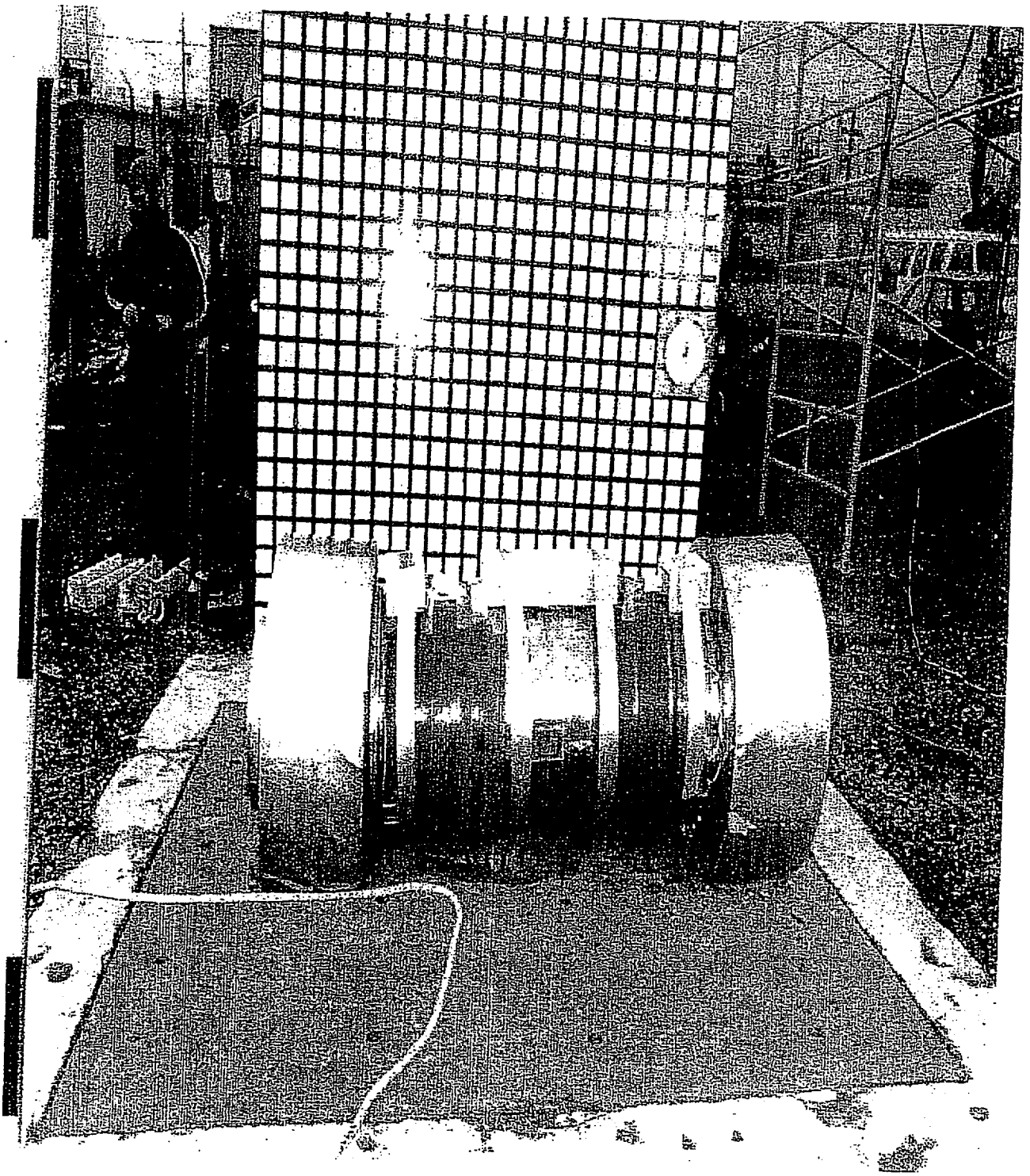

**FIGURE 2.A.5.10 ;** 1/4 SCALE HI-STAR 100 PACKAGING AFTER SLAP DOWN DROP

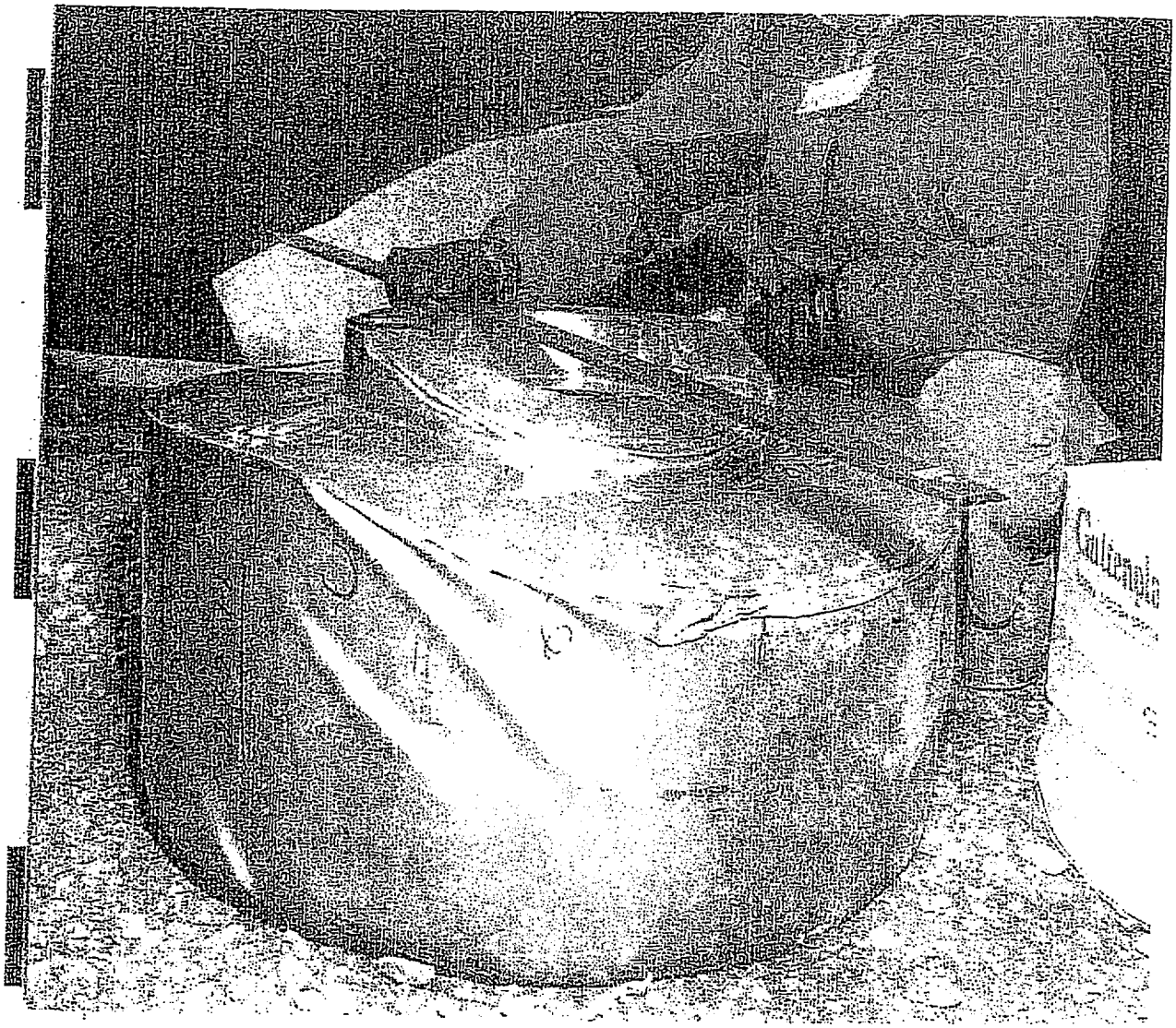

**FIGURE 2.A.5.11 ;** 1/4 SCALE IMPACT LIMITER AFTER C.G. OVER CORNER DROP

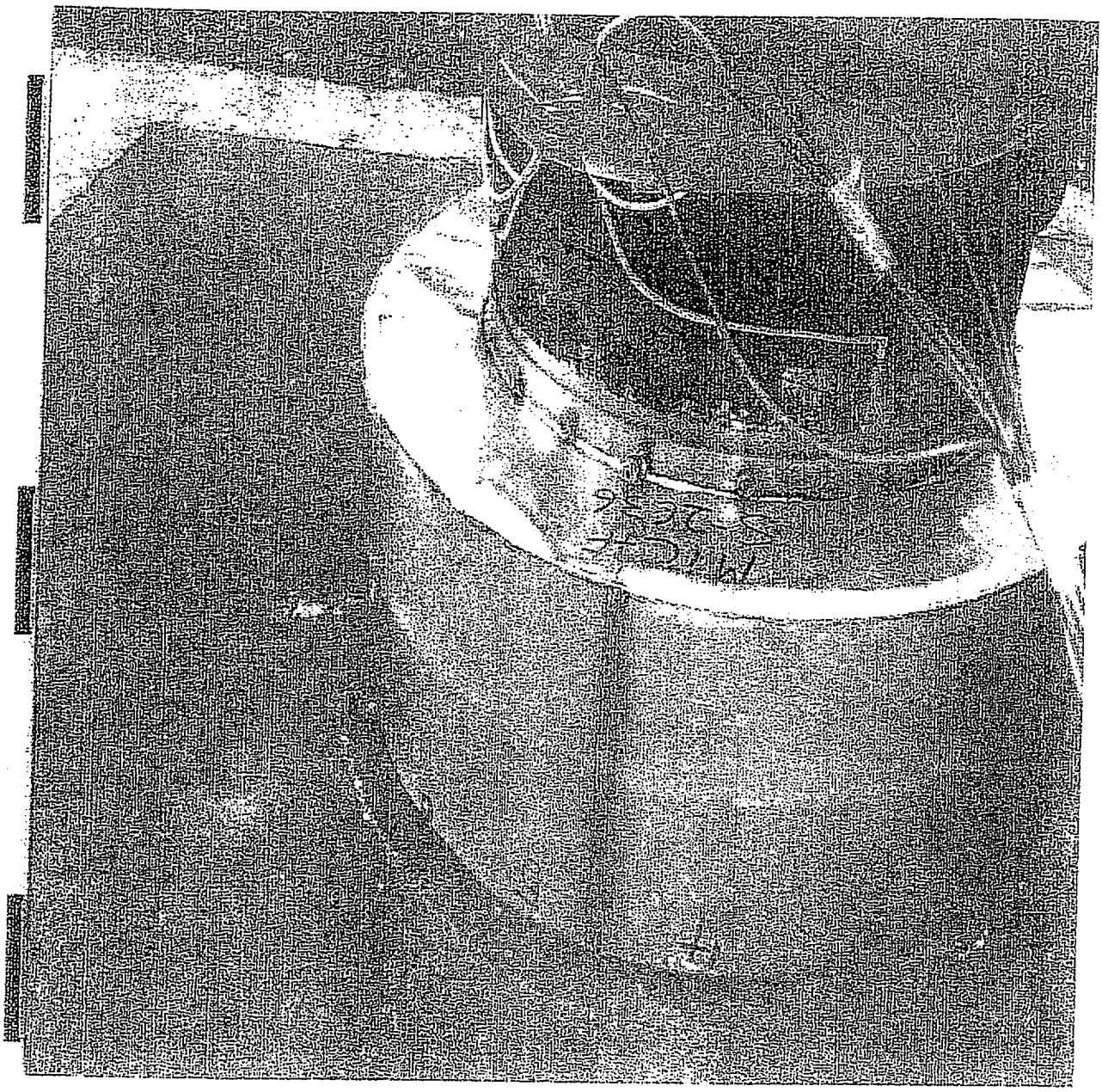

**FIGURE 2.A.5.12 :** 1/4 SCALE HI-STAR 100 PACKAGING AFTER TOP END DROP

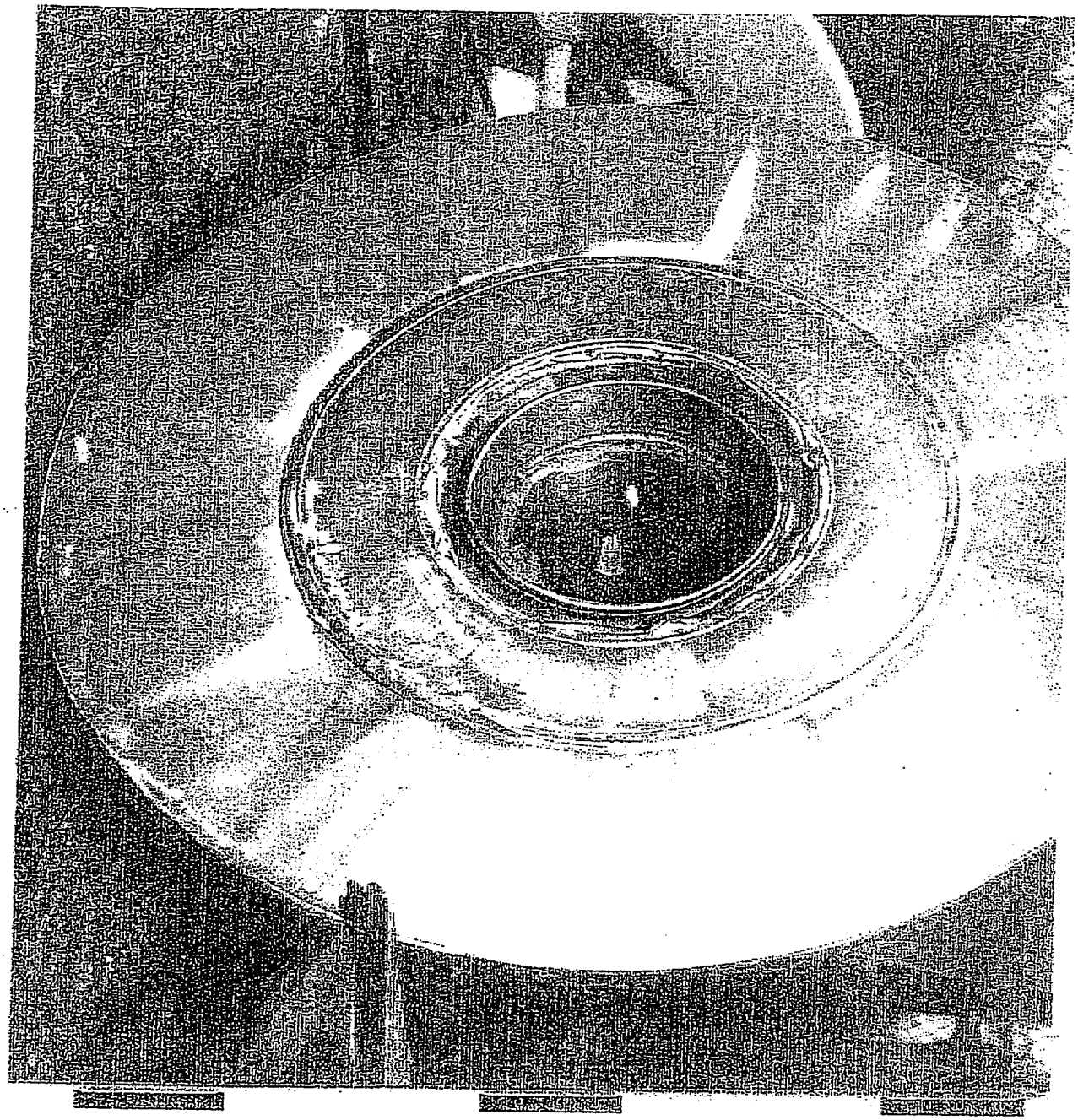

**FIGURE 2.A.5.13 ;** 1/4 SCALE IMPACT LIMITER TOP END DROP

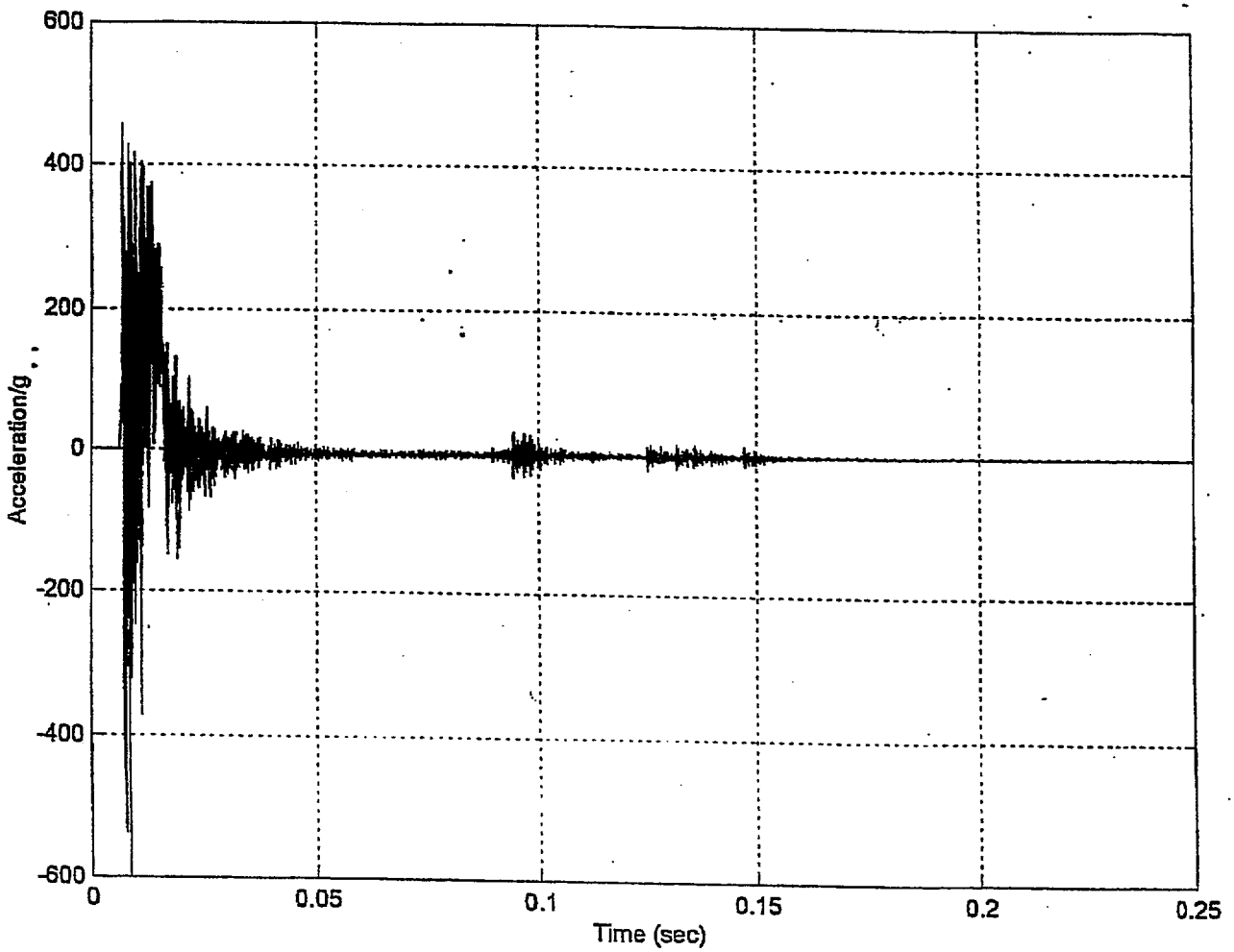


FIGURE 2.A.5.14 ; ACCELERATION RAW DATA FOR TOP END DROP

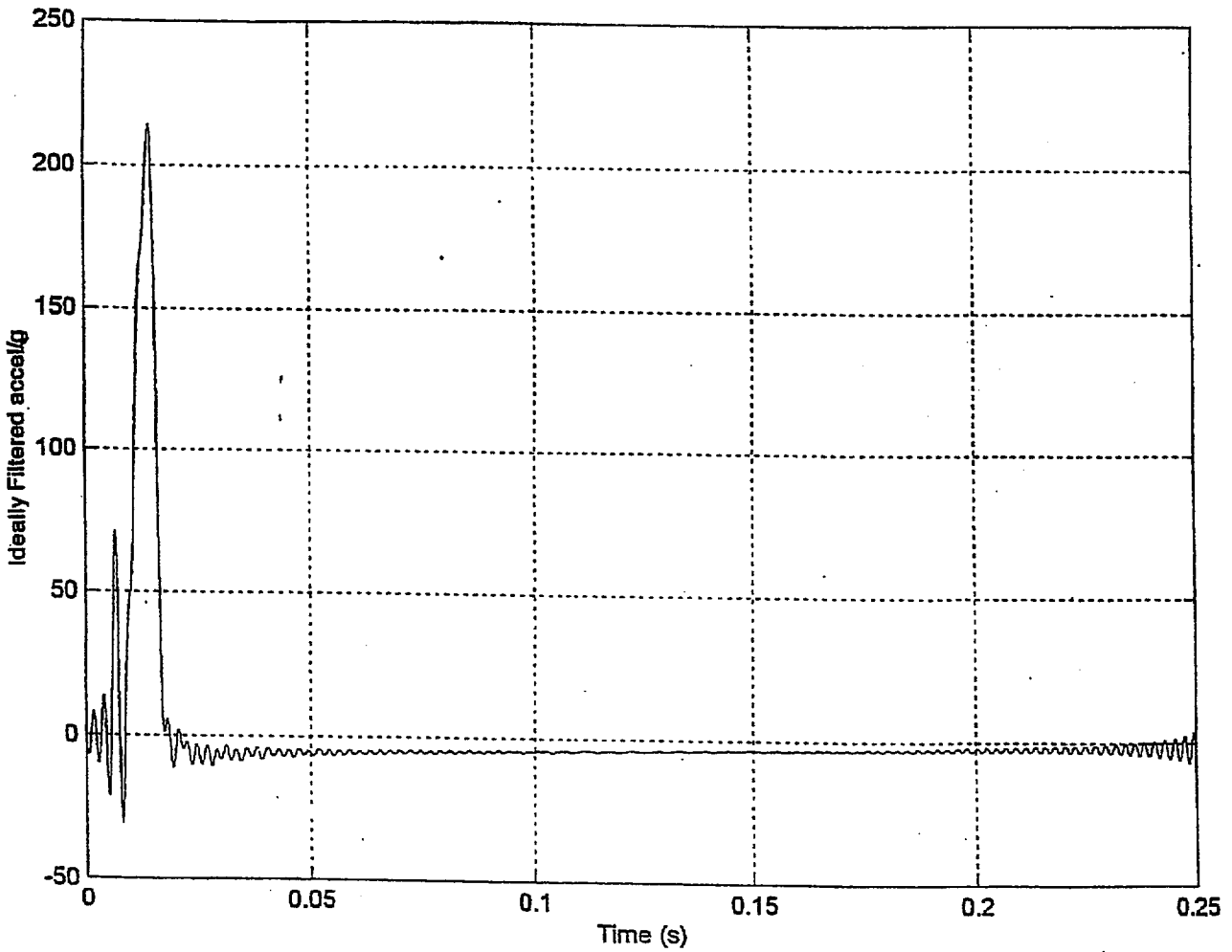


FIGURE 2.A.5.15 ; ACCELERATION DATA FILTERED AT 450 Hz FOR TOP END DROP

## FIGURE 2.A.5.15A ; TOP END DROP

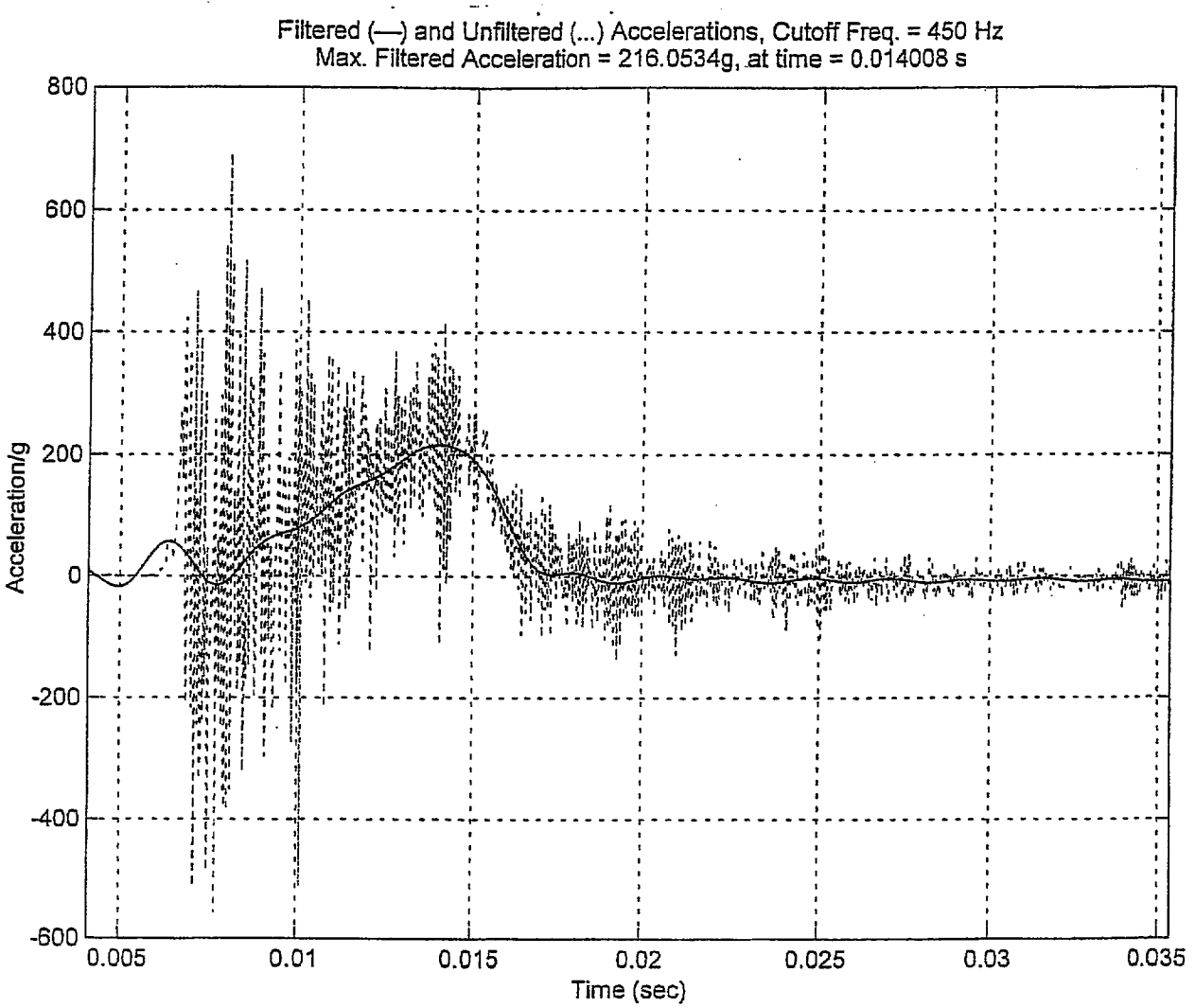

## FIGURE 2.A.5.15B ; TOP END DROP

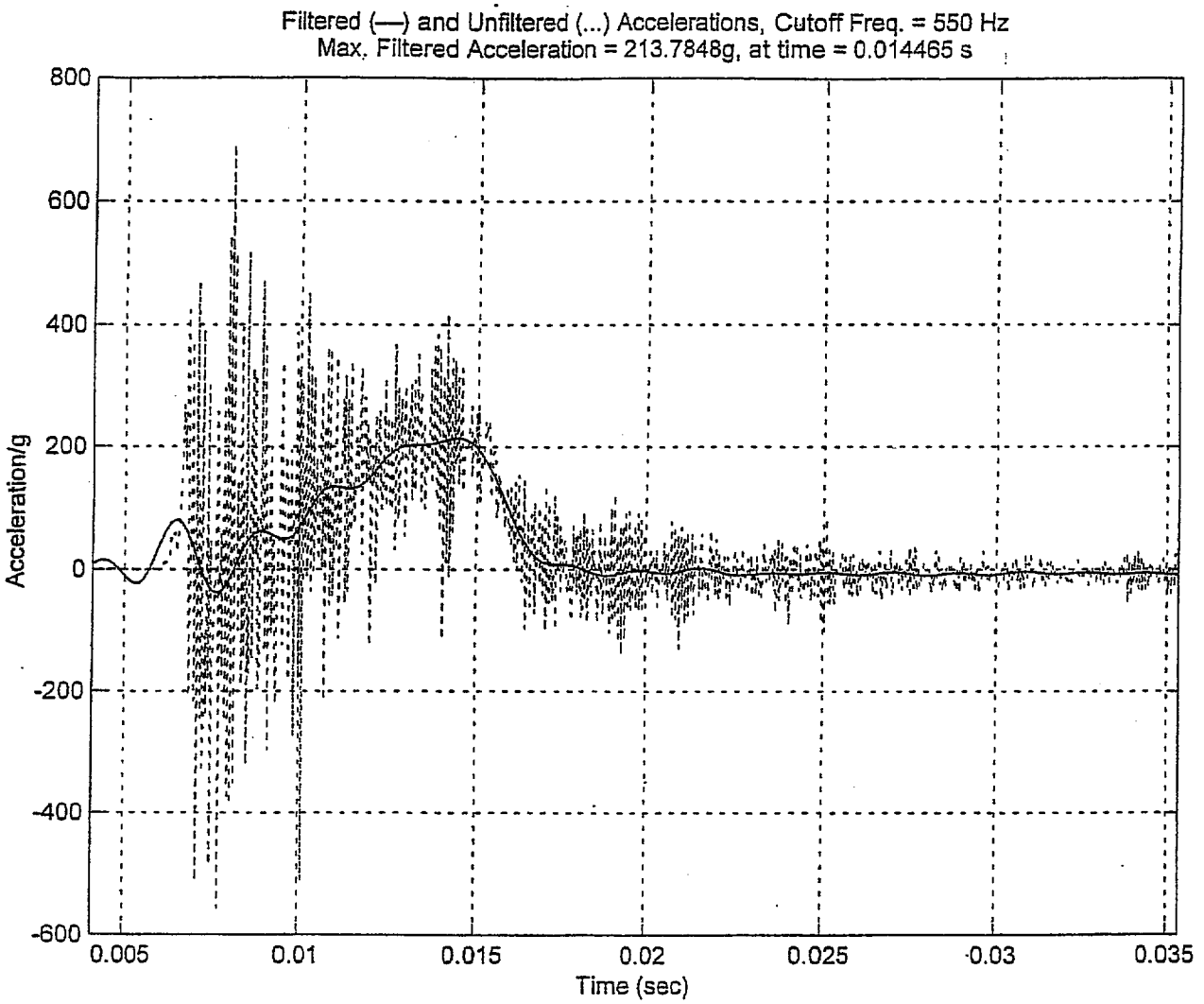

## FIGURE 2.A.5.15C : TOP END DROP

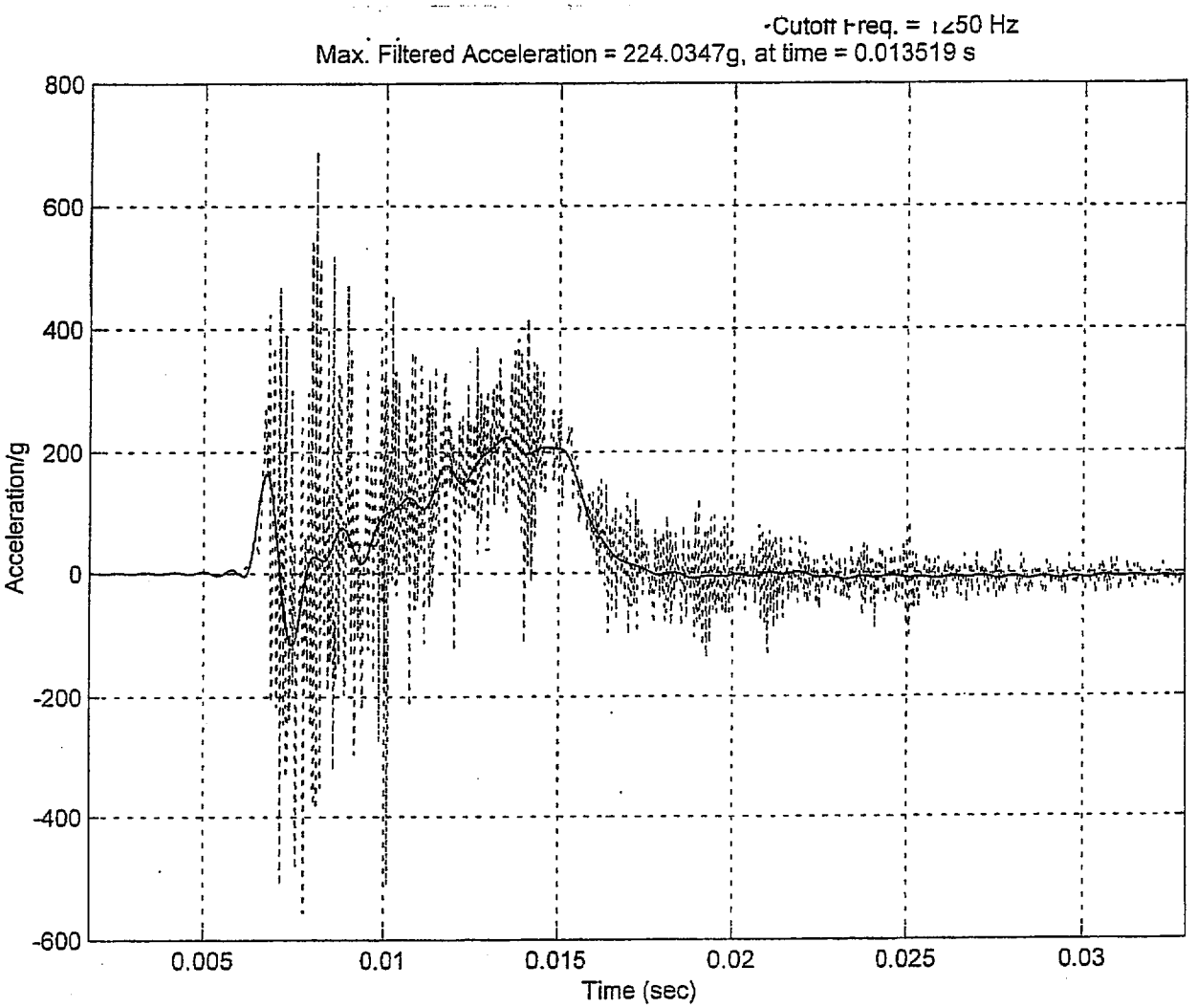

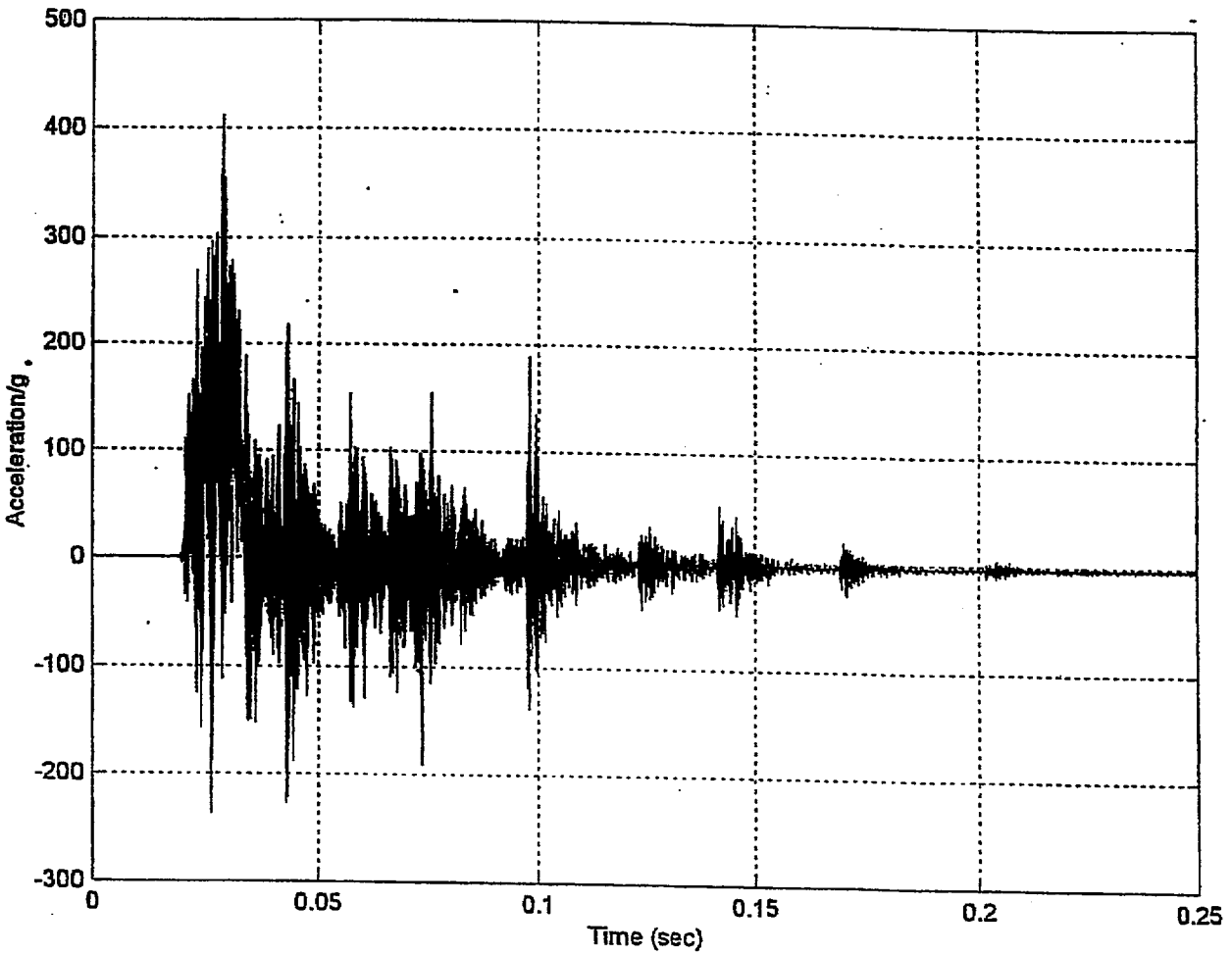


FIGURE 2.A.5.16 ; ACCELERATION RAW DATA FOR C.G. OVER CORNER DROP

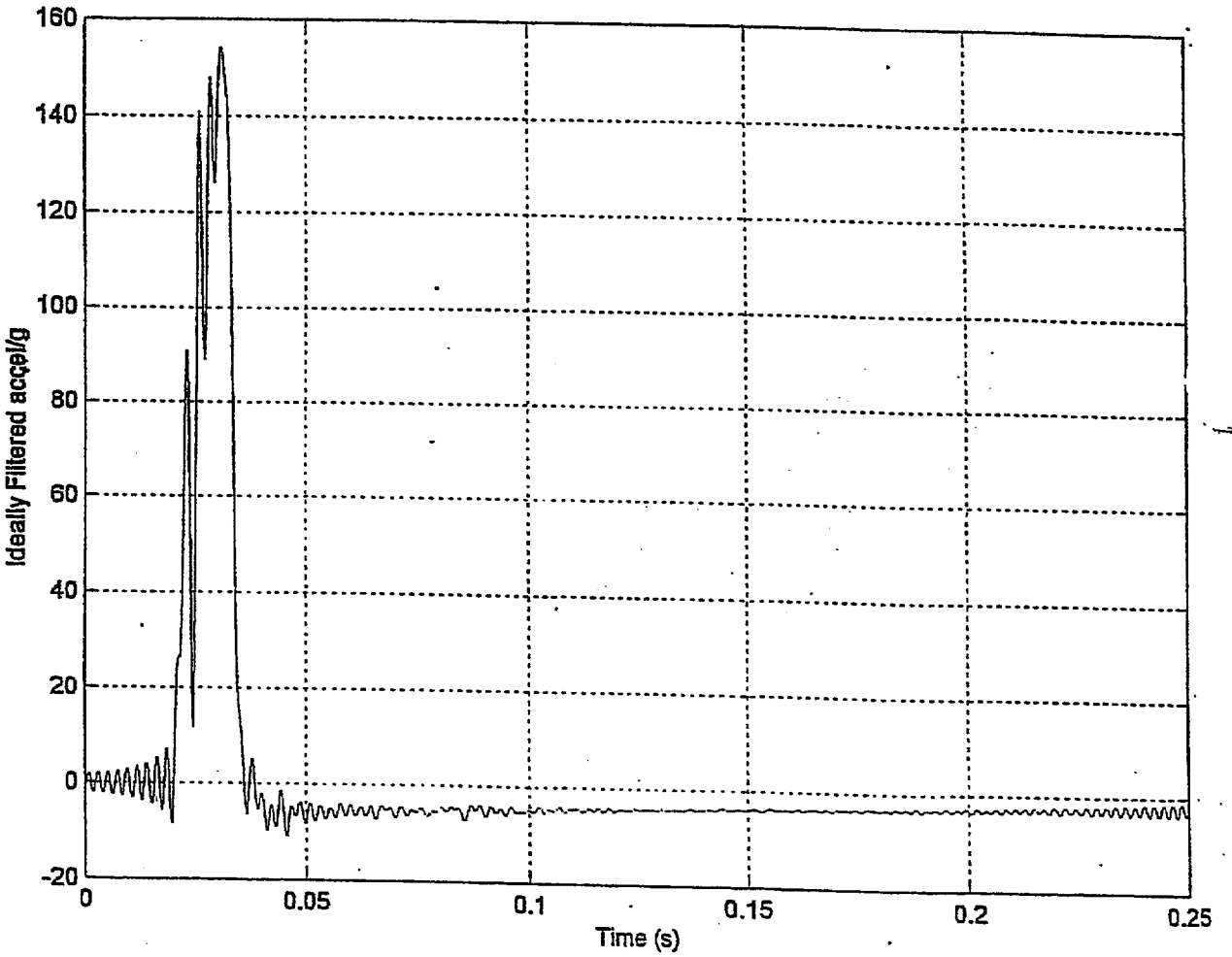


FIGURE 2.A.5.17 ; ACCELERATION DATA FILTERED AT 450 Hz FOR C.G. OVER CORNER

## FIGURE 2.A.5.17A : CG OVER CORNER

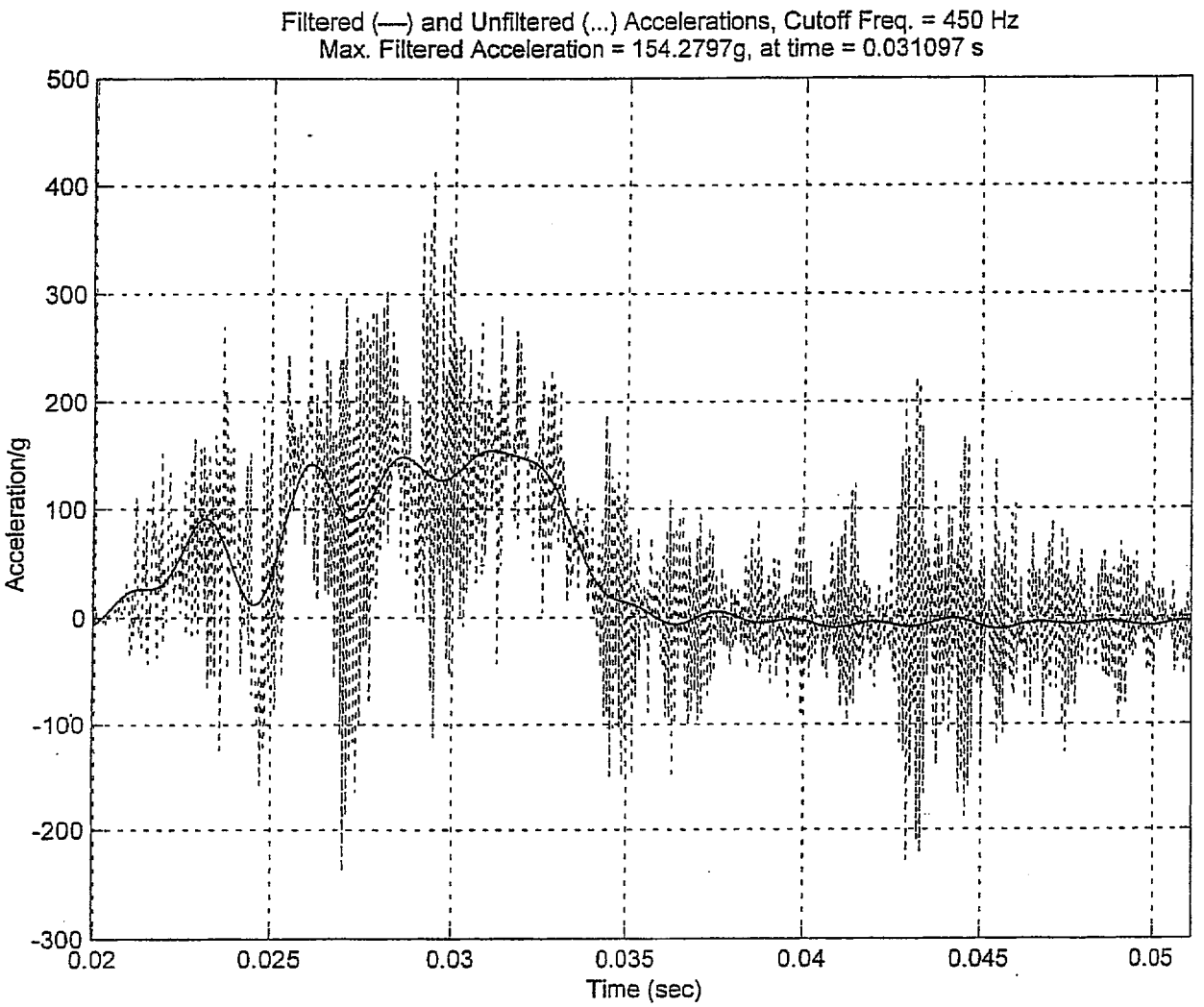

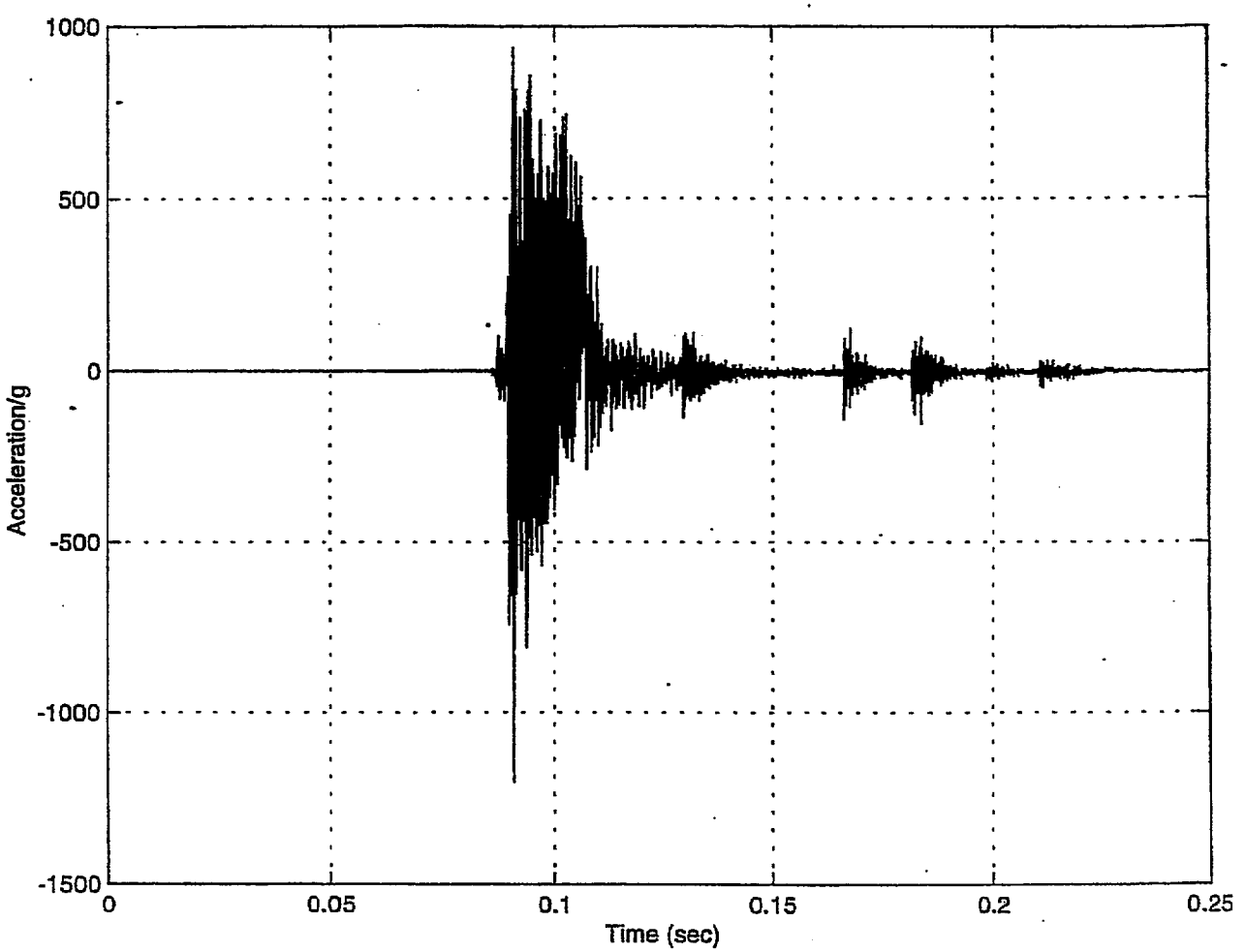


FIGURE 2.A.5.18 ; ACCELERATION RAW DATA AT BOTTOM END DURING SLAPDOWN DROP

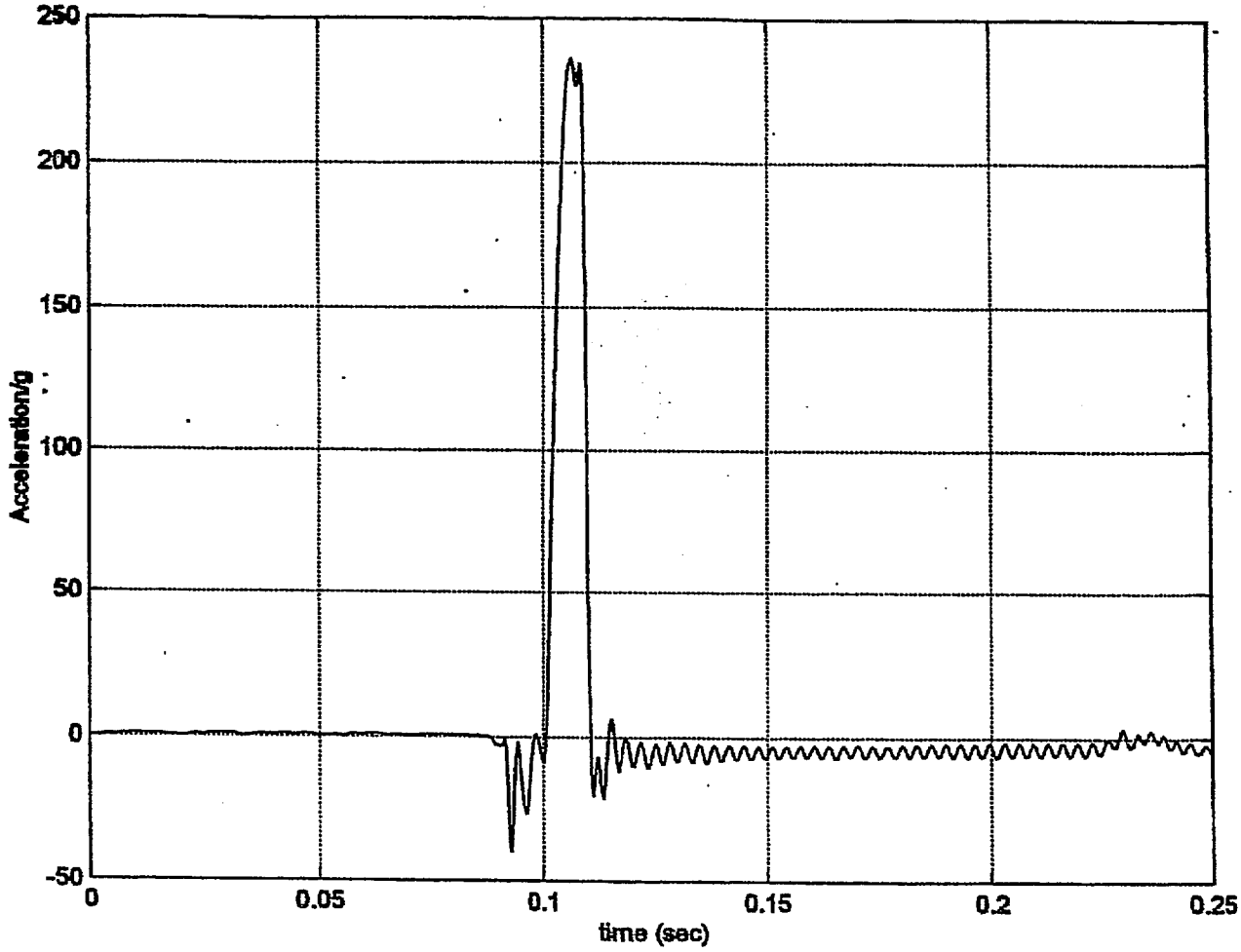


FIGURE 2.A.5.19 ; ACCELERATION DATA FILTERED AT 350 Hz FOR SLAPDOWN DROP

## FIGURE 2.A.5.19A ; : SLAP DOWN

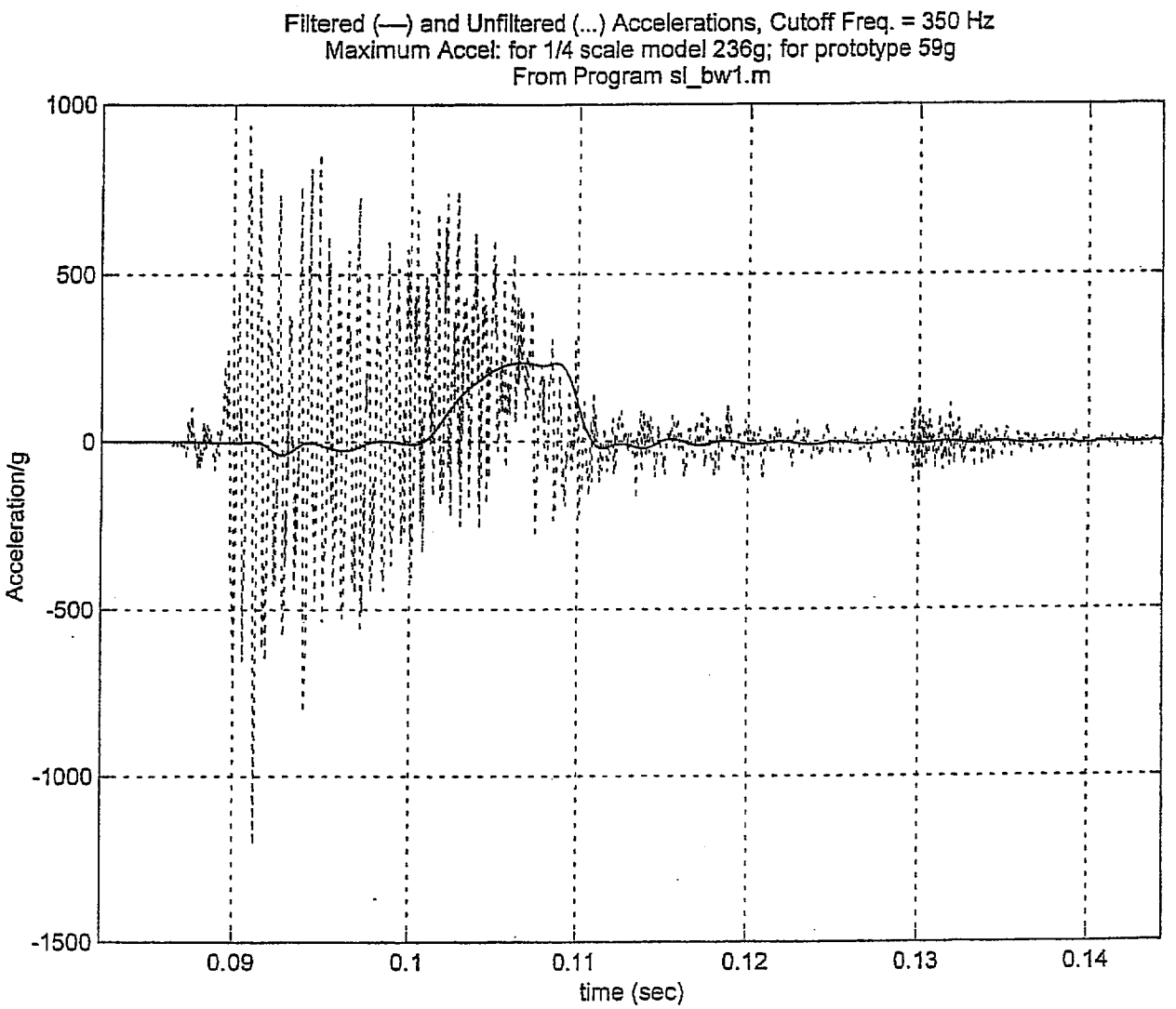

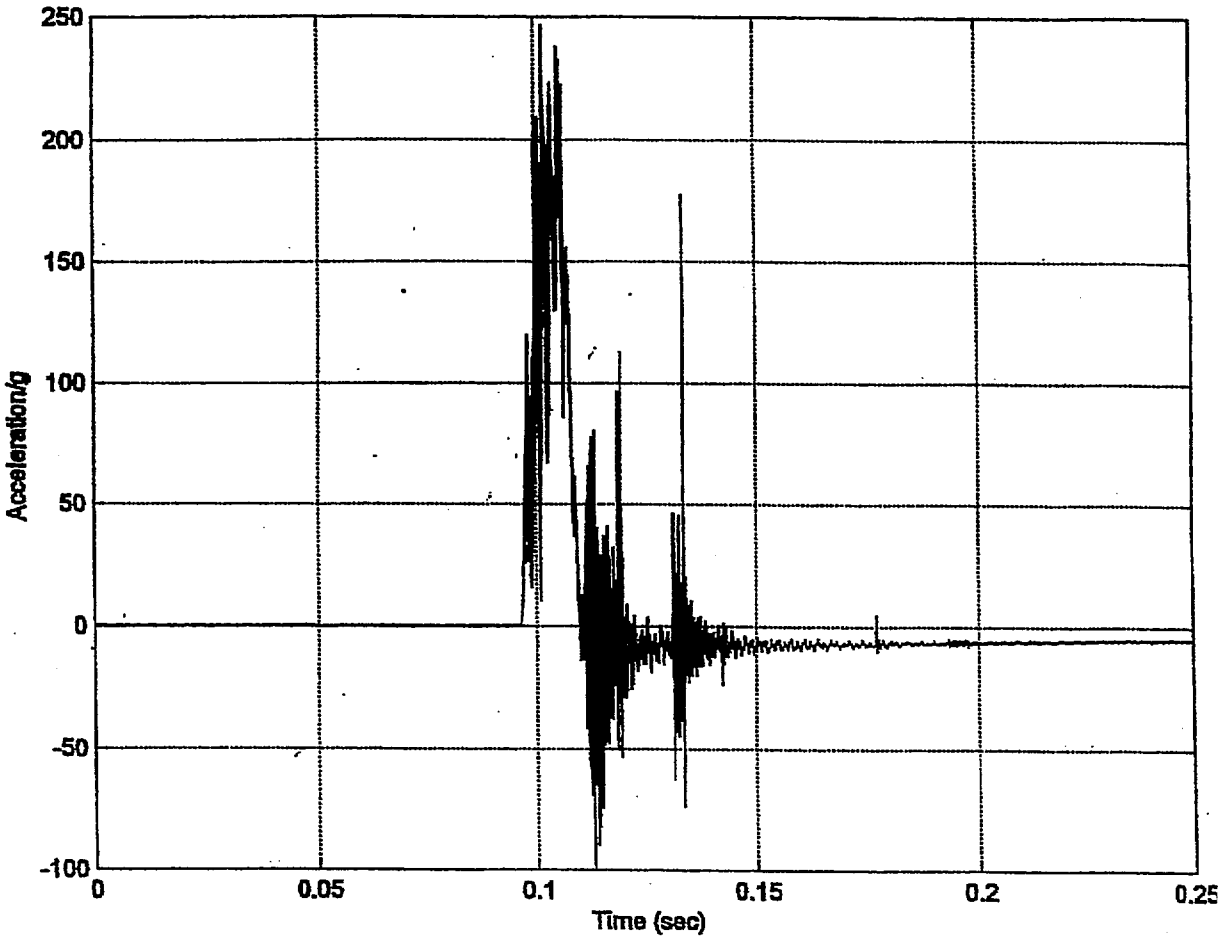


FIGURE 2.A.5.20 ; ACCELERATION RAW DATA FOR SIDE DROP

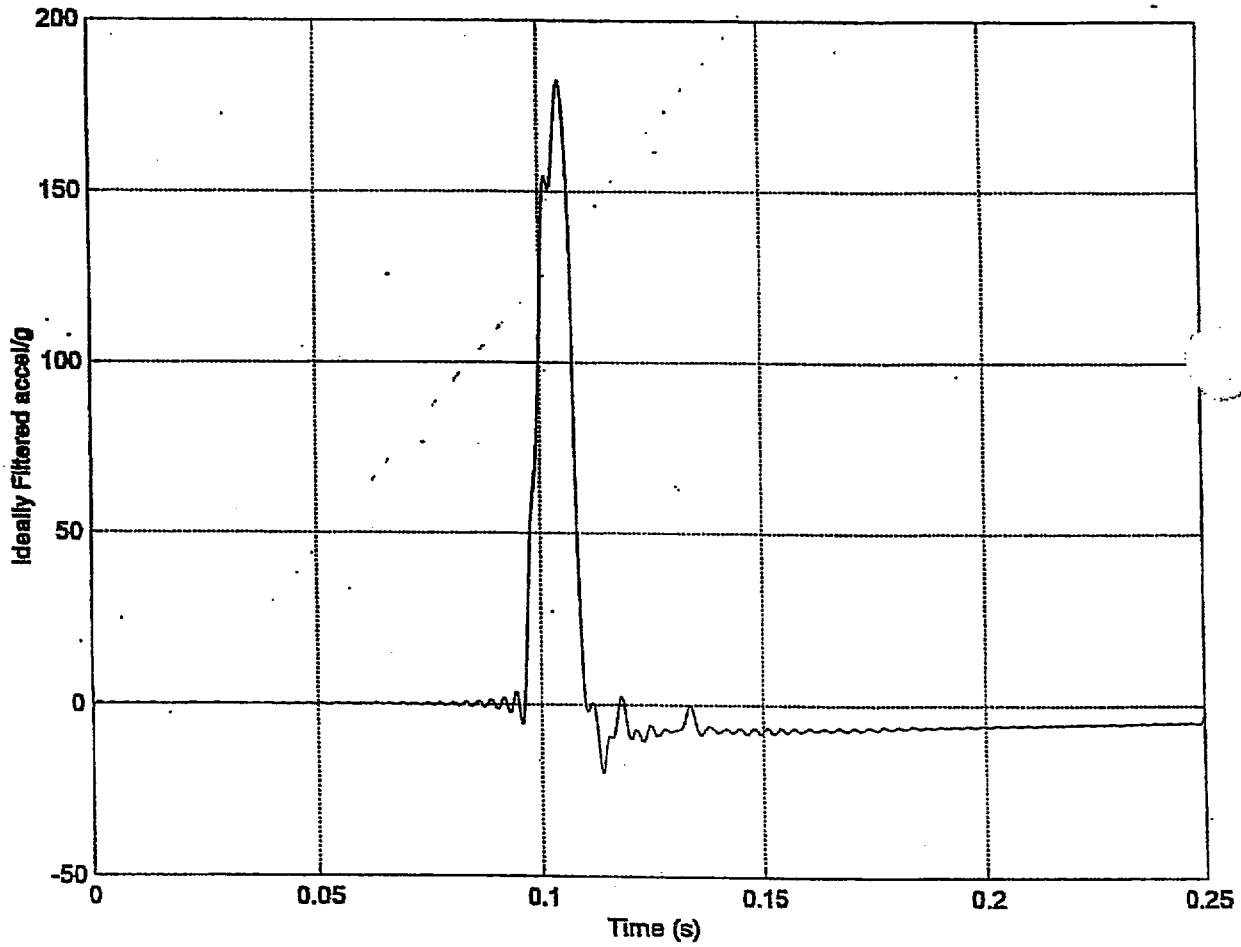


FIGURE 2.A.5.21 ; ACCELERATION DATA FILTERED AT 350 Hz FOR SIDE DROP

## FIGURE 2.A.5.21A

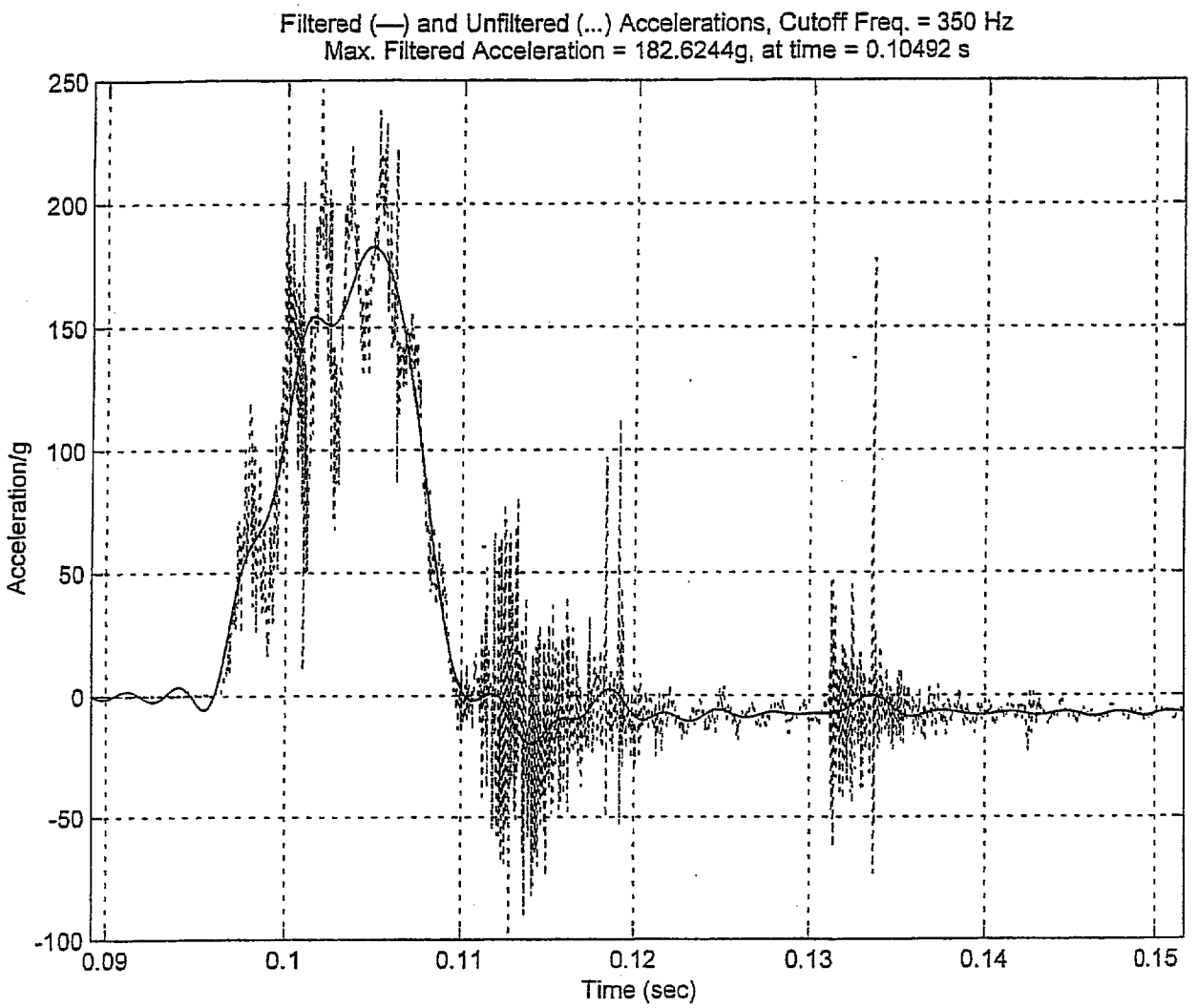

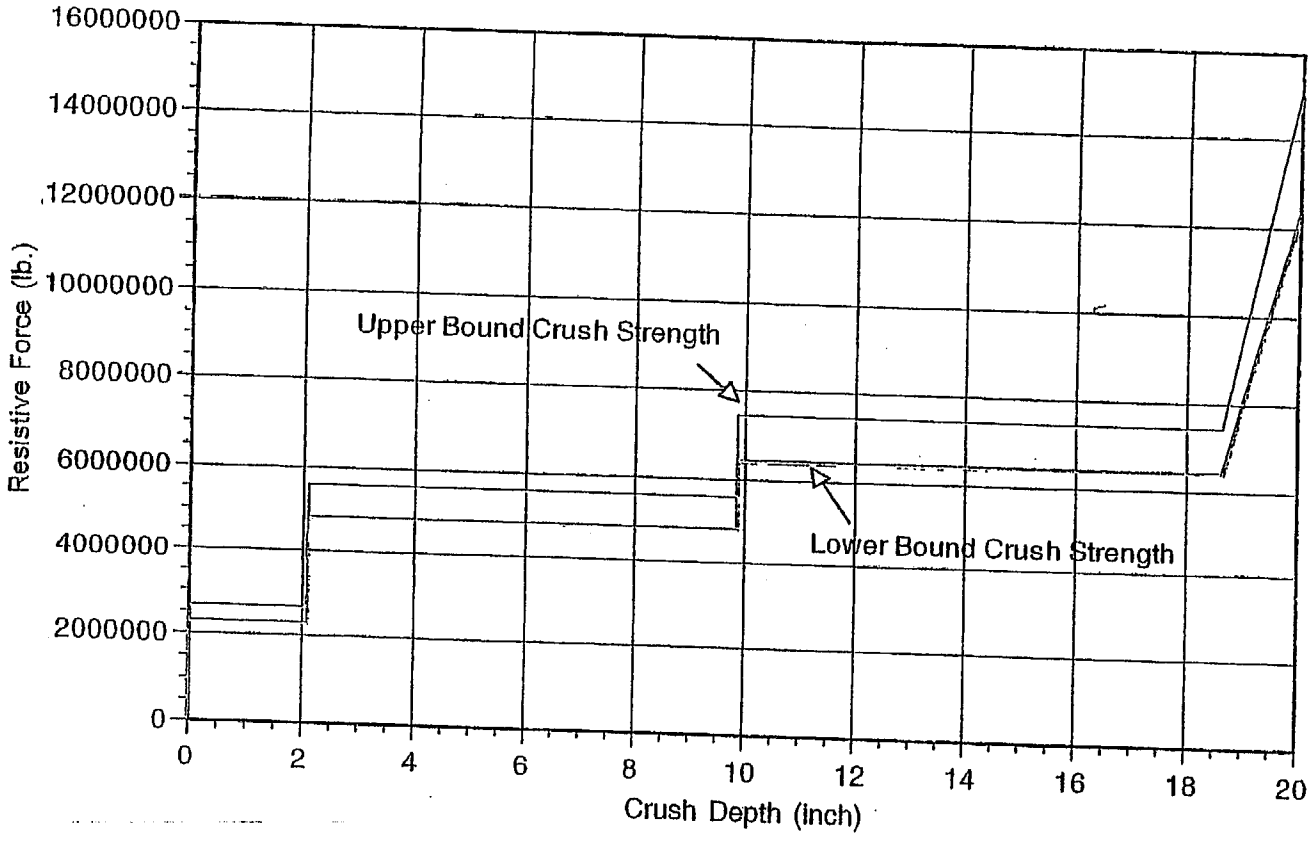


**FIGURE 2.A.6.1 ;** - Impact Limiter Force vs. Crush Depth ($\theta = 90$ degrees)

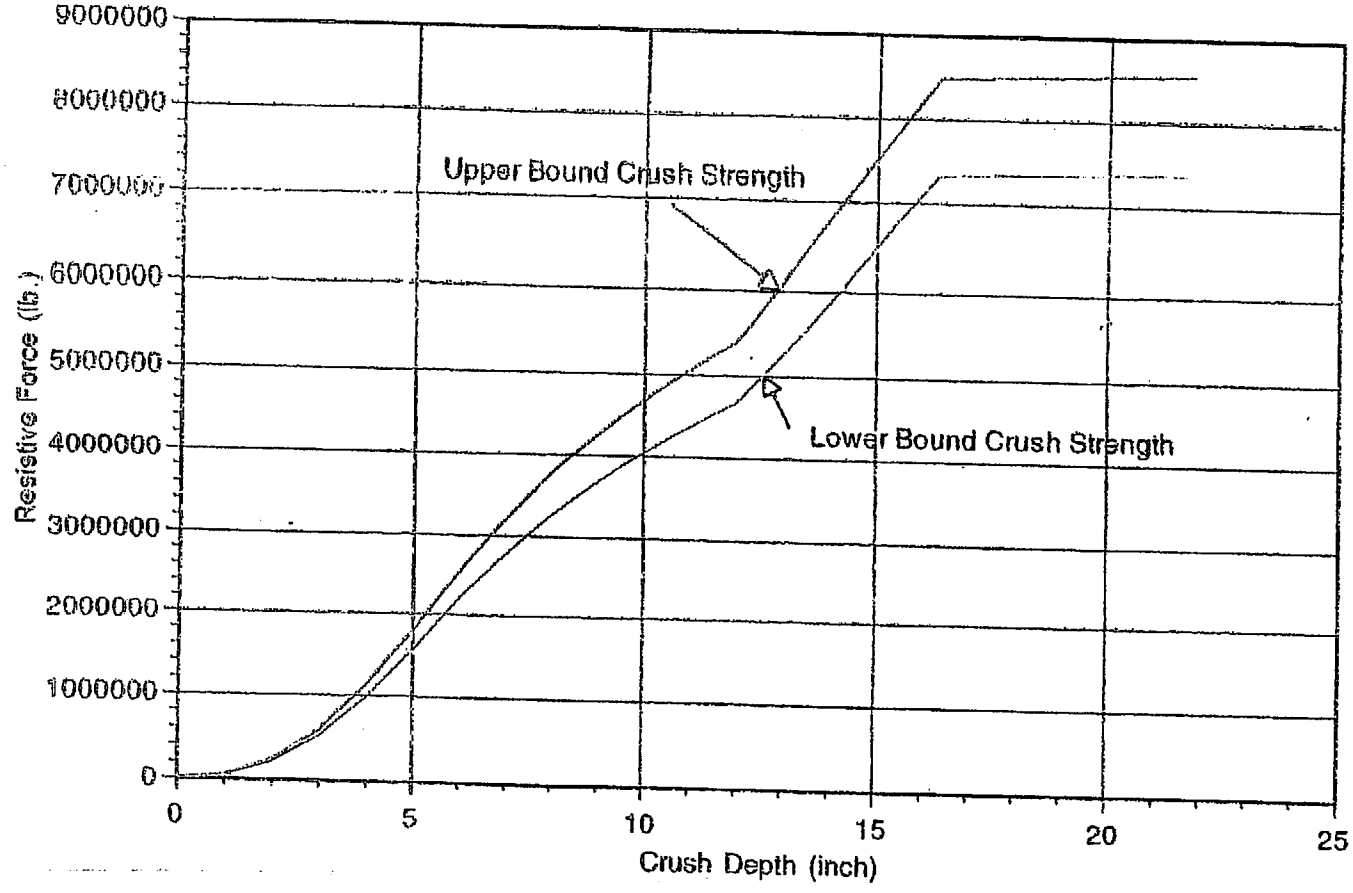


FIGURE 2.A.6.2 ; Impact Limiter Force vs. Crush Depth ($\theta = 67.5$ degrees)

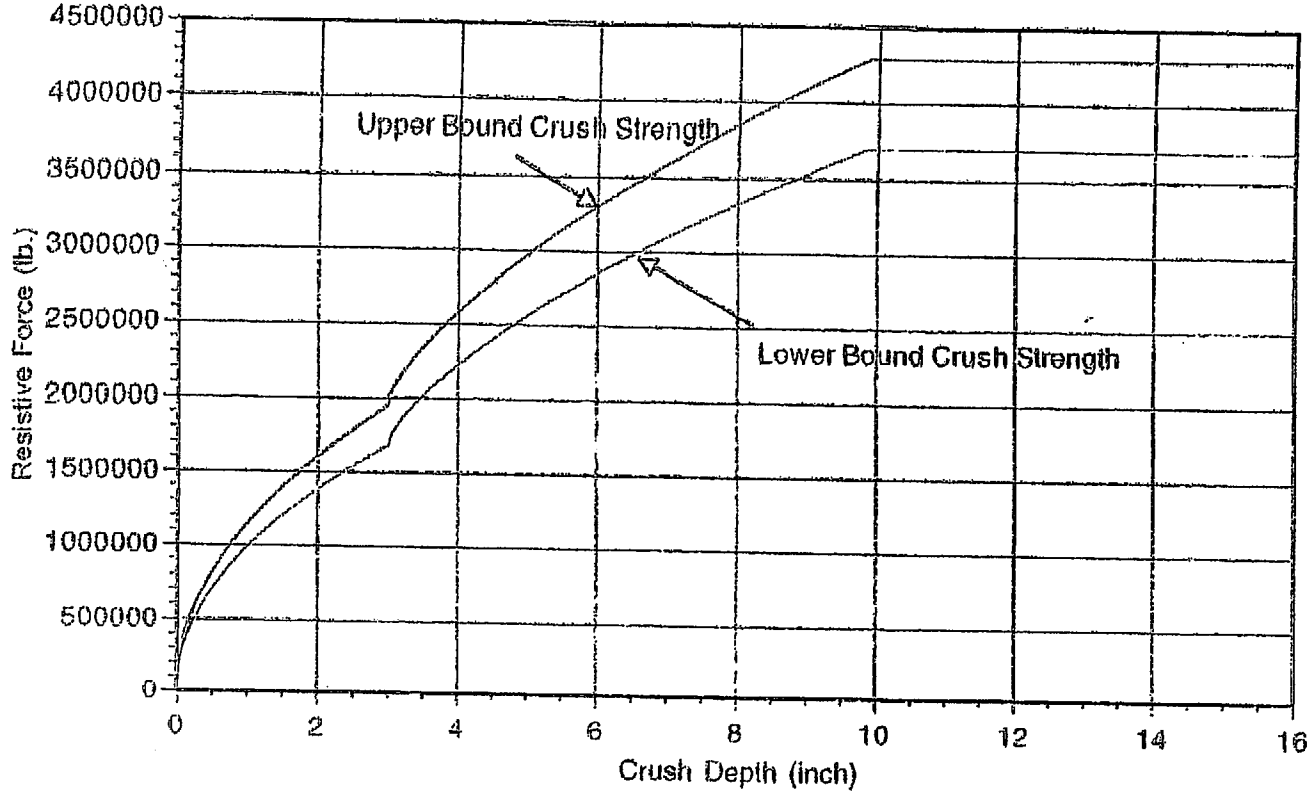


**FIGURE 2.A.6.3 ;** - Impact Limiter Force vs. Crush Depth ($\theta = 0$ degrees)

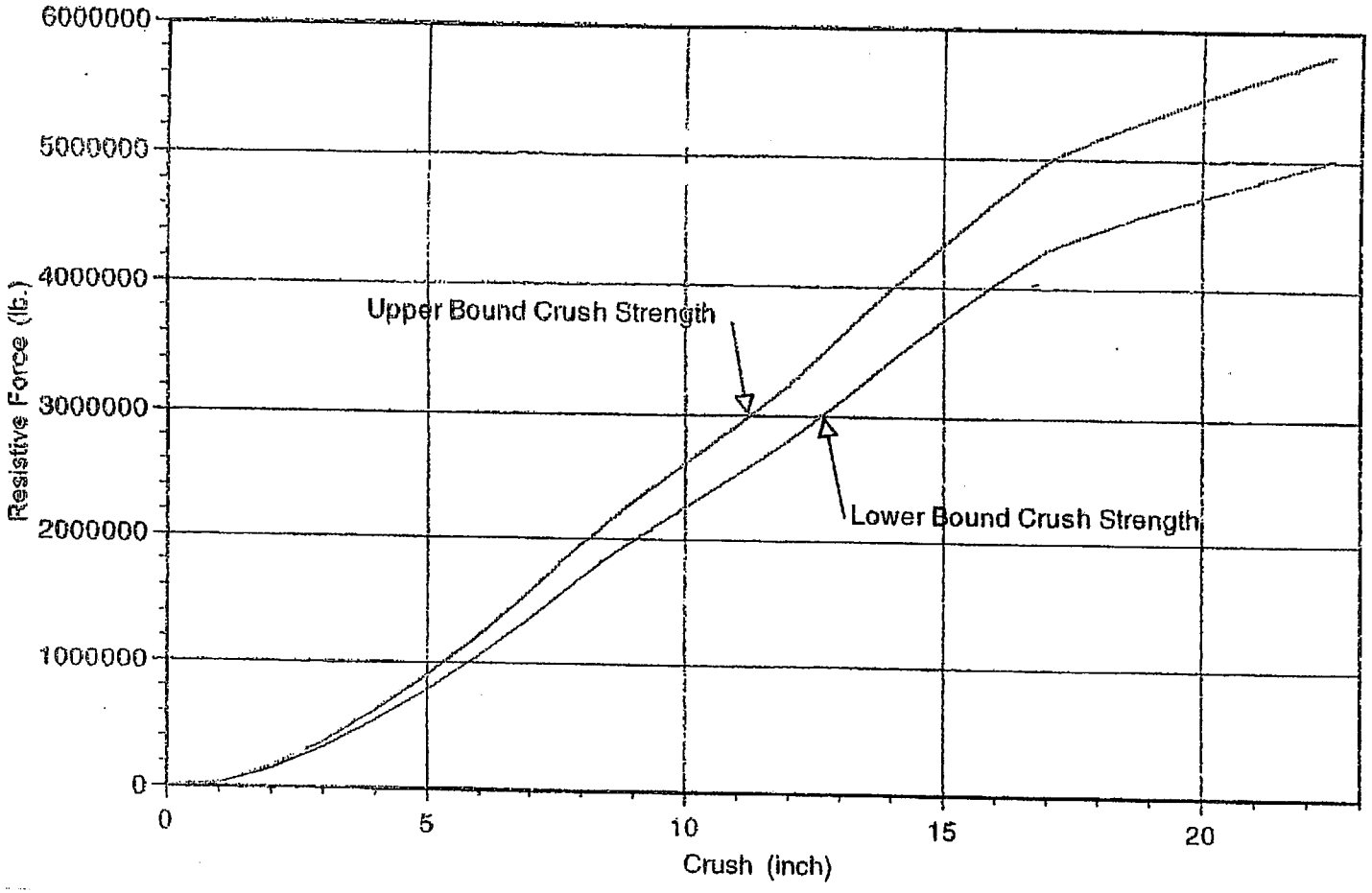


FIGURE 2.A.6.4 ; - Impact Limiter Force vs. Crush Depth ($\theta = 15$ degrees)

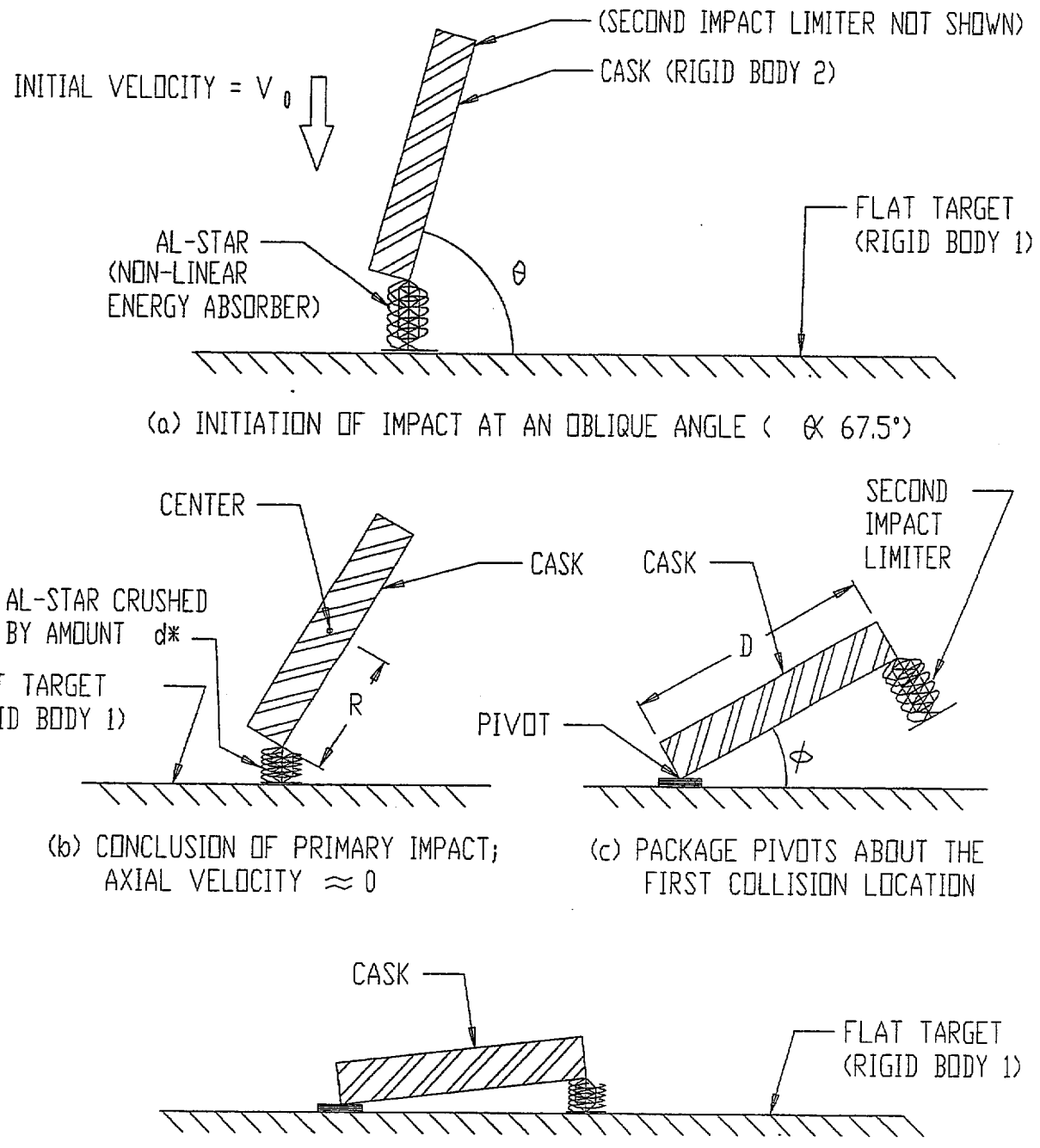


FIGURE 2.A.6.5; DYNAMIC MODEL FOR DUAL IMPACT SCENARIOS

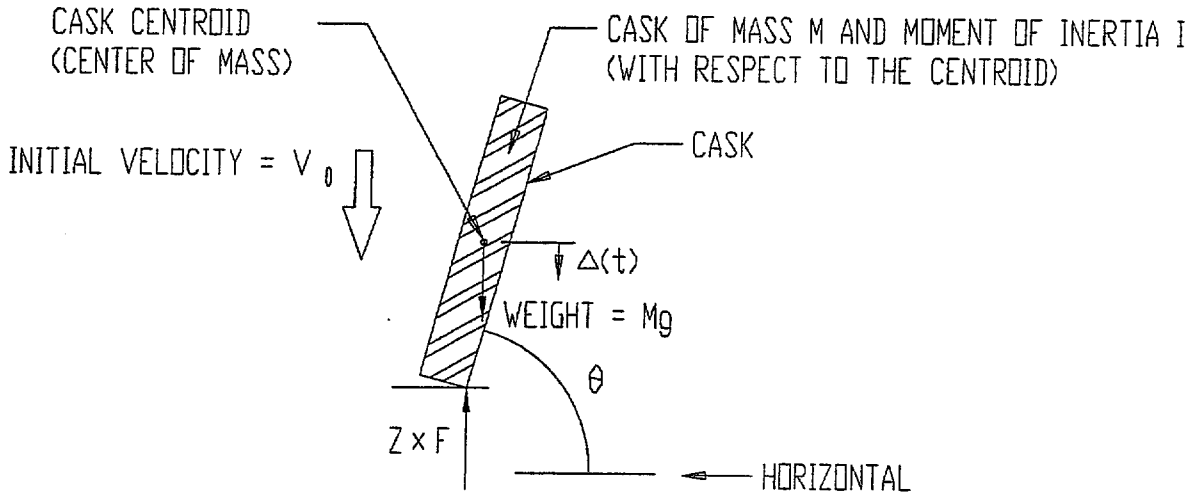


(a) INITIATION OF IMPACT AT AN OBLIQUE ANGLE ( $\theta \leq 67.5°$)

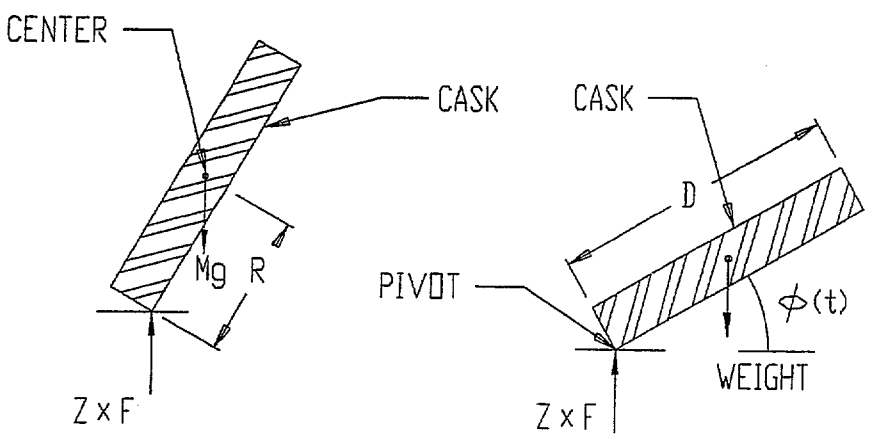


(b) CONCLUSION OF PRIMARY IMPACT; AXIAL VELOCITY $\approx 0$

(c) PACKAGE PIVOTS ABOUT THE FIRST COLLISION LOCATION

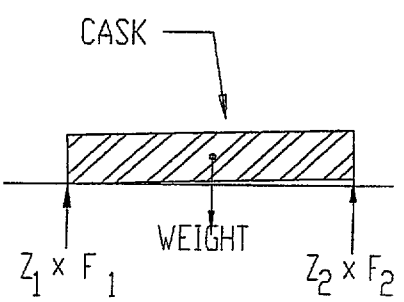


(c) SECONDARY IMPACT AT THE SECOND IMPACT LIMITER

FIGURE 2.A.6.6; FREE-BODY DIAGRAM FOR IMPACT SCENARIOS

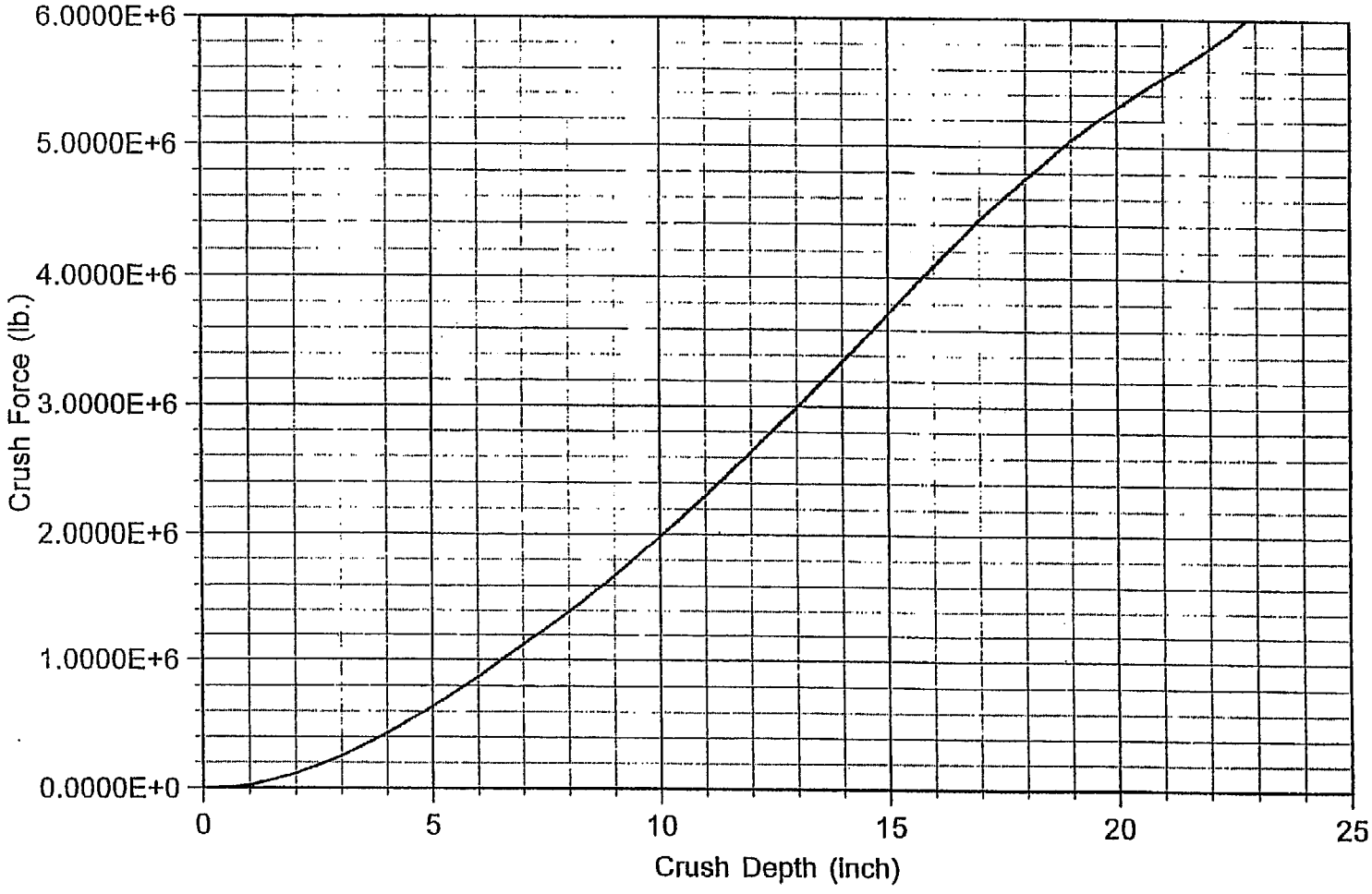


FIGURE 2.A.7.1 ; Static Crush Force vs Crush Depth - Impact at 30 Degrees with Horizontal Target

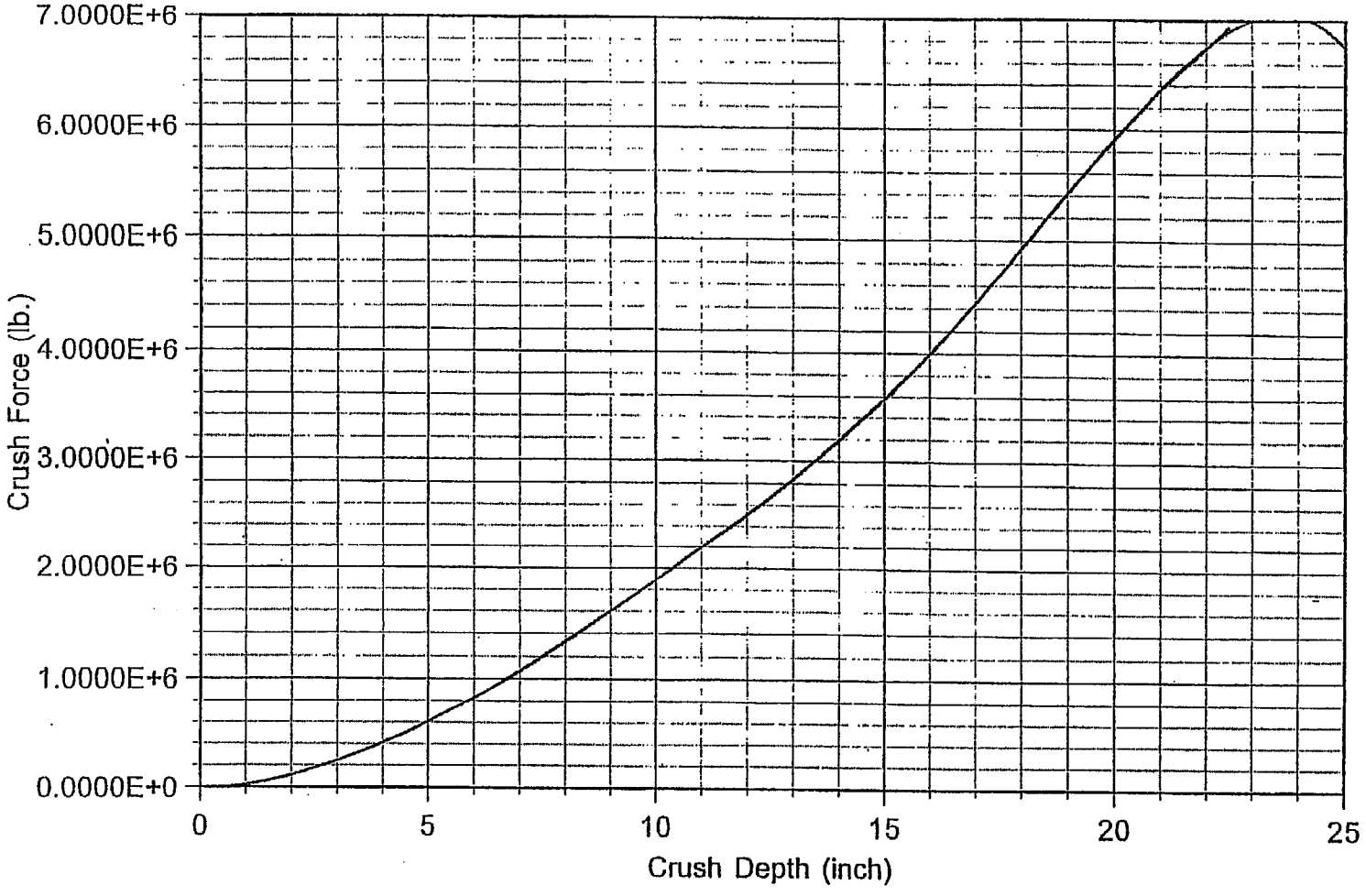


FIGURE 2.A.7.2 ; Static Crush Force vs Crush Depth - Impact at 45 Degrees with Horizontal Target

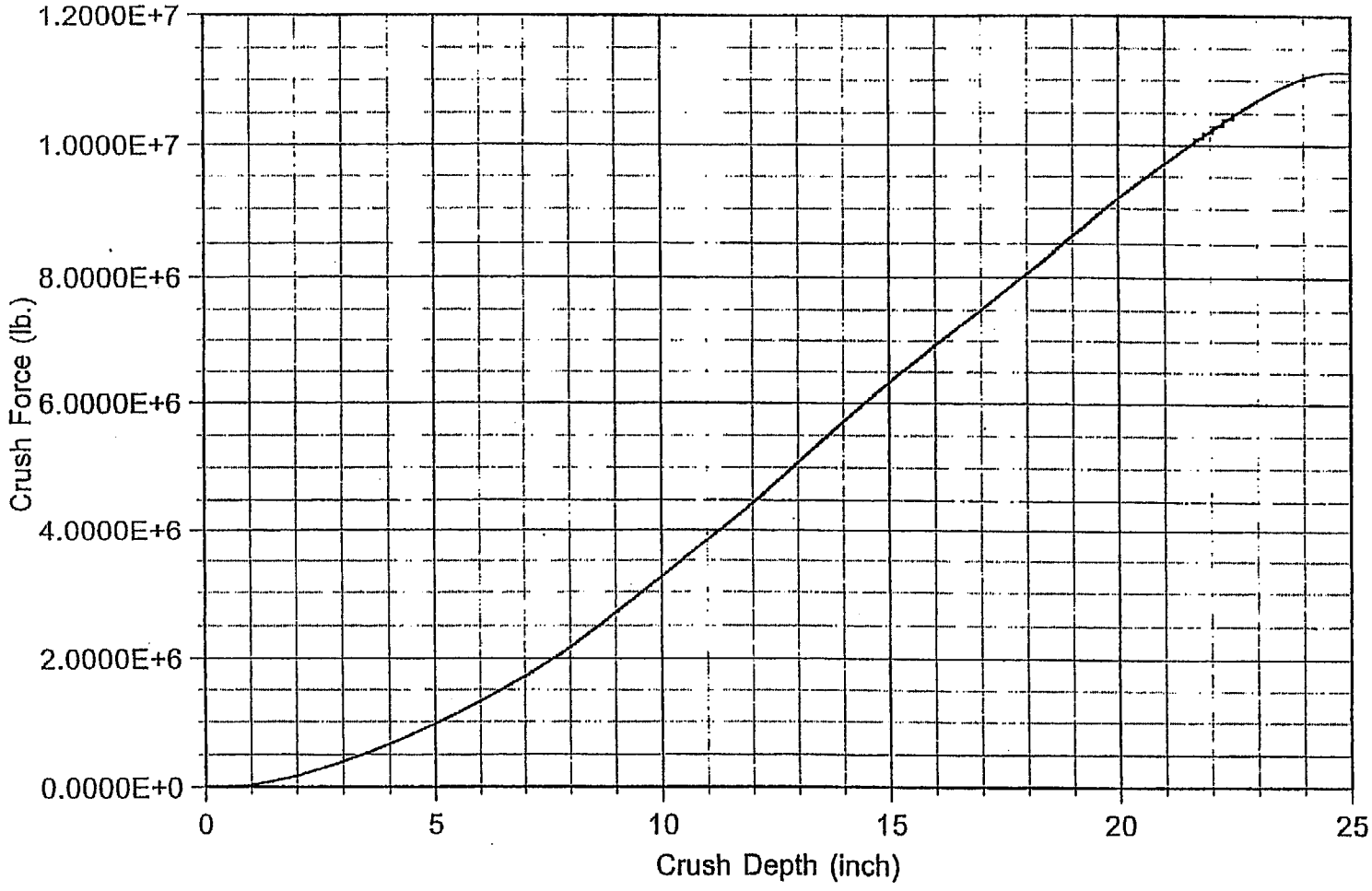


FIGURE 2.A.7.3 ; Static Crush Force vs Crush Depth - Impact at 60 Degrees with Horizontal Target

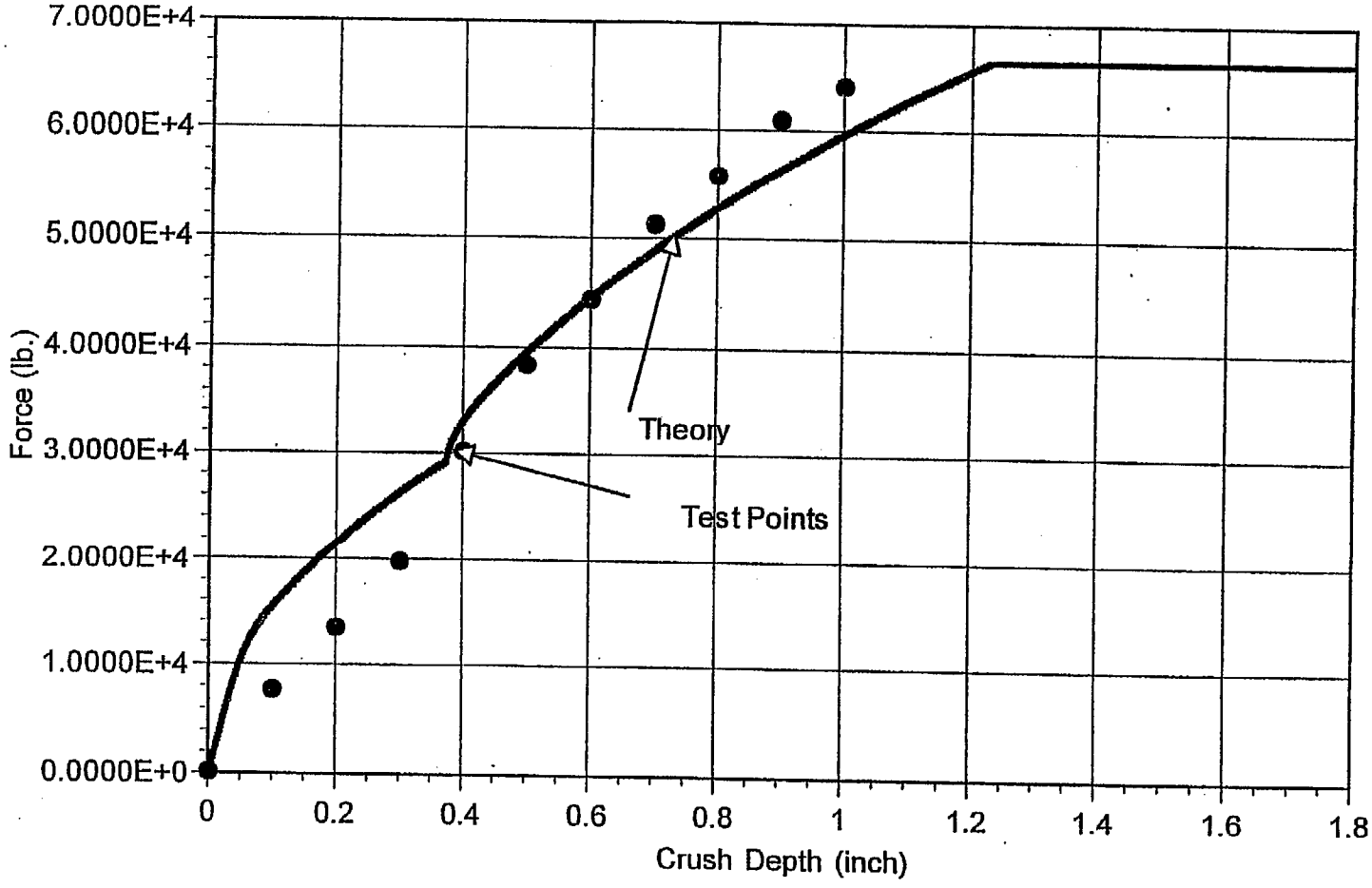


FIGURE 2.A.10.1 ; 1/8th Scale Impact Limiter - Crush Force vs. Crush Depth - Side Orientation -

HI-951251 REV. 10

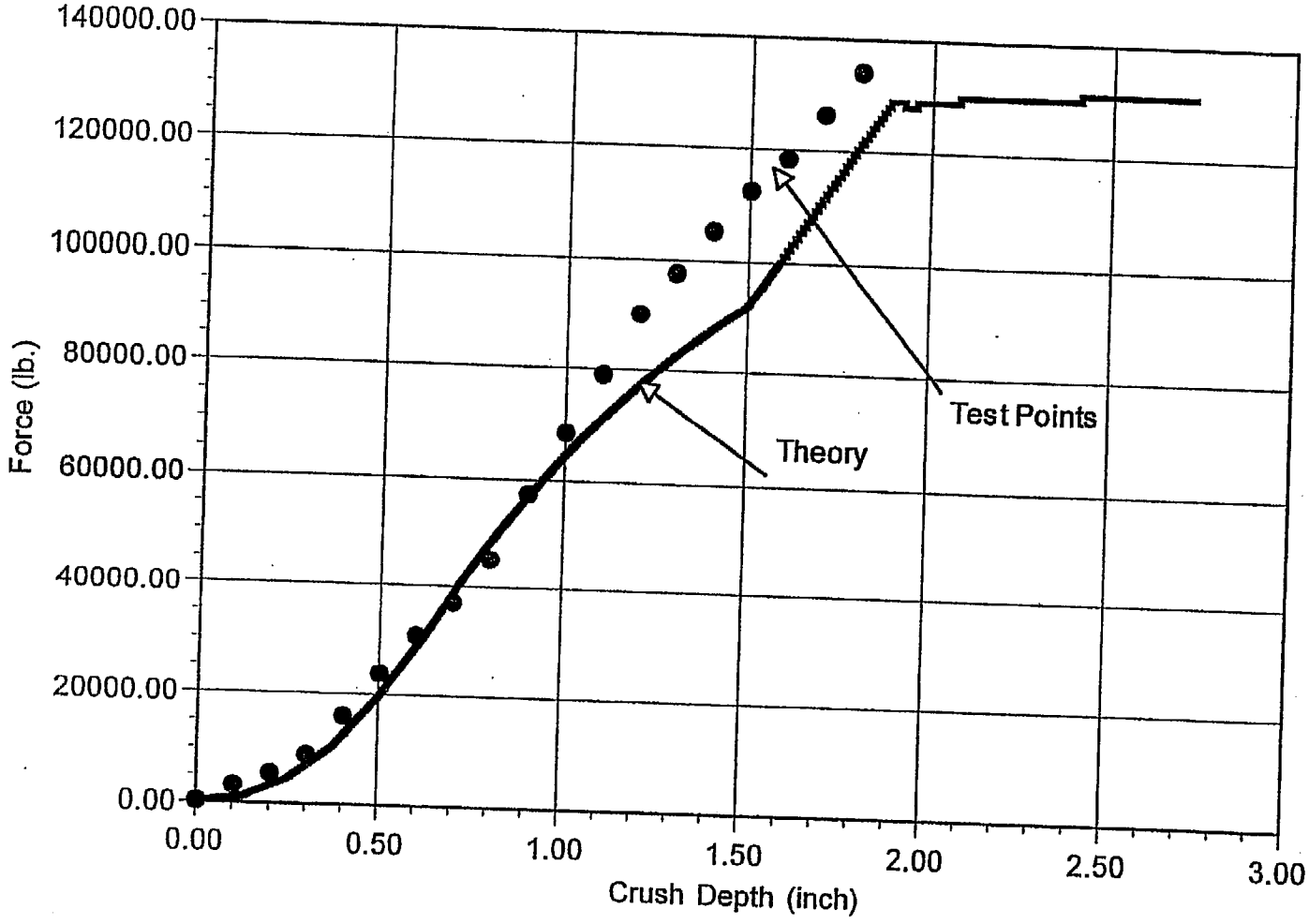


FIGURE 2.A.10.2 ; 1/8th Scale Impact Limiter - Crush Force vs. Crush Depth - Center of Gravity Over Corner Orientation

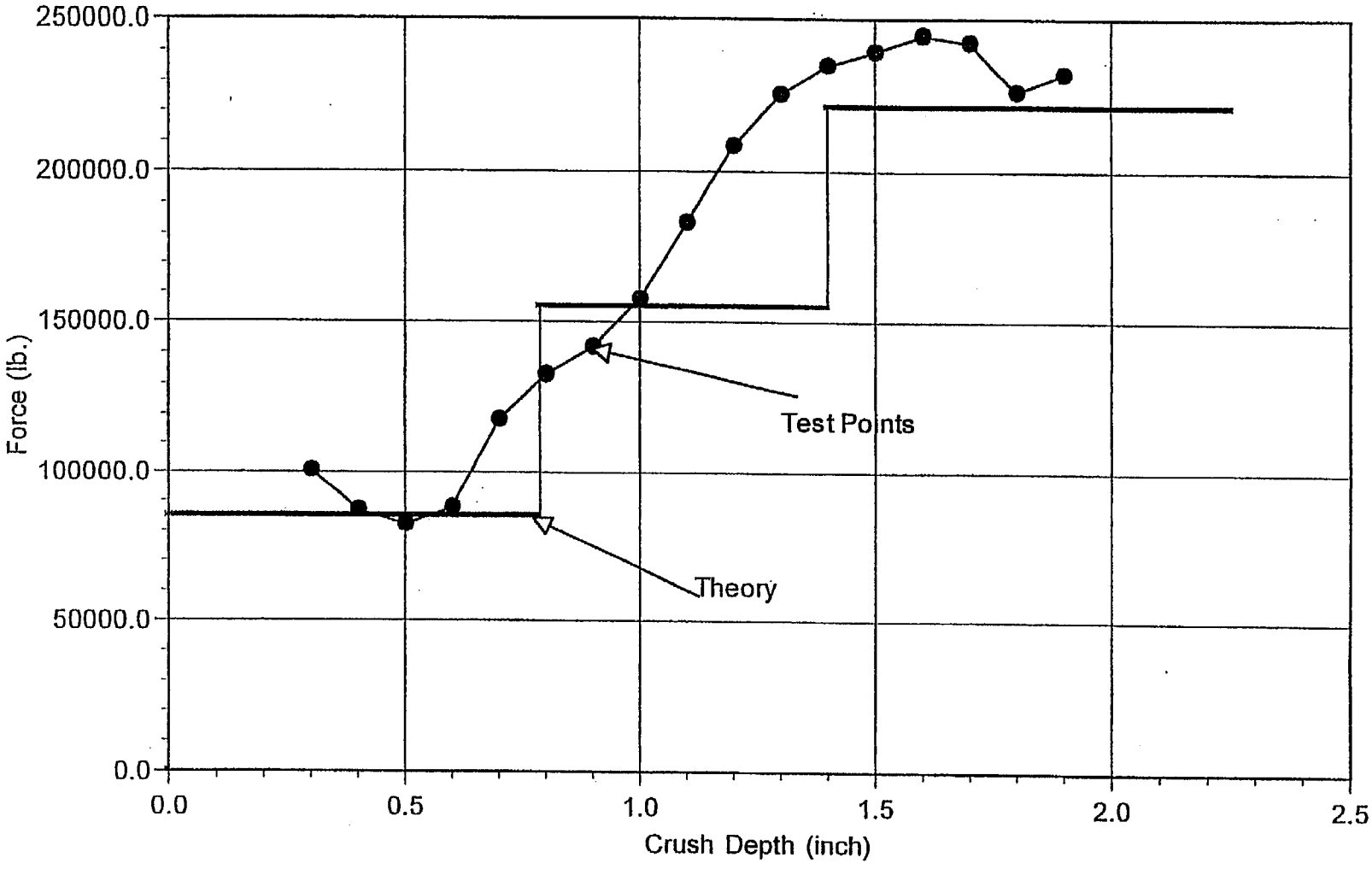


FIGURE 2.A.10.3 ; 1/8th Scale Impact Limiter - Crush Force vs. Crush Depth - End Orientation

# *Appendix 2.B*

## *SUMMARY OF RESULTS FOR STRUCTURAL INTEGRITY OF DAMAGED FUEL CANISTERS*

### *2.B.1 Introduction*

*Damaged Fuel Canisters or Containers (DFCs) to be deployed in the HI-STAR 100 System transport package have been evaluated to demonstrate that the canisters are structurally adequate to support the mechanical loads postulated during normal lifting operations while in long-term storage, and during a hypothetical end drop accident condition. The evaluations address the following damaged/failed fuel canisters for transportation in the Hi-STAR 100 System:*

- *Holtec-designed DFC for Dresden Unit 1 and Humboldt Bay fuel*
- *Transnuclear designed DFC for Dresden Unit 1 fuel*
- *Dresden Unit 1 Thoria Rod Canister*
- *Holtec-designed DFC for Trojan plant fuel*
- *Sierra Nuclear Corporation(SNC)-designed Failed Fuel Can for Trojan plant fuel*

### *2.B.2 Methodology*

*The structural load path in each of the analyzed canisters was evaluated using basic strength of materials formulations. The various structural components were modeled as axial or bending members and stresses computed. Depending on the particular DFC, the load path includes components such as the container sleeve and collar, various weld configurations, load tabs, closure components and lifting bolts. Axial plus bending stresses were computed, together with applicable bearing stresses and weld stresses. Comparison with appropriate allowable strengths at temperature was performed. Input data for all applicable DFC's came from the drawings. The design temperature for lifting evaluation was 150°F (since the DFC is in the spent fuel pool). The design temperature for accident conditions is 725°F.*

*For the SNC-designed Trojan Failed Fuel Can, the existing calculations prepared by SNC were reviewed by Holtec and determined to bound the loadings applicable to the HI-STAR 100 System. Therefore, no new calculations were prepared for the Trojan Failed Fuel Can.*

### *2.B.3 Acceptance Criteria*

*The upper closure assembly must meet the requirements set forth for special lifting devices used in nuclear applications [1]. The remaining components of the damaged fuel canister are governed by the stress limits of the ASME Code Section III, Subsection NG and Section III, Appendix F, as applicable [2].*

*2.B.4 Assumptions*

*Buckling is not a concern during an accident since during a drop, the canister will be supported by the walls of the fuel basket.*

*The strength of welds is assumed to decrease the same as the base metal as temperatures increase.*

*An inertia load factor 1.15 is applied to all loads during a lifting analysis, except for the lifting analysis of the Trojan failed fuel can which assumes a 10% dynamic load factor.*

*2.B.5 Summary of Results*

*Table 2.B.1 presents minimum safety factors for each DFC from among all of the computations and evaluations performed on the different damaged fuel canisters to be certified for transport in the HI-STAR 100 System.*

*2.B.6 References*

*[1] ANSI N14-6-1993, "American National Standard for Special Lifting Devices for Shipping Containers Weighing 10,000 Pounds (4,500 kg) or More for Nuclear Materials", ANSI, Inc.*

*[2] ASME Boiler and Pressure Vessel Code, Section III, Subsection NG and Appendix F, 1995.*

*Table 2.B.1*

*SUMMARY OF SAFETY FACTORS FOR DAMAGED FUELCONTAINERS*

| ***Unit – (Maximum weight including contents -lbs)*** | ***Component*** | ***Calculated Stress (ksi)*** | ***Allowable Stress (ksi)*** | ***Safety Factor = (Allowable Value)/(Calculated Value)*** | ***Remarks*** |
|---|---|---|---|---|---|
| *Holtec-designed Dresden/HB BWR DFC* | *Lifting – Upper Closure Assembly* | *1.687* | *1.9251* | *1.141* | *Allowable weld stress includes a 0.35 quality factor* |
| | *60g end drop* | *10.667* | *37.920* | *3.6* | *Level D stress limits* |
| *Transnuclear DFC (550 lb.)* | *Lifting – Lid Frame Assembly* | *0.526* | *4.583* | *8.7* | *Bearing Stress* |
| | *60g end drop* | *12.316* | *37.920* | *3.1* | *Level D stress limits* |
| *Dresden Thoria Rod Canister (390 lb.)* | *Lifting – Lid Frame Assembly* | *0.3735* | *4.583* | *12.27* | *Bearing Stress* |
| | *60g end drop* | *8.733* | *37.920* | *4.3* | *Level D stress limits* |
| *Holtec-designed Trojan DFC (1680 lb.)* | *Lifting – Lifting Bolt* | *13.702* | *25.000* | *1.825* | |
| | *60g end drop* | *11.618* | *26.586* | *2.3* | *Spot welds* |
| *Trojan Failed Fuel Can* | *Lifting – Lifting Bar* | *6.2* | *6.37* | *1.03* | *Bending Stress* |
| | *124g end drop* | *9.1* | *16.0* | *1.76*[†] | *Level D stress limits* |

[†] *Conservatively based on bounding 124g vertical end drop used in SNC calculations. Per Table 2.1.10, the design basis deceleration for the HI-STAR 100 is 60g.*